Spatially-induced Momentum Transfer over Water-worked Gravel Beds

Volume 1

James Russell Cooper

A thesis presented for the degree of Doctor of Philosophy

The University of Sheffield
Department of Civil and Structural Engineering

September 2006

Summary

The spatial variability in turbulent flows over water-worked gravel beds has been studied. Spatially distributed measurements of velocity were obtained using Particle Image Velocimetry for a range of hydraulic conditions over two water-worked gravel beds. A different approach to bed formation was achieved by feeding sediment into a flume to form deposits that result from the arrangement of the grains by the flow, as would be observed in a river.

It was shown that, even over macroscopically flat deposits, time-averaged streamwise velocities display considerable spatial variability. However, the level of variability was a magnitude lower for time-averaged vertical velocities. The degree of spatial variability in both streamwise and vertical velocities was shown to increase with relative submergence. Spatial flow variability was present in the logarithmic and outer regions of the flow, which contradicts previous thinking that spatial variability is only present in the near bed form-induced sublayer. The time-averaged flow velocities displayed a considerable degree of organisation over both beds, indicating the existence of spatially coherent time-averaged flow structures.

Form-induced stresses caused by the spatial heterogeneity in the flow were estimated. These were found to be significant for flows over both beds, and did not disappear above the form-induced sublayer as previously thought. Measurements of Reynolds stress alone, whether spatially-averaged or not, cannot be used to determine the mean bed shear stress over water-worked gravel beds. Increases in relative submergence resulted in changes in the level of momentum carried by spatial deviations in the flow, and by inference, those carried by the turbulent fluctuations. This occurred even when the average rate of momentum transfer at the bed was the same. It was concluded that relative submergence could have a more important influence on the spatial variability of fluid stresses than the bed surface topography of water-worked gravel deposits.

Acknowledgements

I wish to express my gratitude for the support, advice and encouragement given by Dr. Simon J. Tait during his supervision of this thesis. I would like to thank him for the opportunity to undertake this research, his unwavering investment of time into the project, and continuing guidance beyond.

In addition, I wish to acknowledge the thoughtful and insightful comments and suggestions of my second supervisor, Professor Robert I. Ferguson

The excellent technical assistance I received was gratefully appreciated, in particular that of Mr. Mick Moore and Mr. David Hobart who were always on hand to offer assistance when I needed it most.

The financial support for this study was provided by a University of Sheffield Project Studentship.

I would like to thank my parents, my partner Miss. Lucy Davison and friend Mr. David Johnson for their love and support which sustained me through the course of this thesis.

This thesis is dedicated to the loving memory of Mr. George Arnold Henry Taylor.

CONTENTS

	Contents	Page No.
1	INTRODUCTION	1
1.1	Background	1
1.2	Prediction Methods	1
1.3	Objectives of this Study	4
2	LITERATURE REVIEW	5
2.1	Introduction	5
2.2	Spatial Variability in Time-averaged Flows over Water-worked Gravel Beds	6
2.3	Characterising Momentum Transfer over Water-worked Gravel Beds	13
2.4	Theoretical Limitations of using the Reynolds Equations for Characterising Momentum Transfer over Water-worked Gravel Beds	15
2.5	Errors Associated with the use of the Reynolds Equations for Characterising Momentum Transfer over Rough Boundaries	17
2.5.1	Water-worked Sand Beds	19
2.5.2	Dune-shaped Bedforms	20
2.5.3	Regular Roughness Elements	22
2.5.4	Water-worked Gravel Beds	24
2.6	Double-averaged Navier-Stokes Equations	26
2.6.1	Formulation	26
2.6.2	Advantages over Reynolds Equations	35
2.7	Form-induced Stress over Rough Boundaries	38
2.7.1	Water-worked Gravel Beds	39
2.7.2	Vegetation Canopies	43
2.7.3	Urban-like Canopies	46
2.7.4	Dune-shaped Bedforms	49
2.7.5	Regular Roughness Elements	52

2.8	Why has the Significance of Spatial Variability in the Flow over Water-worked Gravel Beds been Largely Ignored?	53
2.9	Potential Implications	55
2.10	Outcome of Literature Review	57
3	EXPERIMENTAL APPARATUS AND PROCEDURES	61
3.1	Outline of Experimental Programme	61
3.2	Laboratory Channel Apparatus	62
3.3	Particle Image Velocimetry	62
3.3.1	Introduction	62
3.3.2	Apparatus	64
3.3.3	Experimental Arrangement	66
3.3.4	Image Processing Routines: Cross-correlation	71
3.3.5	Image Processing Routines: Validation	74
3.3.6	Measurement Accuracy and Resolution	75
3.4	Bed Surface Topography Measurement	76
3.5	Bed Production	77
3.5.1	Sediment Mixtures	77
3.5.2	Methods of Bed Production	79
3.5.3	Sediment Feeding as a Method of Bed Production	80
3.6	Bed Surface Properties	83
3.6.1	Digital Elevation Models	83
3.6.2	Probability Density Function of the Bed Surface Elevations	87
3.6.3	Second-order Structure Functions of the Bed Surface Elevations	90
3.7	Experimental Procedures	98
3.7.1	Experimental Phases	98
3.7.2	Particle Image Velocimetry Measurements	102
3.7.3	Mean Velocity Characteristics	108
3.8	Summary	114
4	THE SPATIAL VARIABILITY IN TIME-AVERAGED STREAMWISE VELOCITY	116
4.1	Introduction	116

4.2	Distribution of Time-averaged Streamwise Velocities over the Bed	116
4.2.1	Degree of Spatial Variability	119
4.2.2	Skewness	121
4.2.3	Kurtosis	123
4.2.4	Degree of Normality	124
4.3	Vertical Distribution in the Degree of Spatial Variability	125
4.4	Parameterisation of the Degree of Spatial Variability	130
4.5	Variability in the Degree of Spatial Variability with Relative Submergence	131
4.5.1	Absolute Spatial Variability	131
4.5.2	Relative Spatial Variability	134
4.6	Variability in the Degree of Spatial Variability with Bed Slope	135
4.6.1	Absolute Spatial Variability	135
4.6.2	Relative Spatial Variability	138
4.7	Variability in the Degree of Spatial Variability Under Conditions of Constant Bed Shear Stress	139
4.7.1	Absolute Spatial Variability	141
4.7.2	Relative Spatial Variability	144
4.8	Does Relative Submergence or Bed Slope have the Greater Influence on the Degree of Spatial Variability?	145
4.8.1	Absolute Spatial Variability	146
4.8.2	Relative Spatial Variability	150
4.9	The Pattern of Spatial Deviations over the Bed	155
4.9.1	Unimodal Bed	156
4.9.2	Bimodal Bed	165
4.10	Vertical Change in the Pattern of Spatial Deviations over the Bed	167
4.10.1	Unimodal Bed	168
4.10.2	Bimodal Bed	184
4.11	The Relationship between the Pattern of Spatial Deviations and Bed Surface Topography	186
4.11.1	Visual Examination	186
4.11.2	Cross-correlation	187
4.12	Summary	194

5	THE SPATIAL VARIABILITY IN TIME-AVERAGED VERTICAL VELOCITY	197
5.1	Introduction	197
5.2	Distribution of Time-averaged Streamwise Velocities over the Bed	197
5.2.1	Degree of Spatial Variability	198
5.2.2	Skewness	200
5.2.3	Kurtosis	202
5.2.4	Degree of Normality	202
5.3	Vertical Distribution in the Degree of Spatial Variability	203
5.4	Parameterisation of the Degree of Spatial Variability	206
5.5	Variability in the Degree of Spatial Variability with Relative Submergence	210
5.5.1	Absolute Spatial Variability	212
5.5.2	Relative Spatial Variability	213
5.6	Variability in the Degree of Spatial Variability with Bed Slope	214
5.6.1	Absolute Spatial Variability	214
5.6.2	Relative Spatial Variability	217
5.7	Variability in the Degree of Spatial Variability Under Conditions of Constant Bed Shear Stress	219
5.7.1	Absolute Spatial Variability	221
5.7.2	Relative Spatial Variability	223
5.8	Does Relative Submergence or Bed Slope have the Greater Influence on the Degree of Spatial Variability?	224
5.8.1	Absolute Spatial Variability	225
5.8.2	Relative Spatial Variability	228
5.9	The Pattern of Spatial Deviations over the Bed	231
5.9.1	Variability with Relative Submergence	232
5.9.2	Variability with Bed Slope	239
5.9.3	Variability with Under Conditions of Constant Bed Shear Stress	245
5.10	Lateral Variability in the Pattern of Spatial Deviations over the Bed	248
5.10.1	Unimodal Bed	248
5.10.2	Bimodal Bed	250

5.11	Vertical Scaling of the Pattern of Spatial Deviations over the Bed	251
5.12	The Relationship Between the Pattern of Spatial Deviations and Bed Surface Topography	255
5.13	Possible Interaction Between the Pattern of Spatial Deviations and the Water Surface	268
5.14	Spectral Analysis of the Dynamics of Turbulent Water Surfaces	273
5.14.1	Variability with Relative Submergence	274
5.14.2	Variability with Bed Slope	280
5.14.3	Variability with Under Conditions of Constant Bed Shear Stress	285
5.14.4	Scaling	287
5.15	Potential Significance of Changes in the Water Surface	288
5.16	Summary	293
6	FORM-INDUCED STRESS OVER WATER-WORKED GRAVEL BEDS	295
6.1	Introduction	295
6.2	Deriving Form-induced Stress	295
6.3	Quantifying Form-induced Stress	301
6.4	Vertical Distribution of Form-induced Stress	303
6.5	Variability in Form-induced Stress with Relative Submergence	308
6.6	Variability in Form-induced Stress with Bed Slope	311
6.7	Variability in Form-induced Stress Under Conditions of Constant Bed Shear Stress	313
6.8	Does Relative Submergence or Bed Slope have the Greater Influence on Form-induced Stress?	317
6.9	Lateral Variability in the Form-induced Stress over the Bed	319
6.10	Form-induced Stress at the Point Measurement Scale	325
6.11	Spatial Variability in Form-induced Stress over the Bed at the Point Measurement Scale	328
6.12	The Relationship Between the Form-induced Stresses at the Point Measurement Scale and Bed Surface Topography	329
6.13	The Effect of Averaging Area on the Estimation of Form-induced Stress	331

6.14	Averaging Area Required for a Representative Estimate of Form-induced Stress	341
6.14.1	Definition	341
6.14.2	Variability with Relative Submergence	345
6.14.3	Variability with Bed Slope	346
6.14.4	Variability with Under Conditions of Constant Bed Shear Stress	347
6.14.5	Parameterisation	350
6.14.6	Interpretation	355
6.14.7	Relationship with Observational Scale	359
6.15	Summary	361
7	DISCUSSION: THE PHYSICAL SIGNIFICANCE OF FORM-INDUCED STRESS AND SPATIAL VARIABILITY IN THE TIME-AVERAGED FLOW FIELD	363
7.1	Introduction	363
7.2	Is Spatial Variability Form-induced or an Inherent Property of the Flow?	363
7.2.1	Evidence Against Spatial Variability Being Form-induced	366
7.2.2	Evidence For Spatial Variability Being Form-induced	368
7.3	Physical Interpretation of Form-induced Stress	371
7.4	Implication for Point Measurements	373
7.4.1	Quantifying Variables Derived form Spatial-averaging	373
7.4.2	Number of Point Measurements Required to Quantify Accurately Variables Derived from Spatial Averaging	377
7.5	Potential Implications for Solute and Suspended Sediment Transport	379
7.6	Implications for Bedload Transport	382
7.6.1	The Effect of Spatial Variability in the Time-averaged Flow Field	382
7.6.2	The Effect of Relative Submergence	387
7.7	Summary	394
8	CONCLUSIONS	397
9	FURTHER WORK	402

9.1 Introduction 402
9.2 Approaches Using Existing Data 402
9.3 Approaches Using Additional Data 405

REFERENCES 408

NOTATION 424

CHAPTER 1
INTRODUCTION

1.1 Background

Rivers convey water, sediment and solutes from the natural landscape, together with pollutants from rural and urban areas. They provide distinctive and valuable ecological habitats, whose protection and enhancement are now enshrined in E.U. and U.K. legislation through the Water Framework Directive. Rivers have an important economic role in our society, with great significance for drainage, irrigation and navigation. Environmental engineers and managers require information on the upstream characteristics of a river, but they must also understand the details of in-channel flow at a point within the river, since this controls sediment and pollutant transport, as well as being a key aspect of ecological habitats. Traditional engineering hydraulics treat river flows in 1-D (cross-sectional averaged), but many emerging issues require an understanding of 2-D or even 3-D flow characteristics, including those relating to the turbulence which all rivers possess. This thesis is a contribution to understanding 3-D turbulent flow.

1.2 Prediction Methods

River flow is, in principle, fully described by the Navier-Stokes equations of conservation of mass and momentum together with an appropriate continuity equation and the thermodynamic equation of state. These Navier-Stokes equations can be written in 3-D, but are often simplified to 2-D (depth-averaged) or 1-D. In the full 3-D version turbulence is usually represented statistically as being random fluctuations around a time-average, following Osborne Reynolds suggestions in 1895. When the Navier-Stokes equations are time-averaged (Reynolds-averaged) and supplemented by this decomposition, the products of the fluctuating velocities give rise to an additional turbulent stress term, the Reynolds stress, which, in practice, represents the momentum transfer by turbulence. In this Reynolds-averaged approach, on which most Computational Fluid Dynamics (CFD) models are based, turbulence is assumed to be spatially and temporally homogeneous. However, there is mounting evidence that the

flow is both temporally and spatially coherent (see for example Ashworth *et al.*, 1996) and there is much speculation over whether this structure in the flow is induced by the details of the bed microtopography, or is an intrinsic property of turbulent flow.

There is an increasing need to understand the fate of soluble pollutants once they enter a river and to quantify effluent mixing. This is important for operating flow discharges and designing biological and chemical monitoring in order to comply with current water quality regulations. The Reynolds-averaged approach has led to the development of numerical models for the prediction of pollutant transport based on the assumption that the flow is laterally and vertically uniform. The limitations imposed by the Reynolds decomposition of the flow have meant that the information on spatial variability in the flow has yet to be fully incorporated into prediction methods. For example, the models have assumed that shear stress is simply equal to the Reynolds stress, which does not reflect the spatial nature of turbulence, and they make no explicit consideration of the influence of spatial patterns in the flow on transport and accumulation. Clearly new prediction techniques are required for the modelling of solute transport processes. Fundamental to the development of such tools is a better understanding of the spatial patterns in the flow, and how this spatial heterogeneity is influenced by hydraulic and bed conditions.

The impact of pollutants on the ecology of a river is dependent on the local spatial patterns within the flow, because it controls the accumulation and transport of pollutants at a scale similar to the ecology of the river. However, there is a lack of good predictive hydraulic tools for local scale flow dynamics. Therefore by understanding spatial flow patterns it will also be possible to obtain information on the flow at scales that are important to the ecology of a river. This knowledge will be useful in developing tools that can assess the ecological impact from pollutants being released into rivers.

Fundamental to these prediction methods is an ability to describe accurately the resistance imposed by a river bed on the flow. Most flow resistance prediction methods are based on a modification of fluid relationships derived from 1-D approaches, which assume that the flow and the bed surface are laterally and vertically homogeneous. This has led to some flow resistance models taking into account the resistance imposed by the bed on the flow by using a representative grain-size, and by making empirical adjustments to the law of the wall to correct any discrepancies in model predictions.

Therefore models have been developed based on the assumption that the effect of the bed on the flow is spatially constant and has the same effect at all flows. This has led to difficulties in accurately predicting flow depth at a given discharge within rivers of varying morphologies. These approaches have made little consideration of the flow processes occurring within a river and the influence they have on momentum transfer. In order to understand the resistance imposed by a river bed on the flow it is clear that an understanding is required of the spatial structure of the flow, and how this affects the transfer of momentum. Only by quantifying the degree of spatial variability in the flow can true assessments be made of the validity of existing flow resistance models that assume spatially homogenous flow.

The majority of sediment transport prediction methods rely, to some greater or lesser extent, on some kind of empirically based relationship which relates the ability of the flow to move sediment and the ability of the sediment, both moving and stationary, to remove momentum from the moving body of fluid. Most calculations of sediment transport rate, including those in numerical models of aggradation and degradation, are 1-D, whereby the flow is taken to be spatially homogeneous over the bed. Therefore a reliable prediction of the effect of spatial variability in the flow on momentum transfer mechanisms will also improve the prediction of sediment transport, and ultimately morphological change.

Observations of spatial patterns in the flow and the influence of this on momentum transfer under different hydraulic and bed conditions are required to provide an indication of the river situations in which traditional 1-D or 2-D approaches are inappropriate for predicting flow depth, pollutant and sediment transport and for assessing the ecological impact from pollutants. This is imperative for successful implementation of the Water Framework Directive. Once understanding based on these observations has been achieved, reliable numerical models can be constructed which model actual physical flow mechanisms, in contrast to those which are just fitted to known datasets. The ability, therefore, to characterise the 3-D nature of the flow forms an important component of the future management of rivers.

1.3 Objectives of this Study

In this study detailed and high spatial resolution measurements of the flow are made in the laboratory over water-worked gravel beds. A different approach is taken to forming gravel beds within the laboratory flume, in order to produce beds more representative of natural gravel-bed rivers. Sediment is fed into a flume to form sediment deposits that result from the arrangement of the grains by the flow, as would be observed in a river. A range of flow depths and bed slopes are investigated so that changes in the spatial structure of the flow can be related to hydraulic conditions. The relationship between the spatial patterns and the bed surface topography is examined by taking grain-scale measurements of the bed surface topography. The potential of these spatial patterns for transferring momentum within the flow is assessed.

The ultimate aim of this work is to develop relationships which are able to account explicitly for spatial variability within the flow, and how this changes with hydraulic and bed conditions.

CHAPTER 2
LITERATURE REVIEW

2.1 Introduction

Turbulent flow has been classically viewed as statistically random. This led to the expectation that turbulence could be clarified experimentally by performing a single point velocity measurement, and describing it by means of conventional statistical tools (Nezu and Nakagawa, 1993). It envisaged turbulence as a stochastic phenomenon, arising from the superposition of individual quasi-periodic fluid motions over a wide range of scales (Clifford and French, 1993). Nowadays it is well established that turbulent flows are far from random, and exhibit a remarkable degree of coherence in time and space. For water-worked gravel beds, initial efforts concentrated on describing the bursting phenomenon that existed within this structure. In particular, investigations were made of the manner in which ejections and sweeps impart intermittency in momentum transfer over water-worked gravel beds. Most recently the use of flow visualisation (e.g. Kirkbride, 1993; Roy *et al.*, 1999; Schvidchenko and Pender, 2001) and networks of point velocity measurements (e.g. Ferguson *et al.*, 1996; Buffin-Bélanger *et al.*, 2000; Roy *et al.*, 2004) over gravel bed surfaces have enabled researchers to turn their attention to the spatial structure of flow. In particular, many studies have reported on the existence of vortically-based, large-scale flow structures over water-worked gravel surfaces. The generally accepted model for these structures is the presence of cyclic and alternating patterns of large regions of faster and slower moving wedges of fluid, which occupy a large portion of the flow depth and extend into the outer layer of the flow (Kirkbride and Ferguson, 1995; Ferguson *et al.*, 1996; Buffin-Bélanger *et al.*, 2000; Schvidchenko and Pender, 2001; Roy *et al.*, 2004).

This increasing recognition of spatial coherency within the flow has promoted a greater interest in understanding if the spatial nature of flows influences the processes occurring within gravel-bed rivers. This has led to a greater need to characterise the spatial variability in transport processes so that spatially-derived relationships can be sought between the flow and these processes. For example, many studies have quantified the degree of spatial variability in bedload transport (e.g. Drake *et al.*, 1988: Gomez, 1991;

Konrad *et al.*, 2002), suspended sediment transport, solute transport (e.g. Boxall and Guymer, 2003; Guymer *et al.*, 2005) and in the ecological structure (e.g. Bouckaert and Davis, 1998; Lancaster, 1999; Matthaei and Huber, 2002). It has therefore become increasingly important that information is gathered on the spatial nature of flows over water-worked gravel beds. So far the majority of studies have concentrated on how spatial variability in the instantaneous flow field influences momentum transfer. Thus the characterisation of the spatial variability in the time-averaged flow field, and the potential influence this has on momentum transfer, has almost totally been neglected.

2.2 Spatial Variability in Time-averaged Flows over Water-worked Gravel Beds

This neglect has occurred even though it has long been known that there is some degree of spatial variability in the vertical profiles of time-averaged streamwise velocity over the bed (Wiberg and Smith, 1991). For example, Clifford (1996) examined the spatial variability in vertical velocity profiles within pools and riffles. He used an Electromagnetic Current Meter (ECM) to measure flow velocities, at four different flow stages within the River Hodder, which were grouped into low and high discharges. The time-averaged streamwise velocities were found to be up to 10 times higher at one location than another within a riffle unit at a given flow. This was even greater within a large pool unit, with over a 13 fold difference between locations being discovered. The spatial variability was always greater in large pools and riffles than smaller units. On the whole this variability increased with discharge within a given riffle or pool. However, he only carried out measurements at three relative heights above the bed, and was not able to characterise the near-bed velocities. Also this study was not able to examine if there is any lateral variability in velocities across the bed. Clifford stated that the spatial variability in time-averaged streamwise velocities was due to the effects of the microtopography of the bed surface on the flow.

This relationship between the flow and the bed was further examined by Buffin-Bélanger and Roy (1998) in Eaton North River, a gravel-bed river in Québec, Canada. They examined the flow characteristics upstream and downstream of a single pebble cluster using velocity measurements from an ECM. They found that upstream of the cluster, the time-averaged streamwise velocities increased with distance above the bed and the time-averaged vertical velocities revealed that the flow was mainly moving

down towards the bed. On top of the cluster, the flow was accelerated as water depth was reduced, and the flow reversed from moving downward to experiencing significant upward motion. In the proximal downstream section, where the flow expanded, the time-averaged streamwise velocities were highly reduced and the flow was recirculated in the lee of the cluster, where a small zone of separation was present. For the distal downstream section, the time-averaged streamwise velocities were similar to the upstream section, although the maximum velocity was not as high. The result was that locally, time-averaged streamwise velocities varied by as much as half of that experienced elsewhere in the flow, and the time-averaged vertical velocities displayed slightly higher degrees of variability. Yet again the lateral variation in the time-averaged flow was not measured. Very similar degrees of variation in time-averaged streamwise velocities were also found by Smart (1999) in five gravel-bed rivers in New Zealand using an electronic pilot tube, but this time measuring a cross-section of the flow rather than a transect, showing that time-averaged streamwise velocities also vary laterally.

Lawless and Robert (2001) also investigated the effect of pebble clusters on the flow but this time in a laboratory flume, enabling a more detailed study of the flow. Two of the beds they examined were a plane bed, and a plane bed on which large pebble clusters were superimposed. An Acoustic Doppler Velocimeter (ADV) probe was used to take a number of point measurements over the bed surfaces. Vertical velocity profiles were shown to be highly variable even along a transect of the plane bed. Both the magnitude and gradient of the time-averaged streamwise velocities varied greatly, as a function of position (and therefore the underlying bed surface topography) along the transect over each of the bed surfaces. On the plane bed, flow was locally accelerated above the larger particles, and large deceleration occurred in a zone of flow separation downstream of the large protruding particles. Some velocities close to the bed were nearly zero, and this was probably due to increased Doppler noise in the ADV signal, which has been shown to affect greatly the second-order moment statistics (Kim *et al.*, 2000). They found that the time-averaged streamwise velocities could be nearly 13 times larger at one location relative to another. Over the pebble clusters, flow acceleration occurred up the stoss-side of the cluster, and flow separation just downstream of the cluster. This caused the time-averaged streamwise velocities to be as much as 16 times greater at the stoss in comparison to the wake. This spatial variability was however not found to be related to flow depth, in contrast to that found by Clifford (1996).

Lawless and Robert (2001) only took velocity measurements along one transect of the plane bed, "given the lack of protuberant clasts and the consequent absence of significant lateral flow". Yet it seems doubtful that one transect, over what appears to be a complex bed of mixed grain-sizes, fully characterised the spatial patterns over the bed. This is especially given that the ratio of the width of the flume to the D_{50} of the bed mixture was only equal to 48, so the flow is likely to have been dominated by the influence of individual roughness elements, as indeed they describe. They report that their measurements had a high degree of spatial resolution, but it is questionable whether a density of 10 measurements per metre along a transect is a considerably high density. There is also doubt that the beds they used could be considered, as they describe, "natural roughness features" (Lawless and Robert, 2001). The plane bed was artificially placed in the flume and was not water-worked. Furthermore, the pebble clusters were artificially created and placed on the bed at a considerably higher elevation than the surrounding bed, and consisted of clasts much larger than the surrounding material. They were placed in a regular pattern and occupied a high proportion of the width of the flume, but aimed to "emulate natural conditions" (Lawless and Robert, 2001). There is therefore some concern over whether the results presented were representative of what would be found in a gravel-bed river.

A similar effect of large clasts on the time-averaged flow was described by Lane *et al.* (2002; 2004). They report laboratory experiments conducted over a water-worked gravel surface using ADV's, but only at a reasonably low spatial resolution, and they use these measurements to validate a Computational Fluid Dynamics (CFD) model of the flow. Their laboratory and model results further confirm that there can be significant spatial variation in the time-averaged flow in the near-bed region. Upstream of a large particle, there was a clear streamwise velocity gradient and upwelling. The upwelling was strongest where there was a weak stagnation point, indicated by a zone of very slow streamwise velocity and a steep streamwise velocity gradient above this. At the highest point of the protruding particle the core of high velocity extended almost to the bed and the magnitude of upwelling decreased. Downstream of this, the streamwise velocity gradient was reduced and there was strong downwelling in the lee of the particle. The influence of topographic variation on the time-averaged streamwise velocities was limited to essentially the bottom 25 % of the flow. The high time-averaged vertical velocities could approach 40 % of the maximum streamwise velocity, and were associated with local topographic variability. These high velocities were restricted to the

bed, generally in the bottom 5 % of the flow. Yet their laboratory experiments once again involved a low width of flume to D_{50} ratio of 15, meaning that the flow was controlled by isolated roughness elements. Furthermore their flows were likely to be heavily influenced by secondary flows, given that the width of flume to flow depth ratio was 1.25.

More recently the effect of an isolated boulder on the flow has been investigated by Tritico and Hotchkiss (2005) within the field. By carrying out ADV measurements within the South Fork of Clear Water River, a gravel-bed river in Idaho, USA, they found that in the wake of the boulder the time-averaged streamwise velocities were as low as 5% of that further downstream.

McLelland *et al.* (1999) showed how the formation of coarse and fine sediment stripes on a bed composed of a weakly bimodal gravel-sand mixture could also influence the time-averaged flow field. Using a dense network of LDA measurements, they found that the time-averaged streamwise velocities were 25 % higher over the fine stripes. The time-averaged vertical velocities also displayed spatial variability. The prevailing pattern was one of downflow over the central parts of the coarse stripes and an upwelling of flow between the boundary between the coarse and fine stripes. This meant that the time-averaged vertical velocities displayed considerable spatial variability over the bed.

In another set of ECM measurements carried out in Eaton-North River, Roy *et al.* (2004) found that time-averaged streamwise velocity along a transect could vary by as much as 80 % from one location to another. However, the number of measurements along this transect was low. Carling *et al.* (2002) also found very similar differences in velocity within a cross-section of the River Severn, demonstrating that the time-averaged velocities also vary laterally. This was a roughly straight reach of a natural compound channel with a gravel bed and banks with predominately grass covered gravel and silt. It must be noted that the comparisons in velocity between different locations involved measurements that were very well separated in space and had significant differences in flow depth. Also the velocity measurements are likely to have been influenced by secondary currents within the channel.

Byrd *et al.* (2000) have also shown that lateral variations occur in time-averaged velocities. Within North Boulder Creek, Colorado, a coarse gravel and cobble-bedded river, velocity measurements were taken using a current meter at 60 positions, which involved 12 cross-section lines spaced at one metre intervals. Vertical velocity profiles varied within a cross-section from being approximately logarithmic, s-shaped, irregular and approximately linear, which led to one location having double the time-averaged streamwise velocity of that at another location close to the bed. However, it is important to note that this involved a low spatial resolution of measurements, using a velocimeter that can be heavily influenced by high turbulence intensity.

Very similar measurements were also made by Papanicolaou and Hilldale (2002) within a cross-section of Union Flat Creek, Washington, USA. They discovered that close to the bed time-averaged streamwise velocities were as much as four times higher at one location in comparison to another, and up to two times higher close to the water surface. This was concluded to be due to isolated bed roughness and secondary flow currents. The time-averaged vertical velocities also demonstrated considerable spatial variability. They could be as much as two times higher at one location than another, both close to the bed and close to the water surface. Time-averaged lateral velocities displayed even greater spatial variation, with velocities being up to six times higher at one location in comparison to another. These results were from using ADV measurements at only seven different positions within the channel, and were influenced by secondary currents. Despite this, the results again demonstrate that the time-averaged flow field can vary in the lateral direction.

More recently, Legleiter *et al.* (in press) made a more explicit attempt to examine spatial variability in time-averaged flows. They carried out ADV measurements within North Folk Cache La Pudre River, Colorado, a cobble-bedded river. This was performed over a riffle at three different discharges. The effect of individual boulders was again described, with time-averaged streamwise velocities being very low or even negative in their lee. Flow depth was shown to have little influence on the degree of spatial variability in streamwise velocities over the reach, and to have only a slight effect on its spatial distribution. The results showed that time-averaged streamwise velocity at one location could be as much as 12 times higher than at another location in both the streamwise and lateral direction. By using a semivariogram with different streamwise and lateral lag distances, they report that at the shallowest depth the spatial pattern of

the time-averaged streamwise velocities was "rougher", demonstrating the localised effects of roughness elements. However at the highest flow depth, the spatial structure was "smoother", because the effects of the roughness diminished. This was based on only five lag distances, so the conclusions have to be taken tentatively. Furthermore, the fitted lines to the data points are, in some cases, highly questionable.

The time-averaged vertical velocities also displayed considerable spatial variability within the reach, with their spatial distributions showing a degree of dependence on flow depth. At the low and mid submergences some areas of upwelling were discovered within the main thalweg and either slight downwelling or negligible vertical velocities occurred along its margin. Several large values were observed in association with large roughness elements. At the highest flow depth, the flow in the thalweg reversed from upwelling to downwelling. The semivariograms suggested that the spatial structure of time-averaged vertical velocity at lower flows was dominated by small-scale processes such as flow separation and eddy shedding, associated with large roughness elements. Yet this is based on a fit to only five semivariance values. At all three flow depths, downwelling occurred upstream of a large boulder and upwelling occurred around its edges.

The spatial distributions of time-averaged lateral velocities were also shown to have some dependence on flow depth, with an increase in submergence causing progressively higher velocities toward the left bank. They showed that the flow was moving in opposing directions within the reach, and a similar degree of variation in time-averaged lateral velocities could occur both in the streamwise and lateral direction.

Legleiter *et al.* (in press) were the first to attempt to relate quantitatively the spatial patterns in the time-averaged flow field to the bed roughness. This was performed by computing cross-correlograms between the bed roughness and each of the time-averaged velocity components. By applying different streamwise lags, they indicated that there was a strong stage-dependent effect of local boundary roughness on the time-averaged flow. The effects of roughness on time-averaged streamwise velocity diminished, on averaged, within a streamwise distance of 1.5 m for the two highest flow depths, beyond which no clearly-defined relationship with bed roughness was found. Again this was only based on five streamwise lags. By applying a lateral lag, they discovered that the cross-correlation between the velocities and bed roughness increased

with flow depth, suggesting that the flow became more spatially coherent as stage increased. For the time-averaged vertical velocities, the correlation was not as strong or stage-dependent as for the time-averaged streamwise velocities. The highest correlation was at the mid flow depth, with the correlation being essentially identical for low and high flow depths. The correlation was higher at the mid depth due to upwelling that developed in the deeper flow in the thalweg, where bed roughness was also greatest. Neither the streamwise or lateral spatial structure in the velocities were well developed for any of the three submergences. Indeed, the erratic change in the correlation coefficient with lateral lag was concluded to indicate a very localised interaction between vertical velocities and individual clasts as flow was separated and eddies shed. The correlation between bed roughness and the time-averaged lateral velocities was not dependent on flow stage. On the whole, the correlation between bed roughness and each of the time-averaged velocity components was discovered to be weak at all three discharges. Yet they claim the results demonstrate that the flow field at the small-scale is influenced by topographic variability at high spatial frequencies, most noticeable at lower depths, and that the overall large-scale flow pattern primarily reflects the bulk morphology of the channel. This influence is said to change with flow depth, such that the localised influence of bed surface topography is increasingly smoothed out as flow depth increases.

However, because of the low spatial resolution of velocity measurements within the reach and the low number of bed roughness measurements on which to relate these measurements of velocity, their conclusions may not be well supported. The effects of bed roughness on the flow could only be very coarsely determined. It is unlikely that this study has represented fully the spatial patterns in time-averaged flow within the reach. Furthermore, the assessment of the spatial patterns was based on averaging velocity measurements taken within a vertical profile at one location to give a single velocity value for that location over the bed. Often this was based on only one or two measurements in the profile, and it is unclear, at each location, how many values were averaged and the measurement height of these averaged values. The measurement height would heavily influence the averaged value. It could therefore be possible that the spatial variability observed was purely a facet of the variation in velocity with height above the bed surface. This may become clearer in the final published version of their study. Furthermore, measurements were not possible very close to the bed because of errors arising in the ADV measurements and problems with accurately positioning the

probe. It was difficult to attain a stage-dependent trend from only three discharges, and they acknowledge that at the mid discharge the flow patterns could not be well-defined because several of the measurements were discarded due to poor quality.

2.3 Characterising Momentum Transfer over Water-worked Gravel Beds

Despite this evidence of spatial variability in the time-averaged flow field, the traditional approach to studying flows over river beds has been based on the time-averaged Navier-Stokes equations. The Navier-Stokes equations are the fundamental equations of fluid flow and they describe the conservation of momentum for turbulent flows. These are specified in terms of an infinitesimally small control volume, such that the instantaneous momentum transfers in Cartesian-tensor notation can be represented by

$$\frac{\partial u_i}{\partial t} + u_j \frac{\partial u_i}{\partial x_j} = g_i - \frac{1}{\rho}\frac{\partial p}{\partial x_i} + \nu \frac{\partial^2 u_i}{\partial x_j^2} \tag{2.1}$$

where u is instantaneous velocity, t is time, x is distance, g is gravitational acceleration, p is fluid pressure, ρ is fluid density and ν is kinematic viscosity. Normally, when studying the flows over gravel beds, the interest is in averaged turbulence transport quantities rather than instantaneous quantities. Therefore equation (2.1) is averaged over an interval of time, which is small relative to the time-averaged flow but long relative to the scale of turbulent motion, to produce time-averaged Navier-Stokes equations, known more commonly as the Reynolds equations. This time-averaging is supplemented by a Reynolds decomposition of the turbulent flow into slowly varying mean and rapidly fluctuating parts. In other words, the velocity field is decomposed into time-averaged $\overline{u}$ and temporally fluctuating components u', such that $\overline{u} = u + u'$. The Reynolds equations are therefore given by

$$\frac{\partial \overline{u}_i}{\partial t} + \overline{u}_j \frac{\partial \overline{u}_i}{\partial x_j} = g_i - \frac{1}{\rho}\frac{\partial \overline{p}}{\partial x_i} - \frac{\partial \overline{u_i' u_j'}}{\partial x_j} + \nu \frac{\partial^2 \overline{u}_i}{\partial x_j^2} \tag{2.2}$$

$$\frac{\partial \overline{u}_i}{\partial x_i} = 0 \tag{2.3}$$

where the straight overbar denotes the time-average of the flow variables, and p is fluid pressure. Using this approach, the products of the fluctuating velocities give rise to a turbulent stress term $\overline{u_i' u_j'}$, the Reynolds stress. Equation (2.2) has been used, almost universally, for both modelling and experimental data interpretation of flows over gravel bed surfaces.

The right-handed coordinate system is adopted throughout the thesis. For a laboratory flume, the x-axis is orientated along the main flow parallel to the averaged bed slope (streamwise direction, u-velocity component), the y-axis is oriented to the left side of the flume looking downstream (lateral direction, v-velocity component), and the z-axis is orientated towards the water surface (vertical distance from an arbitrary origin, w-velocity component). The tensor notation used earlier, with the Einstein convention, means that x_i $(i = 1, 2, 3)$ corresponds to the directions x, y, and z; and u_i $(i = 1, 2, 3)$ corresponds to the velocity components u, v, and w. If consideration is given to the simplest case of two-dimensional, steady, uniform flow, which has a free surface parallel to the average bed slope, equation (2.2) reduces to

$$gS - \frac{\partial \overline{u'w'}}{\partial z} + \nu \frac{\partial^2 \overline{u}}{\partial z^2} = 0 \tag{2.4}$$

and

$$g \cos\alpha + \frac{1}{\rho} \frac{\partial \langle \overline{p} \rangle}{\partial y} + \frac{\partial \overline{v'w'}}{\partial y} + + \nu \frac{\partial^2 \overline{v}}{\partial y^2} = 0 \tag{2.5}$$

where S is the slope of the averaged bed surface, such that $S \approx \sin\alpha$, which can be considered to be equal to the streamwise slope of the water surface, if the flow is uniform. Equation (2.4) represents the time-averaged momentum equation in the streamwise domain and equation (2.5) in the vertical domain. The Reynolds stress $\overline{u'w'}$ arises because, although the time-averaged turbulent fluctuations are zero, the time-average of their squares and mixed products are not. The temporal fluctuations in velocity in any two directions are on average assumed to be inversely correlated. Therefore parcels of fluid moving towards or away from a rough boundary retain the majority of their streamwise momentum, and this mixes with the parcel of fluid that

preceded it at that location. This would cause the flow to accelerate if it were not retarded by the Reynolds stress. A positive u' is therefore associated with a negative w', and vice versa. The majority of the time, the product $u'w'$ is expected to be negative, and the stress resulting from these motions is positive. Reynolds stress is therefore a consequence of momentum transfer associated with turbulent mixing.

With an assumption of 2-D flow, the equations in the transverse domain disappear. Therefore, by integrating equation (2.4) from z to the water surface z_{ws} the following relationship for the total stress distribution τ is derived for the whole flow depth

$$\frac{\tau(z)}{\rho} = gS[z - z_{ws}] = \nu \frac{d\overline{u}}{dz}(z) - \overline{u'w'}(z) \tag{2.6}$$

where u_* is the bed shear velocity and d is the flow depth. It follows that the gravity force $gS[z - z_{ws}]$ is totally balanced by viscous drag and the Reynolds shear stress, and has been the assumption held by nearly all studies of flows over water-worked gravel beds.

2.4 Theoretical Limitations of using the Reynolds Equations for Characterising Momentum Transfer over Water-worked Gravel Beds

The Reynolds equations exist only for the simplest situation of strictly two-dimensional flow with no temporal variation (i.e. the time-averaged turbulent fluctuations are zero), where velocity gradients only exist in the vertical direction. Therefore only one length and one velocity scale are needed to describe the flow (Yaglom, 1979). Yet the assumptions that these time-averaged momentum equations make, and the limitations placed on their application to flows over water-worked gravel beds, makes the Reynolds equations inconvenient and impracticable. This is because they cannot account for the fact that the time-averaged flow structure is highly three-dimensional and spatially heterogeneous over water-worked gravel beds. As has been shown, velocity gradients exist both in the streamwise and lateral directions, as well as in the vertical direction, as the flow accelerates and decelerates over and around roughness elements. Thus the two-dimensional approximations, made when using the Reynolds equations to express the

total stress distribution within the flow, may not hold for the near-bed region. This can lead to errors in approximating the total fluid stress using equation (2.6) (see below).

The Reynolds equations are only able to relate point derived flow quantities, such as Reynolds stress, to local (point) flow properties. It is therefore not possible to link explicitly spatially-averaged parameters, whether of the fluid or the boundary, to these derived flow properties. Increasingly interest is in developing spatially-averaged parameters to characterise components of gravel bed flows. This need is largely a result of the recognition of the spatial complexity within rivers and the increasing ability to measure over large areas of space fairly rapidly. For example, the development of photogrammetric and laser scanning methods for obtaining bed elevation data (e.g. Butler *et al.*, 1998; 2002; Marion *et al.*, 2003; Smart *et al.*, 2004) has led to many studies attempting to produce a spatially integrated roughness coefficient for gravel-bed rivers that can adequately take into account the spatial heterogeneity in gravel bed surfaces (e.g. Furbish, 1987; Robert, 1988, 1990, 1991; Clifford *et al.*, 1992; Butler *et al.*, 2001; Nikora *et al.*, 1998; Aberle and Smart, 2003; Aberle and Nikora, submitted). However, since the Reynolds equations only derive local flow properties it has been difficult to exploit fully these new roughness characterisation techniques into flow resistance models. Furthermore the advent of velocity measurement techniques that are able to measure simultaneously velocity at many locations within the flow, such as Particle Tracking Velocimetry (PTV) and Particle Image Velocimetry (PIV), has resulted in a greater amount of spatial information on the flow being available. But the limitations imposed by the Reynolds equations has meant that this new information has yet to be fully utilised for characterising momentum transfer over water-worked gravel beds.

The Reynolds equations can account for the three-dimensional nature of the flow, but their estimation of shear stress can only account for the temporal variability in the flow. In some studies the spatial variability in the flow has been simulated by introducing the form drag as an extra body force term (e.g. Lane *et al.*, 2004). Such an approach introduces uncertainties in the interpretation of the modelling results because it does not arise because of rigorous derivation, but intuitive reasoning. Form drag is introduced to describe the generation of wake turbulence at length scales determined by roughness elements. Such a term suppresses turbulent kinetic energy (TKE), but the effect of form drag is to convert mean kinetic energy and large-scale, shear-generated TKE to TKE at

roughness element scales. Therefore, part of the normal inertial eddy cascade process is short-circuited, and causes acceleration in the dissipation rate for large-scale TKE close to the boundary (Wilson and Shaw, 1977; Raupach and Shaw, 1982). A modification such as this leads to a satisfactory momentum equation but does not adequately represent other effects on the roughness elements, since a retarding body force would have the effect of suppressing turbulence as well as extracting momentum from the flow (Wilson and Shaw, 1977).

Increasingly, to model turbulent flows over complex topographies, CFD using the time-averaged Navier-Stokes equations has been used (e.g. Hodskinson and Ferguson, 1998; Sinha *et al.*, 1998; Gessler *et al.*, 1999; Nicholas and Sambrook-Smith, 1999; Booker *et al.*, 2001; Lane *et al.*, 2002; Ferguson *et al.*, 2003; Wilson *et al.*, 2003; Lane *et al.*, 2004; Bates *et al.*, 2005). These studies have demonstrated that it is possible to simulate spatial variability flow velocity over rough boundaries. However, in their models this spatial variability has been induced by the use of complex descriptions of spatial variability in the bed geometry in the definition of the computational grid, rather than through accounting explicitly for the shear stress created by both turbulence and spatial variability in the time-averaged flow field.

The Reynolds equations also fail at a more intuitive level. For example, few studies would ever try to characterise a normal distribution without specifying both a mean and variance. Yet the Reynolds equations assume that one point with+in a whole distribution of velocities over the bed will be able to characterise the velocity field over the bed, and therefore the bed shear stress. The Reynolds equations provide no means of characterising the distribution of velocities. Raupach and Shaw (1982) claim that this forces experimentalists to assume that flow properties measured at one point are equal to those of the flow field spatially averaged over the whole bed.

2.5 Errors Associated with the Use of the Reynolds Equation for Characterising Momentum Transfer over Rough Boundaries

It will now be demonstrated that the assumptions made by the Reynolds equations can cause errors in the estimation of bed shear stress for rough beds. The majority of flows over rough boundaries have high Reynolds numbers, so the viscous drag term $\nu(\partial^2\overline{u}/\partial z^2)$ in equation (2.4) is often assumed to be negligible. Therefore, by

integrating equation (2.4) from z to z_{ws} the following relationship for τ is derived for the whole flow depth by the Reynolds equations

$$\frac{\tau(z)}{\rho} = gS[z - z_{ws}] = u_*^2(1 - \frac{z}{d}) = -\overline{u'w'}(z) \qquad (2.7)$$

A linear fit of τ down to the mean bed elevation provides an estimate of the boundary shear stress τ_0. From equation (2.7) it follows that the gravity force $gS[z - z_{ws}]$, and therefore τ is totally balanced by Reynolds shear stress. The explicit statement made through equation (2.7) is that, for the whole of the flow depth, τ must be comprised entirely of the Reynolds stress. There is an apparent assumption that a linear fit to the Reynolds stress (from one point measurement) can be used to predict τ_0. Therefore any deviation in the Reynolds stress from a vertical linear distributions is likely to give errors in the estimate of τ_0. It also means a violation of the momentum conservation described by the Reynolds equation. Clearly the equations would then be inappropriate for studying gravel bed flows, and for accurately characterising momentum transfer over a water-worked gravel bed.

For smooth wall flows, early studies demonstrated that the Reynolds equations were suitable for characterising momentum transfer. Reynolds stress was shown to follow a linear distribution, such that Reynolds stress could fully account for the momentum being transferred within the flow (e.g. McQuivey and Richardson, 1969; Nakagawa *et al.*, 1975). However, none of these early measurements were made very close to the boundary. The high turbulence intensities encountered near the wall caused many of the standard measurement techniques to suffer from substantial errors, which have proved difficult to diagnose and correct (Raupach *et al.*, 1991). For example, the majority of these studies used hot-film anemometers, but these are known to be sensitive to changes in temperature, and these changes are greater in the near-bed region due to the highly turbulent nature of the flow. When techniques such as Laser Doppler Velocimetry (LDA) and ADV that were able to measure accurately close to the bed were utilised to study smooth-wall flows, discrepancies with earlier studies began to emerge. It was shown by various studies that even over smooth beds there can be a reduction in Reynolds stress close to the bed, relative to an assumed linear distribution. For example, Nezu and Rodi (1986) used a 2-D LDA system to make Reynolds stress measurements

in a laboratory flume of 2-D flows over smooth beds. They found that the reduction began at $z/d \approx 0.15$, the height at which the maximum Reynolds stress occurred, and remained down to the wall. Here and for other studies the relative heights presented by these studies have been approximately converted so that z is the mean bed elevation and d is the mean flow depth. This retardation, relative to a linear stress distribution, was as large as nearly 30 %, and was largest closest to the wall. More recently, Biron *et al.* (2004) carried out ADV measurements over a smooth Plexiglas surface within a laboratory flume. It was possible to make five measurements within the bottom 20 % of the flow so they were able to measure Reynolds stress much closer to the bed than many previous smooth-wall studies. They also showed that Reynolds stress approximately followed a linear decrease down to $z/d \approx 0.15$, below which there was a slight enhancement and then reduction close to the wall.

This reduction in Reynolds stress relative to a linear distribution has been shown to occur also over water-worked gravel beds. This has only been reported relatively recently so it is also necessary to examine studies over other rough boundaries to illustrate further the inadequacy of Reynolds equations for characterising momentum transfer. Many examples exist in the literature, and only a few examples will be given here which are representative of various different hydraulic approaches (field and laboratory) and of different rough boundaries using different velocimetric techniques, to demonstrate that this is a consistent feature of flows over rough boundaries.

2.5.1 Water-worked Sand Beds

Gyr and Schmid (1997) found even larger deviations in Reynolds stress from a linear distribution for flows over mobile, sand beds, again using LDA, in a laboratory flume, than those seen over smooth boundaries. Very close to the bed, the Reynolds stress normalised by u_*^2 was nearly zero, but an assumed linear distribution of shear stress would suggest that it should attain a value close to unity. Therefore, the departures were nearly as large as 100 %, being greatest closest to the bed, with departures still evident up to $z/d \approx 0.15$, which approximately corresponds to the height at which the maximum Reynolds stress occurred, the same relative height as found by Nezu and Rodi (1986) and Biron *et al.* (2004). However, it must be noted that Gyr and Schmid

(1997) based their results on velocity measurements over just one point over the bed, so they may not be representative of the whole bed surface.

Biron *et al.* (2004) also carried out measurements over a mobile sand bed, this time consisting of uniform sized sand. They discovered very similar results to those found by Nezu and Rodi (1986) and for their smooth-wall tests. The departures again began at $z/d \approx 0.15$, where the maximum Reynolds stress was attained, as also found by Gyr and Schmid (1997) over a sand bed, and attained a maximum departure in Reynolds stress from a linear distribution of around 30 %. However, it must be noted that the velocity measurements were taken at a short distance from the flume inlet, so it is questionable whether a boundary layer had fully formed over the measurement section of the bed (Kırkgöz and Ardıçlıoğlu, 1997).

Song and Chiew (2001) further examined the vertical distribution of Reynolds stress over sand beds, but extended this to nonuniform flows. ADV measurements were taken at five positions over a fixed, sand bed in a flume, during accelerating and decelerating flow. At a given point over the bed, they showed the Reynolds stress distribution is not linear in either an accelerating or decelerating flow. In an accelerating flow, it had a concave vertical profile, with its maximum value occurring at the measurement vertical closest to the bed, $z/d \approx 0.05 - 0.1$. But for a decelerating flow, it had a convex form and the maximum value occurred higher in the flow at $z/d \approx 0.05 - 0.1$, below which Reynolds stress reduced.

2.5.2 Dune-shaped Bedforms

This observed reduction in Reynolds stress in the near-bed region has not only been found for flows over flat sand beds. Best and Kostaschuk (2002) carried out an experimental study of a flow over a model, low-angle dune, which was based on a prototype dune from the Fraser River, Canada. LDA measurements were taken at numerous positions over the dune, to characterise the turbulent flow properties in the lower lee, trough, mid-stoss and crest of the dune. For one point within the mid-stoss and at one point on the crest of a dune, the departure began at $z/d \approx 0.1$, the height at which the maximum Reynolds stress was attained, and the degree of departure increased towards the dune surface. Up to a four-fold decrease in Reynolds stress, relative to a

linear distribution, was observed closest to the dune surface. Yet at the lower lee and trough of the dune, where there was a zone of decelerated flow, Reynolds stress was enhanced relative to a linear distribution. This again occurred at $z/d \approx 0.1$, and resulted in the Reynolds stress being almost double that predicted by a linear distribution in the lower-lee of the dune, and around 50 % greater in the trough. This did not occur closest to the dune surface but at $z/d \approx 0.03$. However, they state that because the dune was made of foam, they were not able to capture the effects of skin friction from sediment particles or smaller superimposed bed forms. In addition, the dunes were two-dimensional, had the same size and shape and were impermeable, so they were unlikely to have simulated accurately natural dunes. Most importantly, a low flume width to flow depth ratio of 1.5 is likely to have resulted in the generation of secondary flows within the flume, which will have affected their Reynolds stress estimates (Nezu and Nakagawa, 1993).

An enhancement in Reynolds stress has also been found for various runs over similar two-dimensional sand bedforms by Nikora *et al.* (in press b). By taking ADV and LDA measurements at various positions over one bedform, and averaging these measurements to obtain an estimate of Reynolds stress for a single bedform, they found that enhancement occurred at $z/d \approx 0-0.2$. Reynolds stress then experienced retardation, relative to a linear distribution, below the mean elevation of the bedform, in the trough of the bedform, which is the opposite of that discovered by Best and Kostaschuk (2002). This reduction increased from the mean bed elevation down to the trough of the bedform, such that at the height closest to the dune trough, the Reynolds stress was nearly negligible, despite an assumed linear distribution suggesting that it should attain its maximum at this height.

Again, the limitations of these results are that the measurements were taken over two-dimensional bedforms. With this in mind, Maddux *et al.* (2003) examined flows over fixed, artificial three-dimensional dune shapes in a laboratory flume to gain more representative results for field conditions. Averaging the Reynolds stress over various point measurements taken over a single bedform they found that Reynolds stress was considerably lower than the total fluid stress for the whole of the flow depth. This occurred for two different flow depths. The departure increased from the water surface towards the bedform crest, until the Reynolds stress reached its maximum value at around halfway between the bedform crest and trough, from which the retardation then

increased towards the bedform trough. It resulted in the Reynolds stress being negligible at a height closest to the dune trough, as found by Nikora *et al.* (in press b).

2.5.3 Regular Roughness Elements

A similar retardation in Reynolds stress close to the boundary has been found over regular roughness elements. For example, Nikora *et al.* (2001) carried out a set of laboratory measurements that examined turbulence characteristics over and within a regular arrangement of spheres. Two different discharges were studied, with two locations being measured synchronously by two ADV probes. Each pattern included 16 measurement verticals for the low flow, and seven verticals for the high flow. By examining the Reynolds stress at several neighbouring locations, they discovered that Reynolds stress for both of the flows demonstrated a reasonable agreement with a linear distribution from the water surface down to $z/d \approx 0.15$. Below this Reynolds stress decreased considerably from the linear distribution, such that closest to the bed, Reynolds stress was only 10 % of that predicted by a linear distribution, a very similar degree of retardation as found by previous studies. The Reynolds stress determined by averaging over all the measurement positions over the bed, also departed from a linear distribution at $z/d \approx 0.15$, and become negligible closest to the bed, once again reported by other studies. Very similar results were also found by Nikora *et al.* (2002), who compared the results of Nikora *et al.* (2001) to ones derived from the same sphere bed that had well developed periphyton on its surface.

Measurements were also made by Papanicolaou *et al.* (2001) over spheres packed in different densities. Using LDA measurements, they demonstrated that the degree of departure in the Reynolds stress from an assumed linear distribution in the near-bed region was a function of the packing density. At the lowest density, the largest retardation was found in Reynolds stress, such that it could attain high negative values, but at the mid packing density Reynolds stress remained positive, although the retardation was still very large. At the highest density there was again a significant departure, but in the form of an enhancement in the Reynolds stress close to the bed. The position at which the greatest departures occurred was not a function of packing density and occurred consistently at $z/d \approx 0.1$. The negative Reynolds stress values suggests that there was momentum exchanged from the boundary to the core of the flow, and this was likely to have been caused by secondary currents (Papanicolaou *et*

al., 2001). They conclude that the non-linearity in the Reynolds stress close to the bed is primarily due to flow detachment around a sphere.

A further study on the effect of isolated roughness elements on the flow was made by López and García (2001). A numerical turbulence closure model was constructed to model turbulent flow within simulated vegetation. This was compared with experimental velocity measurements made using ADV probes at four positions within the submerged vegetation. Cylindrical wooden dowels were used to simulate this rigid vegetation, and were arranged in a staggered pattern with a varying density. The experimental results showed that the Reynolds stress, at each of the four positions, began to depart from the linear distribution when it attained its maximum at $z/d \approx 0.12$. Below this, Reynolds stress decreased, such that it was nearly zero closest to the boundary, which equates to an order of magnitude decrease relative to a linear distribution. These results were remarkably similar for each position over the vegetation.

These results were further confirmed by an experimental study made by Poggi *et al.* (2004). They also modelled vegetation using an array of equally spaced vertical cylinders. They varied the density of arrangement of cylinders within a flume, and produced results that are remarkably similar to those found by López and García (2001), demonstrating a consistency in the trend for the retardation of Reynolds stress close to the boundary.

Nikora *et al.* (in press b) have also examined Reynolds stress profiles over regular roughness elements. They took ADV measurements over 2-D transverse ribs along the centreline of a flume. The Reynolds stress was estimated by taking the average from each measurement position within the channel. It was found that this was approximately half of that predicted by a linear stress distribution at the crest of the ribs, at which Reynolds stress was at its maximum. Below the crest the discrepancy increased, such at the measurement position closest to the roughness trough the Reynolds stress was negligible, again indicating an order of magnitude departure for a linear distribution. They attributed these departures to secondary currents, and non-uniformity, which acted to reduce the momentum flux occurring through Reynolds stresses.

2.5.4 *Water-worked Gravel Beds*

Of greatest interest to this study is the observed discrepancy in Reynolds stress from an assumed linear distribution over water-worked gravel bed surfaces. Nikora and Goring (2000) studied turbulent flows in a gravel-bedded irrigation channel in New Zealand. They took ADV measurements at a high discharge, when the bed was weakly mobile, and two flows at mid and low discharges when the bed was static. In the near-bed region, the Reynolds stress again attained a maximum and then reduced toward the bed. This caused retardation in the Reynolds stress, relative to a linear distribution of approximately 90 % for the highest and lowest flow and 50 % for the mid-ranged flow. Again this was attained closest to the bed, with the reduction decreasing with height towards the elevation at which the maximum occurred. This was at $z \approx 2-5$ cm for the low and medium flows, and at $z = 5-8$ cm for the high flow. This corresponded to $z/d \approx 0.02-0.07$ and $z/d \approx 0.05-0.08$, which is much lower than observed previously.

The departure was found to occur at a considerably greater height over a fixed, artificial gravel bed. Campbell *et al.* (2005) examined how turbulent properties changed with the addition of bedload into the flow in a laboratory flume, using three different sediment sizes at two different feed rates. They used 2-D PIV in a plane normal to the bed surface, at one lateral position over the bed. This was to obtain an estimate of Reynolds stress averaged over many points over the bed. They discovered that the departure from a linear distribution began at an increasingly higher position within the flow with the addition of coarser and coarser material. The Reynolds stress reached a maximum at $z/d \approx 0.15$ for the clear water case, and the corresponding heights for the fine, medium, and coarse feeds were $z/d \approx 0.20$, $z/d \approx 0.23$ and $z/d \approx 0.25$, respectively. This trend was independent of bedload transport rate. The largest departures from a linear distribution occurred closest to the bed, and could be as large as a 16 fold decrease, approximately equal to an order of magnitude decrease. This large decrease might be attributed to the effects of a large isolated particle within the measurement area on the flow, which was an artificial feature created through the screeding of the bed surface.

Papanicolaou and Hilldale (2002) performed a field study of the effects of a channel transition on turbulence characteristics. Seven vertical profiles were taken using ADV within a cross-section of a gravel-bed river located downstream of a gradual channel

expansion. Neither of the verticals displayed a linear decrease in Reynolds stress with height, with many displaying a convex form, as found by Song and Chiew (2001) over a sand bed. Reynolds stress was found to deviate from a linear distribution by almost 42 %. This they concluded was caused by secondary currents within the flow.

Carling *et al.* (2002) also attributed the non-linear Reynolds stress distribution they discovered to be due to the three-dimensional nature of the flow. They took various vertical profiles within a cross-section of a gravel-bedded compound channel in the River Severn, England. At different locations within the channel they found substantial retardation in Reynolds stress close to the bed, such that it could become negligible at the measurement positions closest to the bed surface, at the very positions Reynolds stress is assumed to attain its maximum value. The deviation resulted in the Reynolds stress, based on a linear distribution, being six times higher than their observations.

More recently, smaller degrees of departure have been observed by Nikora *et al.* (in press b) over a static, armoured gravel bed. This study took LDA measurements both above and within the roughness elements of the bed. Reynolds stress was averaged over 24 randomly positioned measurements. They discovered that the maximum degree of departure in this Reynolds stress increased with flow depth, such that at the lowest flow it was approximately 70 %, and around 45 % and 40 % at the two higher depths. This again was attained at the measurement positions closest to the mean bed elevation. Unlike other studies, the departure did not begin where the maximum Reynolds stress was attained. Instead, its maximum was observed at around halfway between the maximum and minimum bed elevation of the bed. The flow within the roughness elements of a gravel bed surface has not been measured previously by other studies and could account for this difference.

It has been shown by studies over various roughness types that, on the whole, Reynolds stress decreases in a linear manner down to the height above the bed surface at which the Reynolds stress attains its maximum value. Below this it experiences significant retardation, relative to an assumed vertical linear distribution, such that it can become small close to a rough boundary. This degree of retardation has also been shown to be fairly similar across the different studies, and to occur at similar relative heights. The fact that this occurs, regardless of the roughness of the bed, suggests this might be an inherent feature of turbulent flows over rough boundaries. This is a violation of the

momentum conservation described by the Reynolds equation, which suggests that Reynolds equations are inappropriate for rough-bed flows, and for accurately characterising momentum transfer between the flow and a rough-bed. In addition, given that the Reynolds equations state that for high Reynolds number flows the total fluid stress is entirely composed of Reynolds stress, and that a linear fit to the Reynolds stress can provide an estimation of bed shear stress, the Reynolds equations are also inappropriate for predicting bed shear stress over rough beds. Yet the Reynolds equations have almost universally been applied for such purposes.

2.6 Double-averaged Navier-Stokes Equations

2.6.1 Formulation

The region in which the retardation occurs in Reynolds stress is said to indicate the existence of a roughness sublayer (described in more detail below), where additional mechanisms for momentum extraction emerge (Raupach *et al.*, 1991; Nikora and Goring, 2000; Campbell *et al.*, 2005). It is thought that the most important additional flux is one which arises due to spatial variations in the time-averaged flow, which leads to a streamwise averaged momentum flux (Raupach *et al.*, 1991; Nikora *et al.*, 2001). This spatial variability can only be taken into account explicitly by supplementing the time-averaging of the Navier-Stokes equation with spatial area (or volume) averaging in the plane parallel to the averaged bed surface. This produces new continuity and momentum equations which are averaged both in time and space (double-averaged equations).

The idea of spatial averaging was introduced for studying atmospheric flows over and within vegetation canopies, such as forests and bushes, by Wilson and Shaw (1977), and in hydraulics, by Smith and McLean (1977) for considering vertical velocity profiles averaged above a wavy bed. However, spatial-averaging originally had its roots in multi-phase and porous media hydrodynamics, where spatial averaging was applied to instantaneous variables without any form of pre- or post-time averaging. Studies into atmospheric boundary layers considered spatially averaging the time-averaged flow over a streamwise plane, which was intersected by vegetation, to characterise momentum transfer within a vegetation canopy (Wilson and Shaw, 1977; Raupach and Shaw, 1982). Finnigan (1985) extended these concepts to enable the flow to be

averaged over any volume within the canopy, and derived volume-averaged equations. Both approaches become equivalent when the averaging volume is considered as an extensive, infinitesimally thin streamwise slab. Recently, Gimenez-Curto and Corniero Lera (1996) successfully applied a similar approach to describe oscillating turbulent flows over very rough surfaces. Although the idea of spatial averaging has also been used by a number of other studies (López and Garcia, 1998; 2001; McLean *et al.*, 1999; Hsu *et al.*, 2002; Gimenez-Curto and Corniero Lera, 2003), the potential of this approach for use in hydraulics was only fully realised by Nikora *et al.* (2001), who developed new continuity and momentum equations for rough-bed open channel flows by double-averaging the Navier-Stokes equations. The averaging procedure for spatial area averaging at level z is defined as (Gimenez-Curto and Corniero Lera, 1996; Nikora *et al.*, 2001)

$$\langle F \rangle(x,y,z,t) = \frac{1}{A_f} \int_{A_f} F(x',y',z,t)dx'dy' \tag{2.8}$$

where F is the flow variable defined in the fluid to be spatially averaged over the fluid domain A_f. This fluid domain is assumed to be planar and parallel to the averaged bed surface, and to be the area occupied by the fluid on the x, y-plane at level z within the total area A_0. The total area includes the domains occupied by both fluid and the intervening solid surfaces. Therefore, below the maximum bed elevation A_f is multiply connected due to the intersection of A_0 by roughness elements. The averaging area A_0 is often a thin streamwise slab, with its streamwise extent determined by the scales of the bed roughness and the overall geometry of the flow of interest. A thin slab is chosen to preserve the characteristic spatial variability in the flow in the vertical direction. The square root of A_0 can be interpreted as the scale of this spatial averaging window used to spatially average the flow, with a linear scale $< A_0^{0.5}$ (Nikora *et al.*, 2001). This total averaging area can be described by two linear scales, the streamwise L_0 and lateral W_0 lengths, such that $A_0 = L_0 W_0$. Nikora *et al.* (2001) claim that a convenient choice for scales L_0 and W_0 are the streamwise and lateral correlation lengths of the rough bed elevations.

The definition in equation (2.8) is combined with a decomposition of time-averaged variables into spatially averaged (denoted by angle brackets) and spatially fluctuating (denoted by a wavy overbar) components (Gray, 1975) that is analogous to the Reynolds decomposition for instantaneous variables $F = \overline{F} - F'$:

$$\overline{F} = \langle \overline{F} \rangle - \widetilde{F} \tag{2.9}$$

The spatial fluctuations arise from the difference between the double-averaged $\langle \overline{F} \rangle$ and time-averaged $\overline{F}$ values ($\widetilde{F} = \overline{F} - \langle \overline{F} \rangle, \langle \widetilde{F} \rangle = 0$), similar to the conventional Reynolds decomposition of $F' = F - \overline{F}, \overline{F'} = 0$.

The spatial averaging approach was originally developed with the assumption that the boundary is homogeneous (Wilson and Shaw, 1977; Raupach and Shaw, 1982; Finnigan, 1985), which might be reasonable for vegetation canopies, but is not valid for water-worked gravel beds. For these surfaces, the ratio A_f / A_0 is not constant within the bed and decreases from the maximum bed elevation to the roughness troughs. By applying equation (2.8) and the decomposition used in equation (2.9) to equation (2.2), it is possible to obtain double-averaged (in time and then in space) momentum and mass conservation equations for the flow both above and below the maximum bed elevation z_c. In the flow region above the maximum bed elevation, $z > z_c$, where $A_0 = A_f$ is not constant within the bed,

$$\frac{\partial \langle \overline{u}_i \rangle}{\partial t} + \langle \overline{u}_j \rangle \frac{\partial \langle \overline{u}_i \rangle}{\partial x_j} = g_i - \frac{1}{\rho} \frac{\partial \langle \overline{p} \rangle}{\partial x_i} - \frac{\partial \langle \overline{u_i' u_j'} \rangle}{\partial x_j} - \frac{\partial \langle \widetilde{u}_i \widetilde{u}_j \rangle}{\partial x_j} + \nu \frac{\partial^2 \langle \overline{u}_i \rangle}{\partial x_j^2} \tag{2.10}$$

$$\frac{\partial \langle \overline{u}_i \rangle}{\partial x_i} = 0 \tag{2.11}$$

and in the flow region below the maximum bed elevation, $z < z_c$, where the averaging region is multiply connected because of the intersection by roughness elements

$$\frac{\partial\langle\overline{u}_i\rangle}{\partial t}+\langle\overline{u}_j\rangle\frac{\partial\langle\overline{u}_i\rangle}{\partial x_j}=g_i-\frac{1}{\rho}\frac{\partial\langle\overline{p}\rangle}{\partial x_i}-\frac{1}{\phi}\frac{\partial\phi\langle\overline{u_i'u_j'}\rangle}{\partial x_j}-\frac{1}{\phi}\frac{\partial\phi\langle\widetilde{u}_i\widetilde{u}_j\rangle}{\partial x_j}$$
$$+\frac{\nu}{\phi}\frac{\partial^2\phi\langle\overline{u}_i\rangle}{\partial x_j^2}-\frac{2\nu}{\phi}\frac{\partial\langle\overline{u}_i\rangle}{\partial x_j}\frac{\partial\phi}{\partial x_j}-\frac{\nu\langle\overline{u}_i\rangle}{\phi}\frac{\partial^2\phi}{\partial x_j^2}+\nu\left\langle\frac{\partial^2\widetilde{u}_i}{\partial x_j^2}\right\rangle-\frac{1}{\rho}\left\langle\frac{\partial\widetilde{p}}{\partial x_i}\right\rangle \tag{2.12}$$

$$\frac{\partial\phi\langle\overline{u}_i\rangle}{\partial x_i}=0 \tag{2.13}$$

where ϕ is the normalised value of A_f, $\phi=A_f/A_0$. This has been termed the roughness geometry function (Nikora *et al.*, 2001) because it accounts for the geometry of the bed by deriving the proportion of the bed within A_0, which means that $\phi=f(x,y,z)$. Detailed mathematical analysis and full derivations of equations (2.10) and (2.12) for incompressible turbulent fluid flow are given in detail in Gimenez-Curto and Corniero Lera (1996). Equations (2.10) and (2.12) relate to the time-averaged Reynolds equations, in the same manner in which the Reynolds equations relate to the Navier-Stokes equations for instantaneous flow variables. Velocities and pressures, as well as their moments, in these double-averaged equations represent spatially-averaged flow parameters. These equations have also been formulated for volume-averaging and extended for mobile boundaries (such as waving aquatic plants, moving gravel particles, and developing bedforms on the boundary) (see Nikora *et al.* (in press a) for more information).

The spatial averaging of the Reynolds equations has introduced some additional terms in equations (2.10) and (2.12) to those in equation (2.2). These new terms are form-induced stress $\langle\widetilde{u}_i\widetilde{u}_j\rangle$, form drag $(1/\rho)\langle\partial\widetilde{p}/\partial x_i\rangle$ and viscous drag $\nu\langle\partial^2\widetilde{u}_i/\partial x_j^2\rangle$. The form-induced stress is the streamwise averaged momentum flux which arises due to spatial variations in the time-averaged flow. The two drag terms only appear in equation (2.12) for the flow below the maximum bed elevation. This equation also demonstrates a dependence on the parameter ϕ, and therefore on the roughness geometry. This parameter is important if the density and cross-sections of the roughness elements change spatially, but disappear if they are spatially homogeneous. It means that the spatially-averaged flow parameters can be related to the roughness parameters by averaging in the same spatial domain. The significance of these new terms for different

hydrodynamic and bed roughness conditions awaits proper assessment (Nikora *et al.*, in press b).

If consideration is given to the simplest case of 2-D, steady, uniform flow, in which the flow is in spatial equilibrium and has a free surface which is parallel to the average bed slope, the momentum equations can be derived from equations (2.10) and (2.12). Such a flow possesses the following properties (from Nikora *et al.* (2001)):

1. No long-term trends in flow properties, such that all variations can be considered to have only been caused by turbulence. Therefore the flow would produce steady, time-averaged flow values. In this manner the averaging time is sufficiently long to ensure that many cycles of the rapid turbulent fluctuations in a flow property are captured, but sufficiently short that the external large-scale variations in the flow property are not present.
2. The vertical change in spatially-averaged flow properties is significantly stronger than those in the lateral directions.
3. The time-averaged vertical and lateral velocities, $\langle \overline{v} \rangle$ and $\langle \overline{w} \rangle$ (the double-averaged velocities), respectively are equal to zero throughout the flow depth and there is no correlation between u and v and between v and w.
4. The water surface is parallel to the averaged bed slope such that the energy and bed slope is the same.
5. The bed roughness (i.e. the field of bed elevations) is statistically homogeneous in the x, y-plane. In other words, the bed surface is random, the spatial autocorrelation is stationary and isotopic, and a probability density function of bed elevations can describe a bed uniquely. Therefore, the roughness geometry function ϕ depends only on the vertical coordinate z, i.e. $\phi = \phi(z)$.

For high Reynolds number two-dimensional flows, the viscous drag term $\nu \langle \partial^2 \widetilde{u}_i / \partial x_j^2 \rangle$ is neglected so equations (2.10) and (2.12) can be reduced, to give the momentum equations for the flow region above the maximum bed elevation,

$$gS - \frac{\partial \langle \overline{u'w'} \rangle}{\partial z} - \frac{\partial \langle \widetilde{u}\widetilde{w} \rangle}{\partial z} = 0 \qquad (2.14)$$

$$g\cos\alpha+\frac{1}{\rho}\frac{\partial\langle\overline{p}\rangle}{\partial y}+\frac{\partial\langle\overline{v'w'}\rangle}{\partial y}+\frac{\partial\langle\widetilde{v}\widetilde{w}\rangle}{\partial y}=0 \tag{2.15}$$

and for the flow region below the maximum bed elevation,

$$gS-\frac{1}{\rho}\left\langle\frac{\partial\widetilde{p}}{\partial x}\right\rangle-\frac{1}{\phi}\frac{\partial\phi\langle\overline{u'w'}\rangle}{\partial z}-\frac{1}{\phi}\frac{\partial\phi\langle\widetilde{u}\widetilde{w}\rangle}{\partial z}=0 \tag{2.16}$$

$$g\cos\alpha-\frac{1}{\rho}\frac{\partial\langle\overline{p}\rangle}{\partial y}+\frac{1}{\rho}\left\langle\frac{\partial\widetilde{p}}{\partial y}\right\rangle+\frac{1}{\phi}\frac{\partial\phi\langle\overline{v'w'}\rangle}{\partial y}-\frac{1}{\phi}\frac{\partial\phi\langle\widetilde{v}\widetilde{w}\rangle}{\partial y}=0 \tag{2.17}$$

Equations (2.14) and (2.16) represent the double-averaged momentum equations in the streamwise domain, and equations (2.15) and (2.17) those in the vertical domain.

A further subdivision is possible for the flow by considering the significance of the terms in equations (2.14) to (2.17). Nikora *et al.* (2001) considered the flow in terms of five layers (Figure 2.1) by making the assumption $H >> \Delta$, where H is the maximum flow depth, equal to the distance from the trough of the roughness elements to the water surface and Δ is the roughness height:

1. Outer layer: In this region, the viscous effects and form-induced stress are assumed by Nikora *et al.* (2001) to be negligible, such that the double-averaged momentum equations reduce to the Reynolds equations. The distribution of $\overline{u}$ in this layer is described by the velocity defect law (Nezu and Nakagawa, 1993), and its flow properties are characteristically scaled by the bed shear velocity, the maximum flow velocity, the distance from the bed and flow depth. The turbulent dissipation rate becomes larger than the generation rate, so turbulent energy is supplied from close to the bed into this layer by turbulent diffusion (Nezu and Nakagawa, 1993).
2. Logarithmic layer: Momentum transfer can again be described by the Reynolds equations by assuming that form-induced stresses are negligible. However, the characteristic scales for this region are different from those for the outer layer. These scales are bed shear velocity, distance from the bed and the characteristic scales of the bed surface topography, such as the streamwise and lateral correlation lengths (Nikora *et al.*, 1998) or the standard deviations of the bed surface elevations (Aberle and Smart, 2003). This layer is not strongly influenced by either the rough boundary

or the water surface. The distribution of $\overline{u}$ follows the logarithmic law and it maintains a near-equilibrium turbulent energy budget. This layer exists if $H >> \Delta$, and occupies the flow region $(2-5)\Delta < (z - z_t) < 0.2H$ (Raupach *et al.*, 1991; Nezu and Nakagawa, 1993), where z_t is the height of the troughs of the roughness elements.

3. Form-induced sublayer: The flow in this region is assumed to be influenced by individual roughness elements, so the double-averaged momentum equations are considered to a better description of momentum transfer than the Reynolds equations because all terms in equations (2.14) and (2.15) may be important. This is the region in which Reynolds stress displays retardation relative to a vertical linear distribution (Raupach *et al.*, 1991; Nikora and Goring, 2000; Campbell *et al.*, 2005). It occupies the region of the flow just above the roughness elements, and the name 'form-induced' is used to reflect the assumed appearance of form-induced stress in this region, in comparison with the logarithmic layer. The thickness of the layer may be up to $(1-4)\Delta$ (Raupach *et al.*, 1991).
4. Interfacial sublayer: This layer is also influenced by individual roughness elements and occupies the region of the flow between the roughness troughs and the maximum bed elevation. A new term, form drag appears in this region.
5. Subsurface layer: This layer occupies the flow within the pores of the granular media and is driven by the gravity force and momentum fluxes from the above layers. It lies beneath the roughness troughs. The characteristic scales of the subsurface layer are thought to be bed shear velocity and pore characteristic lengths.

The form-induced and interfacial sublayers together form the roughness layer. The main characteristic scales are the bed shear velocity and the characteristic lengths of the bed surface topography. Bursting phenomena occur most violently in this layer, so the turbulent energy generation exceeds the dissipation rate (Nezu and Nakagawa, 1993). In smooth-wall terms, the flow region occupied by the logarithmic and roughness layer is the wall or inner layer. This suggests that the role of the roughness layer for rough bed flows is similar to that of the viscous and buffer sublayers for smooth beds (Raupach *et al.*, 1991). This demonstrates that the double-averaged momentum equations produce the possibility for scaling considerations and parameterisation based on double-averaged variables which may cover all flow regions, including the interfacial sublayer. This is not possible using the Reynolds equations and time-averaged flow parameters.

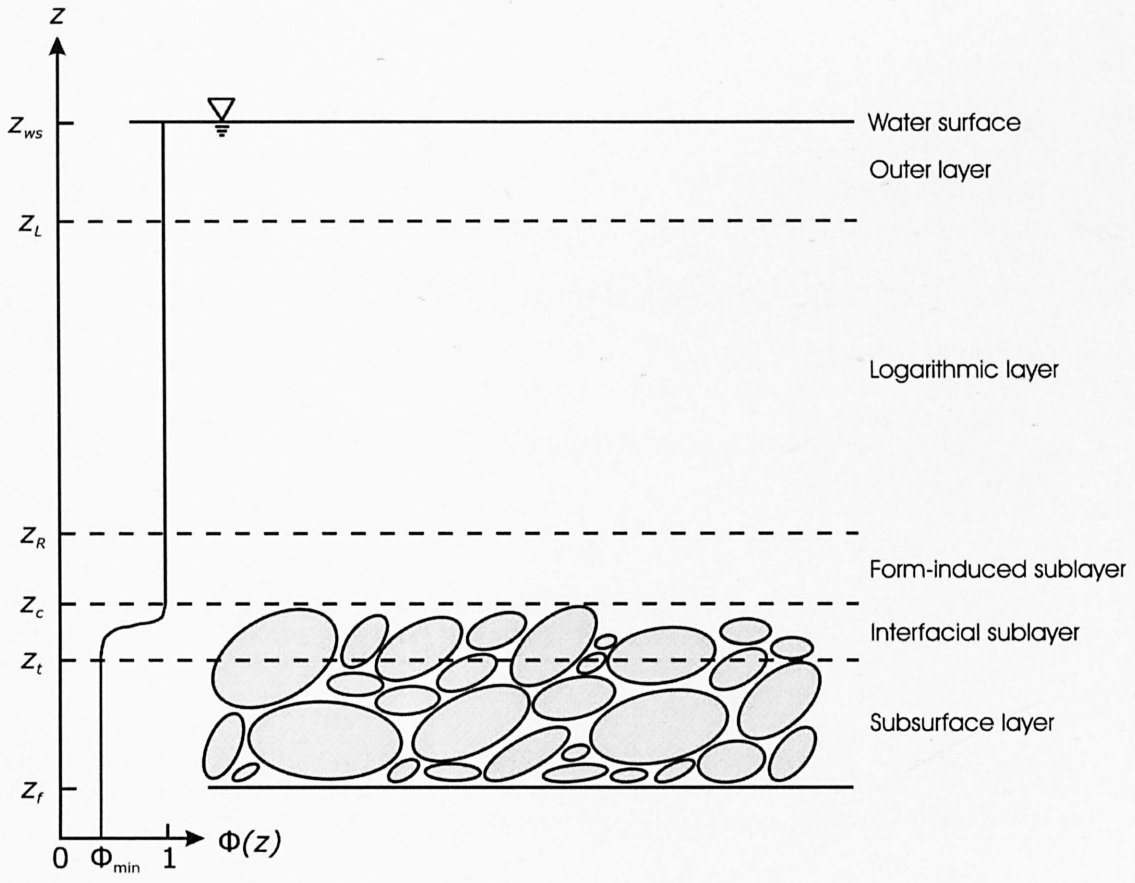

Figure 2.1. Flow subdivision into specific regions over a rough permeable bed, where z_{ws} is the height of the averaged water surface, z_L is the maximum height at which the logarithmic regions is present, z_R is the maximum height at which the form-induced sublayer is present, z_c is the height of the maximum bed elevation and the maximum height at which the interfacial sublayer is present, z_c is the height of the roughness trough, equal to the lowest elevation of a surface grain over the whole surface, and is the minimum height at which the interfacial sublayer is present, and z_f is the height of the channel floor. Redrawn from Nikora *et al.* (2001).

Based on the assumptions made for this subdivision, the total stress distribution can be derived for each flow layer. By integrating equation (2.14) from z to the water surface z_{ws} the following relationship for the total stress distribution τ for the outer and logarithmic layers is given by

$$\frac{\tau(z)}{\rho} = gS[z - z_{ws}] = -\langle\overline{u'w'}\rangle(z) = -\overline{u'w'}(z) \tag{2.18}$$

and for the form-induced sublayer

$$\frac{\tau(z)}{\rho} = gS[z - z_{ws}] = [-\langle\overline{u'w'}\rangle(z) - \langle\tilde{u}\tilde{w}\rangle(z)] \tag{2.19}$$

A similar integration of equation (2.16) provides the total stress distribution for the interfacial sublayer

$$\begin{aligned}\frac{\tau(z)}{\rho} &= gS[z_{ws} - z_c + \int_z^{z_c}\phi(z)dz] = [-\phi\langle\overline{u'w'}\rangle(z) - \phi\langle\tilde{u}\tilde{w}\rangle(z)] \\ &+ \int_z^{z_c}\frac{\phi(z)}{\rho}\left\langle\frac{\partial\tilde{p}}{\partial x}\right\rangle dz\end{aligned} \tag{2.20}$$

and the subsurface layer

$$\begin{aligned}\frac{\tau(z)}{\rho} &= gS[z_{ws} - z_c + \int_{z_t}^{z_c}\phi(z)dz + \phi_{\min}(z_t - z)] \\ &= \phi_{\min}[-\langle\overline{u'w'}\rangle(z) - \langle\tilde{u}\tilde{w}\rangle(z)] + \int_{z_t}^{z_c}\frac{\phi(z)}{\rho}\left\langle\frac{\partial\tilde{p}}{\partial x}\right\rangle dz + \frac{\phi_{\min}}{\rho}\int_{z_t}^{z_c}\left\langle\frac{\partial\tilde{p}}{\partial x}\right\rangle dz\end{aligned} \tag{2.21}$$

It follows that the gravity force $gS[z - z_{ws}]$ is balanced by the Reynolds stress in the outer and logarithmic layers. Therefore the assumption made by Nikora *et al.* (2001) is that form-induced stresses are not significant, and spatial averaging of the Reynolds stress is not required, above the form-induced sublayer. It implies that in the outer and logarithmic layers of the flow the total stress must be comprised entirely of the Reynolds stress. The implication is an assumption that a linear fit to the Reynolds stress (from one point measurement, rather than from spatially-averaged measurements) in these regions can be used to predict the total boundary shear stress.

In the form-induced sublayer the gravity force is balanced by both spatially-averaged Reynolds stress and form-induced stress, and these are supplemented with additional stresses due to form drag in the interfacial sublayer and subsurface layer. This implies

that spatial variability in the flow field, and the influence that this has on momentum transfer, must be taken into account in the form-induced layer, interfacial sublayer and the subsurface layer. The difference between the double-averaged equations and the Reynolds equations is as fundamental as that between the Reynolds equations and Navier-Stokes equations.

2.6.2 Advantages over Reynolds Equations

The clear advantage of the double-averaged equations over the Reynolds equations is the explicit appearance of drag terms and form-induced stresses that account for the spatial heterogeneity in the time-averaged flow. These new terms appear as a result of spatial averaging rather than as additional *ad hoc* terms through intuitive reasoning. For example, form-induced stress arises from the correlation in point-to-point spatial deviations in the time-averaged flow field. The explicit derivation of these new terms has important implications for the numerical modelling of rough-bed flows. The double-averaged Navier-Stokes equations (DANS) represent a better basis for modelling compared to the conventional time-averaged Navier-Stokes equations (TANS). The key advantages of DANS over TANS include this explicit representation of the form and viscous drag on the rough bed, and also for momentum fluxes due to roughness-induced flow heterogeneity. Although in some early modelling works the drag terms were intuitively added as *ad hoc* terms into TANS, the form-induced fluxes have never been considered, either implicitly or explicitly.

This advantage for modelling rough-bed flows has mainly been recognised in atmospheric studies. The first application of the DANS-based approach was presented by Wilson and Shaw (1977) for terrestrial canopy flows, and in recent years, this approach has almost become the standard method in atmospheric applications (e.g. Ayotte *et al.*, 1999; Finnigan, 2000; Siqueira and Katul, 2002; Ca *et al.*, 2002; Katul *et al.*, 2004; Poggi *et al.*, 2004; Lien *et al.*, 2005). It also appears to be preferable in porous media hydrodynamics (e.g. Antohe and Lage, 1997; Pedras and de Lemos, 2000; 2001; Nield, 2001). Within hydraulics, the DANS-based approach has been used, explicitly or intuitively, mainly in modelling vegetated channels (e.g. Murota *et al.*, 1984; Shimizu and Tsujimoto, 1994; Naot *et al.*, 1996; López and Garcia, 1998; 2001; Rowinski and Kubrak, 2002; Neary, 2003; Hoffmann, 2004) and tested for simple flow experiments (Walters, 2002). This lack of application in hydraulics is mainly related to a number of

unsolved problems related to the parameterisation of surface integrals and form-induced stress in the double-averaged equations (Nikora *et al.*, in press a). Therefore, the contribution of the form-induced stresses and fluxes to the momentum and mass balances may be significant and have to be parameterised and presented in the models. To achieve this goal, an improved understanding of these fluxes is needed that requires specially designed laboratory and field experiments (Nikora *et al.*, in press a). This is important because the DANS-based approach is a natural extension of traditional methods and represents further generalisation of hydrodynamic fields with an increased level of averaging. Furthermore it has reduced requirements for boundary conditions on rough surfaces, such that boundary conditions for TANS-based models become, in an integral form, an inherent part of the DANS governing equations. It is also a more straightforward approach and provides explicit guidance in closure development and parameterisations. Therefore, DANS-based models may successfully fill a gap in modelling capabilities for environmental rough-bed flow problems where the TANS-based models are less suitable (e.g. flows over gravel and sand-wave beds, and flows over biologically modified beds such as plants and mussels). For field-scale problems such as flow over flood plains and coastal circulation, the DANS-based approach provides a quantitative method for incorporating sub-grid stresses and fluxes (Nikora *et al.*, in press a).

The double-averaged equations also provide a consistent link between spatially-averaged roughness parameters and double-averaged flow variables. This is because the spatially-averaged flow parameters can be related to the roughness parameters by averaging in the same spatial domain. Nikora *et al.* (2001) demonstrates this by developing flow resistance relationships for flows with high relative submergence, flows with small relative submergence and flows with partially inundated rough bed.

The double-averaging methodology may also help in improving the definitions of hydraulic variables for the case of gravel bed flows. It has long been recognised that there is a degree of confusion or lack of clarity between different studies of the meaning of hydraulic variables, because different investigators employ different definitions. Even the most basic definitions, which are clear for flat bed flows, are sometimes confusing when applied for describing gravel bed flows. This is partly because a clear and widely applicable definition has not been possible within the conventional framework of the Reynolds equations. Three examples of how the double-averaged

equations can improve hydraulic definitions for gravel bed flows are given in Nikora *et al.* (in press a), and these will be briefly considered here.

Uniform flow is defined within the conventional time-averaging approach as occurring if $\partial\overline{u'v'}/\partial x = \partial\overline{u}/\partial x = \partial\overline{p}/\partial x = \partial H/\partial x$. This might apply for flat-bed flows but for gravel bed flows these conditions cannot always be met and are never satisfied near the roughness elements, because the time-averaged flow is three-dimensional and therefore non-uniform. The double-averaging procedure solves this problem by providing revised conditions for flow uniformity: $\partial\langle\overline{u'w'}\rangle/\partial x = \partial\langle\overline{u}\rangle/\partial x = \partial\langle\overline{p}\rangle/\partial x = \partial\langle\overline{H}\rangle/\partial x$, and therefore $\partial\langle\widetilde{u}\widetilde{w}\rangle/\partial x$. Thus it is possible that a rough-bed flow may be non-uniform within the Reynolds framework, but within the DANS framework the same flow may appear to be uniform.

Within the Reynolds framework, two-dimensional open-channel flow satisfies the following conditions: $\overline{v} = \overline{u'v'} = \overline{v'w'} = \partial\overline{u'w'}/\partial y = \partial\overline{u}/\partial y = \partial\overline{p}/\partial y = 0$. Although these conditions can be appropriate for flows over two-dimensional rough surfaces, they can never be met close to a three-dimensional water-worked gravel bed. It therefore leads to the conclusion that the near-bed flow is three-dimensional. Spatial averaging, however, may change this conclusion, as a three-dimensional time-averaged flow may appear to be two-dimensional after spatial smoothing. Using the double-averaged equations, the revised conditions of flow two-dimensionality in the case of rough-bed flows are: $\langle\overline{v}\rangle = \langle\overline{u'v'}\rangle = \langle\overline{v'w'}\rangle = \partial\langle\overline{u'w'}\rangle/\partial y = \partial\langle\overline{u}\rangle/\partial y = \partial\langle\overline{p}\rangle/\partial y$ and, additionally $\partial\langle\widetilde{u}\widetilde{w}\rangle/\partial y$.

Bed shear stress is probably one of the most used terms in environmental hydraulics. Yet for gravel bed flows it still remains poorly defined. Quite often it is not defined at all (even in some hydraulic textbooks), perhaps with the assumption that the term is too well known to necessitate definition. This introduces some confusion when studying bed shear stress values from different studies, especially when data from different sources are compared. This can occur, for example, when bed shear estimates at fixed spatial points are compared to spatially-averaged estimates. In addition, the degree of spatial averaging is rarely specified.

For flows over flat beds, within the Reynolds framework the bed shear stress is defined for a single point on the bed surface. Clearly, this definition is not suitable for water-

worked gravel beds with complex bed geometry. In this case, the bed shear stress is the sum of viscous friction and form drag, but the Reynolds equations only provide an estimate of the viscous shear stress at the boundary. Therefore, spatial-averaging is implicit in defining the bed shear stress over a rough boundary, but is never explicitly specified. The double-averaging methodology resolves this uncertainty by providing a consistent way for relating spatially-averaged flow properties with the bed shear stress obtained within the same spatial averaging domain. In this manner, bed shear stress τ_0 is given by

$$\tau_0(A_0) = gS\left[z_{ws} - z_c + \int_{z_t}^{z_c}\phi dz\right] - \frac{1}{\rho}\int_{z_t}^{z_{ws}}\frac{\partial\phi\langle\overline{p}\rangle}{\partial x}dz - \int_{z_t}^{z_{ws}}\frac{\partial\phi\langle\overline{u'w'}\rangle}{\partial z}dz - \int_{z_t}^{z_{ws}}\frac{\partial\phi\langle\widetilde{u}\widetilde{w}\rangle}{\partial z}dz \tag{2.21}$$

This explicitly demonstrates that the bed shear stress consists of two components, viscous drag and form drag, and that it is a function of the streamwise extent of the averaging domain (given that averaging is carried out over thin streamwise slabs of fluid) and may depend on the spatial location of the domain over the bed. The dependence of the bed shear stress on the size of the averaging domain suggests that equation (2.21) may serve as a better basis for consistent scale partitioning of bed shear stress compared to existing phenomenological approaches, especially for the case of multi-scale roughnesses (e.g., grain and bedform roughnesses).

2.7 Form-induced Stress over Rough Boundaries

For the flow above the bed, the form-induced stress needs to be accounted for to balance equation (2.14), whilst for the flow within the bed, estimates are required of both form-induced stress and form drag for equation (2.16). Analytical or numerical solutions of equations (2.14) and (2.16) are therefore not possible without the parameterisation of form-induced stress and form drag. For example, parameterisation is required for the application of DANS for numerical modelling of gravel bed flows. The form-induced stress is the most poorly understood term in the double-averaged equations (Raupach, 1994; Finnigan, 2000), but is it also speculated to be the additional momentum flux term that can correct the imbalance in the momentum equations that arises because of

the departure of Reynolds stress from a linear vertical distribution. Therefore, the contribution of the form-induced stresses and fluxes to the momentum and mass balances has to be parameterised. To achieve this goal, an improved understanding of these fluxes is needed and this requires specially designed laboratory and field experiments (Nikora *et al.*, in press a).

2.7.1 Water-worked Gravel Beds

Despite this, only two studies have attempted to characterise form-induced stresses over water-worked gravel beds. The first was by Campbell *et al.* (2005) who examined the proportion of form-induced stresses of the total fluid stress for flows over an artificially created, glued, fixed gravel bed. They examined how this changed with the addition of fine, medium and coarse bedload using three different feed rates, in comparison to a clear-water case. This was performed at just one discharge and bed slope. A 2-D Particle Image Velocimetry (PIV) system was used in a plane normal to the bed surface to provide measurements of the streamwise and vertical velocities at a high spatial resolution. They restricted their analysis of this data to the flow region above the maximum bed elevation within the lower half of the flow depth. The total fluid stress was assumed to be the summation of the spatially-averaged Reynolds stress and the form-induced stress. The significance of form-induced stress was examined by computing the proportion of this measured summation contributed by the form-induced stress. Form-induced stress was found to make both positive and negative contributions to the total fluid stress. A positive contribution indicates that the form-induced stress is acting downstream, and a negative contribution that it is acting in the upstream direction. If the total fluid stress is assumed to be a summation of the spatially-averaged Reynolds stress and the form-induced stress, then a positive contribution also implies that $-\langle\overline{u'w'}\rangle < \tau$ and a negative contribution that $-\langle\overline{u'w'}\rangle > \tau$. A positive contribution by form-induced stress could be described as being 'constructive' in nature relative to $-\langle\overline{u'w'}\rangle$ because the momentum flux arising from the Reynolds stress and form-induced stress reinforce each other. However, a negative contribution could be described as being 'destructive' because the momentum flux arising from the Reynolds stress is reduced by the form-induced stress (Lien and Yee, 2004).

It was discovered by Campbell *et al.* (2005) that the form-induced stress contributions were largest for the clear-water case, making positive contributions of up to 30 % to the

total fluid stress. This occurred at $z/d \approx 0.08$, below which it decreased rapidly to be near negligible at $z/d \approx 0.04$. Below this, the contributions became negative and were as high as approximately 6 % at $z/d \approx 0.03$. Above $z/d \approx 0.08$, the contributions decreased rapidly until at $z/d \approx 0.15$ the contributions became negligible for the rest of the flow depth. This was claimed to indicate that the roughness sublayer persisted up to $z/d \approx 0.08$. The form-induced stress contributions were reduced with the addition of bedload, but all these runs still had the same vertical pattern of change as the clear water case. Form-induced stresses were found to make positive contributions approaching 15 %, and a slight negative contribution of around 1 % with the addition of coarse bedload at the lowest of the two feed rates. The addition of fine bedload reduced the contributions further at this rate, such that the positive contributions had a maximum of only approximately 12 %, although the negative contributions were similar in magnitude. For medium sized bedload the positive and negative contributions were much lower, approaching 2 %. This showed that form-induced stress contributions did not have any consistent relationship with the size of bedload. However, it was shown that the positive contributions were typically a few per cent lower at the higher feed rate for all three bedload sizes, with negative contributions remaining approximately the same. For example, an increase in feed rate for the fine particles caused the average form-induced stress to drop by over 50 %. Campbell *et al.*'s (2005) results demonstrate that form-induced stress cannot be ignored over gravel beds.

To understand the likely cause of these form-induced stresses, the variation in $\widetilde{u}$ and $\widetilde{w}$ in the streamwise direction were visually compared by Campbell *et al.* (2005) with an image of the bed. This was performed for one height above the bed, the height at which the form-induced stresses were typically the highest. This, however, was only carried out for the higher of the two feed rates, and only the runs using fine and coarse bedload were compared to the clear water case. They showed that one large particle on the bed produced virtually all of the form-induced stress over the bed. With no bedload transport, there was a large retardation in the time-averaged streamwise velocity and an augmented time-averaged vertical velocity as the flow was forced over and around this particle. This effect was greatly reduced with the addition of fine bedload, because it was said that the bed irregularities had been smoothed to some extent by the fine bedload collecting in the interstices of the bed. However, the addition of coarse bedload caused the spatial deviation in the time-averaged flow to become more erratic as the bed

roughness was greatly enhanced. They claim this was because the coarse material had a tendency to become temporarily lodged on the fixed bed, thereby forming transient clusters. However it is important to recognise that the isolated particle that produced the majority of form-induced stress is an artificial feature of the bed, formed through the screeding of the bed, not through any rearrangement of the bed surface by the flow. Indeed, the image of the bed they supply clearly shows that this heavily protrudes into the flow, relative to the rest of the bed. They claim that the time-averaged flow field was spatially averaged over an area "chosen to be representative of the fixed sediment bed topography throughout the flume" (Campbell *et al.*, 2005), but this appears to be unlikely. Therefore there is some question over whether the form-induced stress contributions they present are representative of what is likely to be found over a water-worked gravel bed. This is further suggested by the fact that the addition of bedload reduced the influence of the isolated particle on the flow, and therefore caused a large reduction in form-induced stress contributions.

In addition, the form-induced stresses were derived from just one lateral position over the bed, and over a streamwise length of 67 mm. Therefore the area they used to spatially average the flow field was small, and thus it is even more doubtful that the results they present could accurately characterise the form-induced stress over their gravel bed. Furthermore the measurements were made over a nonporous bed, and they acknowledge that momentum transfer, and therefore the contributions made by form-induced stresses, are likely to be different to that over natural, porous sediment beds where particles are free to move. It is important to note that this experiment was not specially designed for measuring form-induced stress, with the main focus to examine the change in turbulent properties with the addition of bedload to the flow. Indeed only one paragraph of the paper was given to form-induced stresses. Although they present important effects of bedload transport on form-induced stresses, no attempt was made to parameterise this stress. It is still therefore unclear how it is influenced by variables such as bed shear velocity and flow depth.

The first specially designed study of form-induced stresses over water-worked gravel beds is being undertaken at present, with a set of early results presented in Nikora *et al.* (in press b). These results concentrated on estimating form-induced stress contributions to the total fluid stress within the interfacial sublayer, the first study to do so for water-worked gravel beds, but they also present measurements further into the flow for

comparison. This was examined over a static, armoured water-worked gravel bed for three different discharges, one at the discharge used to produce a static bed and at two lower discharges, so that the bed was static for all three runs. Twenty four randomly distributed vertical profiles of velocities were taken over a bed area of 2400×360 mm using LDA, allowing measurements all the way down to very close to the roughness trough. This extends the work of Campbell *et al.* (2005) by examining form-induced stresses over a porous, water-worked gravel bed. Their results showed that form-induced stresses above the maximum bed elevation were significantly lower than those reported by Campbell *et al.* (2005) for the clear water case, being only as large as around 10 %, which is more comparable to the tests that Campbell *et al.* carried out with the addition of bedload. Furthermore, only positive contributions were seen in this region of the flow, and the decrease in contributions were not rapid as seen by Campbell *et al.* Nikora *et al.* (in press b) were also able to show that form-induced stresses are not negligible within the interfacial sublayer, and they are a significant component in the momentum balance over water-worked gravel beds. They found that form-induced stress can make both positive and negative contributions to the total fluid stress in this layer. This could range from a negative contribution of nearly 20 % to a positive contribution of nearly 30 % within the interfacial sublayer, of a similar size to that reported by Campbell *et al.* (2005) for the flow above the maximum bed elevation. The maximum stress occurred two thirds of the way up into the interfacial sublayer. Within the interfacial sublayer the contributions alternated in no consistent manner between positive and negative contributions down to the roughness troughs. In addition, there was no general increase or decrease in form-induced stress contribution with height within the interfacial sublayer. The form-induced stresses balanced changes in the spatially-averaged Reynolds stresses within this sublayer. The contributions did not consistently increase or decrease with flow depth, but it is difficult to extract any trend from just three different discharges. Therefore, no parameterisation was possible. No connection was attempted between the time-averaged flow field and the bed surface topography to understand how these stresses were induced. There is some concern over whether 24 LDA measurements are sufficient for fully sampling the spatial variability in the time-averaged flow field, and therefore for characterising the range of form-induced stress over a complex bed surface (see Aberle and Nikora (submitted) for details of the bed surface).

No study other than those by Campbell *et al.* (2005) and Nikora *et al.* (in press b) has examined form-induced stresses over gravel beds, so the significance of form-induced stresses for different hydrodynamic and bed roughness conditions still remains unclear. Yet the two studies performed so far have indicated it is likely that form-induced stresses form an important component of the momentum balance over and within water-worked gravel beds. There is clearly a great need for a specially designed study able to examine the contributions of form-induced stress to the total fluid stress under a number of different hydraulic conditions, from which trends of change can be derived, and over different water-worked gravel bed surface topographies in order to understand the control of bed surface topography on form-induced stress.

It is also worthwhile briefly considering studies that have examined the significance of form-induced stress on the total fluid stress over different rough boundaries to elucidate the uncertainties and conflicting results in assessing the significance of form-induced stress, to inform the approach required for water-worked gravel beds.

2.7.2 Vegetation Canopies

One of the first studies to investigate form-induced stress was that by Raupach *et al.* (1986). These results were also reported in Raupach (1994) and Kaimal and Finnigan (1994). Raupach *et al.* (1986) considered the flow over bluff elements arranged in a diamond array, to simulate a vegetation canopy, within a wind-tunnel. A hot-wire anemometer was used to measure the streamwise and vertical velocity components at 10 different locations within and above the canopy. They concluded that form-induced stresses are insignificant at heights near and above the top of the canopy. These results have also been found by Mulhearn (1978) over two-dimensional bar roughness, and by Perry *et al.* (1987) and Raupach *et al.* (1980) over several three-dimensional rough surfaces, but from more limited data. Raupach *et al.* (1986) also found that the contributions could be slightly larger in the upper part of the canopy. For example, three quarters of the way up into the canopy the form-induced stress was 5 % of the spatially-averaged Reynolds stress.

However, they acknowledge they were not able to measure form-induced stress reliably within the canopy because of the inability to measure very close to the elements, and also because of the errors induced by the use of hot-wire anemometers. Therefore it was

not possible to examine fully the significance of form-induced stresses. In addition to this, it is questionable whether 10 point velocity measurements, taken at just one streamwise position within the flow, are sufficient for characterising the spatial variability in the flow, and therefore the range of form-induced stresses over a rough boundary. Furthermore these measurements were concentrated in just one region of the diamond array. It could also be questioned whether such an array can accurately represent a vegetation canopy and be representative of natural vegetation canopies. They also acknowledge that errors in the probes are likely to have influenced the reliability of their measurements. These errors have been well documented elsewhere (e.g Raupach *et al.*, 1991), but briefly they include; (i) errors at high turbulence intensities due to short-term flow reversal in the streamwise direction; (ii) errors due to contamination of the instantaneous velocity measurements by lateral velocity fluctuations; (iii) the effect of heat dispersed from one-hot wire on the readings of another; (iv) the effect of fluctuating air temperatures upon the hot-wires; and (v) the loss of high-frequency coherence due to the spatial separation of the wires. This resulted in measurements very close to the boundary in particular being the most unreliable, the area of the flow in which form-induced stresses are most likely to be important. Raupach and Shaw (1982) state that Mulhearn (1978) was also unsuccessful in directly measuring the form-induced stress, further bringing into question the validity of their conclusions that form-induced stresses can be neglected above the canopy.

However, it still led many to assume that form-induced stresses were negligible for canopy flows (e.g. Raupach and Shaw, 1982; Brunet *et al.*, 1994; Ayotte *et al.*, 1999), despite the limited nature of these previous studies, and the lack of data from within the canopy. This may have been because it is a convenient assumption for developing models for the flows (e.g. Wilson and Shaw, 1977; Raupach and Shaw, 1982; Brunet *et al.*, 1994; Ayotte *et al.*, 1999) and associated heat dispersion (e.g. Finnigan, 1985; Legg *et al.*, 1986), because they complicate the equations considerably (Raupach and Shaw, 1982).

Recent work has been able to measure form-induced stresses more accurately, closer to the roughness elements and at a greater number of locations within the canopy. Böhm *et al.* (2000) compared the magnitude of form-induced stress to that of spatially-averaged Reynolds stress in a wind tunnel over and within a sparsely populated model plant canopy. These comparisons revealed that the form-induced stress was much smaller

than the Reynolds stress in the upper canopy, as discovered by earlier studies. Crucially, because it provided the first set of measurements that could reliably estimate form-induced stress in the lower canopy, they discovered that form-induced stresses were of the same order of magnitude as the Reynolds stresses in the lower layers of the canopy. Given that smaller stress levels have been found for dense canopies and for the upper layers of the canopy, (Mulhearn, 1978; Raupach *et al.*, 1980; Raupach *et al.*, 1986), it suggested that the relative importance of form-induced stresses may depend on both canopy density and height within the canopy. This indicated that consideration was required of their importance across all regions of the canopy and for a wide range of canopy roughness densities.

With this in mind, Poggi *et al.* (2004) performed detailed LDA measurements within a hydraulic flume for flows within and above five canopy roughness densities. It was possible to measure throughout the canopy, including close to individual roughness elements. A model canopy was constructed with steel cylinders arranged in a regular pattern. The experiments were conduced for each canopy density at two different Reynolds numbers, and therefore two different flow depths, to assess whether the relative contribution of form-induced stress to momentum transfer vary strongly with Reynolds number. The relative importance was quantified as the ratio of form-induced stress to the spatially-averaged Reynolds stress. For both flows, form-induced stresses were found to be negligible above the canopy, as previous studies have found. Within the canopy the form-induced stresses were far more significant. For the sparsest canopy, the form-induced stress was up to 35 % of the Reynolds stress within the lower-layer of the canopy. This maximum occurred at around a quarter of the way up into the canopy, below which there was a slight decrease in form-induced stress to 20 % at the roughness trough. Above this maximum, there was a rapid decrease in the stress up until the top third of the canopy, where the stress was negligible, and then turned to being up to -10 % of the Reynolds stress. This then reduced to being negligible at the roughness crest. These findings are consistent with Böhm *et al.*'s (2000) sparse canopy measurements. This vertical pattern of change in form-induced stress was found to occur for all five canopy densities at each of the two flows. However, an increase in the canopy density caused a decline in the significance of form-induced stress to momentum transfer, such that form-induced stresses were only up to around 1 % of the Reynolds stress for the densest canopy. This is in accordance with Böhm *et al.*'s (2000) suggestion that canopy density is important to the significance of form-induced stresses to momentum transfer.

It is noteworthy that these results were based on just two flows, making any assessment of the effect of Reynolds number on form-induced stress difficult, and secondly only 11 point measurements were taken within the canopy. These measurements were more densely placed in regions where the flow was exhibiting the most spatial variability, which could have led to an overestimation in the form-induced stress within the canopy. Poggi *et al.* (2004) also discuss the limitations of using a model canopy for extrapolating these findings to real vegetation canopies. For example, in a pine forest, the leaf area density is small in the top third of the canopy yet most dense in the middle layers. Hence, their results imply that the form-induced stresses in a pine forest would be large near the canopy top but small in the middle layers, which is opposite to the findings they report. Therefore, it still remains unclear how a natural distribution of leaf area density affects form-induced stress.

2.7.3 Urban-like Canopies

Cheng and Castro (2002) have also found negligible form-induced stress above the canopy, in this case above urban-like dense canopies. In this study, comprehensive measurements were made over a number of surfaces with the same area density within a wind-tunnel. This was performed for just one free stream velocity. Three urban surfaces were simulated using uniform sized cubes in an aligned and staggered pattern (with cubes of two different heights) to represent buildings within an urban area. A further test was performed over cubes and rectangular blocks arranged in a staggered array. They only present, however, form-induced stress measurements for the surface consisting of aligned cubes and the latter surface because they could only collect a sufficient number of velocity measurements over these canopies. The form-induced stress was found over both surfaces to be two orders of magnitude lower than the spatially-averaged Reynolds stress, and this difference remained fairly constant throughout the depth of the flow. They also demonstrated that vertical changes in Reynolds stress were balanced by changes in form-induced stress. There was no discernible difference in form-induced stress over the two surfaces, despite the difference in surface topography. They recognise that actual urban areas have elements that are not only random in height and shape, but also randomly spaced. Again the stresses within the canopy could not be derived because of the use of a hot-wire anemometer.

To overcome the difficulty of measuring form-induced stresses within an urban-like canopy, subsequent studies have investigated form-induced stresses numerically. Lien and Yee (2004) used TANS equations to model the flow within and above a simple, aligned array of cubes (buildings). They discovered that although the form-induced stress was very small compared to the spatially-averaged Reynolds stress at and above the canopy top, the magnitude of the form-induced stress was comparable to that of the spatially-averaged Reynolds stress below the canopy top. Within the lower half of canopy, the form-induced stresses made negative contributions to momentum transfer, but positive contributions in the upper half, with the maximum stress occurring approximately two thirds of the way up into the canopy. Unfortunately no wind-tunnel experiments are available to validate these results. However, as they point out, even if the spatially-averaged Reynolds stress was under predicted by a factor of two, the same conclusion would be valid.

A similar numerical study was also made by Kanda *et al.* (2004) using Large Eddy Simulation (LES) for flow within and above simple cube arrays. They investigated how form-induced stress changed with cube areal density, and also with different sized cubes at the same density. Above the canopy, the form-induced stress values were small but not insignificant. They ranged from around -5 % of the spatially-averaged Reynolds stress to 10 %, and could remain a similar percentage high into the flow. This is in contrast to previous experimental results (Mulhearn, 1978; Raupach *et al.*, 1981; Raupach *et al.*, 1986; Böhm *et al.*, 2000; Cheng and Castro, 2002; Poggi *et al.*, 2004) in which the form-induced stress above the canopy was found to be negligible. Kanda *et al.* (2004) state that this could have occurred because of the small spatial extent of the velocity measurements made in the previous experimental studies. They state that this can be caused because the extension of the measured region used for spatial averaging is often equal to just one cube area or roughness element area, but the coherent flow structures within the flow are much larger than the unit cube/roughness element scale. Therefore, a small measured region does not necessarily mean, for example, that the double-averaged vertical velocity will be zero within this region. Due to instrumental errors, it is quite difficult to decide if non-zero double-averaged vertical velocities are a real effect or just arise due to instrumental error. Kanda *et al.* (2004) point out that ignoring non-zero double-averaged vertical velocities can lead to a significant underestimation of form-induced stress. Raupach *et al.* (1986) measured a value of double-averaged vertical velocity of –0.15 m/s but attributed it to an error in the hot-

wire anemometer, and therefore its effect was removed from subsequent analysis by assuming it was zero. If Kanda *et al.*'s claims are correct, this could account for Raupach *et al.*'s (1986) small form-induced stress values.

Within the canopy, Kanda *et al.* (2004) found form-induced stresses to be larger than that above the canopy, and for its vertical profile with this region to be dependent on the density of the cube areal density. These profiles could be grouped into those measured at low densities and those at high densities. For low densities, form-induced stress made larger positive contributions to the total fluid stress of up to around 35 %. From the top of the canopy to the canopy floor, the contributions increased rapidly to this maximum, which occurred at approximately three-quarters of the way up into the canopy, a similar height to that observed by Lien and Yee (2004). Below this height it decreased eventually to zero at the ground level. But for the higher densities, form-induced stress contributions were negative near the ground, increasing from zero to up to –10 % at a quarter of the way up the canopy, and then decreased to zero at around half to three quarters of the way up into the canopy. A further increase in height caused the contributions to become positive, up to 20 % and then to become zero at the top of the canopy. This is the opposite of that found by Poggi *et al.* (2004), whereby negative contributions were found in the lower canopy, and positive contributions in the upper canopy. For both the low and high density regimes in Kanda *et al.* (2004), an increase in cube areal density caused a reduction in the size of the positive contributions but an increase in the size of the negative contributions. These broad differences in the vertical profiles between the low and high densities were attributed by Kanda *et al.* (2004) to a difference in flow regime. For the low densities, they described an interfacial flow regime, whereby the cavity flow transported the momentum downwards. For high densities there was a wake flow regime, whereby the recirculation of the flow in wakes of the cubes was fed by the turbulent kinetic energy. This resulted in reverse flow in the lower part of the canopy, which transported momentum upwards. They were therefore able to provide valuable information on the effect of the density of roughness elements on form-induced stress. This is an effect that has been mentioned by previous studies, but never extensively examined in the manner as Kanda *et al.* (2004). Again the use of simple arrays of cubes means that it is difficult to extrapolate these results to natural urban canopies, and no data was available to validate directly their results.

Coceal *et al.* (submitted) was the first study to use Direct Numerical Simulation (DNS) based on the DANS equations to investigate the significance of form-induced stresses over a rough boundary. They also simulated the flows over regular arrays of cubes. Results were analysed in terms of a formal spatial averaging procedure to enable interpretation of the flow within the arrays as a canopy flow, and of the flow above as a rough wall boundary layer. This was performed for staggered, aligned and square arrangement of cubes. They found similar results to Lien and Yee (2004), with form-induced stress being comparable in size to the spatially-averaged Reynolds stress within the canopy. However, the maximum form-induced stress occurred, in this case, at the roughness crest and then decreased to zero at the base of the array. This maximum corresponded with the height at which vortex cores occurred between the cubes. Above the canopy, the form-induced stress was negligible, which is in contrast to that found by Kanda *et al.* (2004), despite similar canopy arrangements being investigated. The vertical profiles of form-induced stress were very similar for the aligned and square arrays, as for the high density arrangements in Kanda *et al.* (2004). For the staggered arrays, Coceal *et al.* (submitted) found that the maximum form-induced stress was similar to that discovered for the aligned and square arrays. Below the height at which this maximum occurred, the contributions within the staggered arrays decreased, remaining positive, as found for the low cube areal densities by Kanda *et al.* (2004). This difference in vertical profiles between the staggered arrays and those from the aligned and square arrays were not found by Cheng and Castro (2002), whose results suggested that geometrical arrangement had little influence on form-induced stress. Note though that this was for arrangements with the same density. The results presented by Coceal *et al.* (submitted) imply the opposite, perhaps because the density changed with the different geometrical arrangements. They describe the change in form-induced stress with geometrical arrangement in terms of the three-dimensional flow structure. The cubes in the staggered configuration had a greater streamwise separation so there was less sheltering of the flow. Furthermore, the flow was diverted laterally because of the staggered cubes in adjacent rows, and was accelerated within the gaps between the cubes, leading to greater pressure on the front face of the cubes. In contrast, the close vicinity of the cubes in the square and aligned arrays, and the absence of lateral flow diversion, resulted in most of the momentum flux from spatial variations coming from above. This explanation is essentially the same as the one given by Kanda *et al.* (2004) for the change in form-induced stress with areal density. Therefore, also given the results of Cheng and Castro (2002), it suggests that it could be the density of the cubes,

rather than the geometrical arrangement, which influences form-induced stress. It is worth noting that Coceal *et al.* (submitted) was the first study to validate their form-induced stress values, in this case using the data from Cheng and Castro (2002), but only for the aligned array. It showed that the model poorly fitted the form-induced stresses within the canopy, the region of the flow in which accurate prediction is most crucial because of their larger magnitude.

2.7.4 Dune-shaped Bedforms

Recent studies have also been made of the significance of form-induced stresses over fixed dune-shaped bedforms. Nikora *et al.* (in press b) calculated the form-induced stress over a single 2-D dune-shaped bedform. A series of runs were carried out over bedforms of three different crest to trough ratios, and at different relative submergences. At the highest crest to trough ratios the contributions from the form-induced stresses were purely negative to the total fluid stress. They were zero at the trough and then increased up to a maximum contribution of nearly 50 %, at the roughness crest. This maximum also occurred at the roughness crest in Coceal *et al.*'s (submitted) study. Above this, the contributions decreased to be negligible for all but a small region close to the roughness crest, demonstrating that form-induced stress can be ignored above the bedform. For the bedform with the mid crest to trough ratio, they constituted only a few per cent of the total fluid stress within the interfacial sublayer. A further reduction in the crest to trough ratio then caused an increase in the contributions, showing that there is no consistent relationship between the geometry of the bedforms and the significance of form-induced stresses to momentum transfer. This was discovered to be the case over urban-like canopies by Coceal *et al.* (submitted). At this lowest ratio, form-induced stress followed a vertical profile similar to that described by Poggi *et al.* (2004). In the lower region of the interfacial sublayer, positive contributions could be as large as nearly 20 %, but the upper canopy was dominated by larger negative contributions of up to 50 %. Contributions were again highest at the roughness crest. It was at this ratio that the effects of relative submergence could be examined. It showed that there was a decrease in the contributions made by form-induced stress with a reduction in relative submergence. However, because this is based on only two different flow depths, it is uncertain whether this is a consistent trend and whether it would occur over a range of flow depths. For all three bedforms, the form-induced stresses acted to balance the variations in Reynolds stress, particularly above the roughness crests. This

demonstrated that where deviations in Reynolds stress from an assumed linear distribution are large, knowledge is required of the form-induced stresses for describing or modelling flow over this kind of roughness. Nikora *et al.* (in press b) highlighted that in order to determine non-uniformity effects for flow field, spatial averaging should be performed over more than one bedform wavelength, preferably at least two or three. Given that this was only carried out over one bedform, they had to make the assumption that the form-induced stress did not vary in the streamwise direction, which appears doubtful. It should also be noted that these are fixed, regular bedforms that are two-dimensional, were of the same shape and size throughout the flume and were impermeable, so are unlikely to represent accurately form-induced stresses over more spatially complex, natural bedforms.

Maddux *et al.*'s (2003) study over fixed, artificial 3-D dune shapes also examined form-induced stresses. They examined flows at two different submergences over a bedform of one geometrical form. They found, like Nikora *et al.* (in press b) for the 2-D dune-shaped bedform with the lowest crest to trough ratio, that the contributions made by these stresses to the total fluid stress were positive in the lower regions of the interfacial sublayer, and negative in the upper regions. The crossover point corresponded to the elevation of the crest line minimum. However, the contributions were typically much lower than over 2-D bedforms. Positive and negative contributions were only as high as around 15 % of the total fluid stress. The maximum contribution within the interfacial sublayer also did not occur at the roughness crest, as found by Nikora *et al.* (in press b) for the 2-D bedforms. Instead it occurred at around three-quarters of the way up within the interfacial sublayer, as found by Kanda *et al.* (2004). The vertical change in stress within the interfacial layer, and the magnitude of the stress, was not influenced by relative submergence, in contrast to that found by Nikora *et al.* (in press b). Unlike many other studies, the form-induced stresses were not negligible above the roughness crest. Instead, they remained significant for nearly the whole flow depth for the lowest submergence, and for up to half of the depth for the highest submergence, and resulted in the maximum stress not occurring within the interfacial sublayer. For the lowest submergence, the maximum occurred in the lower third of the region of flow between the crest and the water surface, and within the bottom 10 % of this region for the highest submergence. The contributions were positive within this region in both cases, and were a maximum of around 20 % of the total fluid stress. The crossover from positive contributions in the region above the crest to negative contributions in the upper region

of the interfacial sublayer occurred at just above the elevation of the maximum of the dune crest line. The tests revealed that there are differences in the significance of form-induced stress to momentum transfer between 2-D and 3-D dune-shaped bedforms. Maddux *et al.* (2003) acknowledge that uncertainties in the position of the ADV probe close to the bed may have introduced uncertainties in the estimates of form-induced stress, especially given that this is where velocity gradients are at their highest. They also state that the grid of point measurements they undertook may not have been fine enough to resolve near-bed gradients accurately.

2.7.5 Regular Roughness Elements

Nikora *et al.* (2001) examined form-induced stresses over and within a regular arrangement of spheres. They fitted a 7th order polynomial to the vertical variation in form-induced stresses from data taken from a number of points over the bed, to provide an estimate of form-induced stress for the whole bed. This revealed that the contributions are not significant above the roughness crests. Within the interfacial layer, the form-induced stresses were comparable (though less) to the spatially-averaged Reynolds stress, as found by Lien and Yee (2004) and Coceal *et al.* (in press). The maximum form-induced stress occurred lower down within the interfacial sublayer than has been reported before, at around a third of the way up into the interfacial sublayer. However, it is important to note that these form-induced stress values are not derived through spatial averaging, largely because of the small number of measurements taken within the arrangement of spheres. In addition, there was a bias of the measurement locations to particular planes within the arrangement. Nikora *et al.* (2002) discovered that the addition of periphyton on the same spheres produced a reduction in the form-induced stress, such that it was less than 5-6 % of the spatially-averaged Reynolds stress. This is despite that, in the presence of periphyton, there was a stronger correlation between the near-bed time-averaged velocity components with the bed topography, and an overall greater degree of flow heterogeneity. In addition, the periphyton caused the vertical height of the maximum form-induced stress to move further away from the bed to the level of the roughness crests.

The significance of form-induced stresses over other regular roughness elements has been examined. Nikora *et al.* (in press b) made an examination over two-dimensional transverse ribs. This was only carried out for one flow depth. As for over two-

dimensional dune-shaped bedforms, measurements were only taken over one single roughness wavelength, and flow non-uniformity could not be directly evaluated from the velocity measurements. They also only present results from one rib spacing. They showed that form-induced stresses are only significant up to just above the roughness crest. The contributions to the total fluid stress were positive within the interfacial layer, reaching a maximum value of nearly 8 % at around two thirds of the way up into the sublayer. Just above the roughness crest the contributions were negative and only around 1 %.

However, over the same type of roughness, Pokrajac *et al.* (2003) have found very different results. They used PIV for just one lateral location over the bed and characterised the flow over one transverse rib within a laboratory flume. This resulted in their measurements only being able to investigate the influence of an individual roughness element on the flow and they only examined the flow above the roughness crest. They discovered that the maximum stress occurred just above the roughness crest and could make contributions as high as nearly 15 % to the total fluid stress. Furthermore this stress remained significant to a greater distance above the roughness crest than was observed by Nikora *et al.* (in press b).

2.8 Why has the Significance of Spatial Variability in the Flow over Water-worked Gravel Beds been Largely Ignored?

It has been shown that many studies have examined form-induced stresses, and therefore spatial variability in time-averaged flow fields, over various types of roughness, but that there is a lack of information for water-worked gravel beds. This is surprising given the clear recognition of its importance in other areas of study, and the fact that a number of studies over these beds have reported spatial variability in the time-averaged flow field and departures in Reynolds stress from an assumed vertical linear distribution. It is worth considering the possible reasons for this in order to identify the approaches now required.

The Reynolds equations can only deal with point flow properties and derive point momentum fluxes. Therefore, until the development of double-averaging methodology, there has been no theoretical framework by which to take explicitly into account spatial variability in the flow. There is then a lack of motivation for investigators to gather

velocity measurements over a number of points over a water-worked gravel bed, given that it does not provide any further information about momentum transfer than a single point measurement would provide. This has led many to assume (either implicitly or explicitly) that point measurements of Reynolds stress can characterise momentum transfer over water-worked gravel beds, either through this theoretical constraint, a lack of understanding of the spatial variability in the flow, or by following, what has become, the paradigm of thought.

It is also related to the suitability of velocimeters for characterising spatial variability in the flow field. Spatial variability in the time-averaged flow field, and the associated form-induced stress, is notoriously difficult to measure (Finnigan, 2000). To do so requires a dense network of measurements at a high spatial resolution over a larger spatial area to fully sample the spatial variability within the flow, and close enough to the boundary to produce a reliable assessment of its significance in the near-bed region. Until relatively recently only point velocimeters have been available. Fortunately, the development of more sophisticated point velocimeters, such as ADV, and in particular LDA, have made it possible to measure time series of turbulent flow velocities closer to the boundary than was previously possible. Yet they still only offer velocity measurements at a point. It is therefore still a significant task within a laboratory, and practically impossible within the field, to provide velocity measurements at a high spatial resolution over a larger area of a water-worked gravel bed. For example, within the field, the time-consuming nature of the measurements makes it very difficult to be certain that flow conditions, and if the bed is mobile, the bed conditions, have not changed during measurement. Furthermore, ADV's at present are the most advanced velocimeter that can be used, which places limitations on how close to the boundary the flow can be measured. The recent realisation that Particle Image Velocimetry (PIV) can be successfully used for studying flows over water-worked gravel beds (Tait *et al.*, 1996), means that there is now a measurement tool available that can make velocity measurements simultaneously at a very high spatial resolution and at many locations over the bed relatively quickly. Despite this recognition, still only one study has applied PIV to gravel bed flows to examine form-induced stress (Campbell *et al.*, 2005). It is clear that PIV could be an important tool for examining form-induced stress and spatial variability in the time-averaged flow over such beds, and there is great need to apply this technique for such purposes. Through its relative speed of operation it can allow measurements to be made at many different hydraulic and bed conditions. It could

therefore provide a significant step towards parameterising spatial variability and form-induced stresses over water-worked gravel beds. Indeed, it is recognised that there is a great need for specially designed laboratory experiments for an improved understanding of form-induced stress (Cheng and Castro, 2002; Nikora *et al.*, in press a).

2.9 Potential Implications

It is clear that a deep understanding of spatial variability in the time-averaged flow field, and the form-induced stress that this creates, is required for an accurate description of momentum transfer over water-worked gravel beds. Experimental results have revealed that the momentum conservation described by the Reynolds equation is violated close to the bed, and that some additional momentum fluxes must be present in order to balance the equations. But form-induced stress is the most poorly understood term in the double-averaged equations (Raupach, 1994; Finnigan, 2000). If momentum transfer is therefore to be fully understood, it needs to be established whether form-induced stresses are significant over water-worked gravel beds and whether it could be one of the additional fluxes. It is also important that it is parameterised for the development of DANS-based models for gravel-bed rivers, as they may successfully fill a gap in modelling capabilities for such flows where the TANS-based models are not suitable.

The determination of form-induced stress is also important for estimating τ_0 over water-worked gravel beds. The present approach is to use a linear fit to the Reynolds stress (from one point measurement). Therefore the deviation in the Reynolds stress from a vertical linear distributions that has been observed by many close to the bed surface, is likely to give errors in the estimate of τ_0. If form-induced stress can account for this departure, then a summation of the Reynolds stress and form-induced stress should provide a more accurate prediction of τ_0.

An accurate description of the spatial variability in the time-averaged flow field is also required for accurate prediction of flow resistance in gravel-bed rivers. Any spatial variability in the time-averaged streamwise velocities is likely to give variable estimates of flow resistance, and therefore flow depth. A prediction of flow depth could therefore be dependent on the position over the bed at which the time-averaged streamwise velocity is measured. Therefore an understanding of the degree of spatial variability in

these velocities and how they change with hydraulic and bed conditions should provide valuable information for determining the uncertainties in current flow resistance estimations. It could also promote the development and use of flow resistance relationships that explicitly take this spatial variability into account, as formulated by Nikora *et al.* (2001).

Spatial variability in the time-averaged flow field may also have important implications for bedload transport. If certain areas of the bed experience, on average, higher velocities they are likely to be sites of preferential entrainment. This could induce spatial variability in entrainment rates and therefore bedload transport. It also has important implications for the prediction of bedload transport in rivers. Most calculations of bedload transport in rivers are 1-D, by averaging hydraulic and transport-rate calculations over the channel width. Since bedload transport laws are non-linear, spatial variability in shear stress over the bed could potentially cause large errors in the prediction of bedload transport using conventional bedload transport models.

Furthermore, spatial variability in the time-averaged flow field could induce spatial variability in the lateral and streamwise advection of solutes and suspended sediment, and therefore also influence the vertical profiles in their concentrations. Differential advection in a soluble or suspended material occurs when parcels of the material within the flow experience different velocities at different spatial location (Guymer *et al.*, 2005). This advection produces a spreading, commonly called 'shear dispersion'. The degree of spatial variability in the time-averaged flow will therefore influence the rate of this shear dispersion. Given that the majority of dispersion models treat the time-averaged velocity to be constant over the bed (a 1-D treatment), any spatial variability in time-averaged velocities will give different estimates of dispersion rates and therefore solute and suspended sediment concentrations. As with flow depth predictions, the calculated dispersion rate and concentration would be dependent on the position over the bed at which the time-averaged streamwise velocity is measured.

Spatial variability in the time-averaged flow could also be important for the promotion of ecological refugia within gravel-bed rivers, by providing areas over the bed where the negative effects of disturbance or severe hydraulic stress are lower than in surrounding areas (Lancaster and Belyea, 1997; Lancaster, 1999). For instance, it could be an important variable for determining the spatial distribution of benthic invertebrates in

gravel-bed rivers, or producing preferential sites for feeding, resting and spawning for drift-feeding fish. Information on the full three-dimensional flow field is important for understanding the interaction between habitat and flow hydraulics and for developing more sophisticated analysis of the parameters that describe habitat availability.

Clearly, spatial variability in the time-averaged flow field could be a fundamental component of many processes within a gravel-bed river, and may be an important variable for promoting spatial heterogeneity in the ecological and sedimentolgical environment.

2.10 Outcome of Literature Review

It has been shown that despite spatial variability in the time-averaged flow field being reported in several studies, it has never been the explicit aim of these investigations to study this variability in any detail, with the exception of the study made by Legleiter *et al.* (in press). There has been no systematic study examining the variables that control both the degree of spatial variability and the spatial pattern in the time-averaged flow field over water-worked gravel beds. In addition, no study has attempted to quantify the degree of spatial variability in the time-averaged flow field. This is despite there being a wealth of evidence that now exists within the literature that such variability and structure exists, and is likely to influence the estimation of bed shear stress. Therefore there is little, or no, consensus of opinion on the degree of spatial variability over water-worked gravel beds and how this is influenced by hydraulic and bed conditions.

For example, several studies have made qualitative assessments of the effects of bed surface topography on the time-averaged flow, describing it in terms of the influence of isolated roughness elements (Clifford, 1996; Robert, 1997; Lane *et al.*, 2002; Papanicolaou and Hilldale, 2002; Lane *et al.*, 2004; Tritico and Hotchkiss, 2005), pebble clusters (Buffin-Bélanger and Roy, 1998; Lawless and Robert, 2001), or in the form of secondary currents (McLelland *et al.*, 1999; Carling *et al.*, 2002; Papanicolaou and Hilldale, 2002). Yet the majority of these studies have examined the flow over beds with large clasts or large pebble clusters, or within a cross-section of a channel, rather than over a flatter section of bed that is more representative of average bed conditions. Therefore, their qualitative interpretations of the effects of bed surface topography on the spatial variability in the time-averaged flow inherently revolve around such bed

surface features. The lack of quantitative examination of the effect of bed surface topography is related to studies not making detailed measurements of bed elevations and, because no study has attempted to carry out velocity measurements at a sufficiently high spatial resolution, to obtain detailed information on the degree of spatial variability and the spatial structure of the time-averaged flow field. Since their measurements often relate to local flow and bed properties, this also further explains why the spatial variability has been examined in terms of the effects of individual roughness elements. It also results in any attempt to relate quantitatively the effects of the bed on the flow being far too coarse (as was shown in Legleiter *et al.* (in press)). No study has been able to examine the influence of the microtopography of water-worked gravel beds on the spatial variability and pattern in the time-averaged flow in a detailed, quantitative manner.

Several studies have also reported the influence of flow depth on the spatial variability, but have often only investigated two or three different depths. Therefore, there still remains confusion of whether an increase in flow depth causes the degree of spatial variability to increase (Clifford, 1996), decrease, or to have little influence (Legleiter *et al.*, in press). Furthermore, only Legleiter *et al.* (in press) have examined how flow depth influenced the spatial patterns, but using measurements at a low spatial resolution and for just three different flows.

It was demonstrated that the spatial variability in the time-averaged flow field makes the Reynolds equations inappropriate for studying momentum transfer over water-worked gravel beds. These equations do not explicitly take into account the momentum which is transferred by this spatial variability. It means that the two-dimensional approximations made when using the Reynolds equations to express the total stress distribution within the flow, cannot hold for the near-bed region. This was shown by discussing a number of studies that have reported deviations in Reynolds stress from an assumed vertical distribution in the near-bed region. Any deviation indicates a violation of the momentum conservation described by the Reynolds equation, which suggests that Reynolds equations are inappropriate for accurately characterising momentum transfer over a water-worked gravel bed. Therefore, the application of Reynolds equations results in errors in approximating the total fluid stress, and for predicting bed shear stress.

The spatial variability in the flow field can be taken into account explicitly by supplementing the time-averaging of the Navier-Stokes equation with spatial averaging. This produces new continuity and momentum equations which are averaged both in time and space, and are therefore double-averaged. This produces new drag terms and form-induced momentum fluxes which appear due to the spatial heterogeneity in the time-averaged flow. This methodology therefore provides the opportunity to study the potential of this spatial variability to carry momentum within the flow and to account for the deviation that is seen in Reynolds stress close to the bed. Despite this, only studies by Campbell *et al.* (2005) and Nikora *et al.* (in press b) have attempted to carry this out over gravel bed surfaces. These have been limited to characterising the stresses based on either a low number of point measurements, or from measurements at just one lateral location over the bed. Furthermore, they have shown discrepancies in the significance of form-induced stresses to contributing to the total fluid stress, but it still remains unclear why this is so. This is largely because each study only examined one bed surface, and for a low number of different flows. It is therefore unclear how form-induced stress changes with hydraulic conditions and over a number of surface topographies.

A review of studies that have investigated form-induced stress over artificial roughnesses demonstrated there is a consensus of opinion that they make significant contributions to the total fluid stress within the interfacial layer. Yet there is a great deal of confusion, or uncertainty, over whether this is so for flows above the bed surface. This has yet to be resolved, again largely because of the limited range of flow and bed conditions that have been investigated. Therefore, a systematic study of form-induced stresses in this layer would seem appropriate.

It was demonstrated that PIV may offer the potential for solving many of the problems that previous studies have encountered when trying to characterise sufficiently the spatial variability in the time-averaged flow field, and therefore accurately estimating form-induced stress. This has yet to be fully utilised for such purposes.

It is therefore clear that the high spatial resolution measurements of velocity that PIV can provide over large spatial areas are required for quantitatively assessing the degree of spatial variability in the time-averaged flow and its potential for transferring momentum over water-worked gravel beds. Furthermore, measurements are required

over a range of hydraulic conditions and over beds of different surface topographies (in particular ones that do not contain isolated roughness elements) to understand how this changes the degree of spatial variability and the spatial structure in the time-averaged flow field over water-worked gravel beds, and its potential for transferring momentum.

CHAPTER 3
EXPERIMENTAL APPARATUS AND PROCEDURES

3.1 Outline of Experimental Programme

The experiments examined the spatial variability and patterns in the time-averaged flow field and the contributions this made to momentum transfer over water-worked gravel beds. The changes in the flow were examined under different hydraulic and bed conditions. Three phases of tests were conducted to study the influence of relative submergence, bed slope and mean bed shear stress. All the flow conditions were below those required for bed movement, so that the beds were static and therefore the bed surface topography was the same for each test. The three phases of tests were carried out twice, using two different bed mixtures; a unimodal gravel mixture and a bimodal gravel-sand mixture. The programme was designed so that the relative submergence and bed slope was the same for each bed, so that results could be compared directly between the two sediment beds. The tests were also carefully designed so the effects of flow depth, bed slope and mean bed shear stress could be isolated using a minimum number of experimental runs. Given that the beds were static throughout all measurements, the effect of different hydraulic conditions on the flow could be isolated for each of the runs. Twelve tests were completed for each bed, 24 tests in total.

In the first phase of the experimental programme, the aim was to examine the effect of relative submergence on the time-averaged flow field, by changing the flow discharge at a single bed slope for six discharges.

In the second phase of the experimental programme, a combination of flow discharges and bed slopes were used so that three runs were at the same relative submergence and a further three groups of two runs had identical relative submergences.

In the third phase of the experimental programme, six experimental runs were carried out that used a combination of flow discharges and bed slopes so that the mean bed

shear stress was almost identical for each run. These tests combined the effects of both relative submergence and bed slope on the time-averaged flow field, but under conditions where the average momentum transfer rate at the bed was the same.

3.2 Laboratory Channel Apparatus

All the experiments were carried out in a 18.3 m long, 0.5 m wide, recirculating, glass-sided flume, with a working length of 15 m (Figure 3.1). The channel slope was adjustable via the use of a hydraulic jack. All the bed and water surface measurements were made relative to a datum plane, defined by two parallel rails running along either side of the flume. The distances from this datum plane to the bed and the water surface were measured using vernier point depth gauges, which had an accuracy of 0.1 mm. The depth of the water was controlled by a sharp-edged adjustable weir at the downstream end of the flume. This was adjusted to minimise drawdown effects and produce the maximum possible reach of uniform flow depth. The flow rate was monitored using a pre-calibrated orifice plate in the upstream delivery pipe and was controlled using an electronically controlled valve within the delivery pipe.

3.3 Particle Image Velocimetry

3.3.1 Introduction

The flow field over the water-worked gravel beds was measured using a 2-D Particle Image Velocimetry (PIV) system. This is an image-based system for obtaining instantaneous whole field velocities, and measures the distance travelled by groups of particles within the flow during a known time interval. Many small and 'neutrally buoyant' seeding particles are introduced into the flow, and given their size and near neutrality with water the particles follow the features of the flow. In order to detect their movement, an area of the flow is illuminated by a laser light sheet. This light sheet is not continuous but the laser produces two intense and very short pulses to produce a stroboscopic effect, freezing the movement of the seeding particles. To detect the position of the illuminated seeding particles a camera is placed at right angles to the light sheet, and particle positions appear as light specks on a dark background on each camera frame (Figure 3.2). An image is taken at the first and second pulse of the light sheet and the time separation between the two images is known. The images are divided

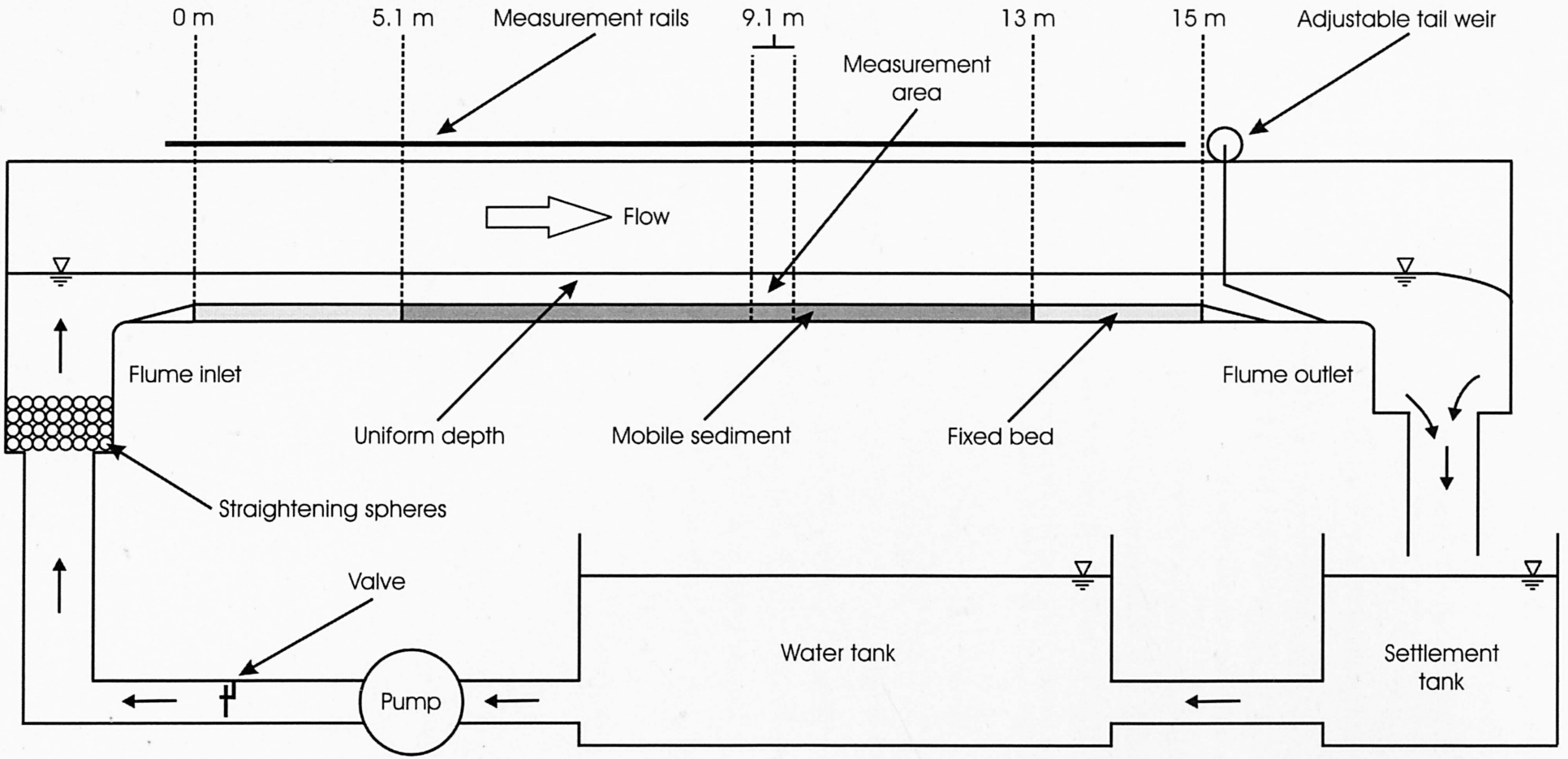

Figure 3.1. A schematic of the laboratory channel layout.

into small rectangular regions called interrogation areas and for each of these areas the images from the first and second pulse are cross-correlated. Any displacement between the pattern of the seeding particles in the first image with the pattern in the second image is taken to be the average displacement vector of the fluid in that small interrogation area. By carrying this out for all the interrogation areas, a vector map of average particle displacements is produced (Figure 3.2). As the time interval between the two light sheet pulses is known, these displacement vectors can be converted into a map of velocity vectors. Given that the time interval is short, these velocities can be considered to be instantaneous. PIV therefore allows the simultaneous measurement of instantaneous flow velocities at many locations within the flow, which is not possible with single-point technologies such as acoustic Doppler velocimetry (ADV) and laser Doppler anemometry (LDA).

Despite the early realisation that PIV can be successfully used for studying flows over water-worked gravel beds (Tait *et al.*, 1996), only one study (Campbell *et al.*, 2005) has attempted to use it to extract information on the significance of spatial variations in the time-averaged flow to momentum transfer. But PIV provides the possibility to make velocity measurements simultaneously at a very high spatial resolution and at many locations over the bed. Therefore it is clear that PIV is an important tool for examining form-induced stress and spatial variability in time-averaged flows over water-worked gravel beds, and there is a great need to apply this technique for such purposes.

3.3.2 Apparatus

This study used a 2-D Dantec PIV system. This consisted of a New Wave Research Minilase-III double pulsed Nd:YAG laser which operated at a radiation wavelength of 532 nm (green wavelength) and a pulse energy level of 50 mJ. Each pulse duration was 10 ns, ensuring that the motion of the seeding particles could be sensibly assumed to be frozen within each camera image. The laser was fitted with beam optics to expand the beam into a sheet of light. The frequency of the double pulse separation (the measurement frequency) is limited to 15 Hz. However given that each double image for one velocity measurement was 2 MB in size, it was operated at 9 Hz due to limitations in the buffer capacity of the acquisition unit. It was possible to either run the measurements at a higher temporal frequency for a shorter period of time, or at 9 Hz over a longer period of time. It was considered that the latter was more desirable given

that the interest is in the time-averaged flow field and that a long measurement period is required to produce steady time-averaged values. This allowed 5 and a half minutes of the flow to be sampled.

A Kodak Megaplus ES1.0 digital camera was used to mage the seeding particles. This contained an 8-bit, 1008×1016 pixel CCD chip and was fitted with a green optical filter on the camera lens. This filtered out any ambient light and only allowed wavelengths corresponding to the laser to be received by the camera. Without the filter, the first of the two images can detect a large amount of ambient light, which can sometimes obscure the actual signal given by the movement of the seeding particles.

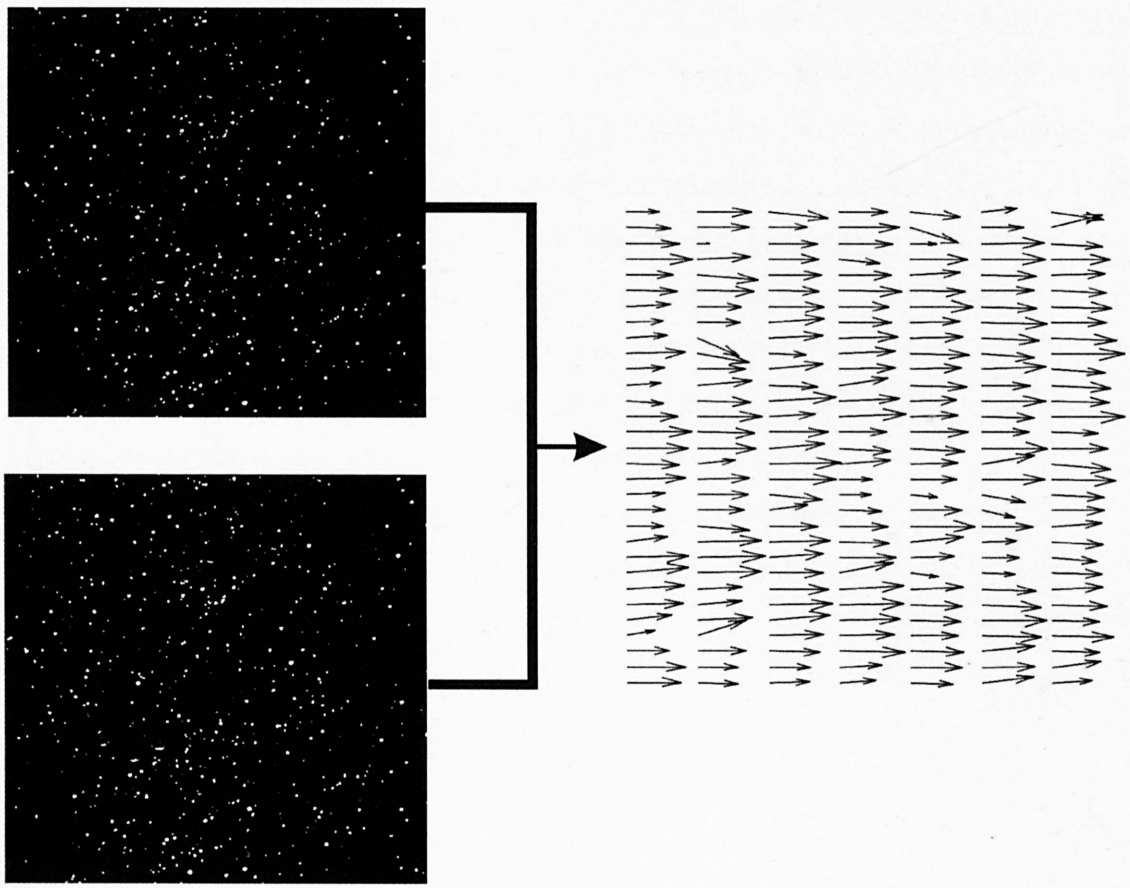

Figure 3.2. An example of the production of a vector map from two Particle Image Velocimetry images taken at each of the two pulses of the laser, which have a short time separation. The particle displacements from the two images are derived, from which a vector map can be produced (the vector map has been magnified and would include many more vectors).

A Dantec FlowMap Processor was connected to the laser and camera in order to synchronise the pulsing light sheet with the recording of the camera images. This included a data input buffer which simultaneously read and stored images from the camera during measurement and transferred them to a PC following the conclusion of measurement. The data buffer had a capacity of 24 GB. The images were processed into vector maps using Dantec FlowManager software, and converted into ASCII files for subsequent analysis in Matlab.

3.3.3 Experimental Arrangement

All previous approaches to utilise PIV to study the hydrodynamics of flows over rough sediment boundaries in laboratory flumes have taken measurements at one lateral position across the bed (usually the centreline of the flume) by using a vertical light sheet orientated normal to the bed surface (in a vertical plane), in order to obtain streamwise and vertical velocities (Tait *et al.*, 1996; Campbell *et al.*, 2005; Pokrajac *et al.*, 2003; Manes, *pers. comm*). One study has attempted a different approach to studying such flows. Barison *et al.* (2003) carried out PIV measurements above an armouring gravel bed with the light sheet located parallel to the bed surface (in a horizontal plane) to obtain streamwise and vertical velocities over a large section of the bed. This however was only achieved at one height above the bed, and at a reasonably high position above the bed. But it did reveal the potential of this approach for examining the spatial distributions of velocities over water-worked gravel beds, because it allows the velocity measurements at many more measurement locations over the bed than is possible with the use of PIV in a vertical plane. In addition, it enables the characterisation of the lateral variability in streamwise velocities, which is not possible with vertical plane measurements.

Previous approaches that have taken vertical plane measurements at one lateral location may not have led to a statistically acceptable level of sampling of the flow field to measure fully the degree of spatial variability. Measurements made in a horizontal plane offer greater information on lateral variability, but they do not provide any information on the spatial variability of vertical velocities and, unless utilised at many heights above the bed, does not characterise the vertical variability in the flow. In addition, previous PIV measurements have been taken for a limited number of hydraulic and bed conditions, which were in some cases only for one flow depth and slope over a single

rough bed (Campbell *et al.*, 2005; Pokrajac *et al.*, 2003). It is clear that PIV measurements in the vertical and horizontal plane each offer important but different information on the spatial variability in the flow field, and that an approach is required that exploits the advantages of both. This study attempts to adopt such an approach by carrying out horizontal plane measurements at many heights above the bed, and vertical plane measurements at a number of lateral locations over the bed. In this way, it is possible to characterise the spatial variability within a large cube of fluid, and if the two PIV configurations are carefully integrated, it can provide pseudo 3-D data at given positions within the cube.

The horizontal plane PIV measurements consisted of the laser light sheet being orientated parallel to the bed surface, with the camera normal to the light sheet (Figure 3.3). This was in order to measure streamwise and lateral velocities at different streamwise and lateral positions, but at one vertical height above the bed. The laser was positioned in a light tight enclosure which was perpendicular to the flume wall (Figure 3.4). This was located on a carriage, which was able to move vertically by the use of screw rods on each of the four corners of the box. A complete revolution of the screw rod was known to give a particular vertical displacement. The positioning of the rods allowed the box to be tilted at a sideways or vertical angle to the flume wall, to take into account the slope of the bed. This was to ensure that the light sheet was orientated parallel to the bed surface. The camera was located in an additional light tight box on the flume rails, and was able to move vertically (Figure 3.4). This was positioned between a distance of 8.9 and 9.4 m along the flume, such that the cameras imaged a measurement area at 9.1 m from the inlet (Figure 3.1). The cameras were positioned on a carriage that was able to move vertically within the box. Once the vertical height of the light sheet and cameras had been set to provide the desired image area, for measurements at different heights above the bed the vertical movement in the light sheet could be counterbalanced by moving the camera by the same vertical displacement, so that the image area and the focus remained the same for each height measurement. The outside of the glass walls of the flume were covered with black boards, and boards were placed upstream and downstream of the box. Curtains were also placed within the camera box and at the ends of these two boards. These measures were found to improve the contrast of the images and allowed the operator to use the system safely.

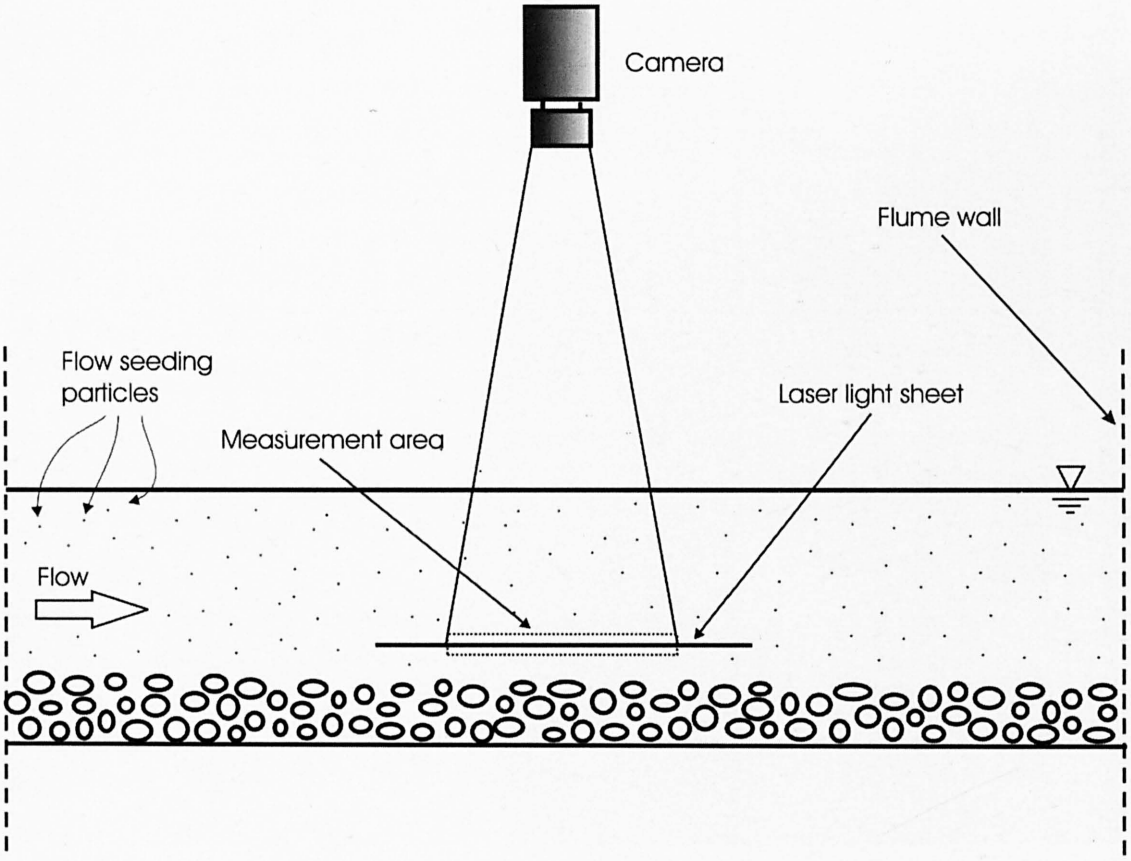

Figure 3.3. A schematic of the horizontal plane Particle Image Velocimetry configuration.

To initially position the cameras and laser, the laser was located so that the light sheet was located at a position parallel and 10 mm above the maximum bed elevation. A board of a depth of 5 mm was placed on the bed surface, and three targets were placed on its surface. These targets were painted with a thin white line such that the white lines were at a height of 5 mm above the board surface. Therefore the white lines were positioned at 10 mm above the maximum bed elevation. The alignment of the light sheet was possible by remotely monitoring the position of the sheet on the targets by the use of the camera. The sheet was positioned correctly when it correlated with the white paint on the targets. The targets were moved to the centre section of the images, all four corners of the image, and at several positions between all four corners and the centre of the image. This was to ensure that the entire span of the light sheet was parallel with the bed. The light sheet could be adjusted to different heights above the bed by evenly adjusting all four screw rods on the laser carriage by a known number of rotations. The light sheet could therefore be adjusted to an accuracy of 0.25 mm.

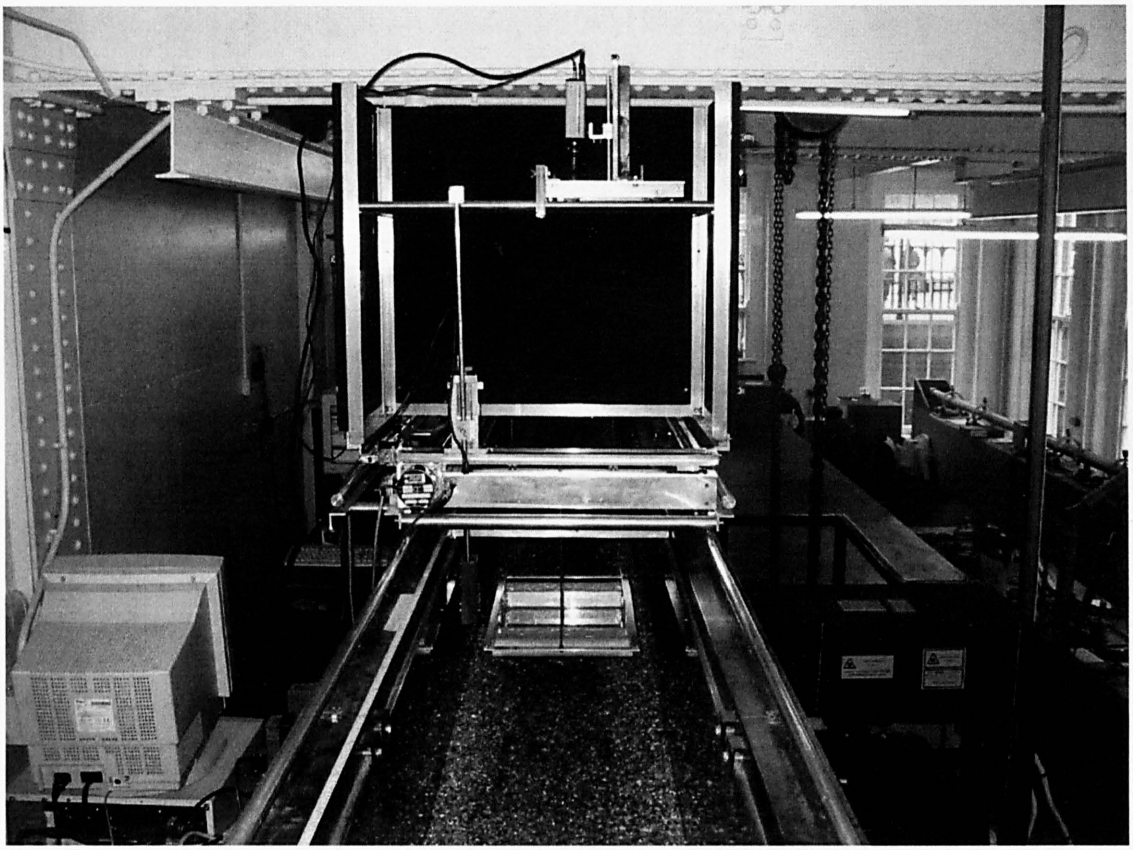

Figure 3.4. The horizontal plane Particle Image Velocimetry configuration, showing the camera located on a height adjustable carriage within a light-tight box on the rails of the flume, the light-tight enclosure on a height adjustable carriage for the laser to the right of the flume walls and a glass plate suspended over the measurement area of the bed.

For measurements on a plane parallel with the bed, the camera was positioned so that the centre of the image was at the centreline of the flume. During PIV measurement, a glass plate (Figure 3.4) was lightly positioned on the water surface to ensure there were no reflections from the rippled water surface. This plate was held in place by two screw rods on the upstream end and one screw rod on the downstream end positioned across both walls of the flume. This enabled fine adjustment of the plate so that the effects of the plate on the underlying flow field were minimised. Measurements were not taken closer than 10 mm to the glass plate to ensure that these effects did not strongly influence the PIV measurements

For the PIV measurements in a vertical plane, the positions of the laser and camera were reversed so that the laser produced a light sheet normal to the bed surface and was

located on a frame that rested on the flume rails, whilst the camera was positioned on a frame at the side of the flume (see Figure 3.4). This enabled streamwise and vertical velocities to be measured above the bed surface, at different streamwise and vertical positions but at a single lateral location over the bed. Before removing the camera from its position for the horizontal plane measurements, the three targets were evenly placed along the centre of the image (the centreline of the flume). Therefore before the positions of the laser and camera were changed it was possible to know the location over the bed at which the light sheet was aligned. The alignment was carried out using the same technique as described above, by aligning the sheet with the white paint on the targets. A vertical sheet was assured by positioning the aperture of the laser at the centreline of the flume to ensure that there was no angle to the sheet as it hit the centreline of the flume at the bed surface. The laser was able to traverse laterally over the bed on a carriage, enabling it to be positioned at different lateral locations across the bed. Therefore it enabled PIV measurement to be made at a number of different lateral locations over the bed. The camera was able to move towards and away from the flume walls within its light tight box so that any lateral movement in the light sheet was counterbalanced by that in the camera, ensuring the image area and focussing was held constant for each lateral measurement position. This configuration did not require the use of the glass plate, since the laser light is intense enough for the light not to be spatially distributed by the water surface. The same blackout boards and curtains were used as in the horizontal plane configuration.

A seeding particle feeder was located at 5.25 m along the flume. This consisted of a drum, which thoroughly mixed the particles with water, and four narrow pipes which were evenly distributed across the width of the flume and used to feed the seeding particles into the water surface. The seeding particles entered the flow 2 m upstream from the measurement area, enabling an even distribution of particles across the width of the flume before entering the PIV measurement area. The use of a feeder enabled the seeding density to be adjusted and ensured a constant rate of delivery. This reduced the likelihood of images being poorly seeded, which can cause considerable errors in PIV measurements.

3.3.4 *Image Processing Routines: Cross-correlation*

Once the raw PIV images were collected they were processed using Dantec's FlowManager software to generate velocity vectors fields. This processing requires the correlation of the movement of the particle between the two light pulses, and the validation of the vectors this generates. The use of a pulsed laser and rapid scanning CCD-camera allowed initial and final particle positions to be registered on separate camera frames. This enabled a cross-correlation technique to be used without the directional ambiguity of auto-correlation. Put simply, it is based on the correlation of light intensity within an interrogation area recorded at the first light sheet pulse with the same property at the second pulse. A high correlation value is observed when many particles within an interrogation area from the first light sheet pulse match up with their corresponding spatially shifted partners in that same area of fluid in the second pulse. A poor correlation is recorded when individual particles match with other (additional) particles. The cross-correlation technique finds the highest correlation peaks and a 2-D curve-fit is used to interpolate width, height and position of the peak from neighbouring points on that particle. This peak corresponds directly to the average particle displacement within the investigated interrogation area. This interpolation is carried out at a resolution of 1/64 of a pixel to avoid reducing the measurement accuracy, and is therefore termed subpixel interpolation (Dantec, 2000).

A small correlation value occurs when seeding particles either enter or leave the interrogation area between pulses, and therefore the initial and final positions are missing. This is referred to as 'loss-of-pairs', and is often caused by a low seeding density within the image. This is one of the reasons for a tendency to bias measurements towards zero, a so-called 'zero-velocity biasing'. Faster moving particles are more likely to have their initial and final position outside the interrogation area so the slower moving particles dominate the calculation of average displacement and effectively bias results towards zero. In addition, a loss-of-pairs can cause outliers in the vector map. These tend to be vectors longer in length than the other vectors and random in direction. This means that the average of several outliers is zero, which can again lead to zero-velocity biasing.

The spatial resolution of the PIV measurements is determined by the size of the image captured and the size of the interrogation area. This determines the radius of the

smallest structures that can be measured. In other words it determines the resolution of the velocity structures that can be characterised. Many previous PIV studies have used image areas which could be considered to be too small to sample fully the spatial variability in the flow. For example, Campbell *et al.* (2005) only examined an area of 61×67 mm over a gravel bed, which was sufficient for investigating the role of individual topographic features on the flow, but is unlikely to have represented the degree of spatial variability in the time-averaged flow and the contributions made by form-induced stress to momentum transfer. Pokrajac *et al.* (2003) used an area of 65 x 65 mm, which only characterised the flow over one 2-D square bar, rather than a number of bars, so it was unclear whether their estimates of form-induced stress were representative of the rest of the flow. A larger area was therefore used here. The horizontal plane measurements used a measurement area of 198.4×200.0 mm, but a smaller area of 143.0×144.1 was used for the vertical plane measurements. A smaller image provides a smaller separation distance between measurements, so for the vertical plane measurements this enabled a greater number of measurements at different heights above the bed to be made for low flow depths. The measurement area is still more than double the area used by previous studies, and is shown in the next chapter to provide very similar estimates of the degree of spatial variability in the time-averaged flow to those produced by the horizontal plane measurements. A larger seeding of 200 μm was used, in comparison to a size of 5 to 90 μm which is usually used. This was in order to satisfy subpixel interpolation conditions, in which the seeding particles must be greater than 2 pixels in diameter for there to be sufficient data points for it to fit a 2-D curve to the correlation peaks.

The choice of the size of the interrogation area for cross-correlation is a compromise between a higher number of measurements within the flow field (higher spatial resolution) being offset by a lower degree of measurement confidence. The size of the interrogation area should be such that there is little variation in velocity values within an interrogation area, ensuring that the flow can be considered homogenous within this area. This is an assumption made in the cross-correlation technique and means that all seeding particles in the interrogation areas can be considered to have approximately the same displacement. Velocity gradients within an interrogation area can cause outliers and zero-velocity-bias. To minimise the problem of biasing, an area should be chosen so that particle displacements are equal to or less than a 1/4 of the length of the interrogation area.

Four different sized interrogation areas were available within the FlowManager software, 16×16, 32×32, 64×64 and 128×128 pixels. Preliminary tests for a range of experimental runs revealed that an area of 16×16 produced an unacceptable level of outliers (> 5 % of the total number of vectors) because of significant velocity gradients within the interrogation areas, whilst 64×64 and 128×128 oversampled the flow and averaged out much of the spatial variability in velocity between the interrogation areas. As such, an area of 32×32 pixels was chosen as a compromise between spatial resolution and measurement confidence. For the measurements in a horizontal plane this corresponded to an area of 6.30×6.30 mm, whilst for the vertical plane measurements, this was an area of 4.54×4.54 mm. Although the interrogation area is smaller for the vertical plane measurements, it was still found to be large enough to enable a sufficient seeding density in each interrogation area. For both these areas a time separation between the two light sheet pulses of 1000 μs was chosen to ensure that particle displacements were highly unlikely to be larger than a 1/4 of the length of this interrogation area.

The interrogation areas were overlapped in both the streamwise and lateral direction for the horizontal plane measurements, and in the streamwise and vertical direction for the vertical plane measurements, to increase the probability that particles near the edges of an interrogation area contributed to the velocity calculation. It increased the chance that all particle pairs were completely within one interrogation area, which reduced the risk of a loss-of-pairs. Overlapping produces more vectors, but this does not equate to an increase in spatial resolution. Instead, it can be considered as an oversampling of the flow field. An overlap of 50 % was used here, in order to have sufficient matching pairs without the significant increase in processing time involved in using an overlap of 75 %. For the horizontal plane measurements this provided 61 velocity measurements in each lateral direction and 62 measurements in each streamwise direction, and resulted in 3782 measurements within the image area. It resulted in a separation distance of 3.15 mm between each velocity vector measurement (in both the streamwise and lateral direction) within the horizontal plane measurements. The number of measurements at different heights above the bed for the vertical plane measurements was dependent on the area of the image occupied by the flow and therefore varied with flow depth. But for all measurements, 61 velocity measurements were always provided in the streamwise direction. The separation distance between measurements, in both the streamwise and vertical direction was 2.25 mm. The spatial resolution of the velocity measurements is

equal to length of the interrogation area. This gives a spatial resolution of 6.30 mm and 4.54 mm for the horizontal and vertical plane measurements. This allows the flow field to be measured at the grain-scale. This means that the PIV measurements were able to resolve large scale structural features rather than those with dimensions of the Taylor's microscale, which is generally the case in PIV (Dantec, 2000).

The interrogation area within the second image was offset relative to the first in the streamwise direction, by a pixel length which approximately corresponded to the average particle displacement. This was performed to cancel out the effect of in-plane motion which can contribute to the loss-of-pairs problem. It is also enabled the use of a smaller interrogation area to maximise the spatial resolution of the measurements. For example, in order to detect vortices which are transported streamwise by the bulk flow, without an offset a fairly large interrogation area would be required to measure the large displacements in the bulk flow, but it would not be possible to detect the small-scale spatial variations in the flow. However, the use of an offset based on the bulk velocity allows the use of a smaller interrogation area and the detection of small-scale variations.

3.3.5 Image Processing Routines: Validation

Since PIV is an instantaneous measurement technique all spatial information is sampled at the same time, and this leads to a finite statistical likelihood that there will be some regions within the flow where there is no meaningful output from the seeding particles. This, as has been explained, can be caused by a loss-of-pairs. Therefore it is necessary to subsequently validate the vector map. A moving-average validation was chosen to validate, reject and substitute vectors. In strongly 2-D flow this method has been found to be robust (Westerweel, 1994). The validation was based on a comparison between a given vector and the average of the vectors in a rectangular neighbourhood. This assumed continuity in the flow field behaviour, whereby there is a practical limit to the change in velocity from one vector to its neighbouring vectors. This assumption is reasonable given that the fluid accelerations are modest and that the flow field is oversampled using a 50 % overlap in interrogation areas.

The routine was set so that vectors that deviated by more than 10 % of the maximum deviation in a rectangular neighbourhood were rejected. This value of 10 % was set based on an examination of a significant number of vector maps from a range of

experimental runs so that it was set at least so high that all visible outliers were removed. The choice is not critical, since if it is set too high such that some vectors that are not outliers are rejected, the vector that substitutes them will be very close to the rejected vector. These rejected vectors were substituted by the average of the vectors within the neighbouring area. This area was set at 3×3 vectors, as suggested by Dantec (2000).

3.3.6 Measurement Accuracy and Resolution

Since the cross-correlation technique uses subpixel interpolation, it allows a measurement accuracy of better than 1/10 of a pixel (Dantec, 2000). For the horizontal plane measurements this gave a spatial accuracy of better than 0.0197 mm, and 0.0142 mm for the vertical plane measurements. The upper limit of the particle displacements that can be measured is largely determined by the size of the interrogation area, since cross-correlation constrains particle displacements to being equal to or less than a 1/4 of the length of the interrogation area. Therefore the upper limit d_{max} is given by $0.25L_{int}$, where L_{int} is the length of the interrogation area. The upper limit of the possible velocity range V_{max} that can be measured is then derived from d_{max}/t_s, where t_s is the time separation between the two light sheet pluses. The lower limit of the velocity range is given by $-V_{max}$. For the horizontal plane measurements the velocity range was –1.57 to 1.57 m/s and for the vertical plane measurements was –1.13 to 1.13 m/s, with no offset of the second interrogation area. This fully covered the range of velocities that were measured.

The spatial resolution at which the particle displacements are resolved is different from the spatial resolution of the velocity measurements within the flow field. This is related to the ability to resolve very small displacements between the first and second images. In optical terms it is related to the ability to distinguish between images of two different particles in the image plane which are distinct or separated in the object plane. Therefore in these terms the smallest resolvable displacement would be the dimensions of the seeding particle images on the PIV image map. However, because PIV is not a particle tracking technique but a correlation process, it has to be considered differently. Cross-correlation uses subpixel interpolation to calculate the displacement of the particles between the two images. This is carried out at a resolution of 1/64 of a pixel.

This results in velocities being resolved at an extremely high resolution of 0.00308 mm for the horizontal plane measurements and at 0.00222 mm for the vertical plane measurements. Given the time separation between the two correlated images this gave a velocity resolution of 0.00308 m/s and 0.00222 m/s, respectively.

3.4 Bed Surface Topography Measurement

The bed surface topography was measured from an orthogonal grid of bed surface elevation measurements. The elevation of each point was measured using a Keyence LC-2450 laser displacement sensor. This was moved over the bed surface in a pre-determined grid of measurement points by an automated positioning system located on the flume rails. The laser displacement sensor could measure to a resolution of 0.5 μm in the vertical, with each measurement being integrated over an area of 20×45 μm.

Bed surface topography was measured over an 250×250 mm area of the bed at a spacing of 1 mm in both the streamwise and lateral directions. The measurement area was centred on the flume centreline. This was positioned to measure the bed surface topography over which the PIV measurements were taken, so that the measurement positions of the velocity vectors and the bed surface elevations exactly corresponded. The location of the PIV image area within the topography scan was found by positioning a thin board over the bed surface and positioning four L-shaped targets on the board to the four corners of the image (within ± 2 pixels, ± 393 μm) and carrying out a topographic scan. An area of 250×250 mm was chosen, rather than an area of 198.4×200 mm, which was the size of the horizontal plane used for PIV measurements, so that when examining the correlation between the flow and the bed surface topography a range of streamwise lags could be applied to take into account the downstream propagation of the flow relative to the bed. The resolution of the sensor and the measurement grid was believed to be capable of describing the features of the bed surface arrangement at a grain scale, and therefore when combined with the PIV measurements, this represents a high spatial resolution study of the interaction between the bed and the flow.

The bed elevation measurements produced a matrix of 250×250 points. The vertical elevations were measured relative to an arbitrary datum position that was dependent on the original vertical position of the laser displacement sensor. The sensor had a valid

vertical measurement range of ±8 mm relative to this datum. Given the range of the grain size distribution of the sediment mixtures used to produce the beds (see Figure 3.5), the vast majority of the elevation measurements were within this range. However, due to occasional large variations in bed elevation and the slope of the bed, a small number of out of range values were recorded. The worst data set contained 0.1 % out of range readings, while it was typically 0.08 %. None of these readings were elevations that were too large, but rather being too low, meaning that the estimations of maximum bed elevation were not affected. Each out of scale reading was replaced by the average elevation of the adjacent points of the grid of data. The same procedure was applied for any missing data points. Given the low percentage of outliers and missing data points, these corrections can be assumed not to have significantly altered the results drawn from the topography measurements.

Since the sensor was located on the positioning system on the flume rails, the sensor was not parallel to the bed surface. The data was therefore de-trended in both the lateral and streamwise directions using a simple linear interpolation to remove any spatial bias arising from this non-parallelism. The mean elevation was found and set to zero so that all elevations were given relative to the zero mean elevation of the bed surface.

3.5 Bed production

3.5.1 Sediment Mixtures

Two different sediment mixtures were used to produce two different sediment deposits within the flume. They were chosen to characterise the two types of grain-size distributions observed in gravel-bed rivers: a log-normal, unimodal grain-size distribution and a slightly bimodal grain-size distribution (Figure 3.5). The former consisted of 100 % gravel quarried from alluvial deposits, which was not crushed and had the rounded properties of grains found in gravel-bed rivers. The bimodal mixture contained 75 % of the same gravel and 25 % sand obtained from the same deposits. Table 3.1 provides a summary of the parameters of the mixtures. The two mixtures were designed to produce similar values of D_{50}, the grain size at which 50 per cent of the bed material is finer.

(a)

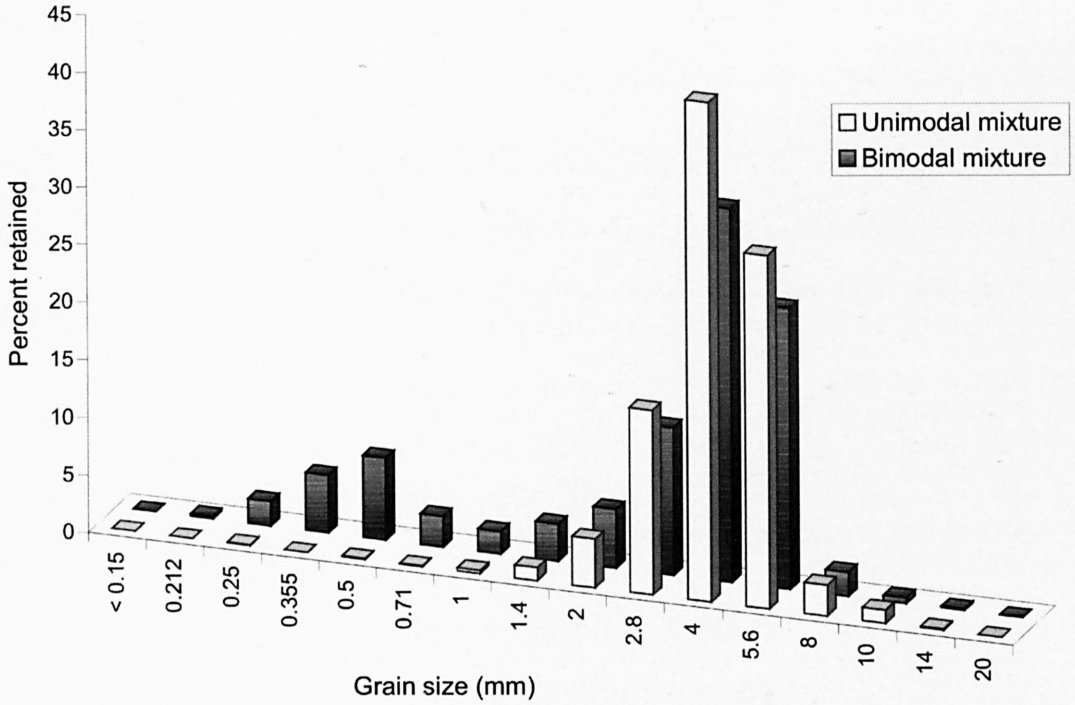

(b)

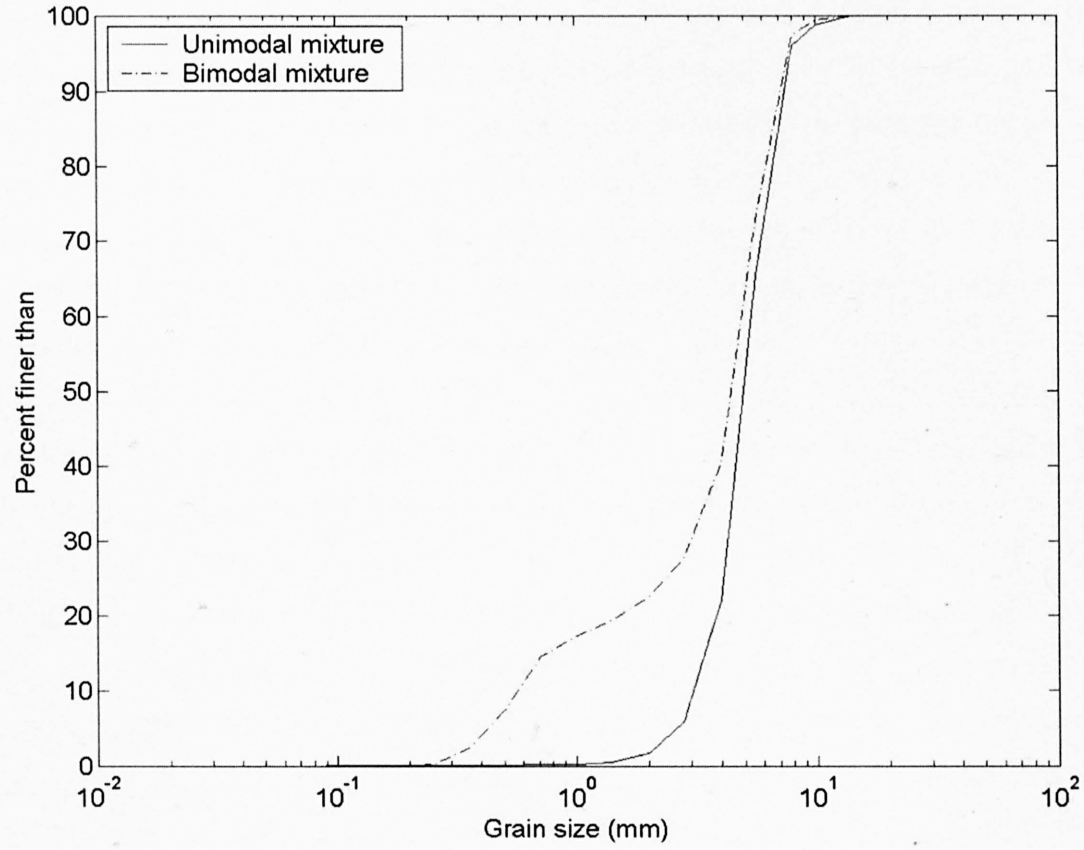

Figure 3.5. Grain-size distributions of the two mixtures used to form the two beds.

Table 3.1. A summary of the parameters of the two mixtures used to form the two beds, where D_{50} is the grain size at which 50 per cent of the bed material is finer, D_{84} is the grain size at which 84 per cent of the bed material is finer, $D_{\bar{x}}$ is the mean grain-size, σ_D is the sorting coefficient, Sk_D is the skewness of the grain-size distribution and K_D is the kurtosis of the grain-size distribution.

Bed Mixture	D_{50} (mm)	D_{84} (mm)	$D_{\bar{x}}$ (mm)	σ_D (mm)	Sk_D (mm)	K_D (mm)
Unimodal	4.97	7.00	4.95	1.40	1.96	1.09
Bimodal	4.42	6.59	3.80	1.90	1.23	1.17

3.5.2 Methods of Bed Production

The difficulty in the laboratory is creating a water-worked gravel bed that is able to represent faithfully the conditions found in gravel-bed rivers. Representative natural water-worked surfaces were thought to be important in order to produce flow fields that exhibit degrees of spatial variability and spatial patterns that can be considered as representative of those found in gravel-bed rivers. Commonly in laboratory studies, a simulated river bed has been produced by placing a given depth of randomly mixed sediment on to the base of the flume which is then scraped level (screeded). Flow and sediment transport measurements are then made either over this bed or after the bed has been water-worked for a period of time.

However, these beds are in essence a mixture of randomly sorted grains. Visually this method appears to result in the sediment deposit having a lower degree of particle imbrication and higher porosity than observed in natural gravel-bed rivers. This is a further simplification of a river system, in addition to those already imposed by the use of a laboratory flume. The flow fields over such beds may not be fair representations of natural conditions. Recently, Barison *et al.* (2003) discovered that the near-bed spatial distribution of time-averaged streamwise velocity over gravel beds in the near-bed region was significantly different over screeded beds than that over a water-worked bed. Initially over the screeded bed, the distributions were highly positively skewed, with a low proportion of smaller velocities. As the bed surface became more water-worked the

flow velocity distributions became flatter, wider and less skewed. This indicated that the way in which the beds are formed in the laboratory might have an important effect on the flow field.

Buffin-Bélanger *et al.* (2003) have recently developed a casting procedure which accurately reproduces gravel-bed surfaces. Moulds are taken of a gravel-bed in the field from which casts are produced and placed in the flume. It is clear that this will create a surface with the complexity of a natural gravel-bed, but it is impermeable and does not replicate vertical sorting. In addition, in narrow laboratory flumes, the size of the 'grains' on the cast are not well scaled with the width of the flume and prototype channel, possibly causing individual clasts to dominate the flow pattern within the flume width and to cause isolated roughness effects and interaction of the flow with the flume walls. This can promote the generation of secondary currents within the flow that can influence velocity measurements and the assumption of steady, 2-D uniform flow for subsequent calculations not to hold. Clearly it would be advisable to use a different method from those used in previous studies to improve the simulation of natural gravel-bed flows.

3.5.3 Sediment Feeding as a Method of Bed Production

The method chosen was based on the concept developed to form beds in laboratory flumes in order to study downstream fining (Paola *et al.*, 1992; Seal *et al.*, 1997; Toro-Escobar *et al.*, 2000), whereby sediment is fed into a running flume to form a sediment deposit. There are no studies that have measured velocities over such beds. For the work here, a conveyor belt was used to inject gravel into the flow (Figure 3.6) at twice its transport capacity in order to form a deposit. The transport capacity was estimated from the Meyer-Peter and Müller (1948) equation for bedload transport discharge q_s

$$q_s = \left[\left(\frac{4\tau_0}{\rho((\rho_s/\rho)-1)}\right) - 0.188\right]^{3/2} \left[(\rho_s/\rho - 1)gD_{50}{}^3\right]^{1/2} \tag{3.1}$$

where τ_0 is the mean bed shear stress, ρ is the fluid density, ρ_s is the sediment density and g is the gravitational acceleration. From this value, combined with a sediment feed rate, an estimate could also be made of the time taken for the bed of a known volume to

form. A channel slope of 0.0055 and a constant discharge of 0.0295 m^3/s were selected for the formation of both beds so that the time-scale was long enough to allow a progressive formation of the bed, but short enough for the bed to form within a reasonable time. The downstream adjustable weir was laid flat to the flume floor to allow the flow depth to adjust naturally to the changing bed conditions. The conveyor belt was mounted so that the sediment fell from the belt at approximately 200 mm above the fixed bed (Figure 3.6), with its downstream edge being 0.5 m upstream of the edge of the static bed (see Figure 3.1). This resulted in the sediment descending, saltating and rolling over the static bed before falling onto the steel flume floor. There was a concern that a deposit may not form over this floor due a low degree of roughness imposed on the grains by the steel floor, and consideration was given to whether it would be useful to add a layer of course grains on the plates in increase bed roughness (to act as a kind of bedrock or static roughened layer). However, it was felt that this would be hard to replicate for each bed formation, causing differences in boundary conditions for both bed formations. Nonetheless it was found that no grains were completely transported out of the flume upon entry to the steel floor, and indeed came to rest very quickly upon impact with the floor.

The conveyor belt did not produce a continuous feed but gave an injection period of 17 minutes before the belt was wound back (which took 12 minutes) and started again. The injection rate was calculated from the speed of the conveyor belt, the dimensions of the sediment sheet on the belt and its mean density (of sediment and void space). The sheet was scraped level using a plastic scraper to give the desired sheet thickness, and the width of the sheet was fixed at 0.45 m.

The bed and water levels were recorded at 0.5 m intervals along the working length of the flume at 30 minute intervals during the formation of the deposits. This allowed the changes in the bed slope to be monitored. Side view photographs were taken at distances of 5.12 m, 6.0 m and 7.0 m along the length of the flume to observe the vertical formation of the deposit. Each bed formation was split approximately evenly over three days, to allow more detailed measurements to be made of the deposit at the end of each day. This included taking bed surface topography measurements of an area of 250×250 over the PIV measurement section, and taking plan view photographs along the centreline of the flume at 0.5 m intervals along the whole length of the

deposit. Side view photographs were also taken at six positions along the flume, 4.87 m, 5.12 m, 5.5 m, 6.0 m, 6.5 m and 7.0 m.

Feeding was halted when the bed slope remained steady over a period of three hours. This was defined as occurring when the bed slope of the deposit was within 5 % of the bed slope measured for the previous measurement period. Since the bed slope was measured every 30 minutes this meant ensuring that this condition was met for six measurements of bed slope. A steady value of bed slope was taken to indicate conditions of equilibrium, where feed rate was equal to bedload transport rate. This state occurred after 10.5 hours for the unimodal mixture and 9 hours for the bimodal mixture, owing to the higher bedload transport rate and therefore higher feed rate.

Figure 3.6. The conveyor belt loaded with sediment that was used to form each of the two water-worked gravel-beds. A fixed bed section is shown underneath on which the sediment fell and saltated over until falling into the steel floor section of the flume.

Both beds formed through the downstream propagation of a distinct and well-formed gravel front, which was approximately semi-circular in shape (Figure 3.7). Downstream of the front very few grains were visible for the unimodal mixture, whereas discrete patches of sand (typically of the order of 0.15 m in width and 0.3 m in length) were present in the case of the bimodal mixture. For the unimodal bed, it took 90 minutes before the front began to migrate downstream at a relatively constant rate. This rate had a mean of 3.13×10^{-4} m/s and a standard deviation of just 7.68×10^{-5} m/s. The constant rate occurred just after an hour for the bimodal bed, and attained a mean rate of 5.00×10^{-4} m/s, and a similar standard deviation of 8.30×10^{-5} m/s. This higher rate and shorter time reflects the higher feed rate for the bimodal bed. The standard deviation values suggest that feeding conditions and bed formation processes were similar throughout feeding for a given bed. In the case of both mixtures, the grains were observed to be transported and deposited in the manner of conventional bedload transport, resulting in the grains finding the most sheltered local position, and creating a configuration of imbricated grains. Figure 3.8 shows a photograph of the surface of the deposit after three hours of feeding and clearly displays particle clusters on the bed surface and preferential orientation of the grains in the direction of the flow. This surface was then later covered after further feeding. It means that the layers within the deposit were all water-worked. The deposit would increase in depth through this process of feeding, transport and deposition, meaning that throughout the depth of the deposit the grains would be imbricated and represent all grain sizes present in the feed material. This created vertically sorted deposits through natural processes of transport and deposition. This is not possible with any other method of bed production that has been used before. The resulting deposits adopted a bed slope of 0.00225 and 0.00224 (relative to a channel slope of zero), which are remarkably similar, reflecting the repeatability of the bed production approach.

3.6 Bed Surface Properties

3.6.1 Digital Elevation Models

A screeded bed was also created in the flume using the same unimodal mixture so that the bed surface properties of the water worked beds could be compared to that of a screeded bed. The bed surface topography was measured over an area of 200×200 mm over this bed. The surface texture of the two fed beds and the screeded bed can be

visualised by representing the bed elevations from the zero mean surface elevation on a bi-dimensional plane and associating the elevations with a colour of the grayscale so that higher points appear lighter and lower points appear darker (Figure 3.9). This produces a Digital Elevation Model (DEM) of the bed surface. It shows that the surface topography of the screeded bed is irregular with random grain-scale protrusions around the mean bed elevation. It has a fairly flat uniform surface and the pore space between individual grains is clearly visible, providing an impression of a loose surface.

Figure 3.7. The downstream front of the sediment deposit formed through feeding of the unimodal mixture after 3 hours. The front is located at a distance of 10.1 m along the flume. It shows a well-formed front, semi-circular in form, with very few particles downstream. The downstream movement of this front was the manner in which the deposit propagated downstream. The imbrication of the particles is visible by the small pore spaces between the particles. It also shows that a flat (at the macroscopic scale) deposit is always present throughout the feeding.

Figure 3.8. The surface of the sediment deposit formed through feeding of the unimodal mixture after 3 hours. Even after a short period of feeding the surface exhibits properties of a water-worked bed with a high level of particle imbrication, preferential alignment of the particles in the direction of the flow (diagonally from right to left) and the presence of particle clusters. This was later covered through further feeding, demonstrating that the whole depth of the deposit has an imbricated form. A pen is added for scale.

In contrast, the unimodal fed bed is well imbricated, with pore space being minimal and is therefore well-packed. It also has a more organised pattern (Figure 3.9b). There is a zone of higher elevations towards the top right of the plot, followed by a larger zone of lower elevations which is diagonally orientated, and then a small area of lower elevations located in the bottom right of the plot where a depressed diagonal zone is evident from the bottom left to the mid-right of the image. This suggests the presence of a longitudinal trough within the image, flanked by two ridges to the top and bottom which are often a feature of water-worked gravel beds (Nezu and Nakagawa, 1993; Tait, 1993; McLelland *et al.*, 1999; Schvidchenko and Pender, 2001). This is in accordance to

what could be seen along the whole deposit. Apart from these features the bed was relatively flat (at the macroscopic scale) and had a uniform bed slope along the whole length of the deposit, and displayed no larger-scale structuring. However, there was evidence of an abundance of particle clusters along the whole length of the deposit, which are commonly associated with water-worked gravel beds.

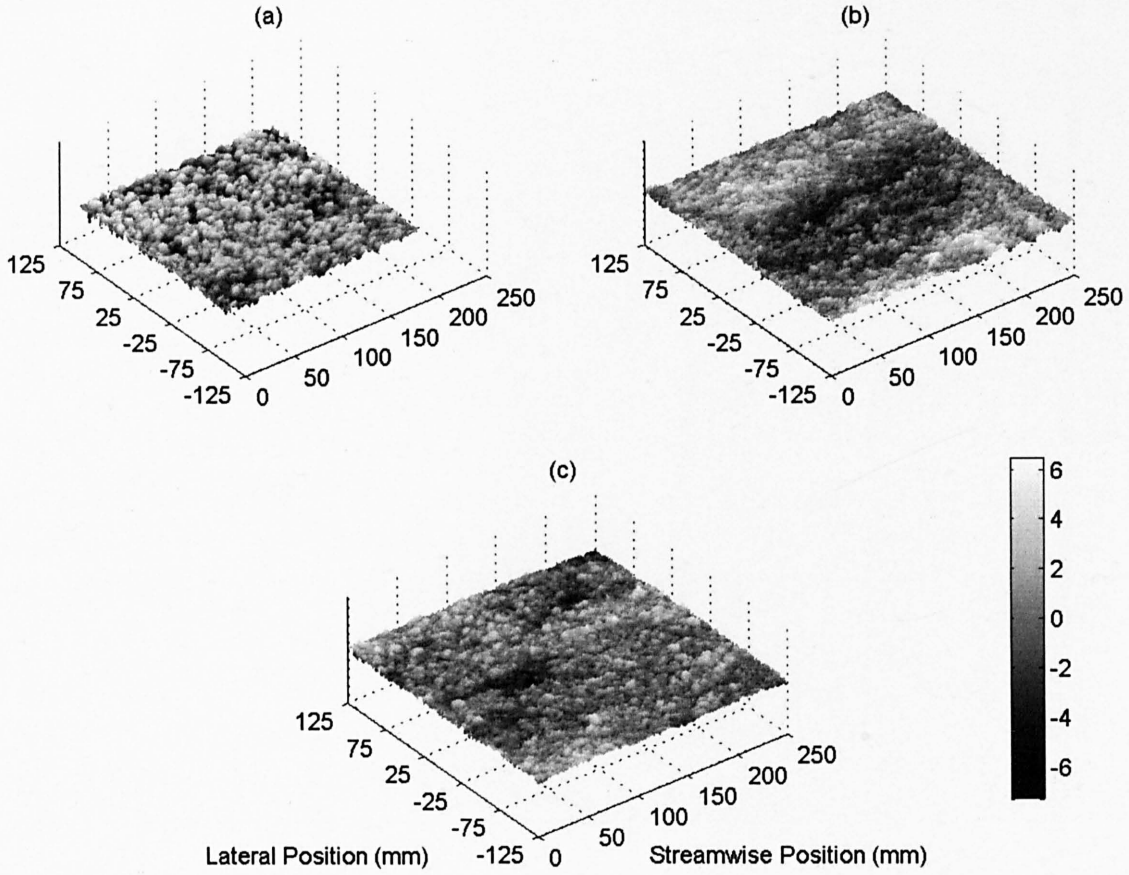

Figure 3.9. Digital Elevation Models of the bed surface topography of (a) the screeded bed; (b) the unimodal bed; and (c) the bimodal bed produced by a laser bed scanner. The grayscale relates to the departure in elevation from the zero mean surface elevation (mm). A lateral position of 0 mm denotes the centreline of the flume and the increasing values in the streamwise position are in the direction of the flow.

The bimodal bed is equally well packed and imbricated, but, unlike the unimodal bed, there is no clear structuring of the bed. There are only local depressions and local areas of higher elevation, which do not appear to be part of any organised pattern. However,

this bed also displayed an abundance of particle clusters (Figure 3.10) on a flat (at the macroscopic scale) surface (Figure 3.11). The important feature is that the surface textures of both fed beds are distinctly different from the screeded bed, but feeding still produces relatively flat (at the macroscopic scale) deposits that are suitable for achieving uniform flow within the flume.

Figure 3.10. An example of the presence of sand within the interstices of the gravel framework and examples of particle clusters on the surface of the bimodal bed. A pen is added for scale. Flow is from left to right.

3.6.2 Probability Density Function of the Bed Surface Elevations

The probability density functions (*pdf*'s) of the bed elevations from the zero mean surface elevation z_b reveal differences between each of the three beds (Figure 3.12). The screeded bed has a slightly negatively skewed distribution of z_b, but the distributions for the two fed beds are very slightly positively skewed (Table 3.2).

Positive skewness is said to indicate an armouring effect on the bed (Nikora *et al.*, 1998; Smart *et al.*, 2004) where, in general, the surface of an armoured bed is composed of larger stones with finer particles filling in the interstices between, thus reducing the magnitude of surface elevations below the mean bed level. The positive skewness is slightly higher for the unimodal bed, reflecting the rougher surface seen in the DEM (Figure 3.9b). The increased range of bed elevations can be quantified by the standard deviation in bed surface elevations σ_{z_b} (Table 3.2) which can be interpreted as a characteristic vertical roughness length of gravel beds (Nikora *et al.*, 1998; Aberle and Smart, 2003). It shows that roughness length is less over the two fed beds, more so over the bimodal bed, reflecting the differences in the DEMs of the three beds. All three of the distributions have kurtosis values close to three, suggesting that they approximately follow a normal distribution.

Figure 3.11. Looking downstream over the bimodal bed demonstrating its flat structure at the macroscopic scale but its surface roughness at the grain-scale.

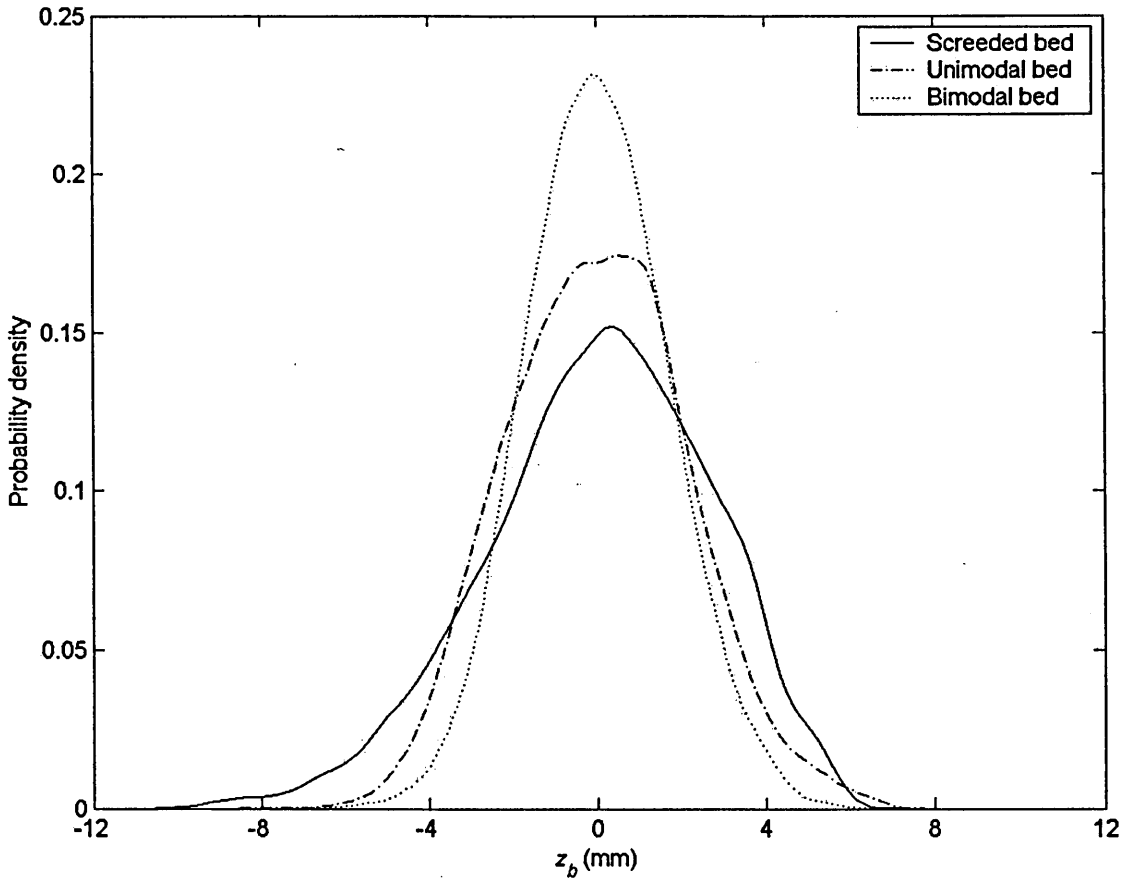

Figure 3.12. The probability density function of the bed elevations from the zero mean surface elevation z_b for (a) the screeded bed; (b) the unimodal bed; and (c) the bimodal bed produced by a laser bed scanner.

To confirm this more formally a linear regression can be made between the theoretical probability associated with the ordered observation z_{b_i} from a standard normal distribution and the observed probability for z_{b_i}. This theoretical probability is given by

$$pr(Z \leq z_i) = \frac{i - 3/8}{N + 1/4} \tag{3.2}$$

where $Z \sim N(0,1)$ and z_i is an observation taken from Z. An estimate of the percentage variability in z_b explained by a perfect normal distribution is given by R^2. A distribution should only be considered to approximately follow a normal distribution when R^2 is very high, say above 0.99. The R^2 values in Table 3.2 show that the distributions for the two fed beds can be considered to follow approximately a normal

distribution, but the screeded bed display some departure. Smart *et al.* (2004) concluded that skewed distributions of gravel bed surfaces might be well fitted by a lognormal frequency distribution. However, a similar analysis showed that the hypothesis of a lognormal distribution must be also rejected for the screeded bed. Hence, although the *pdf* is bell shaped and may be considered as near-Gaussian, the negative skewness is the main reason for the rejection of the hypothesis of a normal or lognormal distribution for the screeded bed.

Table 3.2. A summary of the bed surface properties of the three beds, where σ_{z_b} is the standard deviation in bed surface elevations z_b, Sk_b and K_b are the skewness and kurtosis of the distributions of z_b, respectively, R^2 is from the regression between the probability density function of z_b and the probability density function of a model normal distribution, l_{x_0} and l_{y_0} are the correlation lengths of z_b in the streamwise and lateral directions, respectively, and H_x and H_y are the Hurst exponents for the streamwise and lateral variation in z_b, respectively.

Property	Screeded	Unimodal	Bimodal
σ_{z_b} (m)	0.00266	0.00214	0.00170
Sk_b	-0.397	0.0985	0.0462
K_b	2.99	2.837	3.015
R^2	0.980	0.993	0.999
l_{x_0} (m)	0.00576	0.0135	0.00764
l_{y_0} (m)	0.00523	0.0149	0.00778
H_x (m)	0.472	0.452	0.463
H_y (m)	0.371	0.320	0.368

3.6.3 Second-order Structure Functions of the Bed Surface Elevations

Although the *pdf*'s show some evidence of differences in the bed surface between the three beds, they fail to clearly describe the degree of particle organisation on the bed

surface. This can be assessed by using a 2-D second-order structure function of the bed surface elevations, as used by Goring *et al.* (1999). The structure function $D_b(l_x,l_y)$ of bed surface elevation $z_b(x,y)$ is defined as

$$D_b(l_x l_y) = \frac{1}{(N_b - n_b)(M_b - m_b)} \sum_{i=1}^{N_b - n_b} \sum_{j=2}^{M_b - m_b} \{z_b(x_i + n_b\delta x, y_j + m_b\delta y) - z(x_i, y_j)\}^2 \qquad (3.3)$$

where $l_x = n_b\delta x$, and $l_y = m_b\delta y$ are spatial lags, n_b and m_b are multiplying coefficients, δx and δy are the sampling intervals, and N_b and M_b are the total number of measured bed elevations, in the streamwise x and lateral y directions, respectively. Values of $\delta x = \delta y = 1$ mm and $N_b = M_b = 250$ applied here. The second-order structure function of a globally homogeneous random field has the following relationship with the correlation function $R_b(l_x,l_y)$

$$D_b(l_x l_y) = 2\left[\sigma_{z_b}^2 - R_b(l_x,l_y)\right] \qquad (3.4)$$

Thus, at large lags l_x and l_y when $R_b(l_x,l_y) \to 0$ and $D_b \to 2\sigma_{z_b}^2$ the data are spatially uncorrelated and the lags l_x and l_y at which $D_b \to 2\sigma_{z_b}^2$ can be used to derive characteristic streamwise and lateral length scales (Nikora *et al.*, 1998).

Figure 3.13 shows the second-order structure functions for the three beds. It is reasonable to compare the three beds directly given the similarity in the D_{50} of the beds (Table 3.2). This is plotted in terms of $D_b(l_x,l_y)/2\sigma_{z_b}^2$. Figure 3.13a shows the variation in $D_b(l_x,l_y=0)/2\sigma_{z_b}^2$ with l_x and Figure 3.13b shows the variation in $D_b(l_x=0,l_y)/2\sigma_{z_b}^2$ with l_y. Low values of $D_b(l_x,l_y)/2\sigma_{z_b}^2$ indicate high levels of correlation with l_x and l_y such that at a value of zero a perfect correlation exists. As $D_b(l_x,l_y)/2\sigma_{z_b}^2$ increases to unity, the degree of correlation decreases. At unity, the bed elevations have no correlation and the bed surface topography can be sensibly considered random in organisation. Values of $D_b(l_x,l_y)$ larger than unity are associated with negative correlation.

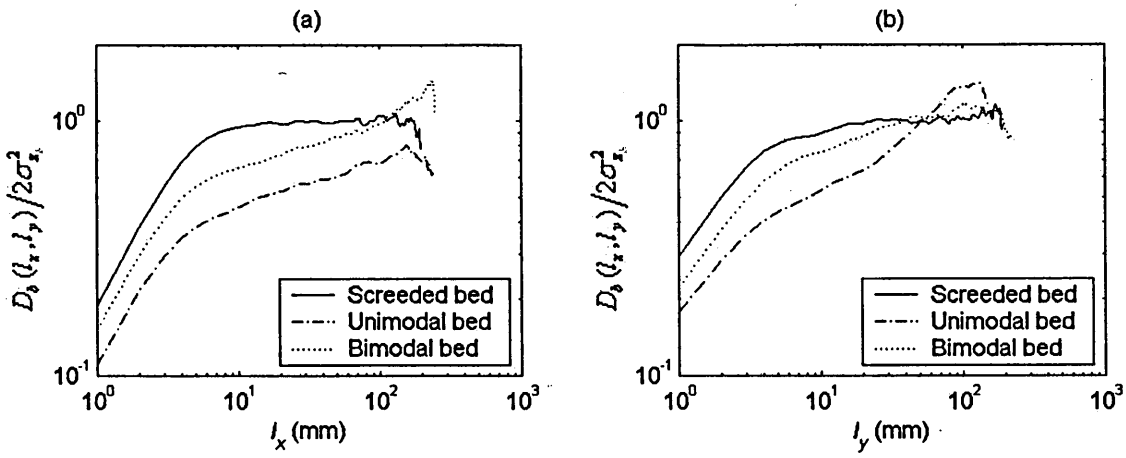

Figure 3.13. Second-order structure functions D_b of the bed surface elevations normalised by $2\sigma_{z_b}^2$ for (a) $l_y = 0$ and (b) $l_x = 0$, where σ_{z_b} is the standard deviation in bed surface elevations, and l_x and l_y are spatial lags in the streamwise and lateral direction, respectively. The horizontal dashed line indicates where the normalised function equals unity.

It is believed that all second-order structure functions for water-worked beds can be subdivided into scaling, transition, and saturation regions (Nikora *et al.*, 1998; Nikora and Walsh, 2004). Given that the second-order structure functions in Figure 3.13 follow the pattern that has been observed in various investigations (Robert, 1988; 1991; Nikora *et al.*, 1998; Butler *et al.*, 2001; Nikora and Walsh, 2004; Aberle and Nikora, submitted), such a subdivision can be applied. The region at small spatial lags, where the structure functions can be approximated by the power function $D_b(l_x, l_y = 0)/2\sigma_{z_b}^2 \propto l^{2H_x}$ and $D_b(l_x = 0, l_y)/2\sigma_{z_b}^2 \propto l^{2H_y}$ (Nikora *et al.*, 1998), corresponds to the scaling region, while at large lags the structure functions approach the saturation region where $D_b(l_x, l_y)/2\sigma_{z_b}^2 = 1$. The scaling exponent H is known as the Hurst exponent. Only one of these functions does not reach this region. Between these two regions, the structure functions are curved in the so-called transition zone (Nikora *et al.*, 1998; Nikora and Walsh, 2004). Figure 3.13 shows that for $D_b(l_x, l_y = 0)/2\sigma_{z_b}^2$ and $D_b(l_x = 0, l_y)/2\sigma_{z_b}^2$ the extent of the scaling region is up to $l_x \approx 3-4$ mm which is very similar for each of the three beds and in both the streamwise and lateral direction, suggesting that the surface structure is similar at small lags. But the transition zones are much longer over the two fed beds. This may indicate

that over these two beds there are bed features that are larger than the grain scale, given that the scaling region only exists up to $l_x \approx 3-4$ mm. However, the very short transition zone for the screeded bed may indicate that this bed is unlikely to have this scale of bed structure.

A comparison of $D_b(l_x, l_y = 0)/2\sigma_{z_b}^2$ and $D_b(l_x = 0, l_y)/2\sigma_{z_b}^2$ shows that for a given bed the shapes of the curves are similar, although the curves are separated by a small vertical offset $(D_b(l_x = 0, l_y)/2\sigma_{z_b}^2 > D_b(l_x, l_y = 0)/2\sigma_{z_b}^2)$. The vertical offset is consistent with the difference in two-dimensional second-order structure functions in these two directions (Aberle and Nikora, submitted). This is due to a lower degree of coherency in bed elevations in the lateral direction. The parallel nature of the two curves, and the similarity in the extent of the scaling region, indicates an isotropic scaling at small spatial lags, which has also been observed by others (Nikora *et al.*, 1998; Butler *et al.*, 2001; Nikora and Walsh, 2004; Aberle and Nikora, submitted).

The difference in spatial lags at which $D_b(l_x, l_y)/2\sigma_{z_b}^2 \to 0$, the lower limit of the saturation region, reflects the difference in the correlation lengths of the bed elevations. Figure 3.14 shows the manner in which the streamwise correlation length l_{x_0}, and in a similar way, the lateral correlation length l_{y_0} can be estimated from the curves in Figure 3.13. These values are given in Table 3.2 and show that there is a considerable difference between the screeded and fed beds. The fed beds have longer correlation lengths in both the streamwise and lateral direction. The lengths are higher over the unimodal bed than the bimodal bed, which reflects the greater structure in the bed elevations, as shown by the DEMs (Figure 3.9). The third scale, the vertical correlation length scale is given by σ_{z_b} (Nikora *et al.*, 1998).

The scaling (or Hurst) exponents H_x and H_y can estimated from the condition that $D_b(l_x, l_y = 0)/2\sigma_{z_b}^2 \propto l^{2H_x}$ and $D_b(l_x = 0, l_y)/2\sigma_{z_b}^2 \propto l^{2H_y}$ within the scaling region (Figure 3.14). These estimates are shown in Table 3.2 and show that they are higher over the screeded bed than the fed beds, and that the lowest values are found over the unimodal bed. The scaling exponents can be interpreted as a measure of the complexity in the topography, in which larger values of H_x and H_y indicate a less complex

topography (Bergeron, 1996). The exponents once again reveal that the screeded bed has a less complex topography then the fed beds, and that the unimodal bed has a more complex structure than the bimodal bed. The H_x values range from 0.45 to 0.47, which is smaller than has been reported before (Nikora *et al.*, 1998; Butler *et al.*, 2001; Nikora and Walsh, 2004; Aberle and Nikora, submitted) owing to the smaller grain sizes on the bed surface (Robert, 1988; Bergeron, 1996; Aberle and Nikora, submitted).

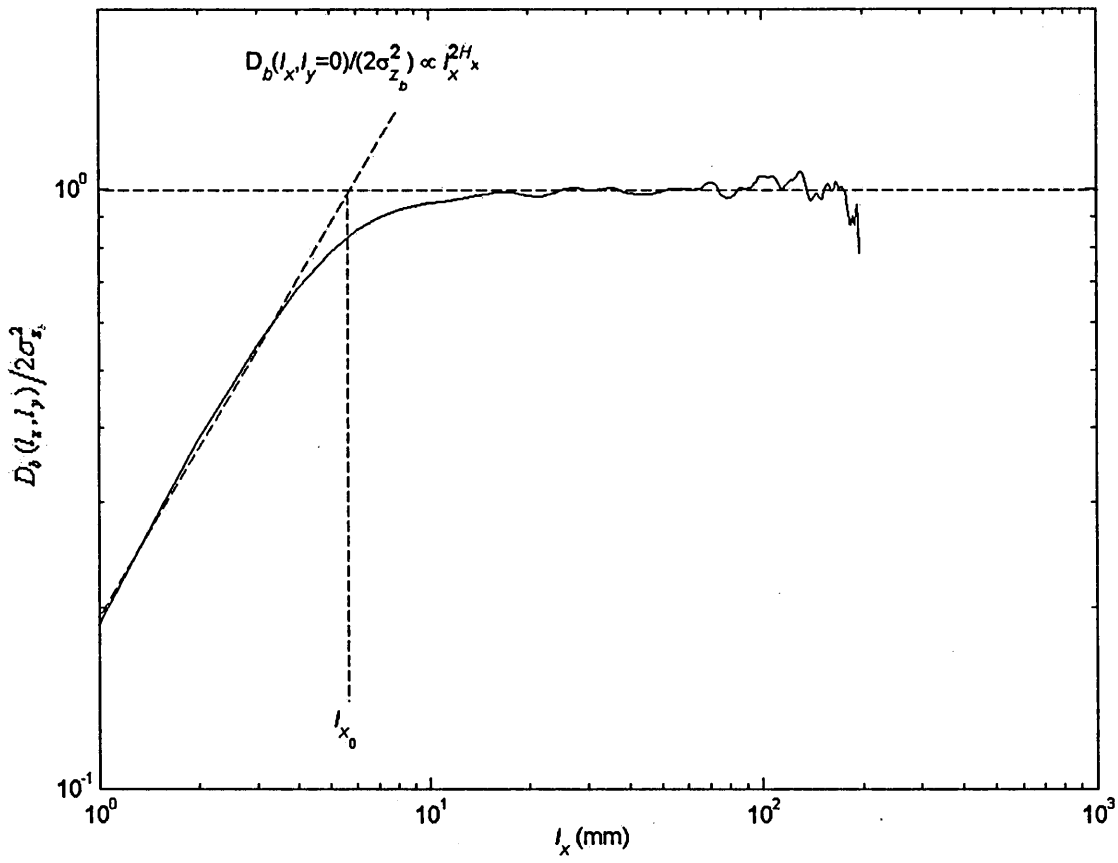

Figure 3.14. The procedure for determination of the streamwise correlation length of the bed surface elevations l_{x_0} and the Hurst exponent for the streamwise variation in bed surface elevations H_x. A similar procedure is applied to determine these parameters in the lateral direction.

Contour plots of $D_b(l_x,l_y)/2\sigma_{z_b}^2$ are useful for identifying isotropy/anisotropy within the random field (Butler *et al.*, 2001; Nikora and Walsh, 2004). These are shown in Figure 3.15. Observations suggest that particles on the surfaces of water-worked beds prefer to rest on the bed with their *a*-axis parallel to the flow direction, their *b*-axis

perpendicular to the flow direction, and with their *c*-axis orthogonal to the flow direction (Komar and Li, 1986; Robert, 1991). Such a prevailing arrangement of the particles on the bed surfaces should reveal itself in the contour plots. The contour lines for the 2-D structure function for the screeded bed are largely circular, suggesting that the particles are not oriented in any prevalent direction. This indicates an isotropy in this surface structure. However, the contour lines for the 2-D structure function for the two fed beds are characterised by an elliptical shape, reflecting an anisotropic surface structure. The major axes of the elliptical contours are aligned in the direction of the flow (aligned with increasing l_x) indicating that the majority of particles tend to rest on the bed with their *a*-axis along the flow. The minor axis of the contour lines is aligned with the prevailing orientation of the *b*-axis of the particles, which is perpendicular to the flow. This suggests that the two fed beds exhibit evidence of armouring of the bed surface. The elliptical form is more prominent over the unimodal bed, demonstrating that this bed exhibits stronger degrees of armouring. The large areas of separately formed elliptical patterns, such as at $l_x = 0, l_y = -40$ for the unimodal bed and $l_x = 0, l_y = 40$ over the bimodal bed are larger than the maximum grain size in the bed mixture and could represent either clusters of small particles or depressions between large particles (Nikora and Walsh, 2004).

If $D_b(l_x,l_y)/2\sigma_{z_b}^2$ is plotted as a surface, the variation in the structure functions with different spatial lags can be further visualised and new interpretations can be drawn (Marion *et al.*, 2003) (Figure 3.16). In these plots, an isoline of $D_b(l_x,l_y)/2\sigma_{z_b}^2$ indicates that the bed topography has a uniform level of bed elevation correlation in the direction $\tan^{-1}(l_x,l_y)$ to the streamwise direction of flow. This property may be used to identify the dominant correlation direction of the bed surface structures.

The screeded bed appears to have no correlation in either direction and is random in organisation (Figure 3.16a). In contrast, the unimodal bed has a strong streamwise coherence, particularly at the smaller lateral lags (Figure 3.16b). This indicates the presence of longitudinal grain-scale structures (Marion *et al.*, 2003), as seen in the DEM of the bed (Figure 3.9a). These structures do not appear to have a single dominant lag in the lateral direction. The lateral correlation becomes negligible at small lateral lags, indicating that the longitudinal structures are relatively narrow in their lateral extent.

This plot is very similar to those presented by Marion *et al.* (2003) for beds undergoing mobile armouring through upstream sediment input, which is the conditions that were present in the production of the unimodal bed. The plot for the bimodal bed also has coherence in the streamwise direction, which increases at the smaller lateral lags (Figure 3.16c). From this, it is difficult to infer whether any structures are present, but it does confirm that the surface is not totally random in organisation.

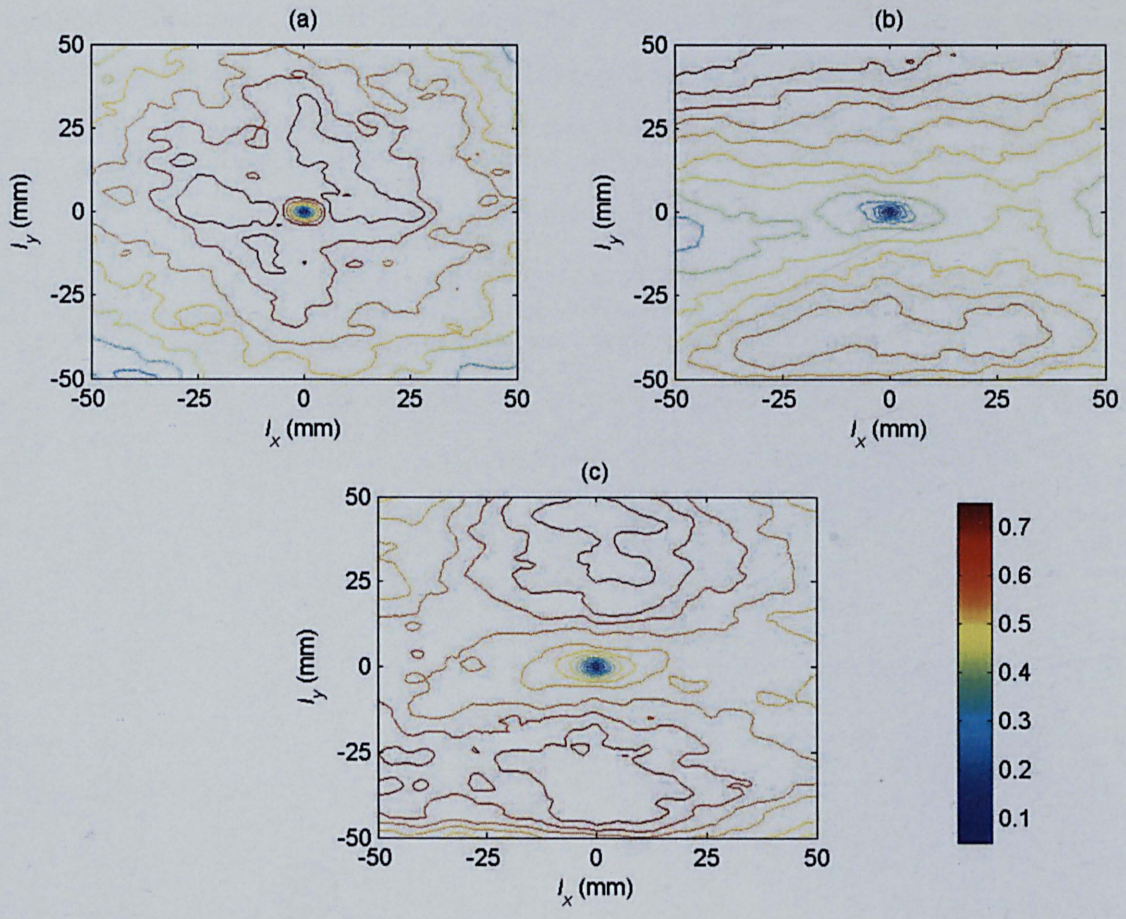

Figure 3.15. Contour plots of the second-order structure functions D_b of the bed surface elevations normalised by $2\sigma_{z_b}^2$ for (a) the screeded bed; (b) the unimodal bed; and (c) the bimodal bed, where σ_{z_b} is the standard deviation in bed surface elevations, and l_x and l_y are spatial lags in the streamwise and lateral direction, respectively.

The bed surface topography measurements have revealed that fed beds exhibit a greater degree of imbrication, and are more organised than screeded beds, particularly in the streamwise direction. There is evidence that they exhibit varying degrees of mobile armouring and particle organisation, and have greater surface complexity than screeded beds. Since the fed beds were also sorted vertically, because they were formed through transport and deposition, it can be suggested that the fed beds formed here represent more faithfully the bed conditions found in gravel-bed rivers, than the screeded beds. The bimodal fed bed had a surface that was less organised and complex than the unimodal bed, and much flatter in both appearance in the DEM and in its structure function surface plot. This is likely to be due to the infilling of the interstices between the gravel particles by the sand (Figure 3.10) producing a smoother surface.

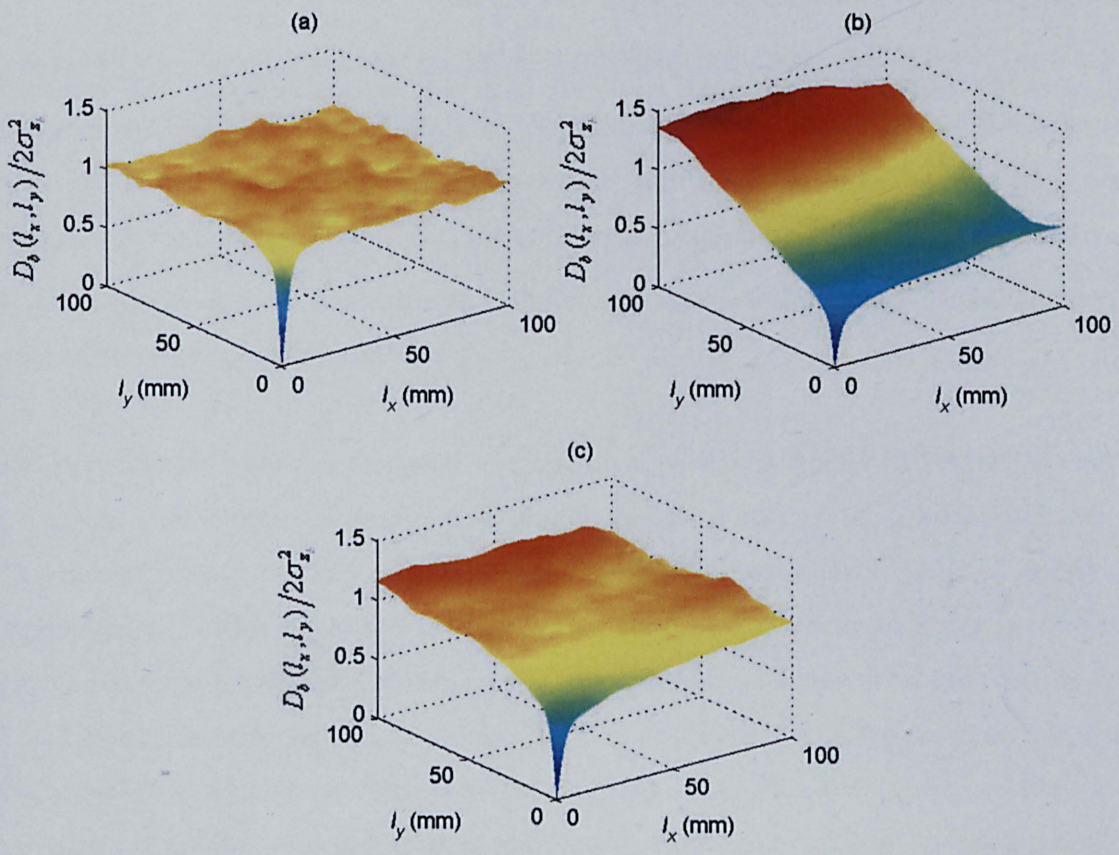

Figure 3.16. Surface plots of the second-order structure functions D_b of the bed surface elevations normalised by $2\sigma_{z_b}^2$ for (a) the screeded bed; (b) the unimodal bed; and (c) the bimodal bed, where σ_{z_b} is the standard deviation in bed surface elevations, and l_x and l_y are spatial lags in the streamwise and lateral direction, respectively.

3.7 Experimental Procedures

3.7.1 Experimental Phases

The aim was to produce a range of hydraulic conditions in various combinations so that the effects of relative submergence, bed slope, mean bed shear stress and bed surface topography on the time-averaged flow field throughout the flow depth could be isolated and investigated. A total of 12 experimental runs were carried out for each bed (Table 3.3 and 3.4), from which these were combined to produce three phases within the experimental programme. In all runs, the flow conditions were below those required for bed movement, ensuring that the bed surface topography was the same throughout each phase of testing for a given bed. Therefore the effects of different hydraulic conditions could be isolated. Flow conditions were always uniform and steady.

The runs were designed so that the relative submergence d/D_{84} and bed slope were approximately the same for each bed, so that runs could be compared directly between the two beds. Therefore different flow depths were used between the two beds to account for the difference in D_{84}. This allowed the effect of bed surface topography, from the two beds, to be isolated from the effects of differences in relative submergence and bed slope between the two beds.

The experiments were not designed to simulate a particular gravel-bed river, instead conditions were chosen which are believed to be typical of many U.K. gravel-bed rivers. The flow depths were purposefully chosen to represent the typical range of relative submergences, which cover the conditions that are likely to occur within a pool of a gravel-bed river, rather than the lower relative submergences which are more commonly found over riffle sections of a channel. This is in consideration of the macroscopically flat gravel beds which were formed within the flume. The flow depths were selected to simulate conditions observed when depths range from near bankfull to predominant flow conditions in wide U.K. gravel-bed rivers. The range of bed slopes used cover 52 % of the channel slopes observed in 62 U.K. gravel-bed rivers surveyed by Hey and Thorne (1986). The sediment mixtures were chosen to characterise the two types of grain-size distributions observed in U.K. gravel-bed rivers. The ratio of grain size to flume width and range of denismetric Froude numbers resembled conditions in a large, wide U.K. gravel-bed river.

Table 3.3. A summary of the experimental conditions over the unimodal bed, where S is the bed slope, Q is the flow discharge, d is the flow depth, D_{84} is the grain size at which 84 per cent of the bed material is finer, w_c is the width of the flume, $\overline{U}$ is the average flow velocity (calculated from the ratio of flow discharge to the cross-sectional area of the flow), τ_0 is the bed shear stress, Re is the flow Reynolds number (calculated from $\overline{U}d/\nu$, where ν is the kinematic viscosity) and Fr is the Froude number (calculated from $\overline{U}/\sqrt{gd}$, where g is the force due to gravitational attraction).

Experimental Run	S	Q (m^3/s)	d (m)	d/D_{84}	w_c/d	$\overline{U}$ (m/s)	τ_0 (N/m^2)	Re	Fr
1U	0.00285	0.00159	0.0181	2.6	27.6	0.18	0.47	2427	0.42
2U	0.00285	0.00389	0.0286	4.1	17.5	0.27	0.72	5933	0.51
3U	0.00285	0.00635	0.0395	5.6	12.7	0.32	0.95	9680	0.52
4U	0.00285	0.00869	0.0484	6.9	10.3	0.36	1.13	13246	0.52
5U	0.00285	0.0140	0.0628	9.0	8.0	0.45	1.40	21339	0.57
6U	0.00285	0.0280	0.0900	12.9	5.6	0.62	1.85	42618	0.66
7U	0.00375	0.0162	0.0635	9.1	7.9	0.51	1.86	24750	0.65
8U	0.00375	0.0114	0.0482	6.9	10.4	0.47	1.77	17430	0.69
9U	0.00465	0.0123	0.0492	7.0	10.2	0.50	1.87	18720	0.72
10U	0.00555	0.00978	0.0399	5.7	12.5	0.49	1.87	14905	0.78
11U	0.00645	0.00692	0.0335	4.8	14.9	0.41	1.87	10546	0.72
12U	0.00735	0.00655	0.0295	4.2	16.9	0.44	1.90	9977	0.83

Table 3.4. A summary of the experimental conditions over the unimodal bed, where S is the bed slope, Q is the flow discharge, d is the flow depth, D_{84} is the grain size at which 84 per cent of the bed material is finer, w_c is the width of the flume, $\overline{U}$ is the average flow velocity (calculated from the ratio of flow discharge to the cross-sectional area of the flow), τ_0 is the bed shear stress, Re is the flow Reynolds number (calculated from $\overline{U}d/\nu$, where ν is the kinematic viscosity) and Fr is the Froude number (calculated from $\overline{U}/\sqrt{gd}$, where g is the force due to gravitational attraction).

Experimental Run	S	Q (m^3/s)	d (m)	d/D_{84}	w_c/d	$\overline{U}$ (m/s)	τ_0 (N/m^2)	Re	Fr
1B	0.00284	0.00143	0.0173	2.6	28.9	0.16	0.45	2171	0.40
2B	0.00284	0.00276	0.0272	4.1	18.4	0.20	0.68	4198	0.39
3B	0.00284	0.00527	0.0373	5.7	13.4	0.28	0.90	8029	0.47
4B	0.00284	0.00809	0.0455	6.9	11.0	0.36	1.07	12333	0.53
5B	0.00284	0.0127	0.0595	9.0	8.4	0.43	1.34	19333	0.56
6B	0.00284	0.0245	0.0845	12.8	5.9	0.58	1.76	37388	0.64
7B	0.00374	0.01400	0.0594	9.0	8.4	0.47	1.76	21339	0.62
8B	0.00374	0.00939	0.0466	7.1	10.7	0.40	1.71	14305	0.60
9B	0.00464	0.0111	0.0472	7.2	10.6	0.47	1.80	16921	0.69
10B	0.00554	0.00728	0.0371	5.6	13.5	0.39	1.75	11087	0.65
11B	0.00644	0.00550	0.0317	4.8	15.8	0.35	1.77	8385	0.62
12B	0.00734	0.00356	0.0268	4.1	18.7	0.27	1.74	5417	0.52

The occurrence of two-dimensional flow within the measurement section was achieved by ensuring that the measurement section was a sufficient distance from the inlet and weir of the flume, and from the upstream and downstream fixed bed sections, given the depth of the flows (Kırkgöz and Ardıçlıoğlu, 1997). This was checked by taking velocity measurements within an ADV probe within the measurement section to ensure that two-dimensional vertical velocity profiles were present. The flow depths were also chosen so that all the runs had a flume width to flow depth ratio of greater than around four, which has been shown to be required for the generation of two-dimensional flow (Kironoto and Graf, 1994; Song *et al.*, 1994). The runs had Reynolds numbers greater than 2000, indicating that the flows were all fully turbulent.

For each experimental run, a steady flowrate was introduced and the downstream weir adjusted to achieve uniform depth for as large a reach as possible, and its position noted for future use. The hydraulic conditions were monitored to ensure that they were the same for a given run for each recorded measurement. This was achieved by setting the weir to the same position and recording water levels at three locations both upstream and downstream of the measurement area at 0.5 m intervals. Together with the bed level measurements taken following bed formation, the water level measurements were used to ensure that the water surface slope was the same as the bed slope. These were then used to calculate the mean uniform water depth and mean bed shear stress. The procedure used to calculate bed shear stress and water depth dictated that the flow was uniform so that the value of bed shear stress, in theory, was constant everywhere along the working length of the flume. The high values of flume width to flow depth ratio (> 4) mean that is not necessary to take into account the difference in roughness between the bed and flume walls when estimating bed shear stress. Mean bed shear stress τ_0 was therefore calculated from

$$\tau_0 = \rho g R S \tag{3.5}$$

where ρ is the water density, g is the force due to gravitational attraction, S is the bed slope (combined slope of bed surface and channel slope) and R is the hydraulic radius given by $R = A_c / P$, in which A_c is the cross-sectional area of the flow and P is the wetted perimeter of the flume.

The first phase of the tests were designed to investigate the effect of relative submergence on the time-averaged flow field by using six runs at a single bed slope (Tables 3.5 and 3.6). Different flow depths were created using different flow discharges.

The second phase of testing examined the influence of bed slope on the time-averaged flow field by conducting experimental runs at the same flow depths, but different bed slopes. This was achieved using a number of combinations of flow discharges and bed slopes. For each bed, there were four relative submergences at which experimental runs had the same relative submergence (Tables 3.7 and 3.8). A total of nine experimental runs were used for each bed, in which three runs were at the same relative submergence and three groups of two runs had the same relative submergences.

In the third phase of the experimental programme, six experimental runs were carried out that used a combination of different flow discharges and bed slopes, so that the mean bed shear stress was almost identical for each run (Table 3.9 and 3.10). These experimental runs therefore encompass the effects of both relative submergence and bed slope. Under these conditions of near identical mean bed shear stress the implication is that the average rate of momentum transfer at the bed is approximately the same for each of the experimental runs. The aim here was to discover whether changes in relative submergence and bed slope can induce changes in the nature of the time-averaged flow field even when the rate of momentum transfer at the bed is the same. This would indicate whether different momentum transfer processes occur when the rate is the same. For example, if the contributions made by form-induced stresses to momentum transfer change under these conditions, the relative contribution from both the Reynolds stress and form-induced stress must also change, indicating a change in the manner in which momentum is being transferred over the bed. An assessment can be made of whether relative submergence or bed slope has the primary influence on the flow field and the momentum transfer processes by examining which of the effects of the variables, established from the two earlier phases of tests, are evident.

3.7.2 Particle Image Velocimetry Measurements

The priority for the horizontal plane measurements was to carry out as many measurements as possible close to the bed surface. This was because this is the region in which much of the spatial variability in the time-averaged flow field is thought likely to

Table 3.5. A summary of the experimental conditions for the first phase of the experimental programme over the unimodal bed, in which experimental runs were carried out at a single bed slope, where S is the bed slope, d is the flow depth, D_{84} is the grain size at which 84 per cent of the bed material is finer, $\overline{U}$ is the average flow velocity (calculated from the ratio of flow discharge to the cross-sectional area of the flow) and τ_0 is the bed shear stress.

Experimental Run	S	d (m)	d/D_{84}	$\overline{U}$ (m/s)	τ_0 (N/m^2)
1U	0.00285	0.0181	2.6	0.18	0.47
2U	0.00285	0.0286	4.1	0.27	0.72
3U	0.00285	0.0395	5.6	0.32	0.95
4U	0.00285	0.0484	6.9	0.36	1.13
5U	0.00285	0.0628	9.0	0.45	1.40
6U	0.00285	0.0900	12.9	0.62	1.85

Table 3.6. A summary of the experimental conditions for the first phase of the experimental programme over the bimodal bed, in which experimental runs were carried out at a single bed slope, where S is the bed slope, d is the flow depth, D_{84} is the grain size at which 84 per cent of the bed material is finer, $\overline{U}$ is the average flow velocity (calculated from the ratio of flow discharge to the cross-sectional area of the flow) and τ_0 is the bed shear stress.

Experimental Run	S	d (m)	d/D_{84}	$\overline{U}$ (m/s)	τ_0 (N/m^2)
1B	0.00284	0.0173	2.6	0.16	0.45
2B	0.00284	0.0272	4.1	0.20	0.68
3B	0.00284	0.0373	5.7	0.28	0.90
4B	0.00284	0.0455	6.9	0.36	1.07
5B	0.00284	0.0595	9.0	0.43	1.34
6B	0.00284	0.0845	12.8	0.58	1.76

occur, and that very few measurements have been taken, say within 10 mm of the bed surface, over water-worked gravel beds. With this in mind, for each experimental run four heights close to the bed were selected, and above this, further measurements were approximately exponentially distributed within the flow depth (Tables 3.11 and 3.12). Given that the light sheet had a thickness of approximately 2 mm, no measurements were taken closer than 2.75 mm to the maximum bed elevation, to ensure that there was no interference between the light sheet and the bed surface. Furthering the depth of the field of view of the camera would have resulted in the camera imaging parts of the bed rather than just the flow. The vertical positions of the measurements were made at the same relative positions within the flow depth for both bed mixtures, to ensure that they were comparable.

Table 3.7. A summary of the experimental conditions for the second phase of the experimental programme over the unimodal bed, in which experimental runs were carried out at the same relative submergences, where S is the bed slope, d is the flow depth, D_{84} is the grain size at which 84 per cent of the bed material is finer, $\overline{U}$ is the average flow velocity (calculated from the ratio of flow discharge to the cross-sectional area of the flow) and τ_0 is the bed shear stress.

Experimental Run	S	d (m)	d/D_{84}	$\overline{U}$ (m/s)	τ_0 (N/m^2)
2U	0.00285	0.0286	4.1	0.27	0.72
12U	0.00735	0.0295	4.2	0.44	1.90
3U	0.00285	0.0395	5.6	0.32	0.95
10U	0.00555	0.0399	5.7	0.49	1.87
4U	0.00285	0.0484	6.9	0.36	1.13
8U	0.00375	0.0482	6.9	0.47	1.77
9U	0.00465	0.0492	7.0	0.50	1.87
5U	0.00285	0.0628	9.0	0.45	1.40
7U	0.00375	0.0635	9.1	0.51	1.86

The vertical plane PIV measurements were taken at nine lateral positions across the bed: −87 mm, −65 mm, −43 mm, −21 mm, 0 mm, 23 mm, 45 mm, 67 mm, 89 mm. A lateral position of 0 mm denotes the centreline of the flume. These nine positions corresponded with nine lateral measurement locations within the image area for the horizontal plane measurements. The heights of the vertical measurements above the maximum bed elevation (by controlling the size of the interrogation area and image area) were such that they were approximately equal to the vertical heights of the horizontal plane measurements above the bed. Potentially therefore, it is possible to obtain pseudo 3-D velocity data at these vertical positions, and at the nine lateral positions The use of both a horizontal and vertical PIV configuration in this way allows a significant number of measurement cross-sections to be made within a cube of fluid, allowing a substantial proportion of the cube to be characterised.

Table 3.8. A summary of the experimental conditions for the second phase of the experimental programme over the bimodal bed, in which experimental runs were carried out at the same relative submergences, where S is the bed slope, d is the flow depth, D_{84} is the grain size at which 84 per cent of the bed material is finer, $\overline{U}$ is the average flow velocity (calculated from the ratio of flow discharge to the cross-sectional area of the flow) and τ_0 is the bed shear stress.

Experimental Run	S	d (m)	d/D_{84}	$\overline{U}$ (m/s)	τ_0 (N/m^2)
2B	0.00284	0.0272	4.1	0.20	0.68
12B	0.00734	0.0268	4.1	0.27	1.74
3B	0.00284	0.0373	5.7	0.28	0.90
10B	0.00554	0.0371	5.6	0.39	1.75
4B	0.00284	0.0455	6.9	0.36	1.07
8B	0.00374	0.0466	7.1	0.40	1.71
9B	0.00464	0.0472	7.2	0.47	1.80
5B	0.00284	0.0595	9.0	0.43	1.34
7B	0.00374	0.0594	9.0	0.47	1.76

Table 3.9. A summary of the experimental conditions for the third phase of the experimental programme over the unimodal bed, in which experimental runs were carried out at the same mean bed shear stress, where S is the bed slope, d is the flow depth, D_{84} is the grain size at which 84 per cent of the bed material is finer, $\overline{U}$ is the average flow velocity (calculated from the ratio of flow discharge to the cross-sectional area of the flow) and τ_0 is the bed shear stress.

Experimental Run	S	d (m)	d/D_{84}	$\overline{U}$ (m/s)	τ_0 (N/m^2)
6U	0.00285	0.0900	12.9	0.62	1.85
7U	0.00375	0.0635	9.1	0.51	1.86
9U	0.00465	0.0492	7.0	0.50	1.87
10U	0.00555	0.0399	5.7	0.49	1.87
11U	0.00655	0.0335	4.8	0.41	1.87
12U	0.00735	0.0295	4.2	0.44	1.90

Table 3.10. A summary of the experimental conditions for the third phase of the experimental programme over the bimodal bed, in which experimental runs were carried out at the same mean bed shear stress, where S is the bed slope, d is the flow depth, D_{84} is the grain size at which 84 per cent of the bed material is finer, $\overline{U}$ is the average flow velocity (calculated from the ratio of flow discharge to the cross-sectional area of the flow) and τ_0 is the bed shear stress.

Experimental Run	S	d (m)	d/D_{84}	$\overline{U}$ (m/s)	τ_0 (N/m^2)
6B	0.00284	0.0845	12.8	0.58	1.76
7B	0.00374	0.0594	9.0	0.47	1.76
9B	0.00464	0.0472	7.2	0.47	1.80
10B	0.00554	0.0371	5.6	0.39	1.75
11B	0.00644	0.0317	4.8	0.35	1.77
12B	0.00734	0.0268	4.1	0.27	1.74

Table 3.11. The measurement heights of the horizontal plane PIV measurements above the maximum bed elevation for the experimental runs over the unimodal bed.

Run	Measurement heights above maximum bed elevation (mm)									
1U	3.00	5.00	7.00	9.00	11.00	-	-	-	-	-
2U	3.00	5.00	7.00	9.00	11.00	18.00	-	-	-	-
3U	3.00	5.00	7.00	9.00	11.00	18.00	29.00	-	-	-
4U	3.00	5.00	7.00	9.00	11.00	18.00	29.00	38.00	-	-
5U	3.00	5.00	7.00	9.00	11.00	18.00	29.00	38.00	53.00	-
6U	3.00	5.00	7.00	9.00	11.00	18.00	29.00	38.00	53.00	80.00
5U	3.00	5.00	7.00	9.00	11.00	18.00	29.00	38.00	53.00	-
7U	3.00	5.00	7.00	9.00	11.00	18.00	29.00	38.00	-	-
9U	3.00	5.00	7.00	9.00	11.00	18.00	29.00	38.00	-	-
10U	3.00	5.00	7.00	9.00	11.00	18.00	29.00	-	-	-
11U	3.00	5.00	7.00	9.00	11.00	18.00	23.00	-	-	-
12U	3.00	5.00	7.00	9.00	11.00	18.00	-	-	-	-

Table 3.12. The measurement heights of the horizontal plane PIV measurements above the maximum bed elevation for the experimental runs over the bimodal bed.

Run	Measurement heights above maximum bed elevation (mm)									
1B	2.75	4.75	6.50	8.50	10.50	-	-	-	-	-
2B	2.75	4.75	6.50	8.50	10.50	17.00	-	-	-	-
3B	2.75	4.75	6.50	8.50	10.50	17.00	27.25	-	-	-
4B	2.75	4.75	6.50	8.50	10.50	17.00	27.25	35.75	-	-
5B	2.75	4.75	6.50	8.50	10.50	17.00	27.25	35.75	50.00	-
6B	2.75	4.75	6.50	8.50	10.50	17.00	27.25	35.75	50.00	75.25
7B	2.75	4.75	6.50	8.50	10.50	17.00	27.25	35.75	50.00	-
8B	2.75	4.75	6.50	8.50	10.50	17.00	27.25	35.75	-	-
9B	2.75	4.75	6.50	8.50	10.50	17.00	27.25	35.75	-	-
10B	2.75	4.75	6.50	8.50	10.50	17.00	27.25	-	-	-
11B	2.75	4.75	6.50	8.50	10.50	17.00	21.75	-	-	-
12B	2.75	4.75	6.50	8.50	10.50	17.00	-	-	-	-

3.7.3 *Mean Velocity Characteristics*

Vertical profiles of the double-averaged streamwise velocity $\langle\overline{u}\rangle$ as a ratio to the bed shear velocity $u_* = \sqrt{\tau_0/\rho}$ are shown in Figure 3.17 for each of the experimental runs over the two beds. These were derived from the vertical plane PIV measurements because they contain a greater number of measurement positions above the bed surface than the horizontal plane measurements. The heights of the measurement positions from each of the nine lateral locations were referenced to the same maximum bed elevation from the bed topography scan. The relative height of the measurement positions for the nine vertical slices for a given experimental run were near identical (within ± 5 %). This allowed the velocities from each of the nine lateral locations to be assimilated to produce a matrix of $\overline{u}$ measurements over and above the bed for a given experimental run. This assimilation resulted in a matrix of 549 $\overline{u}$ values being produced over the bed for each vertical measurement position. By spatially averaging these values, $\langle\overline{u}\rangle$ could be derived. Figure 3.17 includes the vertical profiles for 22 of the 24 experimental runs for the flow above the bed. Experimental runs 1U and 1B are not shown because they only contained a small number of measurements above the bed, statistically too small to faithfully represent the vertical profile of $\langle\overline{u}\rangle$. These 22 runs are presented to summarise the experimental flow conditions, rather for any parameterisation. As was mentioned in Chapter 2, the vertical profiles can be subdivided into three flow layers; the form-induced sublayer, the logarithmic layer and the outer layer (Figure 2.1). The velocity distribution in the form-induced sublayer is described by

$$\frac{\langle\overline{u}\rangle}{u_*} = A\frac{z}{d} + B \qquad \text{for } 0 \le z \le \delta_F \tag{3.6}$$

where z is the height above the maximum bed elevation and δ_F is the height of the boundary between the form-induced sublayer and the logarithmic layer from the maximum bed elevation. In the logarithmic layer the law of the wall holds

$$\frac{\langle\overline{u}\rangle}{u_*} = \frac{1}{\kappa}\ln\left(\frac{z}{d}\right) + C \quad \text{for } \delta_F \le z \le \delta_L. \tag{3.7}$$

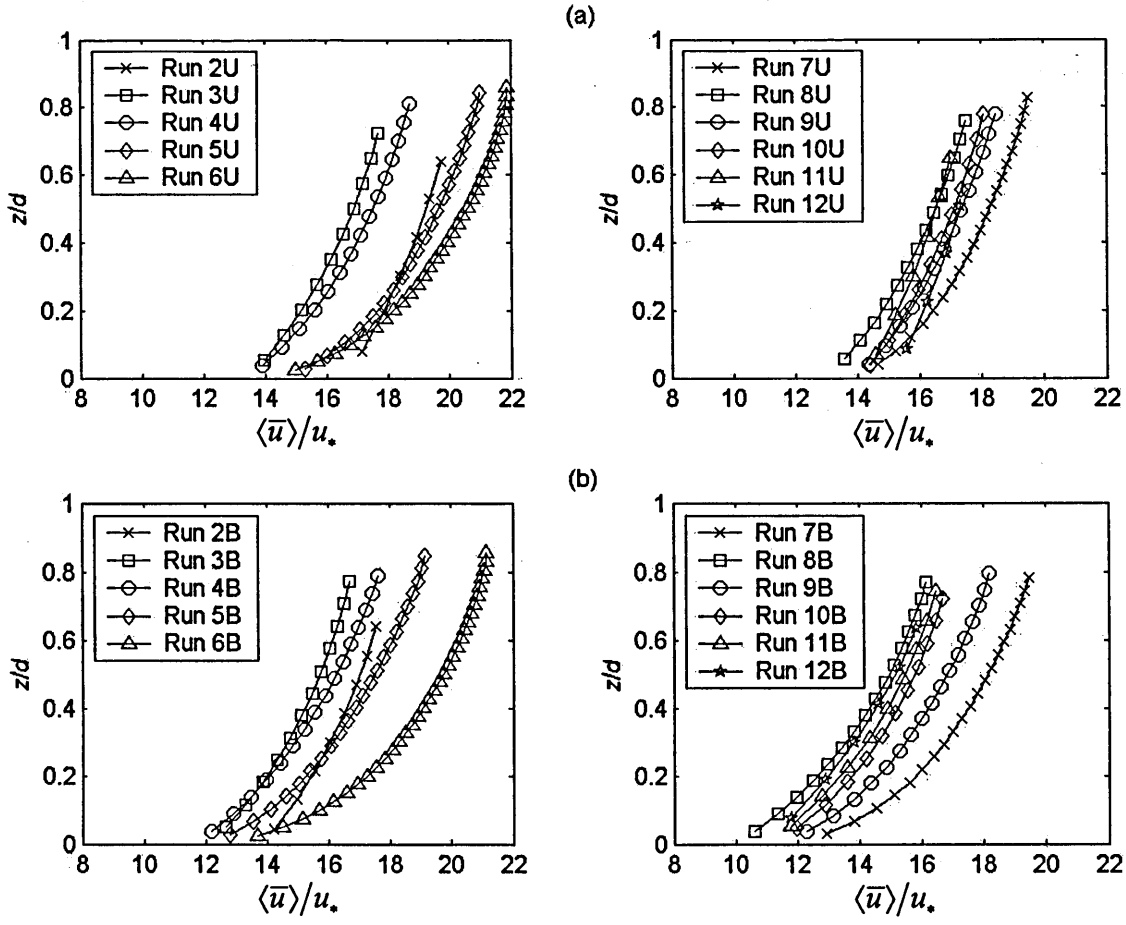

Figure 3.17. Vertical variability in $\langle\overline{u}\rangle/u_*$ with z/d over (a) the unimodal bed; and (b) the bimodal bed, where $\langle\overline{u}\rangle$ is the double-averaged streamwise velocity, u_* is the bed shear velocity, z is the height above the maximum bed elevation and d is the flow depth.

where κ is the von Kármán constant and δ_L is the height of the boundary between the logarithmic layer and the outer layer above the maximum bed elevation. Using these expressions it is possible to estimate δ_F and δ_L.

The value of δ_F was found by carrying out a linear least-squares fit to the variation in $\langle\overline{u}\rangle/u_*$ with z/d of the form of equation (3.6) until there was a significant variation in the parameter A for the fit. This change was defined as occurring at $(z/d)_i$ when $|A_i - A_{i-1}| > |0.05A_{i-1}|$. A value of 0.05 was found to produce a subdivision of the vertical profile of $\langle\overline{u}\rangle/u_*$ that corresponded with subdivision achieved by observation. The boundary between the form-induced sublayer and the logarithmic layer was

assumed to occur midway between $(z/d)_i$ and $(z/d)_{i-1}$. The same procedure was applied for deriving δ_L using a least-squares fit of the form of equation (3.7). The values of δ_F and δ_L are shown in Tables 3.13 and 3.14. There is a remarkable similarity in the absolute height at which δ_F occurs over the two beds. The form-induced sublayer persists up to around a height of 5 mm above the maximum bed elevation for all but the runs carried out at the very highest relative submergences. Koll (pers. comm) found the form-induced sublayer to exist only approximately 2 mm above the maximum bed elevation over a screeded gravel-bed, at a relative submergence of approximately seven. The greater distance found here may be explained by the greater bed roughness due to the surface being water-worked.

Studies have suggested that δ_F may be as high as $(2-5)\Delta$ (Raupach *et al.*, 1991; Nezu and Nakagawa, 1993), where Δ is the roughness height. Several studies have argued that the roughness of gravel beds can be better described by σ_{z_b} than using characteristic grain-sizes such as D_{50} or D_{84} (Nikora *et al.*, 1998; Aberle and Smart, 2003). If σ_{z_b} is used to describe δ_F in terms of Δ, it can be seen from Tables 3.13 and 3.14 there is greater variability in the height of the form-induced sublayer in these terms between the two beds. Over the unimodal bed, it ranges from $(2.1-3.6)\Delta$ but extends to a smaller distance of between $(1.6-2.7)\Delta$ over the bimodal bed. The majority of the values fall within the range suggested by Raupach *et al.* (1991) and Nezu and Nakagawa (1993), but fall short of the upper part of the range.

The values of δ_F/d display much greater variability between the different runs. However, they are similar for the same relative submergences over the two beds. The height of the form-induced layer persists up to z/d values of between 0.08 and 0.3. There is a tendency for this ratio to reduce with an increase in relative submergence. Campbell *et al.* (2005) also found a value of $z/d = 0.08$ over a screeded, gravel bed at a similar depth to the depth used for experimental run 5U, which also had a value of 0.08. The δ_F/d values again fall within the range of values suggested by Raupach *et al.* (1991) and Nezu and Nakagawa (1993).

Table 3.13. A summary of the vertical height and thickness of each of the flow layers above the maximum bed elevation for the experimental runs carried out over the unimodal bed, where d is the flow depth, D_{84} is the grain size at which 84 per cent of the bed material is finer, δ_F is the height of the form-induced sublayer, Δ is the roughness height assumed to be equal to the standard deviation in bed surface elevations (= 2.14 mm), δ_L is the height of the logarithmic layer, ξ_L is the thickness of the logarithmic layer relative to the flow depth, ξ_O is the thickness of the outer layer relative to the flow depth, κ is the von Kármán constant from the logarithmic fit to the vertical variation in $\langle\overline{u}\rangle/u_*$ with z/d in the logarithmic layer, in which $\langle\overline{u}\rangle$ is the double-averaged streamwise velocity, u_* is the bed shear velocity and z is the height above the maximum bed elevation.

Run	d/D_{84}	δ_F (mm)	δ_F/Δ	δ_F/d	δ_L/Δ	δ_L/d	ξ_L	ξ_O	κ
2U	4.1	5.00	2.35	0.25	5.51	0.58	0.33	0.42	0.38
3U	5.6	5.00	2.34	0.16	8.30	0.58	0.42	0.42	0.38
4U	6.9	4.96	2.31	0.12	10.79	0.56	0.44	0.44	0.30
5U	9.0	5.00	2.34	0.086	15.05	0.55	0.46	0.45	0.27
6U	12.9	7.78	3.63	0.087	22.70	0.54	0.45	0.46	0.22
7U	9.1	5.81	2.71	0.10	15.42	0.57	0.47	0.43	0.28
8U	6.9	5.81	2.71	0.14	12.25	0.62	0.48	0.38	0.29
9U	7.0	4.96	2.31	0.12	10.79	0.58	0.46	0.42	0.35
10U	5.7	4.59	2.14	0.15	8.50	0.59	0.44	0.41	0.39
11U	4.8	4.78	2.23	0.24	5.41	0.59	0.35	0.41	0.43
12U	4.2	4.78	2.24	0.30	4.36	0.58	0.28	0.42	0.51

The values of δ_L/d are similar between the two beds. There is only a small variability in these values between runs over a given bed, ranging from 0.51 to 0.62, which falls within the range of relative heights at which the logarithmic layer is expected to occur (Nezu and Nakagawa, 1993). There is a tendency for the δ_L/d values to decrease with an increase in relative submergence over the two beds, with the changes being less consistent over the bimodal bed. There are large differences in the values of δ_L/Δ

between the runs, suggesting that the height of the logarithmic layer is better scaled by flow depth rather than the roughness height of the bed, the opposite to that seen for the height of the form-induced sublayer. This is sensible given that the logarithmic layer occupies a region of the flow depth where the influence of the bed is small.

Table 3.14. A summary of the vertical height and thickness of each of the flow layers above the maximum bed elevation for the experimental runs carried out over the bimodal bed, where d is the flow depth, D_{84} is the grain size at which 84 per cent of the bed material is finer, δ_F is the height of the form-induced sublayer, Δ is the roughness height assumed to be equal to the standard deviation in bed surface elevations (=1.70 mm), δ_L is the height of the logarithmic layer, ξ_L is the thickness of the logarithmic layer relative to the flow depth, ξ_O is the thickness of the outer layer relative to the flow depth and κ is the von Kármán constant from the logarithmic fit to the vertical variation in $\langle\overline{u}\rangle/u_*$ with z/d in the logarithmic layer, in which $\langle\overline{u}\rangle$ is the double-averaged streamwise velocity, u_* is the bed shear velocity and z is the height above the maximum bed elevation.

Run	d/D_{84}	δ_F (mm)	δ_F/Δ	δ_F/d	δ_L/Δ	δ_L/d	ξ_L	ξ_O	κ
2B	4.1	4.58	1.61	0.17	5.60	0.60	0.43	0.40	0.36
3B	5.7	5.08	1.79	0.15	7.37	0.61	0.46	0.39	0.31
4B	6.9	5.08	1.79	0.11	8.16	0.51	0.40	0.49	0.27
5B	9.0	5.08	1.79	0.084	12.94	0.61	0.53	0.39	0.24
6B	12.8	7.72	2.72	0.086	16.26	0.52	0.43	0.48	0.21
7B	9.0	7.44	2.62	0.12	11.38	0.54	0.42	0.46	0.22
8B	7.1	5.18	1.82	0.11	8.20	0.50	0.39	0.50	0.25
9B	7.2	5.10	1.80	0.11	8.96	0.53	0.42	0.47	0.24
10B	5.6	4.99	1.76	0.15	6.54	0.55	0.40	0.45	0.26
11B	4.8	4.77	1.68	0.18	4.87	0.53	0.35	0.47	0.27
12B	4.1	4.94	1.74	0.24	4.13	0.58	0.34	0.42	0.24

The thickness of the logarithmic layer, relative to the depth of the flow, is given by $\xi_L = \delta_L/d - \delta_F/d$. Tables 3.13 and 3.14 show that the thickness of this layer has a tendency to increase with relative submergence over both of the beds, but that the changes are small. The thickness of the outer layer, $\xi_O = 1 - \delta_L/d$, displays small variation between the runs over the unimodal bed, and slightly larger changes over the bimodal bed. There is a slight tendency for the thickness to increase with relative submergence over both of the beds. Given that the thickness of the form-induced sublayer is given by δ_F/d, and that the values of δ_F/d decreased with an increase in relative submergence, it suggests that an increase in relative submergence, on average, causes a decrease in the thickness of the form-induced sublayer but an increase in the thickness of the logarithmic and outer layer. The largest changes occur in the thickness of the form-induced sublayer, followed by the logarithmic layer, with the outer layer displaying the least variability, relative to the depth of the flow.

The values of κ in Tables 3.13 and 3.14 were found by applying a linear least-squares fit of the form of equation (3.7) to the vertical variation in $\langle\overline{u}\rangle/u_*$ in the logarithmic layer within the bounds of the layer established from above. These values show greater variability between the beds and the different experimental runs (Tables 3.13 and 3.14). They are typically lower over the bimodal bed, but do show less variation between the runs than over the unimodal bed. The range of values is consistent with results from a number of different roughnesses.

The vertical profiles of normalised double-averaged vertical velocity $\langle\overline{w}\rangle/u_*$ for the same experimental runs are shown in Figure 3.18. These were constructed from the vertical plane measurements in the same way as described for the profiles of $\langle\overline{u}\rangle/u_*$, by assimilating the time-averaged vertical velocity $\overline{w}$ values from each of the nine lateral locations to produce a matrix of $\overline{w}$ measurements over and above the bed for a given experimental run. The profiles show that the values of $\langle\overline{w}\rangle/u_*$ are very small, and that $\langle\overline{w}\rangle$ can sensibly be assumed to be zero throughout the whole flow depth. This demonstrates that there was unlikely to have been secondary currents within any of the flows, and that the flow can be assumed to be 2-D for all experimental runs.

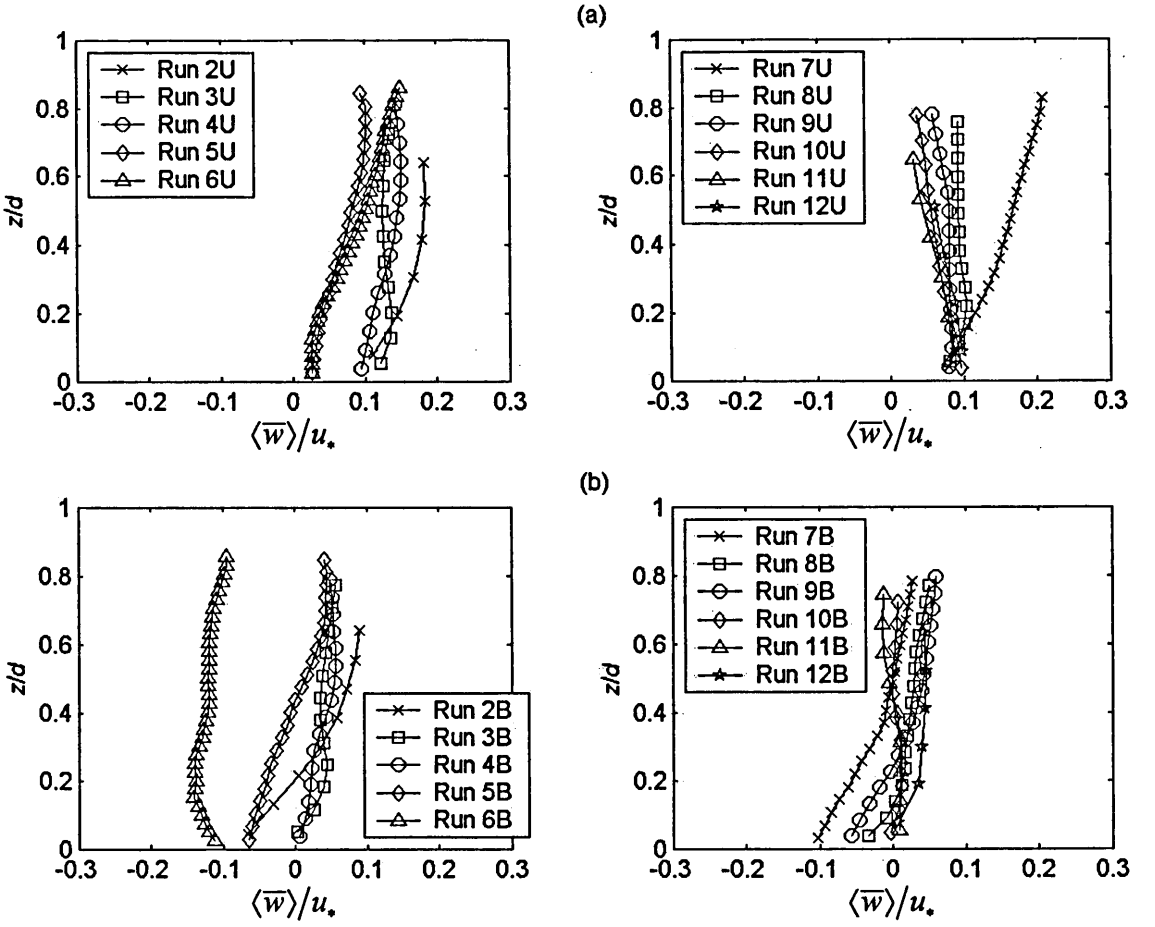

Figure 3.18. Vertical variability in $\langle\overline{w}\rangle/u_*$ with z/d over (a) the unimodal bed and (b) the bimodal bed, where $\langle\overline{w}\rangle$ is the double-averaged streamwise velocity, u_* is the bed shear velocity, z is the height above the maximum bed elevation and d is the flow depth.

3.8 Summary

The experimental programme involved providing high spatial resolution measurements of the time-averaged flow field over two water-worked gravel beds. The flow velocity data was collected using PIV in two configurations enabling, for the first time, a cube of fluid to be characterised in great detail over these beds. This was carried out under a range of hydraulic conditions in a flume, so that the effect of relative submergence and bed slope on the spatial variability in the flow could be sought. Furthermore experimental runs were performed at the same mean bed shear stresses in order to discover whether the time-averaged flow structure changes, and therefore whether momentum transfer mechanisms change, even when the mean rate of momentum transfer at the bed is the same. Consideration was given to the flow depths, bed slopes

and bed mixtures used so that tests were performed under a range of hydraulic and channel conditions that are found in gravel-bed rivers.

A different approach to bed formation was used from the conventional method of manually placing sediment into the base of the flume. A conveyor belt was used to feed sediment into a running flume, which formed flat (at the macroscopic scale), water-worked beds that are believed to represent more faithfully the bed surface topographies that are found in the flat-bedded sections of single threaded and straight gravel-bed rivers. This was in order to ensure that the flow field being measured was more representative of what would be found in these rivers, than in previous studies. The bed surface topography was also measured at a high spatial resolution so that the influence of surface topography on the time-averaged flow field could be considered.

The velocity data will be examined in three results chapters which examine the degree of spatial variability in the time-averaged flow, the manner in which this is distributed over the bed, and the potential it has for producing form-induced stress over water-worked gravel beds. Each of these chapters includes discussion on the implications of the results and the way in which they relate to previous studies. A chapter then follows which aims to draw together the conclusions made from each results chapter in order to discuss the physical significance of the results.

CHAPTER 4
THE SPATIAL VARIABILITY IN TIME-AVERAGED STREAMWISE VELOCITY

4.1 Introduction

This is the first of three results chapters examining the spatial variability in time-averaged flow fields and the significance of these variations for transferring fluid momentum in free surface flows over water-worked gravel beds. This chapter will investigate whether spatial variations exist in time-averaged streamwise velocities. It will be seen how this variability changes through the flow depth and whether the velocity variations remain significant in the regions of the flow where they were previously thought to be negligible. An examination will be made of whether their size is controlled by flow features that scale with flow depth, or by flow structures that are scaled by bed roughness. The chapter will also show how the level of spatial variability changes with relative submergence, bed slope and between two beds with different surface topographies in order to understand what physically controls the size of this spatial variability. Expressions will be derived that describe the vertical variation in the levels of spatial variability and the influence of possible controlling variables. Furthermore, the chapter will examine the organisation of the spatial deviations over the beds and the relationship this has with bed surface topography.

4.2 Distribution of Time-averaged Streamwise Velocities over the Bed

To establish whether time-averaged streamwise velocities $\overline{u}$ vary spatially over water-worked gravel beds, the distributions of $\overline{u}/\langle\overline{u}\rangle$ were examined, where $\langle\overline{u}\rangle$ is the double-averaged streamwise velocity, produced through spatially-averaging $\overline{u}$. These distributions are shown in terms of their probability density function (*pdf*) for a number of experimental runs at different relative heights above the bed. The relative height is given by z/d, where z is the height above the maximum bed elevation and d is the flow depth. The maximum bed elevation corresponds to the maximum elevation within the

250 x 250 mm area measured by the laser bed scans. The elevation over this area was used because the alignment of the height of the horizontal plane of velocity measurements was located relative to this maximum bed elevation. In addition, the maximum bed elevation was the most easily distinguishable bed feature within the vertical plane PIV images as a reference point to the vertical measurement locations, and as such was the most robust choice.

The PIV measurements used in the analysis were collected in a horizontal plane parallel to the bed surface to provide measurements of $\overline{u}$ over the bed at a high spatial resolution. The distributions of $\overline{u}/\langle\overline{u}\rangle$ are shown for the unimodal and bimodal beds in Figures 4.1 and 4.2, respectively. These are indicative of distributions measured for other experimental runs at these relative heights. For each of the two beds, distributions are shown from experimental runs that encompass a range of bed slopes and flow depths to provide an indication of the variability in $\overline{u}/\langle\overline{u}\rangle$ between experimental runs. For different values of z/d, distributions from the same experimental runs have been shown to also demonstrate how the distributions change with distance from the bed. Each of the experimental runs over the bimodal bed was designed so that the relative submergence and bed slope were similar to the runs over the unimodal bed. In addition the relative height of the measurement planes parallel with the bed, from these comparable experimental runs, was similar over each bed. In Figures 4.1 and 4.2 the distributions from these runs and planes are also shown to provide some indication of the variability in the distributions of $\overline{u}$ between the two beds.

The *pdf*'s show that there is considerable spread in $\overline{u}$ over each of the beds. Some areas of the unimodal bed can experience $\overline{u}$ values as low as 60 % of $\langle\overline{u}\rangle$, but others over 120 % of $\langle\overline{u}\rangle$. Over the bimodal bed, the spread in values is higher, resulting in some areas of the bed having $\overline{u}$ values as low as 60 % of $\langle\overline{u}\rangle$ and as high as 140 % of $\langle\overline{u}\rangle$. It means that for both beds, some areas can have $\overline{u}$ values that are over two times higher than over other areas of the bed. The range of $\overline{u}$ values is therefore of a similar magnitude to $\langle\overline{u}\rangle$. The degree of spread in the values not only varies between the two beds, but also between experimental runs, and with z/d. This also applies to the shape of the distributions.

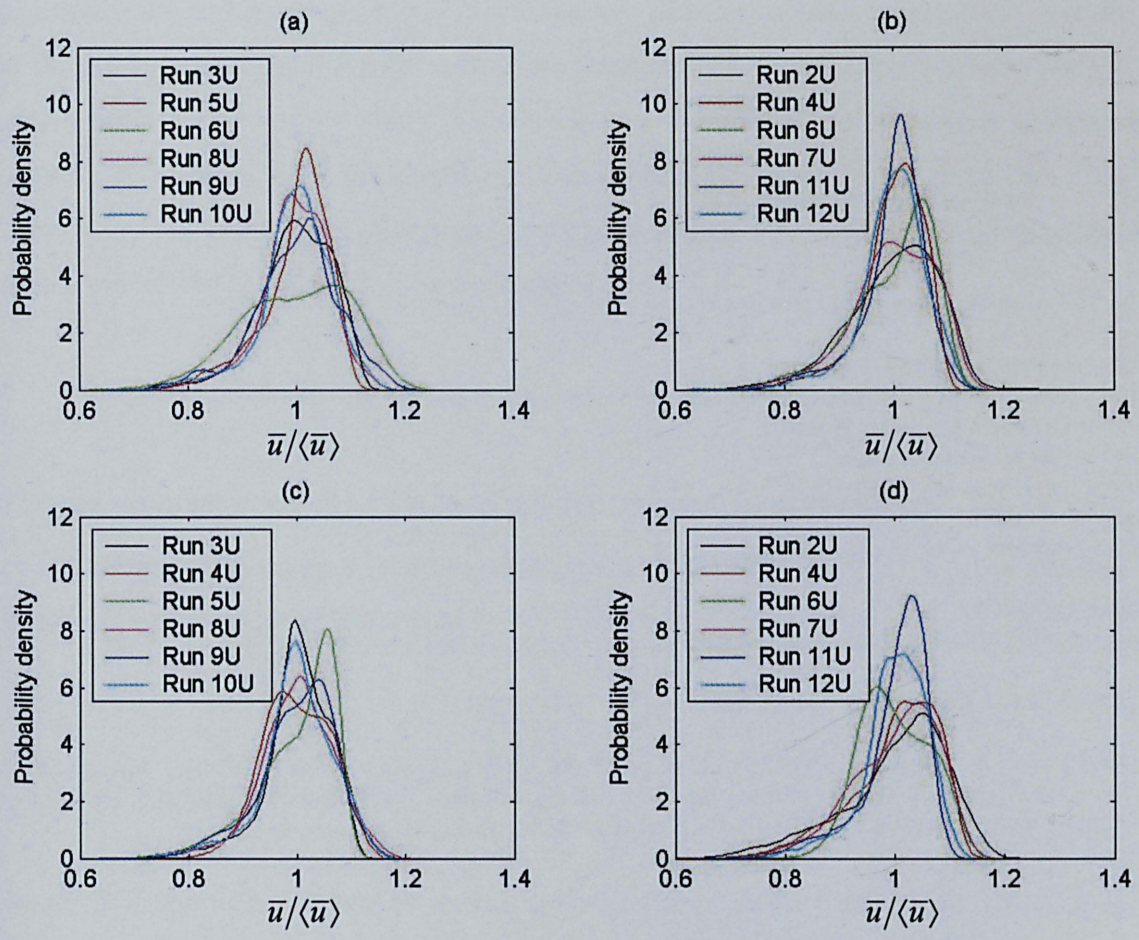

Figure 4.1. Probability density functions of a number of distributions of $\overline{u}/\langle\overline{u}\rangle$ over the unimodal bed at relative heights z/d of (a) 0.08; (b) 0.12; (c) 0.16; and (d) 0.21, where $\overline{u}$ is the time-averaged streamwise velocity, $\langle\overline{u}\rangle$ is the double-averaged streamwise velocity, z is the height above the maximum bed elevation and d is flow depth.

It is useful to quantify the variability in the spread and shape of the distributions. The *pdf*'s only provide a visual representation of the way in which $\overline{u}$ is distributed over the bed, so an examination of the higher-order statistical moments of the distributions was carried out. The standard deviation in $\overline{u}$ over the bed, which is a measure of the degree of spatial variability in $\overline{u}$ over the bed, will be discussed. Then the skewness and kurtosis of the distributions will be examined, followed by how closely the distributions follow a normal distribution. The values of these parameters will be presented in the form of a direct comparison between the two beds in order to enable the distributions from all 22 experimental runs to be examined, producing a summary of the shape of the distributions over the two beds. This means that a total of 184 data sets, each based on 3782 $\overline{u}$ measurements over the bed (from a uniform sampling grid of 61×62

positions), are compared directly between the two beds. It should provide an indication of the effect of the differences in bed surface topography between the two water-worked gravel beds on the way in which $\overline{u}$ is distributed. It will also be possible to quantify what the differences are in the shapes between experimental runs over a given bed. This kind of analysis enables the importance of the tails of the distributions, where the largest spatial variability is observed, to be determined.

4.2.1 Degree of Spatial Variability

The second-order moment of the distributions, its standard deviation, $\sigma_{\overline{u}}$, can be used as a quantitative measure of the degree of spatial variability in $\overline{u}$ at a given vertical height above the bed, and is given by

$$\sigma_{\overline{u}} = \sqrt{\frac{1}{N}\sum_{i=1}^{N}\left(\overline{u}_i - \langle\overline{u}\rangle\right)^2} \tag{4.1}$$

where N is the total number of measurements within the flow field (i.e. 3782). It is equivalent to $\sqrt{\langle\widetilde{u}^2\rangle}$, where $\widetilde{u}$ is the spatial deviation in $\overline{u}$, given by $\overline{u} - \langle\overline{u}\rangle$. Since $\widetilde{u}$ is a component of the form-induced stress, $\sigma_{\overline{u}}$ is an appropriate variable to parameterise in order to assess the significance of spatial variations for transferring fluid momentum. It is absolute, rather than relative, spatial deviations in the time-averaged flow field that produce form-induced stresses. This absolute measure is equivalent in spatial terms to the root mean square fluctuation in instantaneous streamwise velocity.

A comparison of $\sigma_{\overline{u}}$ between the two beds is shown in Figure 4.3a. It can be seen that the $\sigma_{\overline{u}}$ values over both beds are one order of magnitude smaller than $\langle\overline{u}\rangle$, as was implied by the *pdf*'s of the $\overline{u}/\langle\overline{u}\rangle$ distributions. The degree of spatial variability is typically higher over the bimodal bed, with the $\sigma_{\overline{u}}$ values in some cases being more than double that over the unimodal bed. It needs to be established why these differences occur, along with why there is considerable scatter in $\sigma_{\overline{u}}$ over each of the beds. It could be suggested that this scatter is due to differences in relative submergence, bed slope, $\langle\overline{u}\rangle$, bed shear velocity or the distance from the bed surface. This will be the subject of the next section.

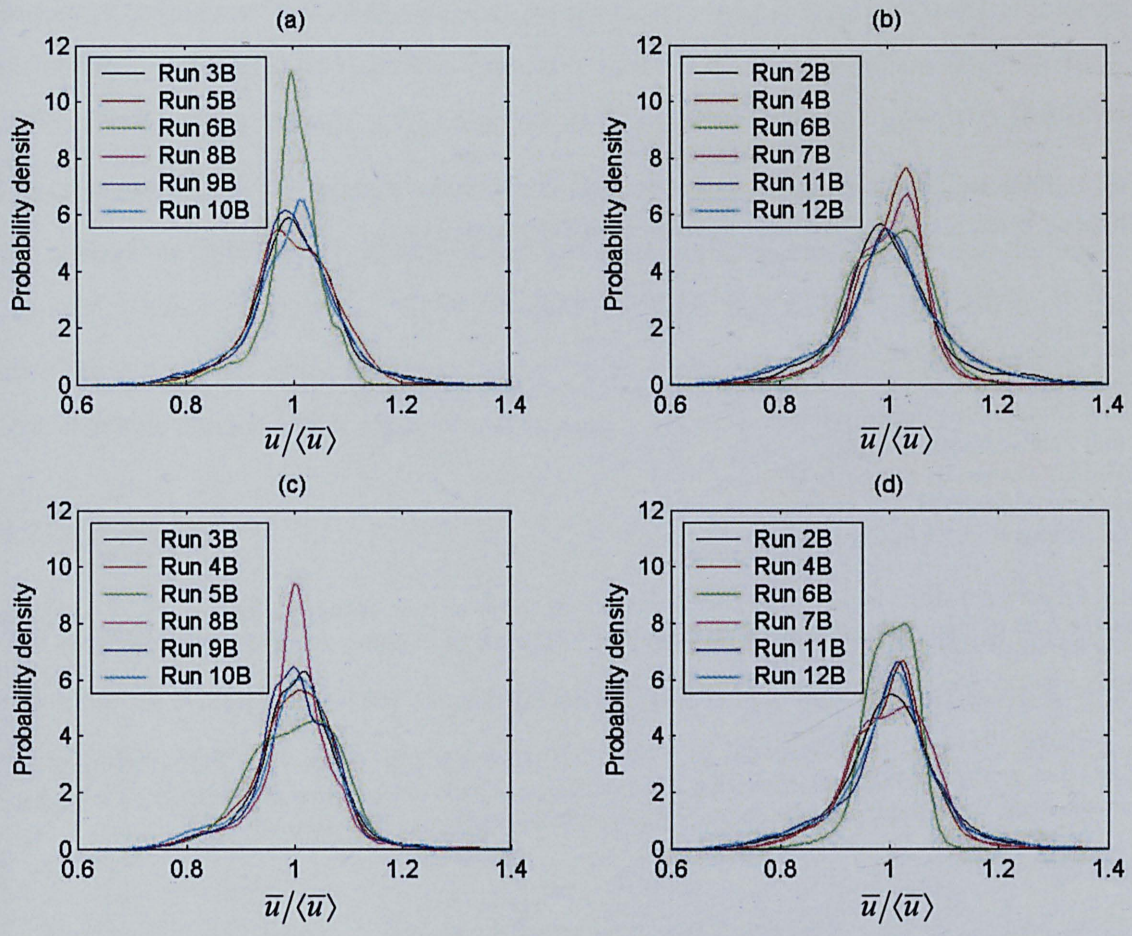

Figure 4.2. Probability density functions of a number of distributions of $\overline{u}/\langle\overline{u}\rangle$ over the bimodal bed at relative heights z/d of (a) 0.08; (b) 0.12; (c) 0.16; and (d) 0.21, where $\overline{u}$ is the time-averaged streamwise velocity, $\langle\overline{u}\rangle$ is the double-averaged streamwise velocity, z is the height above the maximum bed elevation and d is flow depth.

Unfortunately, there are no reported values of $\sigma_{\overline{u}}$ within the literature, but Nikora *et al.* (2001) do present values of $\langle\widetilde{u}^2\rangle/u_*^2$ for two flows over a diamond array of spheres within a laboratory flume. If these values are converted to be equivalent to $\sigma_{\overline{u}}$, it gives values of $\sigma_{\overline{u}}$ that range from being negligible to 0.078. Although the upper end of this range is higher than the maximum values in Figure 4.3a, the majority of the values in Figure 4.3a do correspond with the typical values found by Nikora *et al.* (2001) at similar heights above the bed. It is also useful to compare the $\sigma_{\overline{u}}$ values to their temporal equivalent, the root mean square fluctuation in instantaneous streamwise velocity, the absolute turbulence intensity, to discover the relative importance of the spatial variations. The majority of studies into turbulence quote their measures for the

degree of turbulence in non-dimensional, rather than absolute, values. For the studies of turbulence over gravel bed surfaces that have presented absolute values (e.g. Clifford, 1996; Lawless and Robert, 2001; Carling *et al.*, 2002), it would appear that $\sigma_{\bar{u}}$ is typically lower than its temporal equivalent. Only the higher values of $\sigma_{\bar{u}}$ resemble the lower absolute turbulence intensity values that have been reported for close to the water surface by these studies. But the $\sigma_{\bar{u}}$ values do, however, match very well with the absolute turbulence intensities reported by Buffin-Bélanger and Roy (1998) for flows over a pebble cluster within a gravel-bed stream.

4.2.2 Skewness

The distributions of $\bar{u}$ over the bed are further assessed by examining the third-order moments of $\bar{u}$. This provides a measure of the skewness, or the asymmetry of the distributions, and is given by

$$Sk_{\bar{u}} = \frac{1}{N} \frac{\sum_{i=1}^{N} (\bar{u}_i - \langle \bar{u} \rangle)^3}{\sigma_{\bar{u}}^{\ 3}} \tag{4.2}$$

In earlier turbulence studies, a positive skewness value for a distribution of instantaneous streamwise velocities has been associated with infrequent but large positive fluctuations in streamwise velocity (relative to $\bar{u}$), whilst a negative value has been related to infrequent and very low speed fluid motions. Skewness can therefore reveal the presence of infrequent fluid motions with a large deviation from the mean. Equally it can be used to assess whether smaller negative or positive fluctuations in streamwise velocity dominate. A positive value also suggests that small negative fluctuations in streamwise velocity are dominant. A negative value suggests the reverse, that small positive fluctuations are prevalent over time.

If these ideas are transferred from the temporal to the spatial domain, skewness can be interpreted differently. A positive $Sk_{\bar{u}}$ value implies that the flow has a number of localised areas of distinctly high $\bar{u}$ (relative to $\langle \bar{u} \rangle$), balanced by large areas of just slightly lower-than-average $\bar{u}$. Similarly a negative $Sk_{\bar{u}}$ values implies that the flow

has localised areas of distinctly low $\overline{u}$ balanced by large areas of just slightly higher-than-average $\overline{u}$.

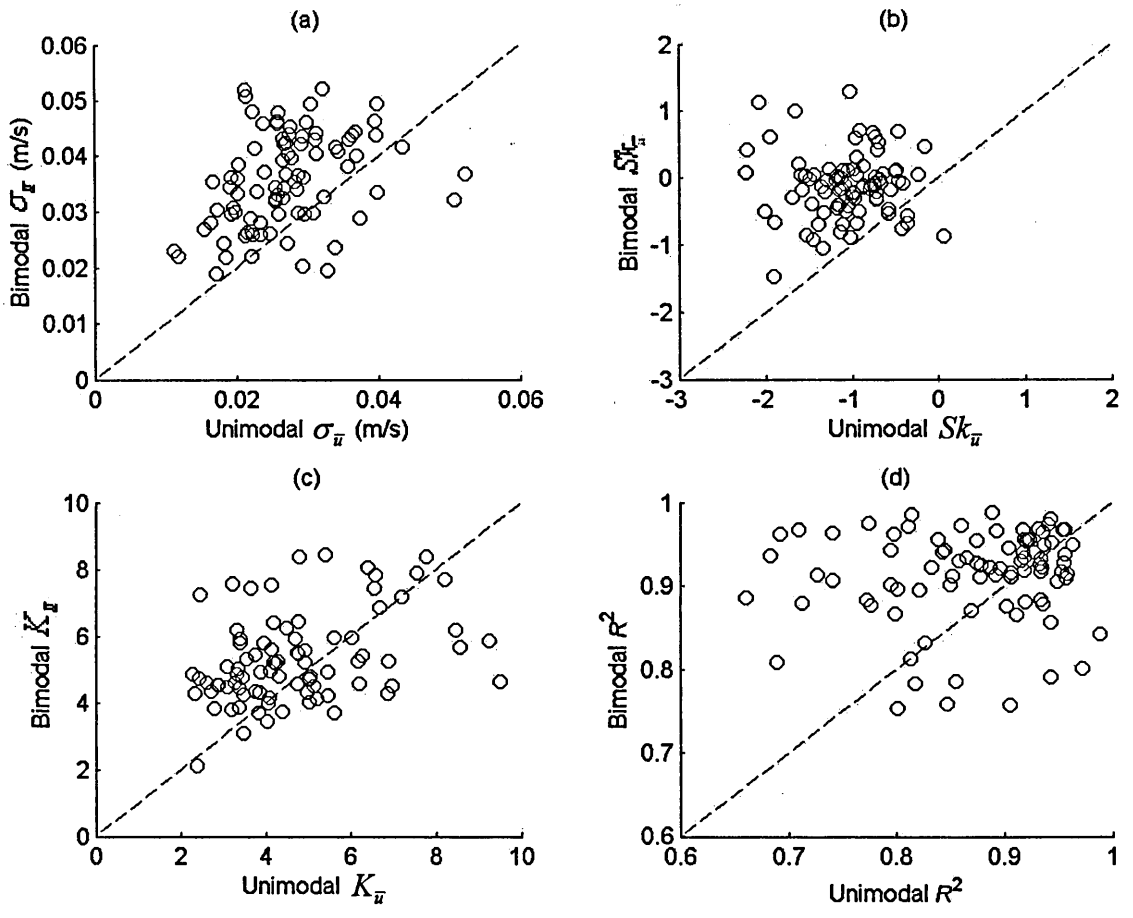

Figure 4.3. A comparison between the two beds of the shape of the distributions of $\overline{u}$ for (a) $\sigma_{\overline{u}}$; (b) $Sk_{\overline{u}}$; (c) $K_{\overline{u}}$; and (d) R^2 of the regression between the probability density function of $\overline{u}$ and the probability density function of a model normal distribution for those $\overline{u}$ values, where $\sigma_{\overline{u}}$ is the degree of spatial variability in $\overline{u}$ over the bed, $\overline{u}$ is the time-averaged streamwise velocity, $Sk_{\overline{u}}$ is the skewness of the distribution and $K_{\overline{u}}$ is the kurtosis of the distribution. The dashed line is a line of equality.

It can be seen from Figure 4.3b that the distributions of $\overline{u}$ are all negatively skewed over the unimodal bed, except one distribution which is near symmetrical. The distributions can, in some cases, be strongly negatively skewed. The implication is that

the flow over the unimodal bed contains localised areas of distinctly low $\overline{u}$ and large areas of just slightly higher-than-average $\overline{u}$. This is also typically the case over the bimodal bed, although it cannot be so simply characterised. The distributions can vary from being slightly positively skewed to slightly negatively skewed, so some distributions suggest that the flow could contain localised areas of distinctly high $\overline{u}$ and large areas of just slightly lower-than-average $\overline{u}$. The $Sk_{\overline{u}}$ values show considerable variability over each of the beds, suggesting that the spatial pattern of $\overline{u}$ over the bed may also be variable.

The only study that presents results of the skewness of the distributions of $\overline{u}$ over a bed is by Barison *et al.* (2003). Although they did not provide any skewness values, the distributions over a mobile armouring gravel bed were all found to be negatively skewed, which is largely in accordance to that seen in Figure 4.3b. Comparisons can also be made to the distributions of instantaneous streamwise velocities. These distributions have typical skewness values of between 0.5 and –0.5 in gravel-bed rivers (Buffin-Bélanger and Roy, 1998; Nikora and Smart, 1997; Nikora and Goring, 2000). The distributions of $\overline{u}$ were more highly skewed, and only in the case of the bimodal bed did they display both positive and negative skewness, as has been found for the distributions of instantaneous streamwise velocities.

4.2.3 Kurtosis

The kurtosis of the distributions of $\overline{u}$ can be calculated to discover how flat or peaked the distributions are in comparison to a normal distribution. This is given by

$$K_{\overline{u}} = \frac{1}{N} \frac{\sum_{i=1}^{N} \left(\overline{u}_i - \langle \overline{u} \rangle\right)^4}{\sigma_{\overline{u}}^4} \tag{4.3}$$

A value of 3 for $K_{\overline{u}}$ indicates that the distribution of $\overline{u}$ is as peaked as a perfect normal distribution. A value above 3 indicates that it is more peaked (leptokurtic), and a value less than 3 means that the distribution is flatter (platykurtic). A value of 1.8 is attained for a perfectly uniform distribution, where the *pdf* is rectangular between the sharp upper and lower limits of the distribution. A value below 1.8 implies a bimodal

distribution. Theoretically, it holds that $K_{\overline{u}} \geq Sk_{\overline{u}}^2 + 1$ so $K_{\overline{u}}$ can only attain values above 1.

The $K_{\overline{u}}$ values in Figure 4.3c show that the majority of the distributions of $\overline{u}$ over the beds are leptokurtic, with just a few having approximately the same kurtosis as a perfect normal distribution, and only one being platykurtic. The bimodal bed has distributions that tend to be slightly more leptokurtic than over the unimodal bed. There are a number of distributions over each of the beds that are highly leptokurtic, of the order of 10.

The distributions presented by Barison *et al.* (2003) became flatter as their gravel bed armoured, but it is impossible to assess whether they were platykurtic or leptokurtic. Very little data is presented for the kurtosis of the distributions of instantaneous streamwise velocities over gravel beds, but some information is available for distributions over artificially created beds in laboratory flumes. McLean *et al.* (1994) discovered that over two-dimensional fixed dune shapes, the distributions were slightly platykurtic or near normal in kurtosis (values of around 2.5 to 3) close to the bed, and slightly more peaked in the outer regions of the flow (around 3 to 3.5) (more results can be found in McLean *et al.* (1996)). Dittrich *et al.* (1996) found similar values for flows above fixed glass spheres. They found that the values varied from around 7.25 to 2.75 close to the bed, and the distributions were roughly normal in kurtosis for the rest of the flow. The later values were also similar to those reported by Durst *et al.* (1987) over a smooth surface, in which the kurtosis values for the distributions of instantaneous streamwise velocity varied from around 6 to 2.3 close to the bed and 3 to 2.3 further into the flow.

4.2.4 Degree of Normality

The results have shown that the distributions are mostly non-symmetric about the mean, and that $K_{\overline{u}}$ is well departed from a value of three, both of which imply non-normality in the distributions of $\overline{u}$. To confirm this more formally, normal probability plots of the distributions can be produced. This plots the theoretical probability associated with the ordered observation $\overline{u}_i$ from a standard normal distribution against the observed probability for $\overline{u}_i$. This theoretical probability is given by

$$pr(Z \leq z_i) = \frac{i - 3/8}{N + 1/4} \tag{4.4}$$

where $Z \sim N(0,1)$ and z_i is an observation taken from Z. Therefore, if the distribution of $\overline{u}$ is a perfect normal distribution, the observed probabilities should form a straight line on a normal probability plot. An example of this for one of the distributions is shown in Figure 4.4. The distance between the tick marks on the vertical axis matches the distance between the quantiles of a normal distribution. The quantiles are close together near the median (probability = 0.5) and stretch out symmetrically moving away from the median. The plot shows the observed probabilities are approximately a straight line for the majority of the range of $\overline{u}$ values, but the curvature at the high values of $\overline{u}$ indicates that the distribution is positively skewed and is therefore likely to be non-normal.

Although this plot provides a visual means by which to inspect the normality of the distributions, a more rigorous approach is required. This can be provided by undertaking a linear regression between the theoretical and observed probabilities, producing an estimate of the percentage variability in $\overline{u}$ explained by a perfect normal distribution R^2. The R^2 value for the normal probability plot in Figure 4.4 is 0.82, which shows that the linear regression can have a high R^2 value even when the distribution is skewed, because the majority of the plot follows a straight line. The importance of the tails, which can heavily determine the normality of the distribution, can be hidden in such a regression. Therefore a distribution should only be considered to approximately follow a normal distribution when R^2 is very high, say above 0.99.

These R^2 values are shown in Figure 4.3d for the two beds. It can be seen that only one of the distributions of $\overline{u}$ can be considered to be reasonably consistent with a normal distribution. The majority of the remaining distributions display significant departures from a normal distribution.

4.3 Vertical Distribution in the Degree of Spatial Variability

It has been seen that there are differences in $\sigma_{\overline{u}}$ between the distributions over each of the beds. A possible cause of this is the different vertical positions above the bed at

which the measurements of $\overline{u}$ were carried out. To explore this, the vertical plane PIV measurements which were taken normal to the bed surface have been utilised because they contain a greater number of measurement positions above the bed surface than the horizontal plane measurements. The heights of the measurement positions from each of the nine vertical plane measurements were referenced to the maximum bed elevation from the bed topography scan so that they were comparable to the results from the horizontal plane measurements. The relative height of the measurement positions for the nine vertical planes for a given experimental run were near identical (within ± 5 %). This allowed the velocities from each of the nine lateral locations over the bed to be assimilated to produce a matrix of $\overline{u}$ measurements over and above the bed for a given experimental run. This assimilation resulted in a matrix of 549 $\overline{u}$ values being produced over the bed for each vertical measurement position. Given this number, it was deemed appropriate to be able to use the vertical plane measurements to assess $\sigma_{\overline{u}}$. This approach provided a statistically significant number of measurements. For example, in the case of experimental run 6B this led to a total of 19215 $\overline{u}$ values being analysed, far more than could ever be produced using a point velocimeter, such as an ADV. The $\sigma_{\overline{u}}$ values were calculated using equation (4.1), with $\langle\overline{u}\rangle$ at a given height above the bed being taken as the double-averaged streamwise velocity for the assimilated matrix of streamwise velocities at that height.

The vertical variation in $\sigma_{\overline{u}}$ in both absolute and non-dimensional forms is given in Figure 4.5. This includes values from 20 of the 22 experimental runs. Experimental runs 1U and 1B are not shown because they only contained a small number of measurements above the bed, statistically too small to represent clearly the vertical profile of $\sigma_{\overline{u}}$. The vertical variation in $\sigma_{\overline{u}}$ in all of its forms is plotted against both z/d and z/D_{84}. This is to discover whether, respectively, spatial variability is controlled by flow features that scale with flow depth, or by flow structures that are scaled by bed roughness. The spatial variability in the time-averaged flow field has been entirely associated with the effects of boundary on the flow (Gimenez-Curto and Corniero Lera, 1996). The assumption is that it "owes its existence to the presence of forms in the boundary". Indeed in the terms of Nikora *et al.* (2001), $\sigma_{\overline{u}}$ would be called the absolute form-induced intensity. It could therefore be assumed that the spatial variability would be scaled by bed roughness. It will be interesting to discover whether $\sigma_{\overline{u}}$ becomes

negligible above the form-induced layer, at a distance where the form of the bed is assumed not to induce spatial variability.

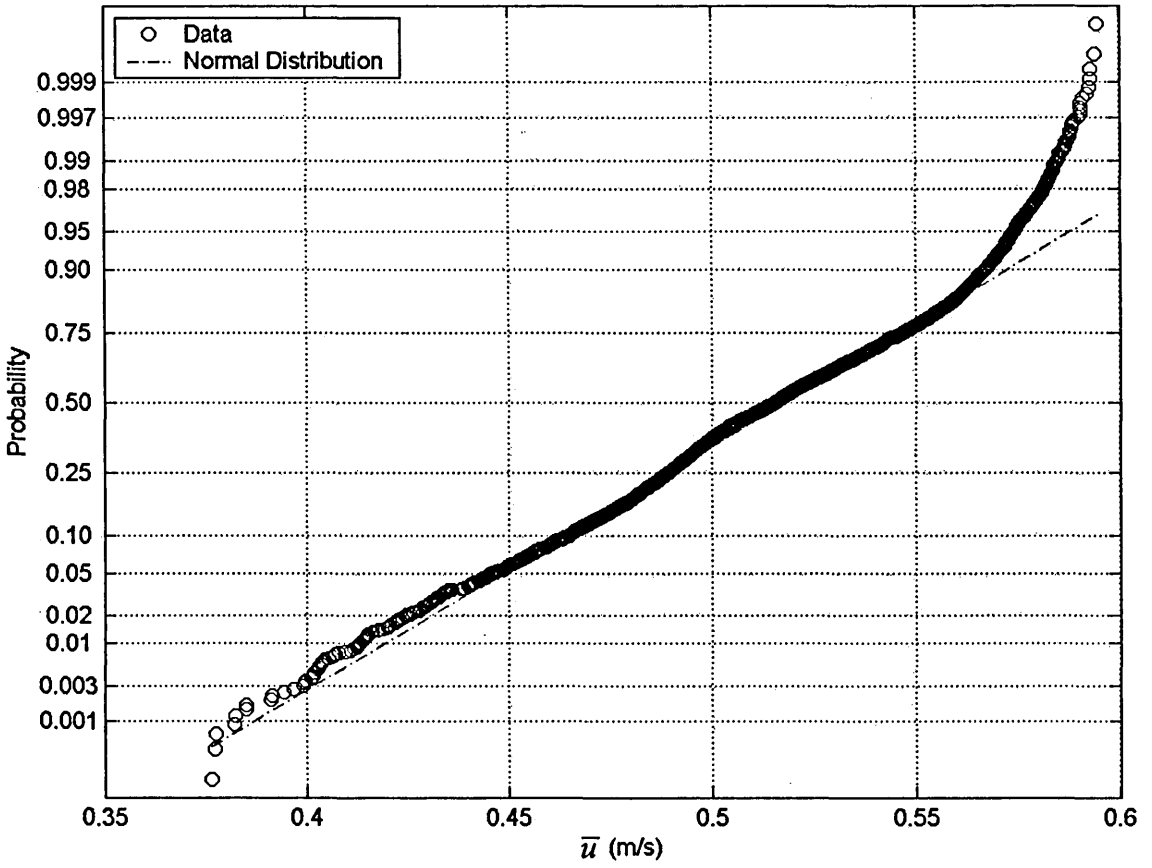

Figure 4.4. An example of a normal-probability plot to test the normality of a distribution of $\overline{u}$ over the bed, in which the theoretical probability associated with the ordered observation $\overline{u}_i$ from a standard normal distribution is plotted against the observed probability for $\overline{u}_i$, where $\overline{u}$ is the time-averaged streamwise velocity.

The vertical variability in $\sigma_{\overline{u}}/u_*$ and $\sigma_{\overline{u}}/\langle\overline{u}\rangle$ is examined to discover whether the variability in $\sigma_{\overline{u}}$ values seen in Figure 4.3a can be accounted for by differences in $\langle\overline{u}\rangle$ or u_*, where u_* is the bed shear velocity given by $u_* = (\tau_0/\rho)^{0.5}$, where τ_0 is the mean bed shear stress, which is defined in equation (3.5) in Chapter 3. The $\sigma_{\overline{u}}$ values in Figure 4.5a and b are very similar to those presented in Figure 4.3a, indicating that it is possible to use the nine vertical plane measurements to assess the degree of spatial variability in $\overline{u}$. Given that the change from measuring in a horizontal plane to a

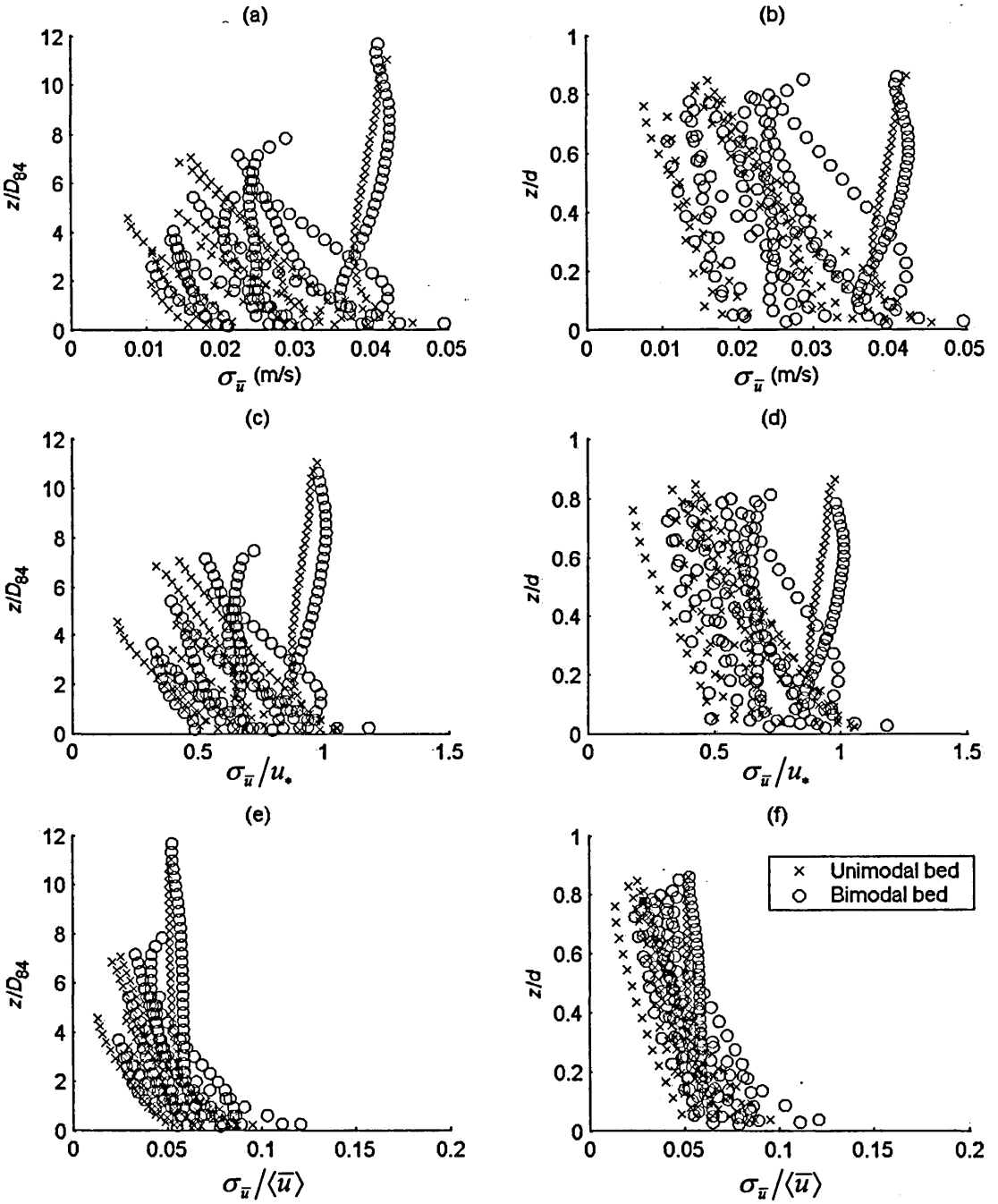

Figure 4.5. Vertical variability in the degree of spatial variability in $\overline{u}$ over the bed, $\sigma_{\overline{u}}$ with (a) z/D_{84} ; (b) z/d, the vertical variability in $\sigma_{\overline{u}}/u_*$ with (c) z/D_{84} ; (d) z/d, and the vertical variability in $\sigma_{\overline{u}}/\langle\overline{u}\rangle$ with (e) z/D_{84} ; and (f) z/d, where $\overline{u}$ is the time-averaged streamwise velocity, z is the height above the maximum bed elevation and d is flow depth, D_{84} is the grain size at which 84 per cent of the bed material is finer, and u_* is the bed shear velocity and $\langle\overline{u}\rangle$ is the double-averaged streamwise velocity.

vertical plane involved a complete rearrangement of equipment, including realignment of the camera and laser and the matching of measurement areas, it suggests that this was carried out accurately. The plots in Figure 4.5a and b reveal that the spatial variability in $\overline{u}$ is not negligible above the form-induced layer (see Tables 3.13 and 3.14), as previously assumed. In some cases it can remain large all the way up to the water surface. This suggests that either the bed has a direct influence further up into the flow than many assume, or that the spatial variability is not entirely induced by the surface topography of the bed. The general decrease in the degree of spatial variability with height above the bed surface suggests that it is not entirely disassociated with the effect of the bed. The influence of bed roughness is diminishing with distance away from the bed.

The difference in u_* between the experimental runs appears to account for some of the spread in the $\sigma_{\overline{u}}$ values between the experimental runs (Figures 4.5c and d), but a good degree of spread still remains. There are no $\sigma_{\overline{u}}/u_*$ values within the literature to compare these values to. A comparison to turbulence intensities, σ_u/u_* for flows over gravel surfaces (e.g. Kironoto and Graf, 1994; Nikora and Smart, 1997; Nikora and Goring, 2000, Papanicolaou and Hilldale, 2002; Campbell *et al.*, 2005) shows that the degree of spatial variability in the flow field is considerably less than the temporal variability. As was found with the absolute turbulence intensities, the higher values of $\sigma_{\overline{u}}/u_*$ that are found mainly close to the bed are only comparable to its temporal equivalent measured in the outer layer of the flow by these studies. Therefore the spatial variations in $\overline{u}$ are likely to induce lower degrees of momentum transfer between the fluid and the bed than those caused by turbulent fluctuations in u.

The difference in $\sigma_{\overline{u}}$ between the experimental runs is at its smallest when non-dimensionalised by $\langle\overline{u}\rangle$. In addition, the vertical profile shapes become more consistent. It suggests that $\sigma_{\overline{u}}$ can be scaled by $\langle\overline{u}\rangle$ in order to describe the vertical variation of $\sigma_{\overline{u}}$. The values of $\sigma_{\overline{u}}/\langle\overline{u}\rangle$ can therefore be used to assess whether $\sigma_{\overline{u}}$ is scaled by bed roughness or flow depth. Close to the bed, the difference in $\sigma_{\overline{u}}/\langle\overline{u}\rangle$ values between the experimental runs is nearly equal when plotted against z/d and z/D_{84}. However, higher up into the flow, $\sigma_{\overline{u}}$ appears to be better scaled by flow depth,

as might be expected. Variability in $\sigma_{\bar{u}}/\langle\bar{u}\rangle$ does however remain between the experimental runs, and the cause of this needs to be established.

The $\sigma_{\bar{u}}/\langle\bar{u}\rangle$ values in Figures 4.5c and d are typically lower than relative turbulence intensities $\sigma_u/\bar{u}$ measured for flows over gravel beds (e.g. Nikora and Smart, 1997; Nikora and Goring, 2000; Lawless and Robert, 2001). The $\sigma_{\bar{u}}/\langle\bar{u}\rangle$ values do however match the turbulence intensity values found by McLelland *et al.* (1999) over a water-worked gravel-sand striped bed and those found by Roy *et al.* (2004) in a gravel-bed river. The comparison with the values of McLelland *et al.* with those from the bimodal bed is interesting, given that a similar grain-size distribution was used. Again the higher values of $\sigma_{\bar{u}}/\langle\bar{u}\rangle$, in general, only compare to the turbulence intensity values measured in the outer layer of the flow.

4.4 Parameterisation of the Degree of Spatial Variability

It will now be explored whether a universal expression for the degree of spatial variability in $\bar{u}$ can be derived. For each individual experimental run over both of the beds, a function of the form

$$\frac{\sigma_{\bar{u}}}{\langle\bar{u}\rangle} = D_{\bar{u}} \exp(-\lambda_{\bar{u}} \frac{z}{d}) \tag{4.5}$$

in which $D_{\bar{u}}$ and $\lambda_{\bar{u}}$ are empirical constants was found to produce an excellent prediction of $\sigma_{\bar{u}}/\langle\bar{u}\rangle$ throughout the whole of the flow depth, except for runs 6U ($R^2 = 0.58$), 5B ($R^2 = 0.71$) and 6B ($R^2 = 0.79$). All the other experimental runs had R^2 values greater than 0.90, with more than half of them having $R^2 > 0.99$. Equation (4.5) is of the form used for describing the vertical variation in turbulence intensity, indicating that there is a similarity in the manner in which both variables decrease with z/d. There was considerable variability in the values of the empirical constants in equation (4.5) between the experimental runs; $D_{\bar{u}}$ ranged from 0.055 to 0.12, and $\lambda_{\bar{u}}$ ranged from 0.31 to 1.88. This is in contrast to that found for turbulence intensities, where the values have found to be more constant for different bed roughness and flow conditions. For example, it has been found that $D_u = 2.30$ and $\lambda_u = 1.00$ provide a

good approximation for flows over smooth beds (Nezu and Rodi, 1986; Nezu and Nakagawa, 1993), and $D_u = 2.04$ and $\lambda_u = 0.97$ for flows over both fixed and mobile gravel beds (Kironoto and Graf, 1994; Song *et al.*, 1994). But Carling *et al.* (2002) found that D_u can vary from 1.86 to 2.31 and λ_u from 0.23 to 2.4 in a compound gravel-bed channel.

The $D_{\overline{u}}$ and $\lambda_{\overline{u}}$ values were not related to d/D_{84}, S, u_*, mean cross-sectional streamwise velocity, fluid Reynolds number or Froude number, so it is not possible to approximate these values. Instead, an equation of the form of equation (4.5) has to be applied to the combined data from the two beds, but this produces a poor approximation, $R^2 = 0.36$, or $R^2 = 0.59$ if runs 6U, 5B and 6B are omitted from the regression. It does not appear that a universal expression can be developed for $\sigma_{\overline{u}}/\langle\overline{u}\rangle$.

4.5 Variability in the Degree of Spatial Variability with Relative Submergence

A possible cause of the spread in $\sigma_{\overline{u}}/\langle\overline{u}\rangle$ values in Figures 4.5e and f is the difference in relative submergence between the experimental runs. To discover whether this is the case, the experimental runs carried out at a single bed slope but varying flow depths, and thus different relative submergences were examined (Tables 4.1 and 4.2). To allow a fair comparison between the runs for the whole of the flow depth the $\sigma_{\overline{u}}/\langle\overline{u}\rangle$ values from each of the runs are plotted against z/d in Figure 4.6. It is also important to examine the effect of relative submergence on $\sigma_{\overline{u}}$, because it is the absolute spatial variability in the time-averaged flow field that induces momentum transfer, therefore the variation in $\sigma_{\overline{u}}$ is also shown in Figure 4.6. Presenting the values in this way enables an examination of whether relative submergence influences the nature of the vertical variability in $\sigma_{\overline{u}}$ and $\sigma_{\overline{u}}/\langle\overline{u}\rangle$.

4.5.1 Absolute Spatial Variability

For the unimodal bed, $\sigma_{\overline{u}}$ decreases nearly-linearly with z/d for all but experimental run 6U carried out at a relative submergence of 12.9 (Figure 4.6a). It was checked whether this run contained any anomalous $\overline{u}$ values, but this was not the case. There is a clear increase in $\sigma_{\overline{u}}$ at the same z/d with relative submergence, with the difference

remaining constant throughout the flow depth, with the exception of this one run. It means that $\sigma_{\overline{u}}$ more than triples from the lowest to the highest relative submergence at the same z/d for the whole of the flow depth. The profiles appear to be grouped into three, at the low, mid and highest relative submergence. The degree of vertical decrease in $\sigma_{\overline{u}}$ also appears to show an increase with relative submergence for four of the profiles.

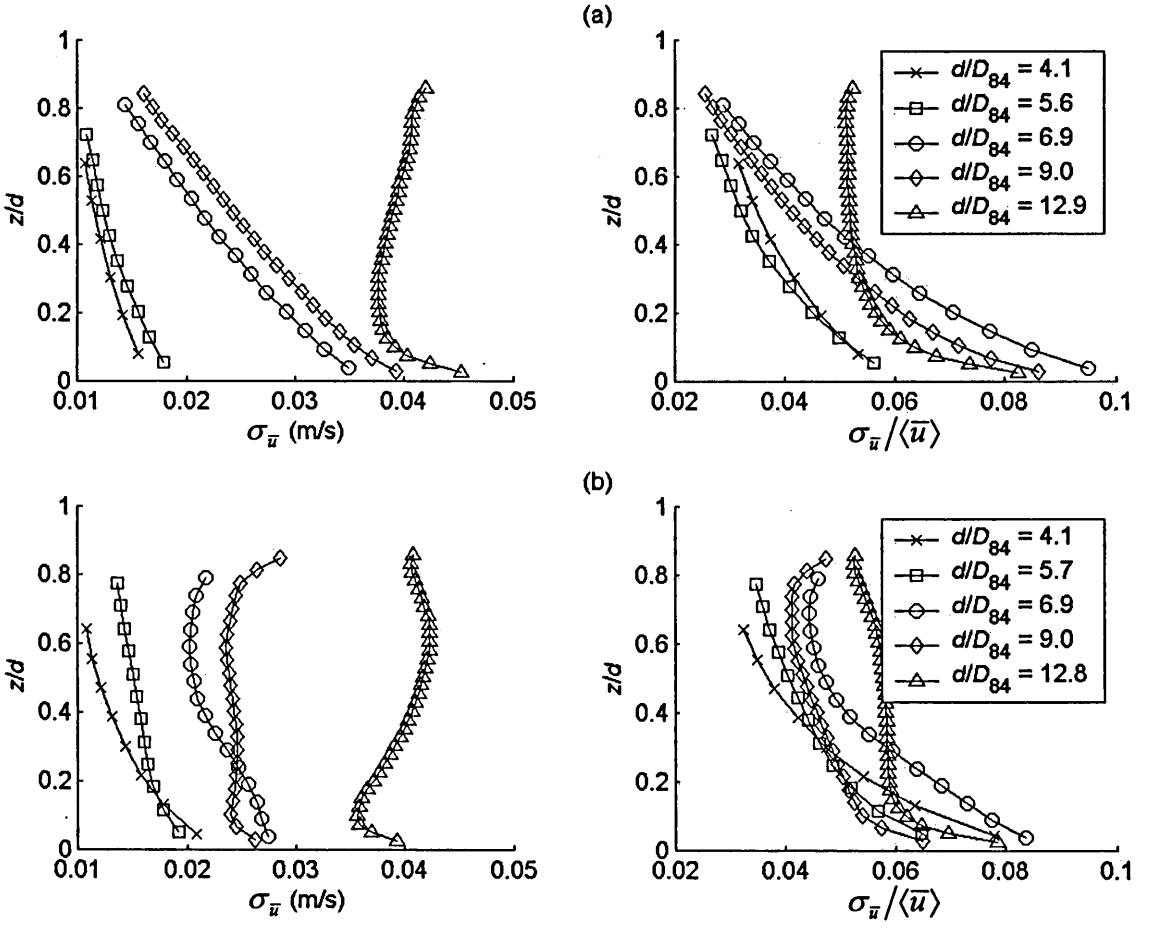

Figure 4.6. Vertical variability in the degree of spatial variability in $\overline{u}$ over the bed, $\sigma_{\overline{u}}$ with z/d and $\sigma_{\overline{u}}/\langle\overline{u}\rangle$ with z/d for the experimental runs carried out at a single bed slope over (a) the unimodal bed; and (b) the bimodal bed, where $\overline{u}$ is the time-averaged streamwise velocity, z is the height above the maximum bed elevation, d is flow depth, $\langle\overline{u}\rangle$ is the double-averaged streamwise velocity and D_{84} is the grain size at which 84 per cent of the bed material is finer.

Over the bimodal bed, $\sigma_{\bar{u}}$ also increases with relative submergence. This can result in similar degrees of increase in $\sigma_{\bar{u}}$ as seen over the unimodal bed. However, the nature of the vertical change in $\sigma_{\bar{u}}$ means that the size of this increase changes through the flow depth, with the difference in $\sigma_{\bar{u}}$ values between the experimental runs being at its lowest closest to the bed. There is a progressive increase in the curvature of the profiles with relative submergence. At the two lowest submergences, $\sigma_{\bar{u}}$ decreases in a near-linear manner with z/d as seen over the unimodal bed, but for the run carried out at a relative submergence of 6.9, the profile displays some curvature in the upper two-thirds of the flow. The runs at a relative submergence of 9.0 and 12.9 both have an inflection point at around 20 % up into the flow and display further inflections at two-thirds into the flow. The result is that $\sigma_{\bar{u}}$ is not at its greatest closest to the bed for these two runs. These two profiles show that the nature of the vertical variation in $\sigma_{\bar{u}}$ at a relative submergence of 12.9 over the unimodal bed is not such an anomalous result as first thought. The degree of decrease in $\sigma_{\bar{u}}$ with z/d appears to decrease with increasing relative submergence, the opposite of that seen over the unimodal bed. However, the profiles do display a similar grouping with relative submergence.

Table 4.1. Summary of the experimental conditions for the experimental runs carried out at a single bed slope over the unimodal bed, where S is the bed slope, d is the flow depth, D_{84} is the grain size at which 84 per cent of the bed material is finer, $\overline{U}$ is the average flow velocity (calculated from the ratio of flow discharge to the cross-sectional area of the flow), τ_0 is the bed shear stress and Fr is the Froude number (calculated from $\overline{U}/\sqrt{gd}$, where g is the force due to gravitational attraction).

Run	S	d (mm)	d/D_{84}	$\overline{U}$ (m^2/s)	τ_0 (N/m^2)	Fr
1U	0.00285	18.1	2.6	0.18	0.47.	0.42
2U	0.00285	28.6	4.1	0.27	0.72	0.51
3U	0.00285	39.5	5.6	0.32	0.95	0.52
4U	0.00285	48.4	6.9	0.36	1.13	0.52
5U	0.00285	62.8	9.0	0.45	1.40	0.57
6U	0.00285	90	12.9	0.62	1.85	0.66

Table 4.2. Summary of the experimental conditions for the experimental runs carried out at a single bed slope over the bimodal bed, where S is the bed slope, d is the flow depth, D_{84} is the grain size at which 84 per cent of the bed material is finer, $\overline{U}$ is the average flow velocity (calculated from the ratio of flow discharge to the cross-sectional area of the flow), τ_0 is the bed shear stress and Fr is the Froude number (calculated from $\overline{U}/\sqrt{gd}$, where g is the force due to gravitational attraction).

Run	S	d (mm)	d/D_{84}	$\overline{U}$ (m^2/s)	τ_0 (N/m^2)	Fr
1B	0.00284	17.3	2.6	0.16	0.45	0.40
2B	0.00284	27.2	4.1	0.20	0.68	0.39
3B	0.00284	37.3	5.7	0.28	0.90	0.47
4B	0.00284	45.5	6.9	0.36	1.07	0.53
5B	0.00284	59.5	9.0	0.43	1.34	0.56
6B	0.00284	84.5	12.8	0.58	1.76	0.64

Clifford (1996) examined how the turbulent properties of flows over riffle-pool sequences in a gravel-bed river changed with flow stage. He found that $\overline{u}$ varied more within a riffle or pool at the highest flow, which is accordance to that seen in Figure 4.6. He also discovered that the absolute turbulence intensity, σ_u became significantly larger at the higher stages. His results suggest that either the spatial variability or temporal variability in the time-averaged vertical and instantaneous vertical velocities, respectively, must decrease with relative submergence, since the total fluid stress is a summation of the Reynolds stress and form-induced stress.

4.5.2 Relative Spatial Variability

Apart from the run carried out a relative submergence of 12.9, the rate of decrease in $\sigma_{\overline{u}}/\langle\overline{u}\rangle$ with z/d increases with relative submergence, as seen for $\sigma_{\overline{u}}$. There does not however appear to be any clear association between $\sigma_{\overline{u}}/\langle\overline{u}\rangle$ and relative submergence at the same values of z/d. But the differences in $\sigma_{\overline{u}}/\langle\overline{u}\rangle$ values become negligible towards the water surface, as the profiles converge. There only remains a grouping of four of the runs into two groups of lower and higher relative submergence, with these

groupings indicating that $\sigma_{\overline{u}}/\langle\overline{u}\rangle$ is generally greater at the higher relative submergences. The degree of decrease in $\sigma_{\overline{u}}/\langle\overline{u}\rangle$ with z/d is also slightly larger at the higher submergences, with the exception of the run carried out at a relative submergence of 12.9.

The profiles of $\sigma_{\overline{u}}/\langle\overline{u}\rangle$ again display more curvature over the bimodal bed than they do over the unimodal bed. They also show that $\sigma_{\overline{u}}/\langle\overline{u}\rangle$ decreases with z/d, but not to such an extent. Neither the rate of decrease in $\sigma_{\overline{u}}/\langle\overline{u}\rangle$ with z/d nor the values of $\sigma_{\overline{u}}/\langle\overline{u}\rangle$ at the same z/d have any consistent association with relative submergence, but $\sigma_{\overline{u}}/\langle\overline{u}\rangle$ is typically slightly greater at the higher relative submergence. This also applies to the degree of curvature in the profiles.

4.6 Variability in the Degree of Spatial Variability with Bed Slope

The experimental runs performed at the same relative submergence are now analysed in order to discover whether bed slope also has on effect on the vertical pattern of spatial variability in $\overline{u}$ (Figures 4.7 and 4.8). For each bed, there are four relative submergences at which experimental runs have the same submergence (Tables 4.3 and 4.4). These runs were created through manipulating combinations of flow discharges and bed slopes.

4.6.1 Absolute Spatial Variability

Over the unimodal bed, it can be seen that $\sigma_{\overline{u}}$ again decreases in a near-linear manner with z/d (Figure 4.7). There is no consistent relationship between $\sigma_{\overline{u}}$ at the same z/d and bed slope. Although, it appears that the difference in $\sigma_{\overline{u}}$ between the experimental runs does decrease when the difference in bed slopes between the runs is lower. Indeed, when the difference in slope is at its lowest (Figure 4.7d), the $\sigma_{\overline{u}}$ values are very similar for the majority of the flow depth. Clearly, bed slope must account for some of the variability, but not in a correlated manner. Bed slope does not appear to influence, however, the degree of decrease in $\sigma_{\overline{u}}$ with z/d, nor the shape of the profiles, with all profiles at the same relative submergence displaying near identical rates of vertical

decrease. But there is an increase in this vertical reduction in $\sigma_{\bar{u}}$ with relative submergence between the four plots, as was seen in Figure 4.6.

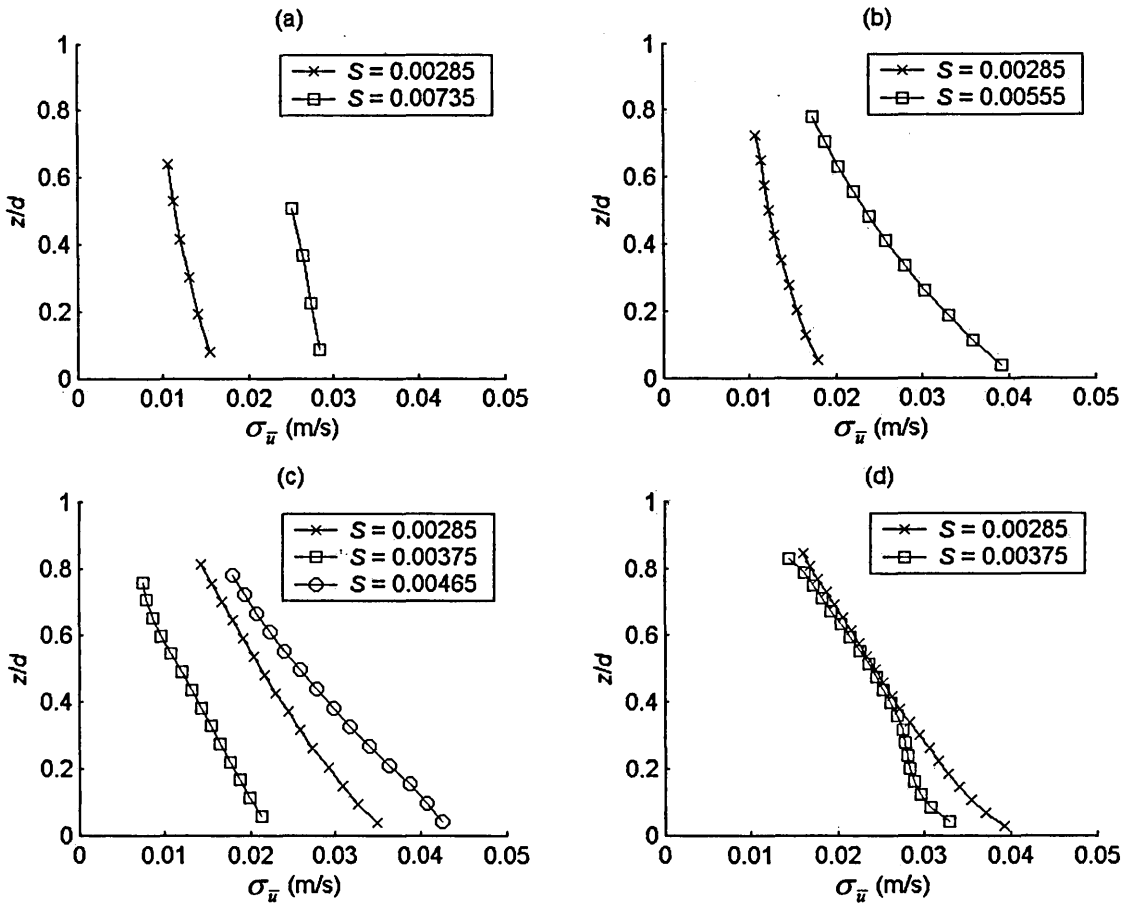

Figure 4.7. Vertical variability in the degree of spatial variability in $\bar{u}$, $\sigma_{\bar{u}}$ over the unimodal bed with z/d for the experimental runs carried out at the same relative submergences (a) $d/D_{84} = 4.1$; (b) $d/D_{84} = 5.6$; (c) $d/D_{84} = 6.9$; and (d) $d/D_{84} = 9.0$, where $\bar{u}$ is the time-averaged streamwise velocity, z is the height above the maximum bed elevation, d is flow depth, D_{84} is the grain size at which 84 per cent of the bed material is finer and S is bed slope.

The vertical profiles also show that $\sigma_{\bar{u}}$ typically decreases with z/d (Figure 4.8), and by similar degrees as seen over the unimodal bed. It is mostly in a near-linear manner, unlike that seen at a single bed slope (Figure 4.6b). The decrease is, in general, greater at the steeper slopes, and the $\sigma_{\bar{u}}$ values at the same z/d also increase with bed slope.

This increase is greatest within the lower reaches of the flow, with differences often being smallest in the outer layer of the flow, as the profiles converge. But bed slope does not appear to have a consistent influence on the degree of variability in $\sigma_{\bar{u}}$ between the experimental runs. The difference in $\sigma_{\bar{u}}$ between runs does not decrease as the difference in bed slopes reduces. However, the degree of curvature in the profiles tends to be greater at the shallower slopes.

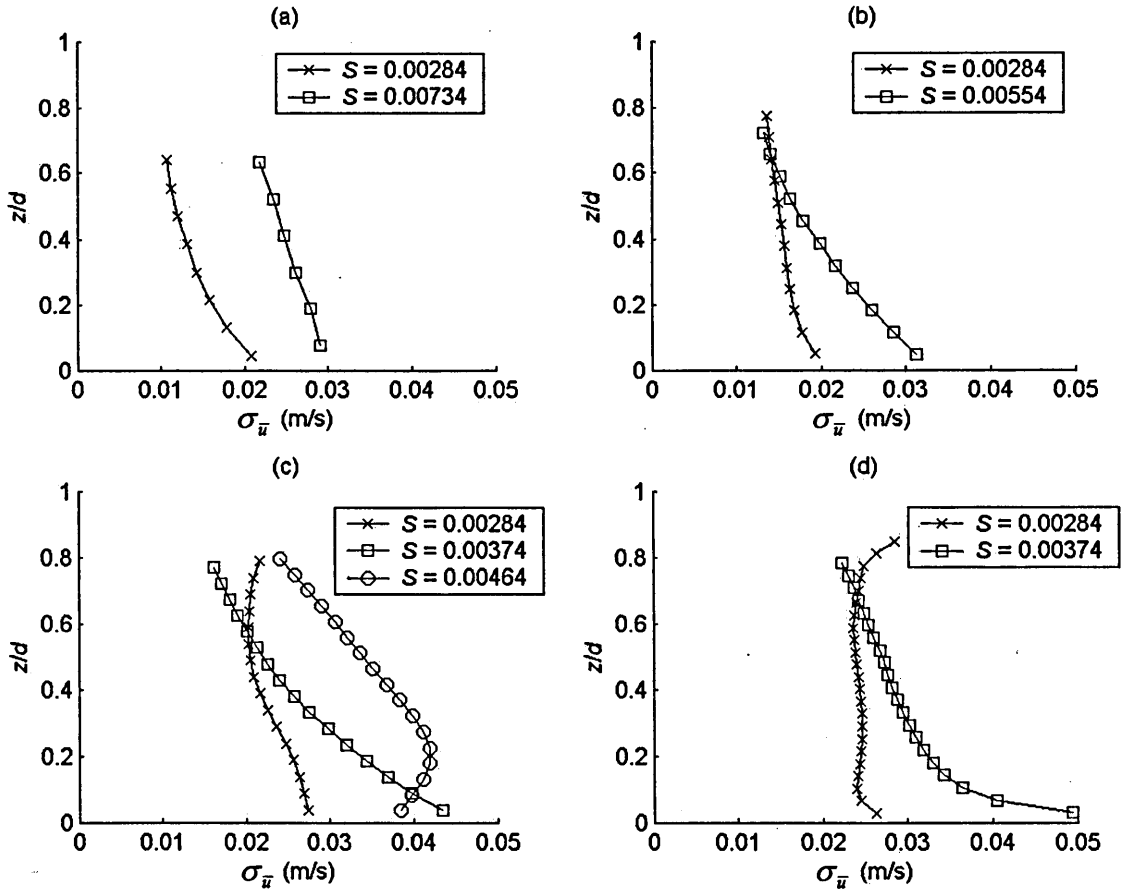

Figure 4.8. Vertical variability in the degree of spatial variability in $\bar{u}$, $\sigma_{\bar{u}}$ over the bimodal bed with z/d for the experimental runs carried out at the same relative submergences (a) $d/D_{84} = 4.1$; (b) $d/D_{84} = 5.7$; (c) $d/D_{84} = 6.9$; and (d) $d/D_{84} = 9.0$, where $\bar{u}$ is the time-averaged streamwise velocity, z is the height above the maximum bed elevation, d is flow depth, D_{84} is the grain size at which 84 per cent of the bed material is finer and S is bed slope.

Table 4.3. Summary of the experimental conditions for the experimental runs carried out at the same relative submergences over the unimodal bed, where S is the bed slope, d is the flow depth, D_{84} is the grain size at which 84 per cent of the bed material is finer, $\overline{U}$ is the average flow velocity (calculated from the ratio of flow discharge to the cross-sectional area of the flow), τ_0 is the bed shear stress and Fr is the Froude number (calculated from $\overline{U}/\sqrt{gd}$, where g is the force due to gravitational attraction).

Run	S	d (mm)	d/D_{84}	$\overline{U}$ (m^2/s)	τ_0 (N/m^2)	Fr
2U	0.00285	28.6	4.1	0.27	0.72	0.51
12U	0.00735	29.5	4.2	0.44	1.90	0.83
3U	0.00285	39.5	5.6	0.32	0.95	0.52
10U	0.00555	39.9	5.7	0.49	1.87	0.78
4U	0.00285	48.4	6.9	0.36	1.13	0.52
8U	0.00375	48.2	6.9	0.47	1.77	0.69
9U	0.00465	49.2	7.0	0.50	1.87	0.72
5U	0.00285	62.8	9.0	0.45	1.40	0.57
7U	0.00375	63.5	9.1	0.51	1.86	0.65

4.6.2 Relative Spatial Variability

The $\sigma_{\overline{u}}/\langle\overline{u}\rangle$ values once again decrease with z/d over the unimodal bed, with all profiles displaying the same profile shape and similar degrees of change with z/d (Figure 4.9). The $\sigma_{\overline{u}}/\langle\overline{u}\rangle$ values at the same z/d do not display any consistent relationship with bed slope, but the variability in values between experimental runs typically decreases as the difference in slope between the runs reduces from one plot to another.

Over the bimodal bed, this also appears to be the case (Figure 4.10), further indicating that bed slope must account for some of the variability in $\sigma_{\overline{u}}/\langle\overline{u}\rangle$ between the experimental runs, but not through any strong correlation. The shape of the vertical profiles is variable between the experimental runs, unlike over the bimodal bed. The

curvature in these profiles tends to decrease with increasing bed slope, meaning that the decrease in $\sigma_{\overline{u}}/\langle\overline{u}\rangle$ with z/d is typically greater at the steeper slopes.

Table 4.4. Summary of the experimental conditions for the experimental runs carried out at the same relative submergences over the bimodal bed, where S is the bed slope, d is the flow depth, D_{84} is the grain size at which 84 per cent of the bed material is finer, $\overline{U}$ is the average flow velocity (calculated from the ratio of flow discharge to the cross-sectional area of the flow), τ_0 is the bed shear stress and Fr is the Froude number (calculated from $\overline{U}/\sqrt{gd}$, where g is the force due to gravitational attraction).

Run	S	d (mm)	d/D_{84}	$\overline{U}$ (m^2/s)	τ_0 (N/m^2)	Fr
2B	0.00284	27.2	4.1	0.20	0.68	0.39
12B	0.00734	26.8	4.1	0.27	1.74	0.52
3B	0.00284	37.3	5.7	0.28	0.90	0.47
10B	0.00554	37.1	5.6	0.39	1.75	0.65
4B	0.00284	45.5	6.9	0.36	1.07	0.53
8B	0.00374	46.6	7.1	0.40	1.71	0.60
9B	0.00464	47.2	7.2	0.47	1.80	0.69
5B	0.00284	59.5	9.0	0.43	1.34	0.56
7B	0.00374	59.4	9.0	0.47	1.76	0.62

4.7 Variability in the Degree of Spatial Variability Under Conditions of Constant Bed Shear Stress

The experimental runs that were carried out at the same mean bed shear stress (Tables 4.5 and 4.6) are now assessed for each bed. These experimental runs involved using a combination of bed slopes and flow depths, and therefore encompass the effects of both relative submergence and bed slope. It means that an assessment can be made of which of these two variables has the primary influence on the degree of spatial variability in $\overline{u}$ by examining which of the effects of the variables, established from above, is evident. Under these conditions of constant mean bed shear stress the implication is that the average rate of momentum transfer at the bed is approximately the same for each of the

experimental runs. Therefore, if the degree of spatial variability in $\overline{u}$ changes under these conditions, it implies that the distribution of $\overline{u}$ over the bed is different. It suggests that the momentum transfer mechanisms might be different between the experimental runs even when the average rate of transfer at the bed is the same. The variable that is the primary cause of these changes can then be inferred.

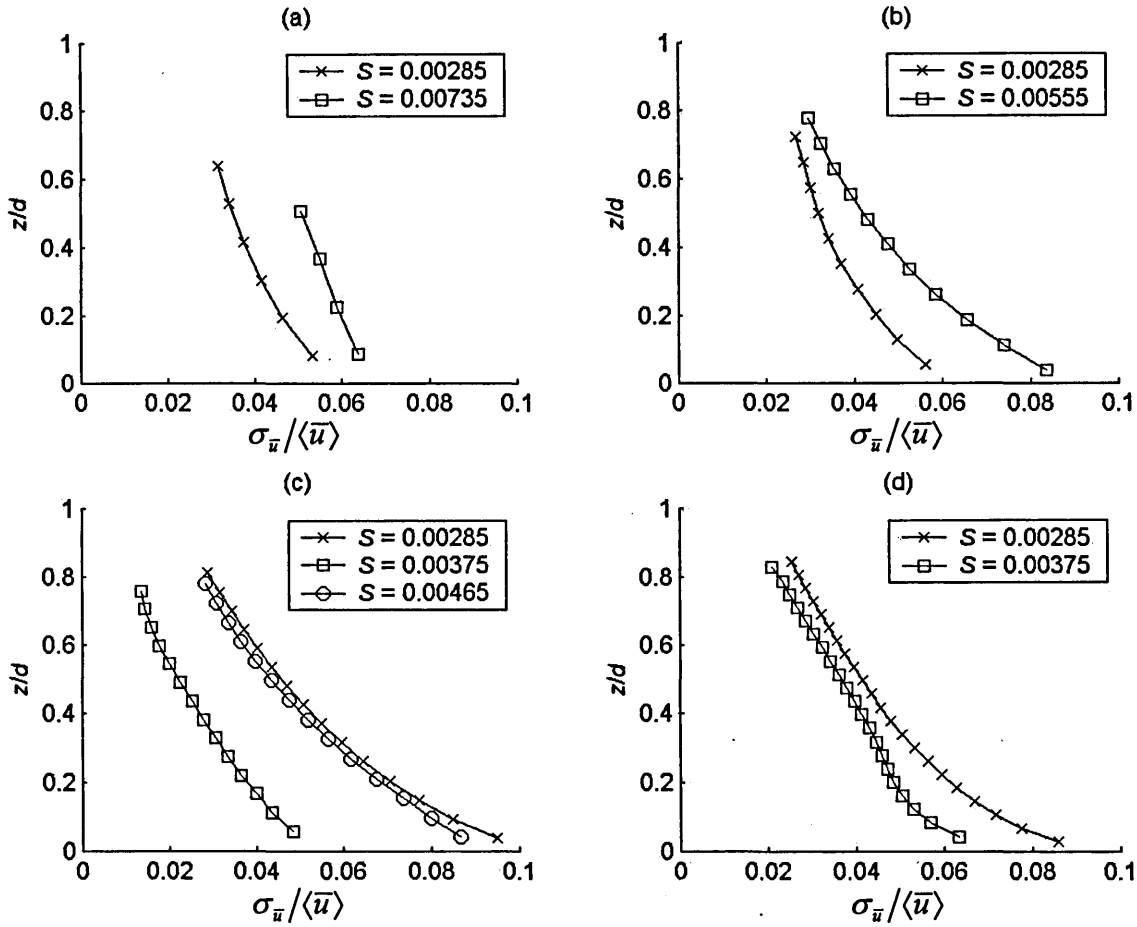

Figure 4.9. Vertical variability in $\sigma_{\overline{u}}/\langle\overline{u}\rangle$ over the unimodal bed with z/d for the experimental runs carried out at the same relative submergences (a) $d/D_{84} = 4.1$; (b) $d/D_{84} = 5.6$; (c) $d/D_{84} = 6.9$; and (d) $d/D_{84} = 9.0$, where $\sigma_{\overline{u}}$ is the degree of spatial variability in $\overline{u}$, $\overline{u}$ is the time-averaged streamwise velocity, $\langle\overline{u}\rangle$ is the double-averaged streamwise velocity, z is the height above the maximum bed elevation, d is flow depth, D_{84} is the grain size at which 84 per cent of the bed material is finer and S is bed slope.

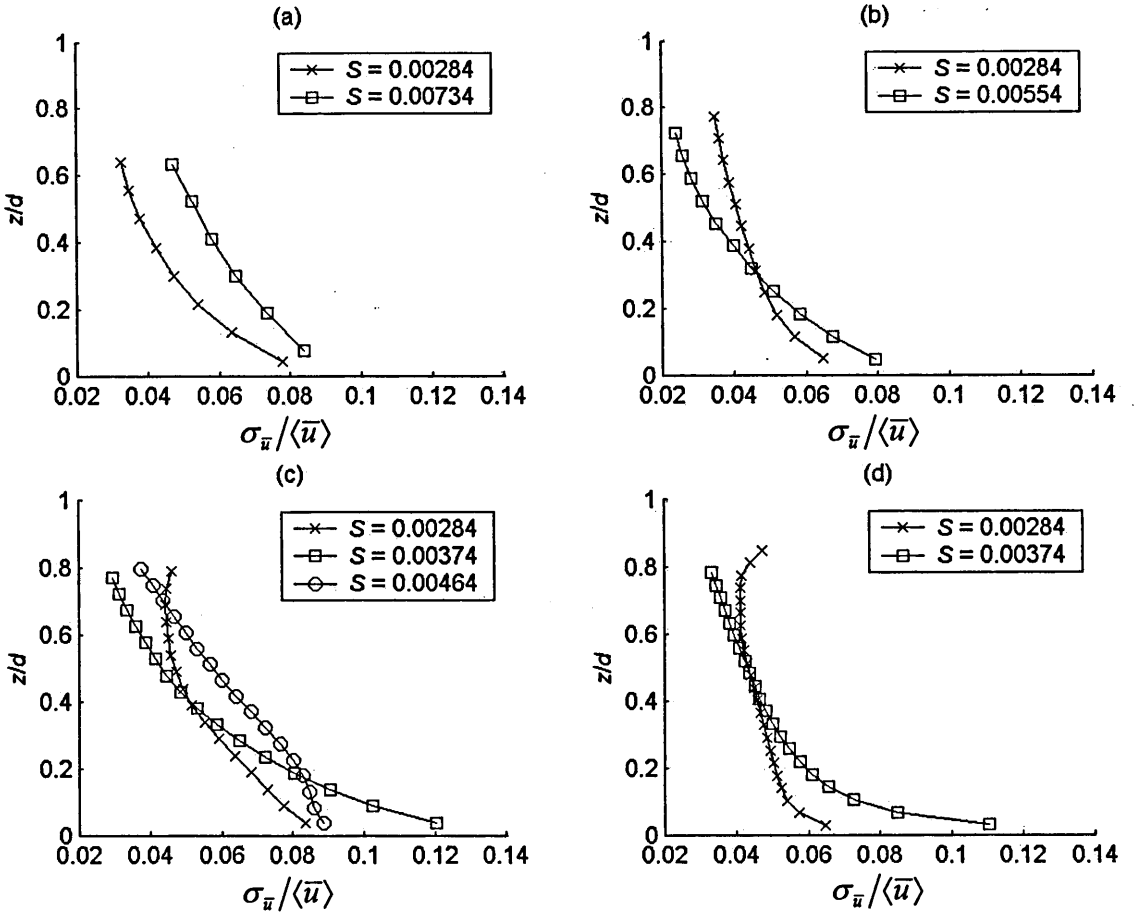

Figure 4.10. Vertical variability in $\sigma_{\bar{u}}/\langle\bar{u}\rangle$ over the bimodal bed with z/d for the experimental runs carried out at the same relative submergences (a) $d/D_{84} = 4.1$; (b) $d/D_{84} = 5.7$; (c) $d/D_{84} = 6.9$; and (d) $d/D_{84} = 9.0$, where $\sigma_{\bar{u}}$ is the degree of spatial variability in $\bar{u}$, $\bar{u}$ is the time-averaged streamwise velocity, $\langle\bar{u}\rangle$ is the double-averaged streamwise velocity, z is the height above the maximum bed elevation, d is flow depth, D_{84} is the grain size at which 84 per cent of the bed material is finer and S is bed slope.

4.7.1 Absolute Spatial Variability

The vertical variation in $\sigma_{\bar{u}}$ under these conditions of constant mean bed shear stress is examined in Figure 4.11 for both beds. The nature of this variation will not be described, because these plots contain the experimental runs that have been previously examined. Over the unimodal bed, it can be seen that the variation in $\sigma_{\bar{u}}$ values

between experimental runs is much lower than that seen previously. This is because u_* is approximately the same for each run, and u_* was established to account for some this variability from the results in Figures 4.5d. Apart from the experimental run carried out at a relative submergence of 12.9 and a bed slope of 0.00285, the profiles of $\sigma_{\bar{u}}$ converge within the upper reaches of the flow, resulting in the difference in $\sigma_{\bar{u}}$ becoming negligible. The grouping of the profiles according to lower and upper relative submergences is not evident as it was at a single bed slope. Indeed, $\sigma_{\bar{u}}$ displays no consistent relationship with relative submergence and therefore bed slope. It is likely that the positive relationship observed with relative submergence at a single bed slope was counteracted by the disassociation with bed slope discovered for the experimental runs performed at the same relative submergence. With the exception of one experimental run, the degree of decrease in $\sigma_{\bar{u}}$ with z/d in Figure 4.11 does however appear to increase with relative submergence, and decrease with bed slope. This was also found for the experimental runs carried out at single bed slope, but not at the same relative submergence. This would suggest that this decrease is likely to be primarily influenced by relative submergence rather than bed slope.

Table 4.5. Summary of the experimental conditions for the experimental runs carried out at the same mean bed shear stress over the unimodal bed, where S is the bed slope, d is the flow depth, D_{84} is the grain size at which 84 per cent of the bed material is finer, $\overline{U}$ is the average flow velocity (calculated from the ratio of flow discharge to the cross-sectional area of the flow), τ_0 is the bed shear stress and Fr is the Froude number (calculated from $\overline{U}/\sqrt{gd}$, where g is the force due to gravitational attraction).

Run	S	d (mm)	d/D_{84}	$\overline{U}$ (m^2/s)	τ_0 (N/m^2)	Fr
6U	0.00285	90.0	12.9	0.62	1.85	0.66
8U	0.00375	63.5	9.1	0.51	1.86	0.65
9U	0.00465	49.2	7.0	0.50	1.87	0.72
10U	0.00555	39.9	5.7	0.49	1.87	0.78
11U	0.00645	33.5	4.8	0.413	1.87	0.72
12U	0.00735	29.5	4.2	0.44	1.90	0.83

Table 4.6. Summary of the experimental conditions for the experimental runs carried out at the same mean bed shear stress over the bimodal bed, where S is the bed slope, d is the flow depth, D_{84} is the grain size at which 84 per cent of the bed material is finer, $\overline{U}$ is the average flow velocity (calculated from the ratio of flow discharge to the cross-sectional area of the flow), τ_0 is the bed shear stress and Fr is the Froude number (calculated from $\overline{U}/\sqrt{gd}$, where g is the force due to gravitational attraction).

Run	S	d (mm)	d/D_{84}	$\overline{U}$ (m^2/s)	τ_0 (N/m^2)	Fr
6B	0.00284	84.5	12.8	0.58	1.76	0.64
8B	0.00374	59.4	9.0	0.47	1.76	0.62
9B	0.00464	47.2	7.2	0.47	1.80	0.69
10B	0.00554	37.1	5.6	0.39	1.75	0.65
11B	0.00644	31.7	4.8	0.35	1.77	0.62
12B	0.00734	26.8	4.1	0.27	1.74	0.52

Over the bimodal bed, the variability in $\sigma_{\overline{u}}$ between the experimental runs is much greater, although there is some evidence of the differences decreasing towards the outer layer of the flow. This variability is not consistently related to relative submergence and bed slope. This is likely to be because of the positive relationships that were observed earlier with relative submergence and bed slope, which oppose each other under these conditions of constant mean bed shear stress. The degree of decrease in $\sigma_{\overline{u}}$ with z/d is typically greater at the higher relative submergences and shallower slopes, as seen over the unimodal bed. This is the reverse to that observed at a single bed slope and for those experimental runs performed at the same relative submergences. The degree of curvature in the profiles also increases with relative submergence, and decreases with bed slope in Figure 4.11. This corresponds with what was observed earlier, but it is not possible to distinguish whether relative submergence or bed slope has the primary influence on the shape of the profiles.

The variability in $\sigma_{\overline{u}}$ between the experimental runs over the two beds further confirms that $\sigma_{\overline{u}}$ is not fully scaled by u_*. Instead at the same mean bed shear stress, different degrees of spatial variability in $\overline{u}$ are observed over both beds. It suggests that, if the

magnitudes of the spatial variations are sufficient to produce form-induced stresses over the bed that transfer momentum within the flow, the momentum transfer mechanisms might be different even when the average rate of transfer at the bed is the same.

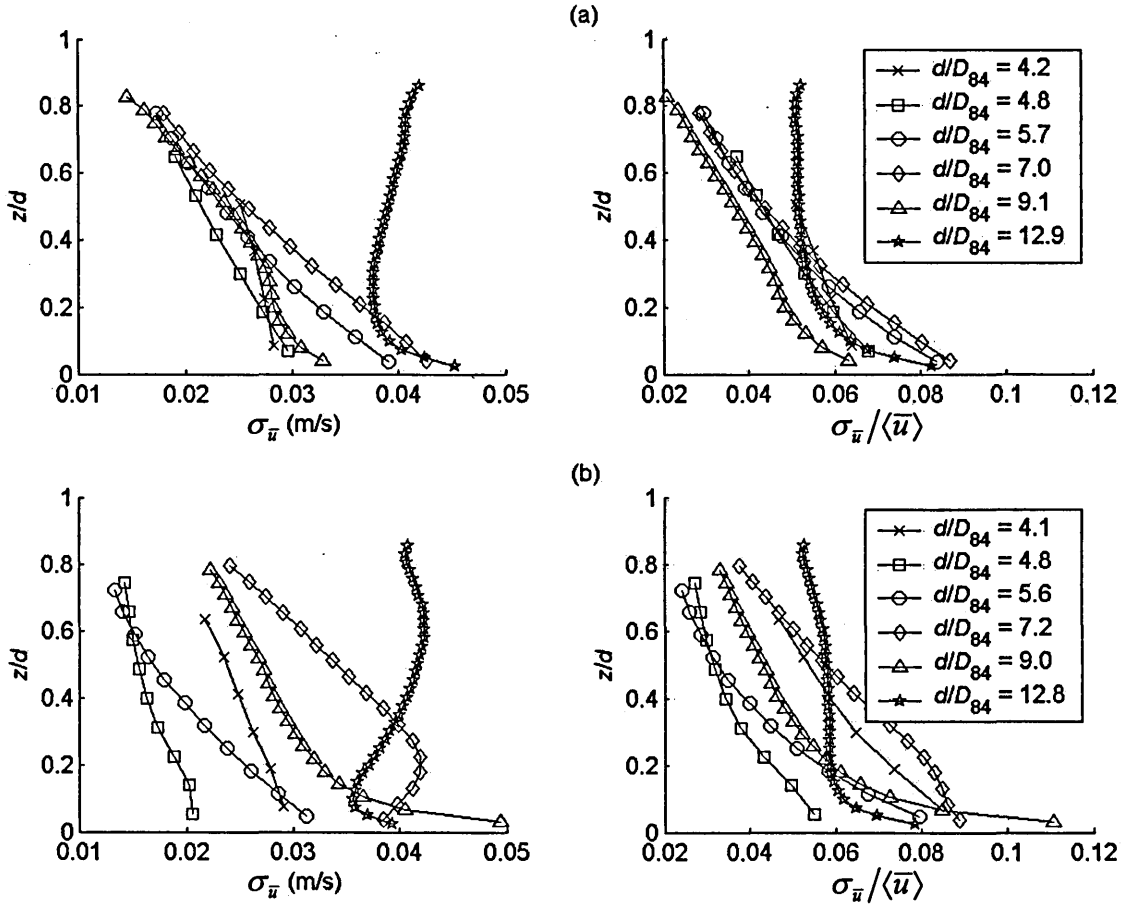

Figure 4.11. Vertical variability in the degree of spatial variability in $\overline{u}$ over the bed, $\sigma_{\overline{u}}$ with z/d and $\sigma_{\overline{u}}/\langle\overline{u}\rangle$ with z/d for the experimental runs carried out at the same mean bed shear stress over (a) the unimodal bed; and (b) the bimodal bed, where $\overline{u}$ is the time-averaged streamwise velocity, z is the height above the maximum bed elevation, d is flow depth, $\langle\overline{u}\rangle$ is the double-averaged streamwise velocity and D_{84} is the grain size at which 84 per cent of the bed material is finer.

4.7.2 Relative Spatial Variability

Over the unimodal bed, $\sigma_{\overline{u}}/\langle\overline{u}\rangle$ at the same z/d is not associated with relative submergence and bed slope in any consistent manner. This was also observed at a single bed slope and for the experimental runs carried out at the same relative submergences.

But the degree of decrease in $\sigma_{\bar{u}}/\langle\bar{u}\rangle$ with z/d, with the exception of the experimental run carried out at a relative submergence of 12.9 and a bed slope of 0.00285, does increase with relative submergence, and therefore reduce with bed slope. This relationship with relative submergence was also observed at a single bed slope, but no such association with bed slope was seen at the same relative submergence. It therefore suggests that the rate of decrease in $\sigma_{\bar{u}}/\langle\bar{u}\rangle$ with z/d is mostly likely to be primarily influenced by relative submergence rather than bed slope.

However, over the bimodal bed the degree of decrease, with the exception of the experimental run carried out at a relative submergence of 12.8 and a bed slope of 0.00284, is fairly similar for each of the experimental runs. It is likely that the disassociation with relative submergence seen at a single bed slope counteracted the positive relationship with bed slope observed for the experimental runs carried out at the same relative submergences. The curvature in the profiles is also fairly similar, with the exception of that one run. Again, the counteracting relationship between curvature and relative submergence and bed slope may have caused this disassociation under these conditions. In addition, the $\sigma_{\bar{u}}/\langle\bar{u}\rangle$ values in Figure 4.11 are not associated with relative submergence and bed slope, which is consistent with what has been reported earlier. The variation in $\sigma_{\bar{u}}/\langle\bar{u}\rangle$ between the experimental runs is greater than over the unimodal bed. It is also larger than that observed at a single bed slope, providing a reason for why u_* did not fully account for the differences in $\sigma_{\bar{u}}/\langle\bar{u}\rangle$ values in Figure 4.5d.

4.8 Does Relative Submergence or Bed Slope have the Greater Influence on the Degree of Spatial Variability?

Although the experimental runs performed at the same mean bed shear stress provide an indication as to whether relative submergence or bed slope has the primary influence on the degree of spatial variability in $\bar{u}$, a more rigorous approach is required. This can be achieved by carrying out a multiple linear regression between the predictor variables, relative submergence and bed slope, and the response variable $\sigma_{\bar{u}}$,

$$\sigma_{\bar{u}} = \alpha + \beta_1 \frac{d}{D_{84}} + \beta_2 S \tag{4.6}$$

This provides a simple model for estimating $\sigma_{\overline{u}}$ at a given z/d, and for calculating the percentage of the variation in $\sigma_{\overline{u}}$ between experimental runs that is explained by differences in relative submergence and bed slope, given by R^2. Bivariate linear regressions were also carried out between $\sigma_{\overline{u}}$ and relative submergence, $\sigma_{\overline{u}}$ and bed slope. These values were taken from each of the 11 experimental runs over the two beds, but for measurement heights high into the flow a lower number of experimental runs were involved in the regression. A regression was not carried out unless seven or more runs were available for regression. The R^2 values from these regressions are compared to establish the relative strength of the relationships of the two variables with $\sigma_{\overline{u}}$, and by what degree each variable contributed to the strength of the associations in equation (4.6). It was found that a simple linear regression between $\sigma_{\overline{u}}$ and relative submergence, and between $\sigma_{\overline{u}}$ and bed slope produced higher R^2 values than through any multiplicative transform of the variables (not shown). This multiple and bivaraite linear regression approach was then repeated for $\sigma_{\overline{u}}/\langle\overline{u}\rangle$.

4.8.1 Absolute Spatial Variability

In Figure 4.12 the R^2 values resulting from these bivariate and multiple regressions for $\sigma_{\overline{u}}$ are shown. It can be seen that over both beds, there is no strong correlation between $\sigma_{\overline{u}}$ and bed slope, as proposed earlier. Relative submergence has a stronger relationship with $\sigma_{\overline{u}}$, and its strength clearly increases with z/d. Over the unimodal bed it means that there is only a weak association close to the bed, but in the upper layers of the flow the relationship is quite strong. This is also seen over the bimodal bed. This vertical variation in the R^2 values of the regression between $\sigma_{\overline{u}}$ and relative submergence largely influences the variation in the R^2 values from the multiple regression over each of the beds. Over the unimodal bed, bed slope improves the performance of this later model, especially close to the bed. However, over the bimodal bed, bed slope has less influence on the R^2 values from the multiple regression, although this model does perform reasonably well for all but the lower fifth of the flow. It is clear that relative submergence in addition to bed slope has far more effect on $\sigma_{\overline{u}}$, than bed slope in addition to relative submergence, over each of the beds. It shows that bed slope does have an effect on $\sigma_{\overline{u}}$, but that its effects operate mainly via relative submergence. The

vertical variation in the β values from equation (4.6) with z/d is also shown in Figure 4.12. Over the unimodal bed, the influence of bed slope is fairly constant throughout the flow, indicating that the magnitude of its influence is also fairly constant. Nevertheless, it is more variable over the bimodal bed.

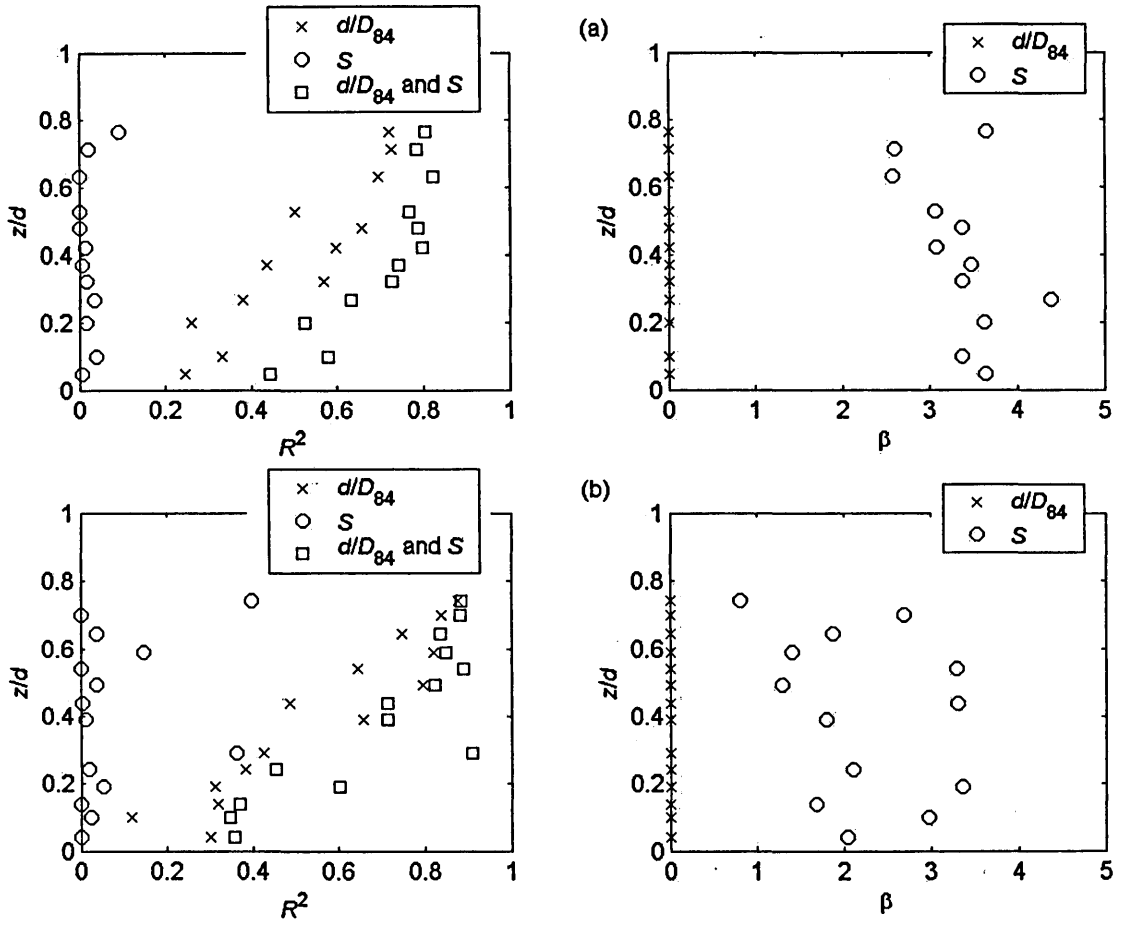

Figure 4.12. Vertical variability in the R^2 of the linear regression between relative submergence d/D_{84} and the degree of spatial variability in $\overline{u}$ over the bed, $\sigma_{\overline{u}}$, in R^2 of the linear regression between bed slope S and $\sigma_{\overline{u}}$, and in the R^2 of the multiple linear regression between predictor variables, relative submergence and bed slope, and response variable $\sigma_{\overline{u}}$, with z/d. Also shown is the vertical variability in the multiplying coefficients of these regressions β with z/d. This is carried out for (a) the unimodal bed; and (b) the bimodal bed, where $\overline{u}$ is the time-averaged streamwise velocity, z is the height above the maximum bed elevation, d is flow depth and D_{84} is the grain size at which 84 per cent of the bed material is finer.

The R^2 values show that the relationship between $\sigma_{\bar{u}}$ and relative submergence is of most importance for estimating $\sigma_{\bar{u}}$. A comparison of this relationship between the two beds for $\sigma_{\bar{u}}$ values performed at the same z/d is shown in Figure 4.13. It shows that there is a near-proportional relationship between $\sigma_{\bar{u}}$ and relative submergence at any given z/d, which implies that there is some association between $\sigma_{\bar{u}}$ and z/D_{84}.

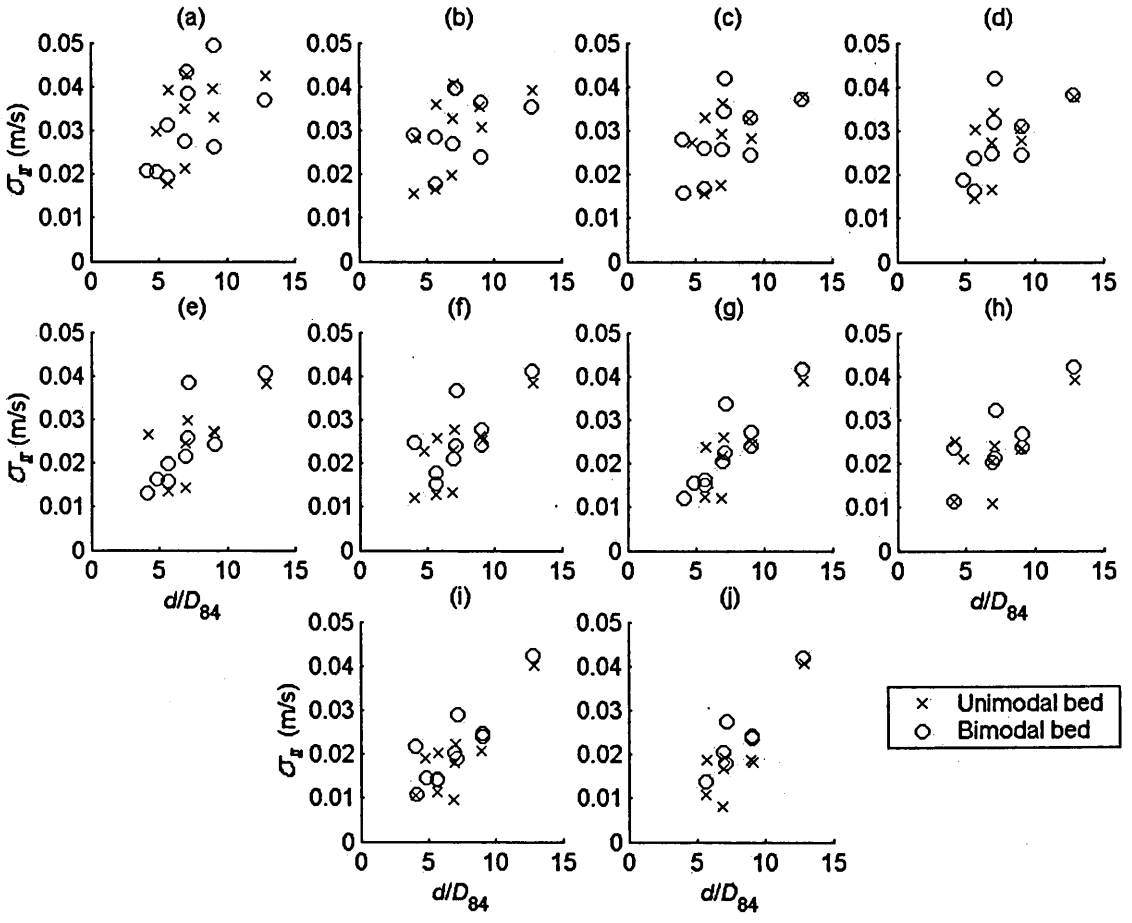

Figure 4.13. The relationship between relative submergence d/D_{84} and the degree of spatial variability in $\bar{u}$ over the bed, $\sigma_{\bar{u}}$ for the two beds at (a) $z/d = 0.044$; (b) $z/d = 0.098$; (c) $z/d = 0.19$; (d) $z/d = 0.25$; (e) $z/d = 0.38$; (f) $z/d = 0.43$; (g) $z/d = 0.49$; (h) $z/d = 0.54$; (i) $z/d = 0.64$; and (j) $z/d = 0.71$, where $\bar{u}$ is the time-averaged streamwise velocity, d is flow depth, z is the height above the maximum bed elevation and D_{84} is the grain size at which 84 per cent of the bed material is finer.

Figure 4.13 also shows that the $\sigma_{\bar{u}}$ values are similar for low and mid relative submergences, but the similarity breaks down at the highest relative submergences, which causes a difference in the gradient of the regression line. This is reflected in the β_1 values for the multiple linear regression for each bed in Figure 4.14. The values are similar over the two beds, and given that the R^2 values for relative submergence were also comparable, it suggests that relative submergence has a very similar effect on $\sigma_{\bar{u}}$ over the two beds. The β_1 values increase with z/d, and this increase matches quite closely the vertical variation in R^2 in Figure 4.12.

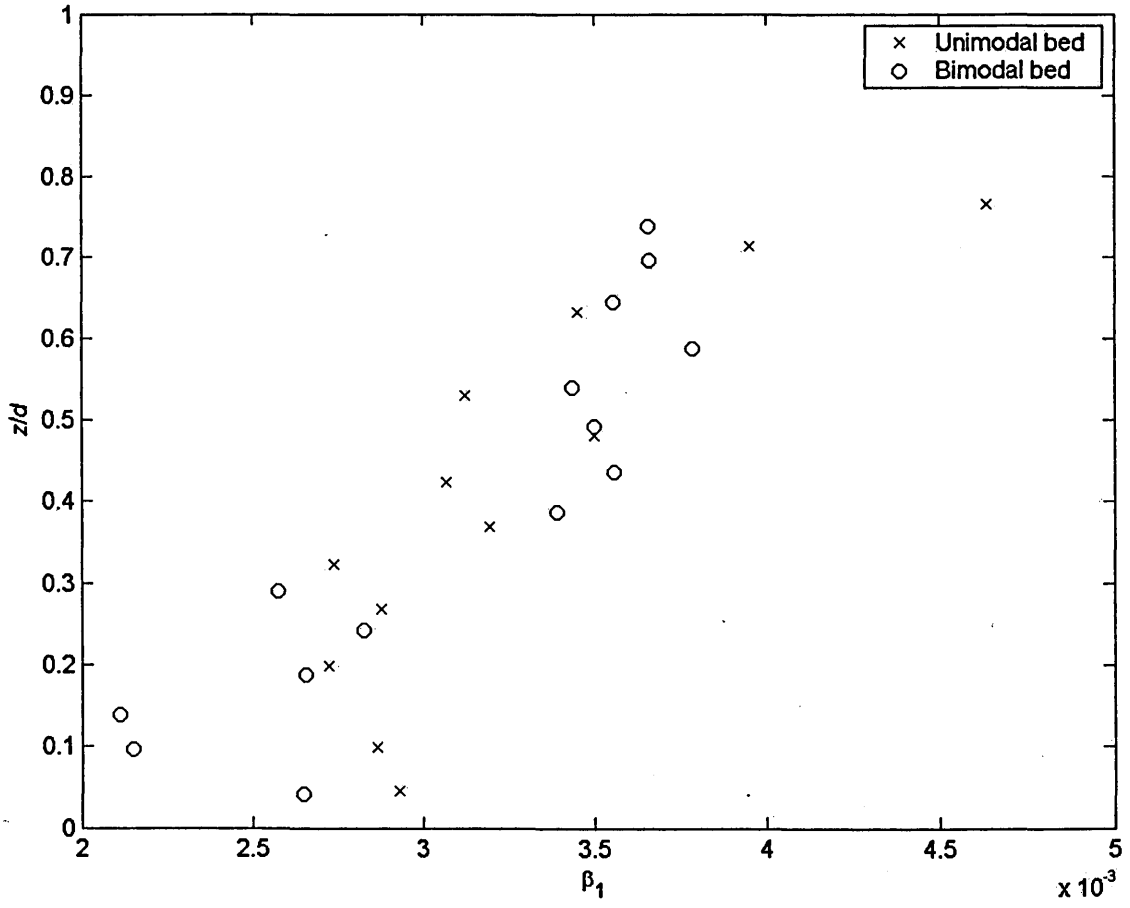

Figure 4.14. Vertical variability in the multiplying coefficient for relative submergence β_1 for the multiple linear regression between predictor variables, relative submergence and bed slope, and response variable, degree of spatial variability in $\bar{u}$ over the bed, $\sigma_{\bar{u}}$ with z/d, where $\bar{u}$ is the time-averaged streamwise velocity, z is the height above the maximum bed elevation, d is flow depth and D_{84} is the grain size at which 84 per cent of the bed material is finer. This is performed for each of the two beds.

The p-values for β_1 and β_2 are shown in Figure 4.15 for each of the beds. Over the unimodal bed it can seen that the association between relative submergence and $\sigma_{\overline{u}}$ is statistically significant at the 5 % level for the whole depth of the flow for all but the measurement position closest to the bed surface (Figure 4.15a). The significance of the relationship also increases with z/d. But bed slope only has a significant relationship with $\sigma_{\overline{u}}$ at two heights above the bed, demonstrating that relative submergence has a greater influence on $\sigma_{\overline{u}}$, and is likely to have mainly caused the change in $\sigma_{\overline{u}}$ under conditions of constant mean bed shear stress. Very similar results are also seen over the bimodal bed (Figure 4.15b). The statistical significance of the association between bed slope and $\sigma_{\overline{u}}$ demonstrates a slight tendency to increase with z/d over the unimodal bed, but does not consistently change with z/d over the bimodal bed. Given that the R^2 and β_1 values for relative submergence, and the statistical significance of its association with $\sigma_{\overline{u}}$ increase with z/d over both beds, it suggests that both the impact of relative submergence and the strength of its association with $\sigma_{\overline{u}}$ increases with z/d. Therefore, the importance of relative submergence to $\sigma_{\overline{u}}$ also increases with z/d.

4.8.2 Relative Spatial Variability

The vertical variability in the R^2 values for the bivariate and multiple regressions for $\sigma_{\overline{u}}/\langle\overline{u}\rangle$ are shown in Figure 4.16. They indicate that relative submergence has a much weaker association with $\sigma_{\overline{u}}/\langle\overline{u}\rangle$ than with $\sigma_{\overline{u}}$. Over the unimodal bed, the strength of this association is similar to that for bed slope, and although it increases with z/d, it still remains weak throughout the flow. Over the bimodal bed, the association is stronger, and its increase with z/d does result in it being reasonably high for the upper third of the flow. The association between $\sigma_{\overline{u}}/\langle\overline{u}\rangle$ and bed slope is still weak over this bed, but much higher than seen for $\sigma_{\overline{u}}$ and the unimodal bed. The R^2 values for the multiple regression largely follow the vertical profile of the R^2 values for the linear regression between $\sigma_{\overline{u}}/\langle\overline{u}\rangle$ and relative submergence over each of the beds. This model cannot be used to predict accurately $\sigma_{\overline{u}}/\langle\overline{u}\rangle$ over the unimodal bed, and only produces reasonable results in the upper third of the flow over the bimodal bed.

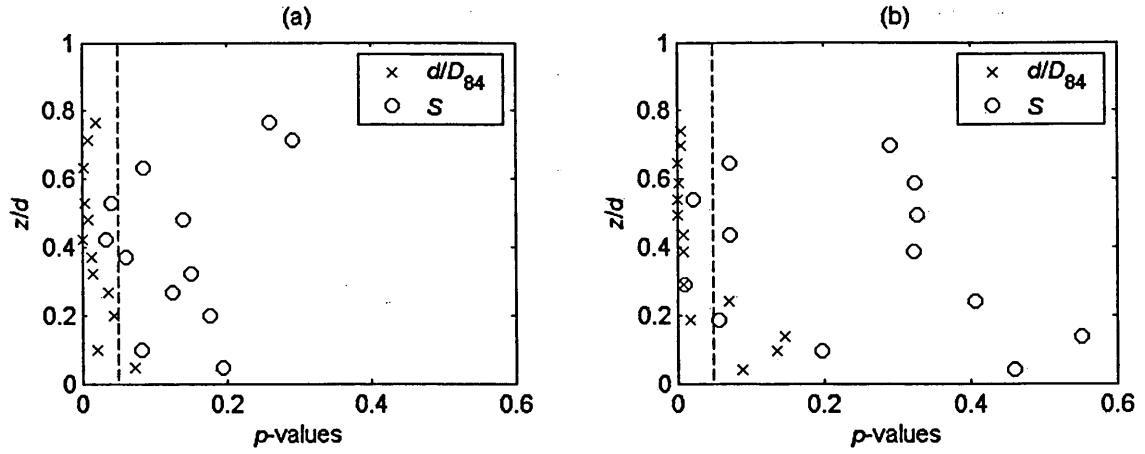

Figure 4.15. Vertical variability in the *p*-values of the multiplying coefficients for relative submergence d/D_{84} and bed slope S for the multiple linear regression between predictor variables, relative submergence and bed slope, and response variable, degree of spatial variability in $\overline{u}$ over the bed, $\sigma_{\overline{u}}$ with z/d for (a) the unimodal bed; and (b) the bimodal bed, where $\sigma_{\overline{u}}$ is the time-averaged streamwise velocity, z is the height above the maximum bed elevation, d is flow depth and D_{84} is the grain size at which 84 per cent of the bed material is finer. The dashed line indicates the 0.05 significance level.

The vertical variation in β for the multiple regression for $\sigma_{\overline{u}}/\langle\overline{u}\rangle$ seen in Figure 4.16 is similar to that observed for $\sigma_{\overline{u}}$. Over the bimodal bed, β_2 changes in no systematic manner with z/d, suggesting that the magnitude and direction of influence of bed slope is not consistent. Again it is fairly constant over the unimodal bed. The β_1 values are shown in more detail in Figure 4.17. It reveals that the influence of relative submergence is again similar over the two beds. The same relationship between β_1 and z/d is seen as for $\sigma_{\overline{u}}$, with the influence of relative submergence on $\sigma_{\overline{u}}/\langle\overline{u}\rangle$ increasing with z/d. However the *p*-values from the multiple regression indicate that neither relative submergence nor bed slope has a statistically significant influence on $\sigma_{\overline{u}}/\langle\overline{u}\rangle$ at the 5 % level over either of the beds (Figure 4.18). Only on three occasions over the bimodal bed, does either variable have a significant influence. The significance of the influence of relative submergence does increase, however, with z/d over this bed, such that in the outer region of the flow it approaches to be being significant at the 5 % level. A similar, but less consistent, increase is also seen over the bimodal bed.

However, the significance of the relationship between bed slope and $\sigma_{\bar{u}}/\langle\bar{u}\rangle$ does not demonstrate any clear change with z/d over either bed. Neither of the variables has a consistently greater influence on $\sigma_{\bar{u}}/\langle\bar{u}\rangle$, unlike was seen for $\sigma_{\bar{u}}$.

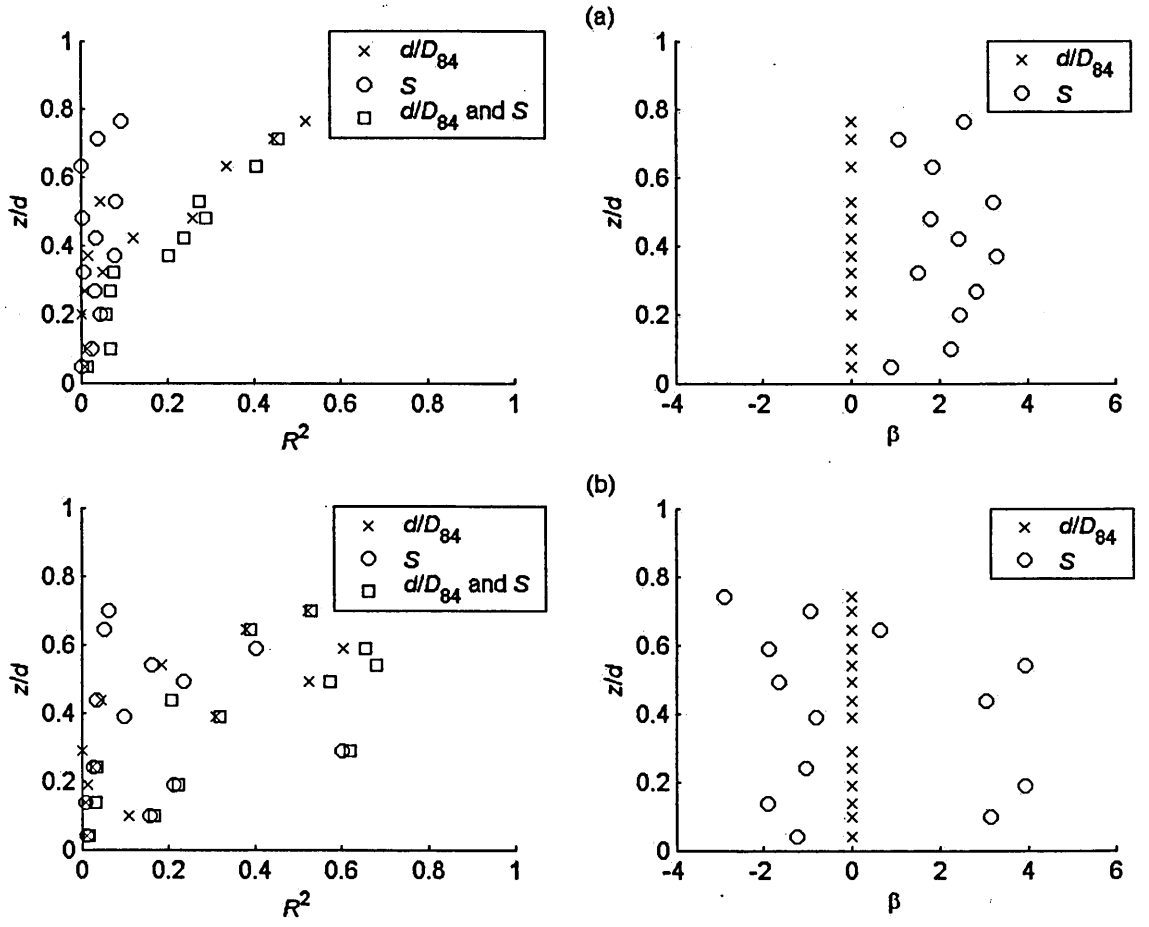

Figure 4.16. Vertical variability in the R^2 of the linear regression between relative submergence d/D_{84} and $\sigma_{\bar{u}}/\langle\bar{u}\rangle$, in R^2 of the linear regression between bed slope S and $\sigma_{\bar{u}}/\langle\bar{u}\rangle$, and in the R^2 of the multiple linear regression between predictor variables, relative submergence and bed slope, and response variable $\sigma_{\bar{u}}/\langle\bar{u}\rangle$ with z/d. Also shown is the vertical variability in the multiplying coefficients of these regressions β_1 with z/d. This is carried out for (a) the unimodal bed; and (b) the bimodal bed, where $\sigma_{\bar{u}}$ is the degree of spatial variability in $\bar{u}$, $\bar{u}$ is the time-averaged streamwise velocity, $\langle\bar{u}\rangle$ is the double-averaged streamwise velocity, z is the height above the maximum bed elevation, d is flow depth and D_{84} is the grain size at which 84 per cent of the bed material is finer.

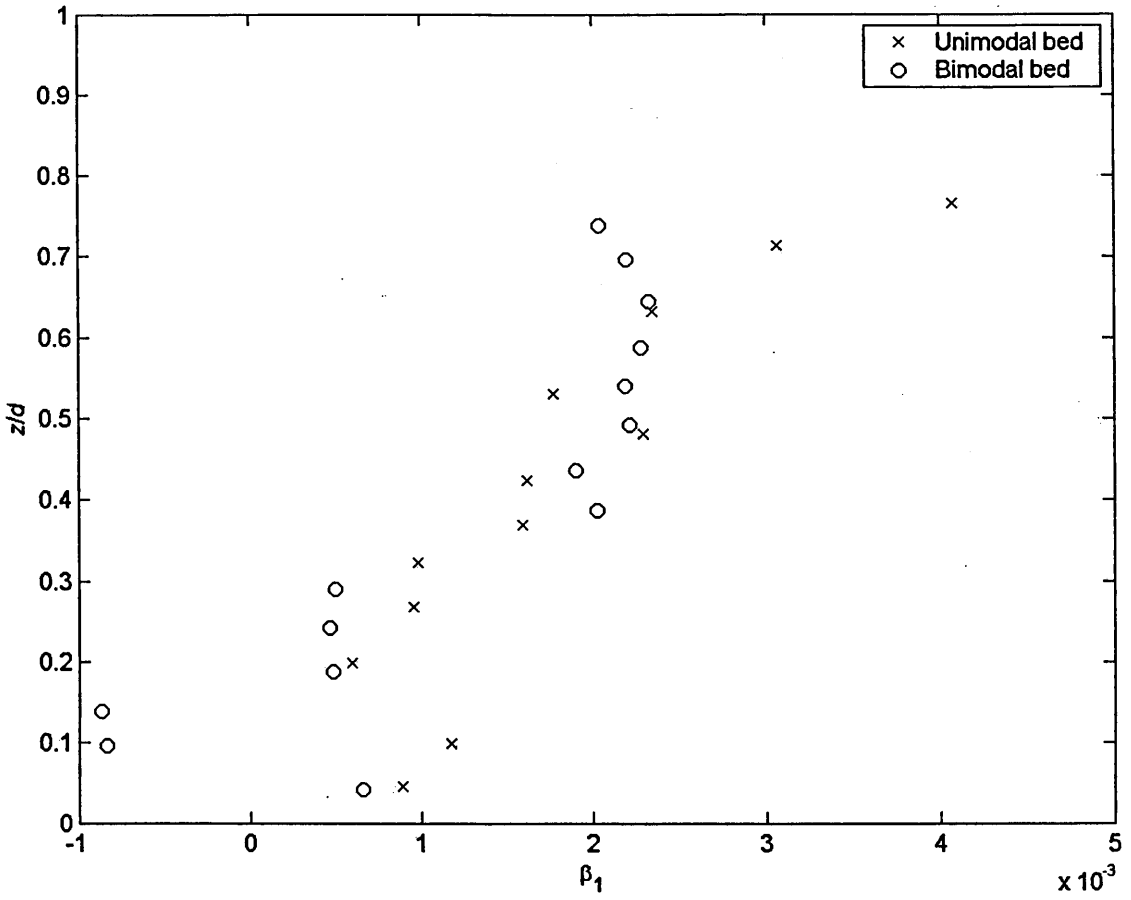

Figure 4.17. Vertical variability in the multiplying coefficient for relative submergence β_1 for the multiple linear regression between predictor variables, relative submergence and bed slope, and response variable $\sigma_{\overline{u}}/\langle\overline{u}\rangle$ with z/d, where $\sigma_{\overline{u}}$ is the degree of spatial variability in $\overline{u}$, $\overline{u}$ is the time-averaged streamwise velocity, $\langle\overline{u}\rangle$ is the double-averaged streamwise velocity, z is the height above the maximum bed elevation, d is flow depth and D_{84} is the grain size at which 84 per cent of the bed material is finer. This is performed for each of the two beds.

The results from the regressions for $\sigma_{\overline{u}}$ and $\sigma_{\overline{u}}/\langle\overline{u}\rangle$ suggest that there might be an important interaction between the influence of relative submergence on $\sigma_{\overline{u}}$ and $\sigma_{\overline{u}}/\langle\overline{u}\rangle$ and its proximity to the bed surface. In other words, there might be an important interaction between the influence of relative submergence and that of the bed. It raises the question of whether bed roughness influences the effect of relative submergence on the flow, such that in a region of the flow where the influence of the bed on the flow is negligible, traditionally thought of as the logarithmic layer and outer layer, the influence of relative submergence is evident at a high level, and explains the higher R^2 and β_1

values, and lower p-values in these regions. Therefore, is the effect of relative submergence always present but only apparent when the affects of bed roughness are less important or have disappeared? The vertical profiles of $\sigma_{\bar{u}}/\langle\bar{u}\rangle$ against z/d and z/D_{84} showed that bed roughness and flow depth can equally account for the variability in $\sigma_{\bar{u}}/\langle\bar{u}\rangle$ between the experimental runs close to the bed, but further up into the flow, flow depth provided a better scaling for $\sigma_{\bar{u}}/\langle\bar{u}\rangle$. This would suggest it might be true. If this were the case, it would indicate that R^2 and β_1 would be better scaled by flow depth rather than bed roughness. If R^2 and β_1 is plotted against z/D_{84}, it does not produce a better collapse of the values (not shown), and confirms that it is correct that flow depth produces a better scaling for R^2 and β_1. It therefore can not be related to the depth of water beneath a given vertical measurement position and how this would influence the effect of relative submergence on $\sigma_{\bar{u}}$ and $\sigma_{\bar{u}}/\langle\bar{u}\rangle$. Otherwise, it could be envisaged that the depth of water influences the effect of bed roughness on $\sigma_{\bar{u}}$ and $\sigma_{\bar{u}}/\langle\bar{u}\rangle$, because it could suppress the effects of bed roughness on that vertical measurement position through the volume/mass of water dampening its effects. Therefore this depth of water, and therefore z/D_{84}, would effect the influence of relative submergence on $\sigma_{\bar{u}}$ and $\sigma_{\bar{u}}/\langle\bar{u}\rangle$.

The idea suggests that the notion of bed roughness affecting the influence of relative submergence on $\sigma_{\bar{u}}$ and $\sigma_{\bar{u}}/\langle\bar{u}\rangle$ could be equally reversed. Perhaps relative submergence influences the degree to which bed roughness effects $\sigma_{\bar{u}}$ and $\sigma_{\bar{u}}/\langle\bar{u}\rangle$? Considering the effect of the depth of water beneath a vertical measurement position once again, the depth of water could determine the vertical position at which the influence of bed roughness disappears. In other words, the disappearance would be scaled by z/D_{84}. But it is known that if R^2 and β_1 is plotted against z/D_{84}, it does not produce a better collapse of the values than z/d. Therefore, it must be concluded that bed roughness (and the vertical extent of its influence, scaled by z/d) is most likely to determine the degree of effect of relative submergence on $\sigma_{\bar{u}}$ and $\sigma_{\bar{u}}/\langle\bar{u}\rangle$, and where its effects become apparent. This will be most significant for $\sigma_{\bar{u}}$ because of the lower p-values.

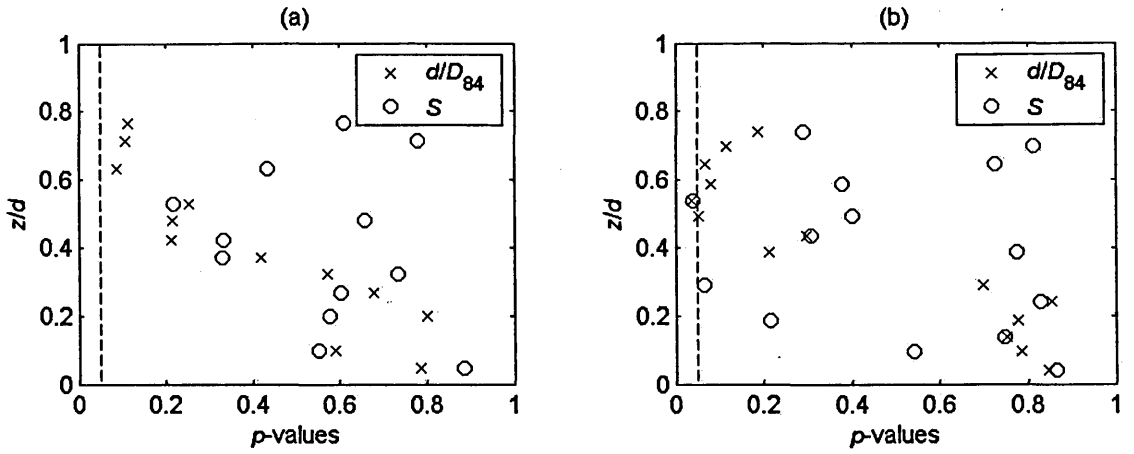

Figure 4.18. Vertical variability in the *p*-values of the multiplying coefficients for relative submergence d/D_{84} and bed slope S for the multiple linear regression between predictor variables, relative submergence and bed slope, and response variable $\sigma_{\overline{u}}/\langle\overline{u}\rangle$ with z/d for (a) the unimodal bed; and (b) the bimodal bed, where $\sigma_{\overline{u}}$ is the degree of spatial variability in $\overline{u}$, $\overline{u}$ is the time-averaged streamwise velocity, u_* is the bed shear velocity, z is the height above the maximum bed elevation, d is flow depth and D_{84} is the grain size at which 84 per cent of the bed material is finer. The dashed line indicates the 0.05 significance level.

4.9 The Pattern of Spatial Deviations over the Bed

The focus so far has been on quantifying the degree to which $\overline{u}$ changes over the bed using a spatially integrated quantity $\sigma_{\overline{u}}$. The attention now turns to the pattern or structure of the spatial deviations in $\overline{u}$ over the bed. Earlier results have implied that spatial variability can exist in the upper regions of the flow where the effect of bed roughness is thought to be negligible, and that flow depth rather than bed roughness might be a better scaling for this variability. An examination of the spatial pattern and the bed surface topography of the beds should further elucidate the relationship between the bed and $\overline{u}$. This time the focus will be on grain-scale deviations and it is these spatial deviations in $\overline{u}$ that contribute to the form-induced stress.

This is best accomplished using the horizontal plane PIV measurements since they provide high spatial resolution measurements of $\overline{u}$ over the bed. This means that there are fewer vertical positions above the bed at which to assess the spatial deviations in $\overline{u}$.

However, given the number of possible contour plots of the spatial deviations that could be produced just using the horizontal plane measurements (184), it would never be possible to assess a larger number of measurements above the bed. Therefore, a selection needs to be made of the contour plots to explore. It has been seen that relative submergence, rather than bed slope, has a strong correlation with $\sigma_{\overline{u}}$ and $\sigma_{\overline{u}}/\langle\overline{u}\rangle$. Also, that the effects of the bed may have an influence on the relationship between relative submergence and $\sigma_{\overline{u}}$ and $\sigma_{\overline{u}}/\langle\overline{u}\rangle$, or vice versa. Thus, only the contour plots produced for the experimental runs carried out at a single bed slope are examined (Tables 4.1 and 4.2).

Contour plots were produced of $\overline{u}/\langle\overline{u}\rangle$ to illustrate the spatial variability in $\overline{u}$ over the bed. This was to enable comparisons to be made between each of the experimental runs, and so that the relative size of the variability could be easily assessed. These plots allow a visual examination of the size of the spatial variations in $\overline{u}$ between different positions over the bed. The horizontal plane measurements that were carried at the same z/d were assessed for the different experimental runs, and this was carried out for a number of heights above the bed.

4.9.1 Unimodal bed

A Digital Elevation Model (DEM) of the bed surface topography of the unimodal bed produced by a laser scan is shown in Figure 4.19 to indicate the topography of the bed over which the $\overline{u}$ measurements were taken. The lighter areas depict zones of higher elevation whilst darker areas indicate zones of lower elevation. A lateral position of 0 mm denotes the centreline of the flume and the increasing values in the streamwise position are in the direction of the flow. The DEM is provided so that it can be seen how the spatial area of the contour plots of $\overline{u}/\langle\overline{u}\rangle$ relate to that of the bed surface, this will be returned to in more detail in a later section.

The change in the spatial distribution of $\overline{u}/\langle\overline{u}\rangle$ with relative submergence over the unimodal bed is shown in Figure 4.20 at $z/d = 0.08$. It is immediately apparent that the spatial pattern is different between the four plots and appears to be associated with the changes in relative submergence between the plots. At the lowest relative submergence of 4.1 (Figure 4.20a), there are four distinct streamwise streaks of flow that is, on

average, moving faster than $\langle\overline{u}\rangle$. There is also some slight evidence that these streaks alternate with thin streamwise streaks of slightly slower than average fluid. The width of the high-speed streaks reduces with streamwise distance, resulting in the streaks of slower fluid expanding. Overlain on these streaks are small, discrete areas experiencing slower than average flow, quite often approaching only 70 % of $\langle\overline{u}\rangle$. With an increase in relative submergence to $d/D_{84} = 6.9$ the distinction of the high-speed streamwise streaks decreases quite markedly, although all four streaks observed at a relative submergence of 4.1 are still present, displaying some degree of spatial persistence (Figure 4.20b). More apparent is that the discrete areas of slower fluid are occurring in exactly the same locations as seen in the previous plot. At a relative submergence of 9.0, there is further reduction in the spatial organisation that results in the complete disappearance of the streaks of faster moving fluid (Figure 4.20c). There are still discrete areas of slower fluid over the bed, but they are less distinct and larger in spatial coverage. Furthermore, only a small number of the areas correspond to those seen previously. A further increase in relative submergence to 12.9, results in the occurrence of two streamwise streaks of higher and lower speed fluid much larger than seen at the lower submergences, and there is even less correspondence in the low-speed spots to the other plots (Figure 4.20d). These spatial patterns are in accordance with the conclusions drawn from the skewness values of the distributions of $\overline{u}$. The skewness values suggested that the unimodal bed is covered by localised areas of distinctly low $\overline{u}$ and large areas of just slightly higher-than-average $\overline{u}$. This is clearly shown in the contour plots of $\overline{u}/\langle\overline{u}\rangle$.

At $z/d = 0.13$ a very similar change in the spatial pattern occurs with an increase in relative submergence (Figure 4.21). The streamwise streaks of higher velocity at a relative submergence of 4.1 are less distinct than seen at the lower relative height (Figure 4.21a). The four streaks are still present but have begun to amalgamate, particularly in the lower half of the plot. The low-speed spots are also still present, and their spatial location corresponds well with those seen at the two lowest submergences in Figure 4.20. However, they do appear to have become enlarged and a small number of new spots have appeared. Increases in relative submergence again cause a decrease in the distinction of the high velocity streamwise streaks and a furthering disassociation between the spatial locations of the low-speed spots with previous plots at this relative height (Figures 4.21b, c and d). It results in the lower two-thirds of the bed at the two

highest relative submergences being covered by a band of higher velocities that are not organised into distinct streamwise strips.

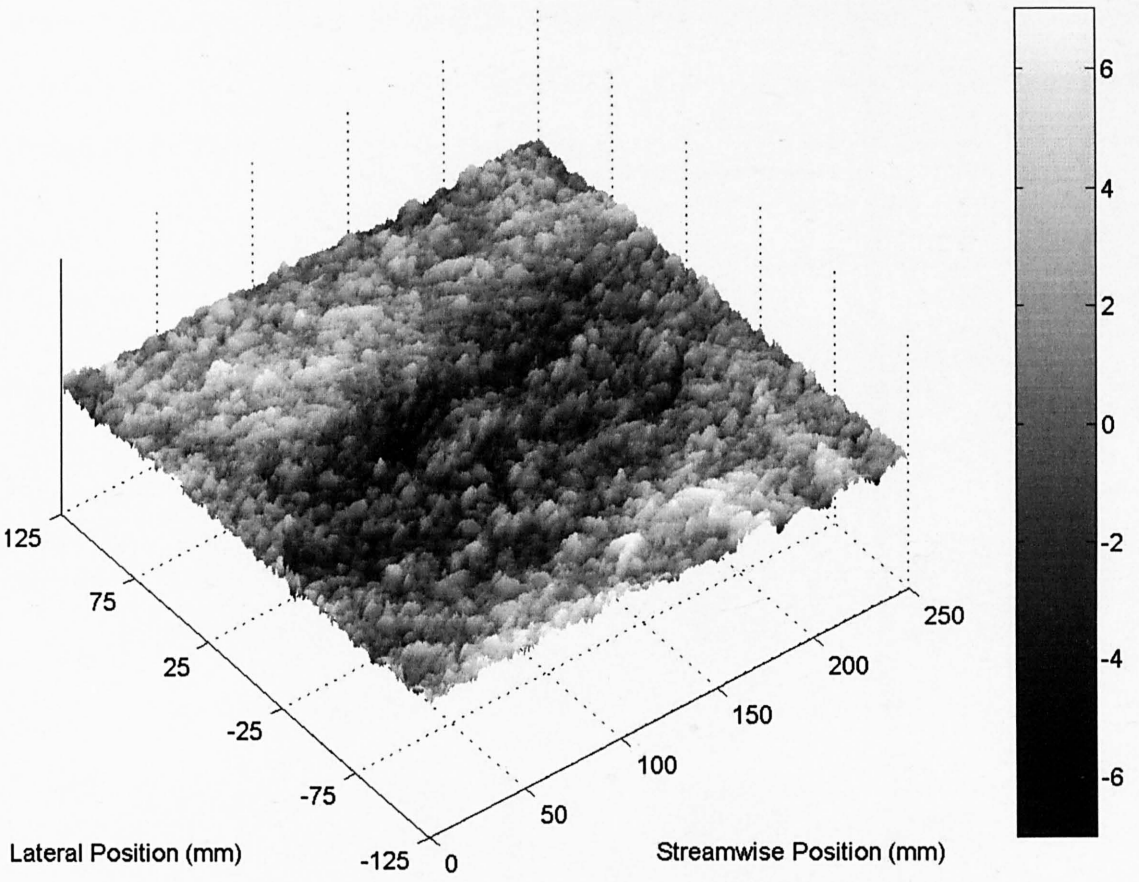

Figure 4.19. A Digital Elevation Model of the bed surface topography of the unimodal bed produced by a laser bed scanner. The grayscale relates to the departure in elevation from the zero mean surface elevation (mm). A lateral position of 0 mm denotes the centreline of the flume and the increasing values in the streamwise position are in the direction of the flow.

A further increase in z/d to 0.16 has again caused a decrease in the distinction and width of the high-speed streamwise streaks (Figure 4.22). In addition, the small areas of bed experiencing slower than average flow are now fewer in number and also less discrete. There is now even less correspondence in the spatial locations of these areas between the plots of different relative submergences at this height. An increase in relative submergence again appears to cause the same effects on the spatial pattern, with the progressive disappearance of the high-speed streaks and decrease in the overall

organisation of the spatial deviations. This change with relative submergence and relative height continues for the plots at and up to $z/d = 0.27$ (Figures 4.23 and 4.24), beyond which the pattern of high-speed streaks over the bed, and in some cases the presence of low-speed spots, all but disappear (Figures 4.25 and 4.26). It means that there is no longer a distinctive change in the spatial pattern of spatial deviations with increases in relative submergence beyond $z/d = 0.27$ (therefore plots have not been included for values of z/d higher than 0.45).

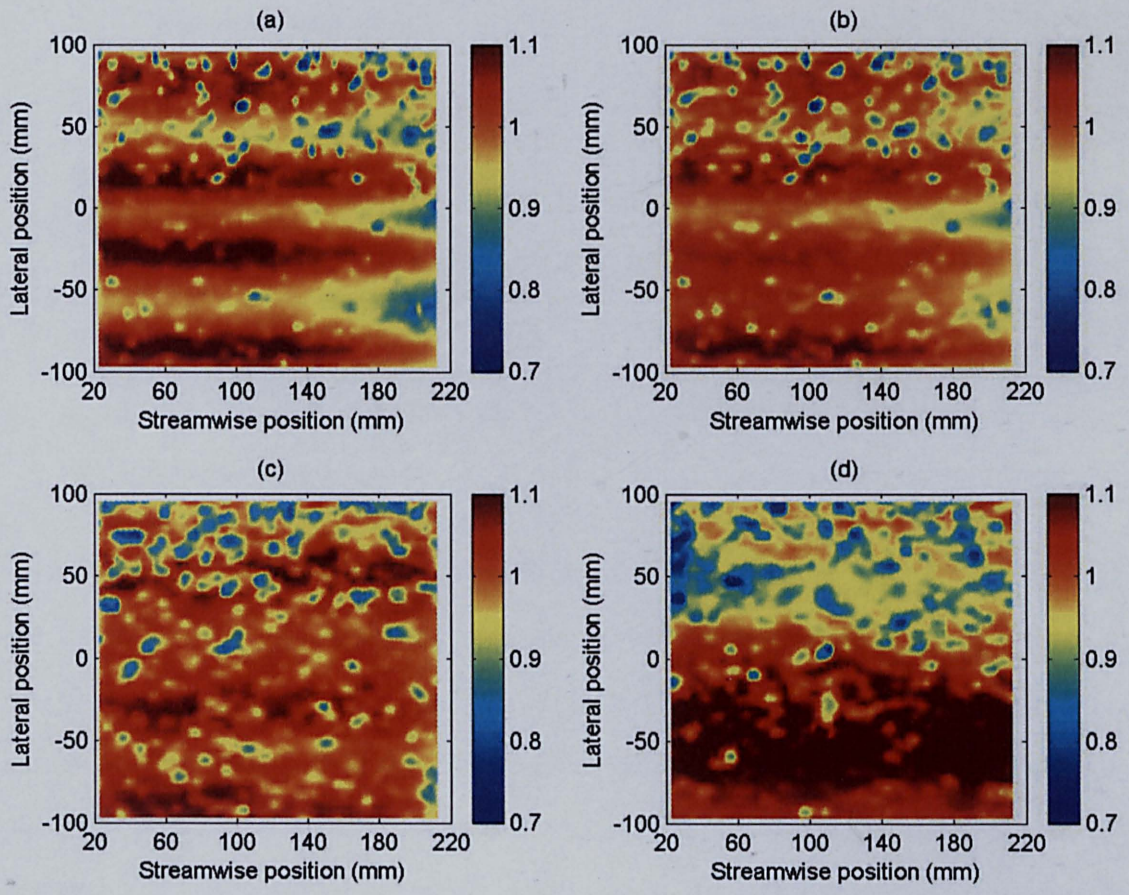

Figure 4.20. The spatial distribution of $\overline{u}/\langle\overline{u}\rangle$ over the unimodal bed at $z/d = 0.08$ for the experimental runs performed at a single bed slope with (a) $d/D_{84} = 5.6$; (b) $d/D_{84} = 6.9$; (c) $d/D_{84} = 9.0$; and (d) $d/D_{84} = 12.9$, where $\overline{u}$ is the time-averaged streamwise velocity, $\langle\overline{u}\rangle$ is the double-averaged streamwise velocity, z is the height above the maximum bed elevation, d is flow depth and D_{84} is the grain size at which 84 per cent of the bed material is finer. A lateral position of 0 mm denotes the centreline of the flume and the streamwise position relates to the position in the DEM of the bed (Figure 4.19).

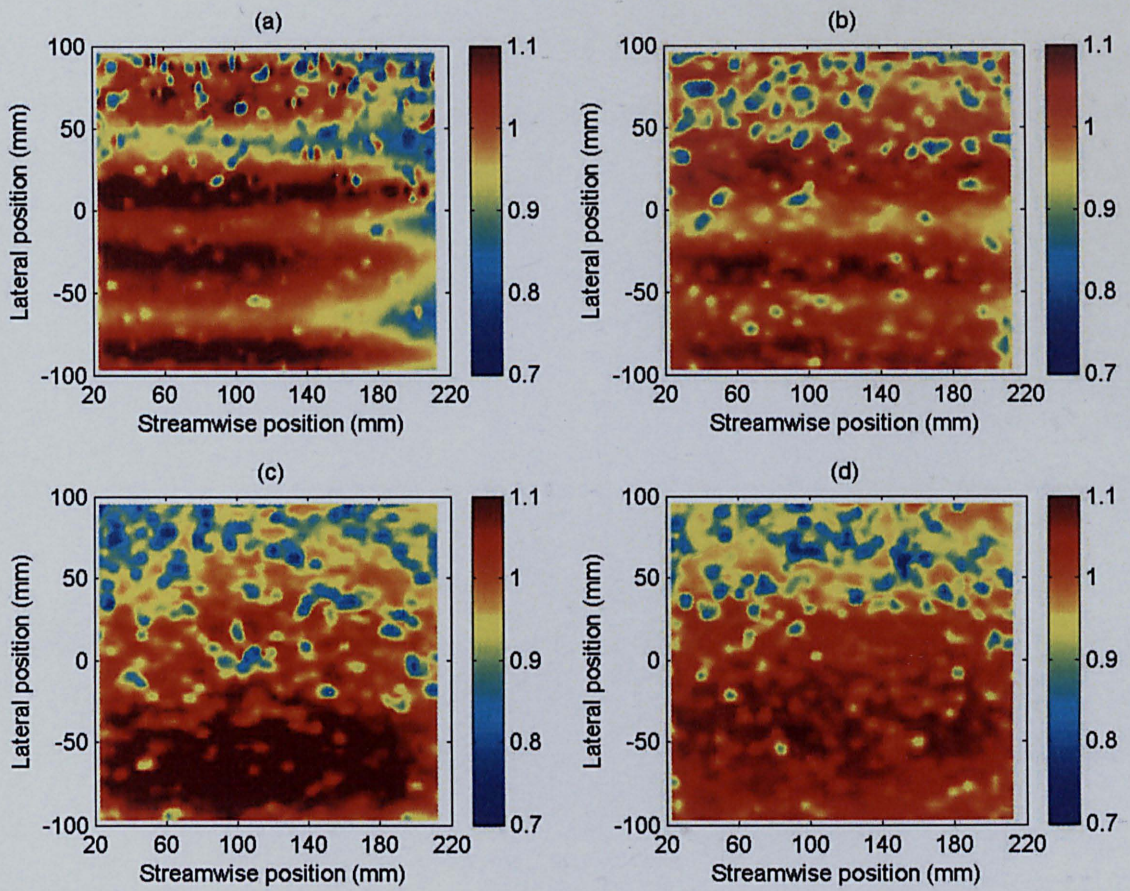

Figure 4.21. The spatial distribution of $\overline{u}/\langle\overline{u}\rangle$ over the unimodal bed at $z/d = 0.13$ for the experimental runs performed at a single bed slope with (a) $d/D_{84} = 4.1$; (b) $d/D_{84} = 6.9$; (c) $d/D_{84} = 9.0$; and (d) $d/D_{84} = 12.9$, where $\overline{u}$ is the time-averaged streamwise velocity, $\langle\overline{u}\rangle$ is the double-averaged streamwise velocity, z is the height above the maximum bed elevation, d is flow depth and D_{84} is the grain size at which 84 per cent of the bed material is finer. A lateral position of 0 mm denotes the centreline of the flume and the streamwise position relates to the position in the DEM of the bed (Figure 4.19).

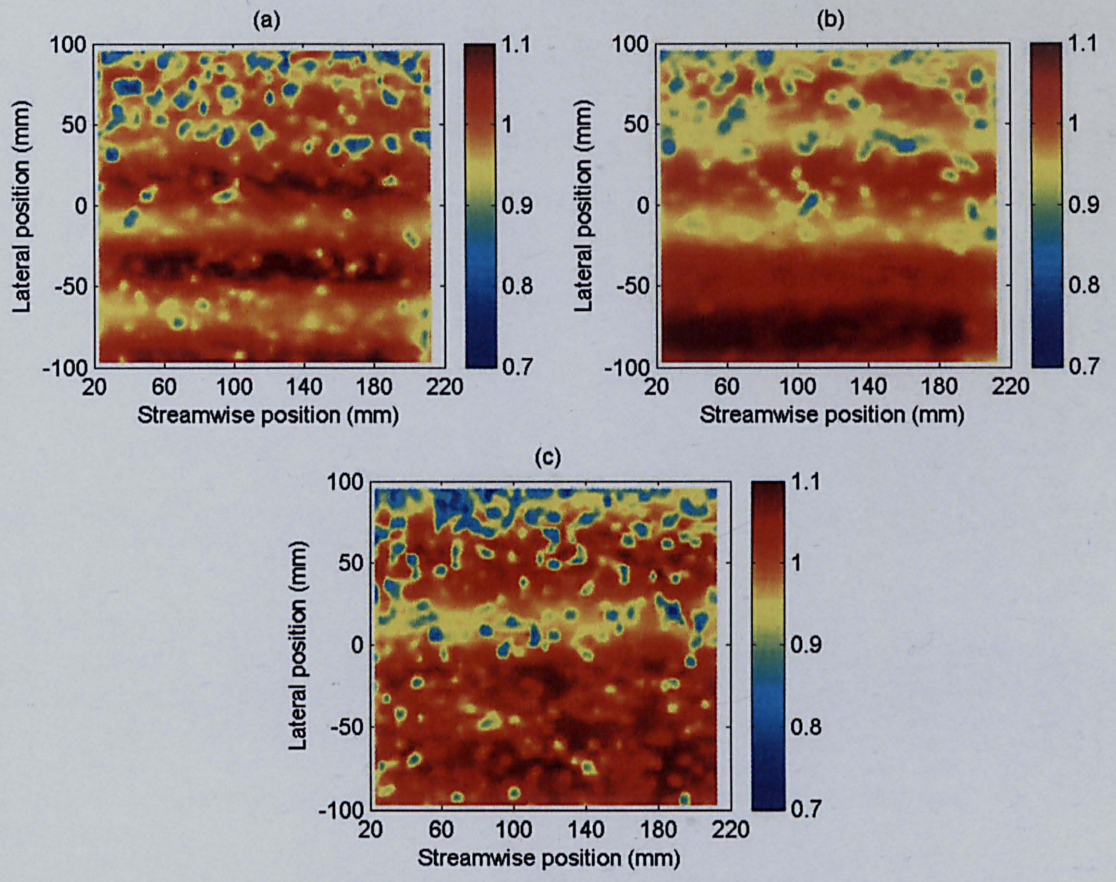

Figure 4.22. The spatial distribution of $\overline{u}/\langle\overline{u}\rangle$ over the unimodal bed at $z/d = 0.16$ for the experimental runs performed at a single bed slope with (a) $d/D_{84} = 5.6$; (b) $d/D_{84} = 6.9$; and (c) $d/D_{84} = 9.0$, where $\overline{u}$ is the time-averaged streamwise velocity, $\langle\overline{u}\rangle$ is the double-averaged streamwise velocity, z is the height above the maximum bed elevation, d is flow depth and D_{84} is the grain size at which 84 per cent of the bed material is finer. A lateral position of 0 mm denotes the centreline of the flume and the streamwise position relates to the position in the DEM of the bed (Figure 4.19).

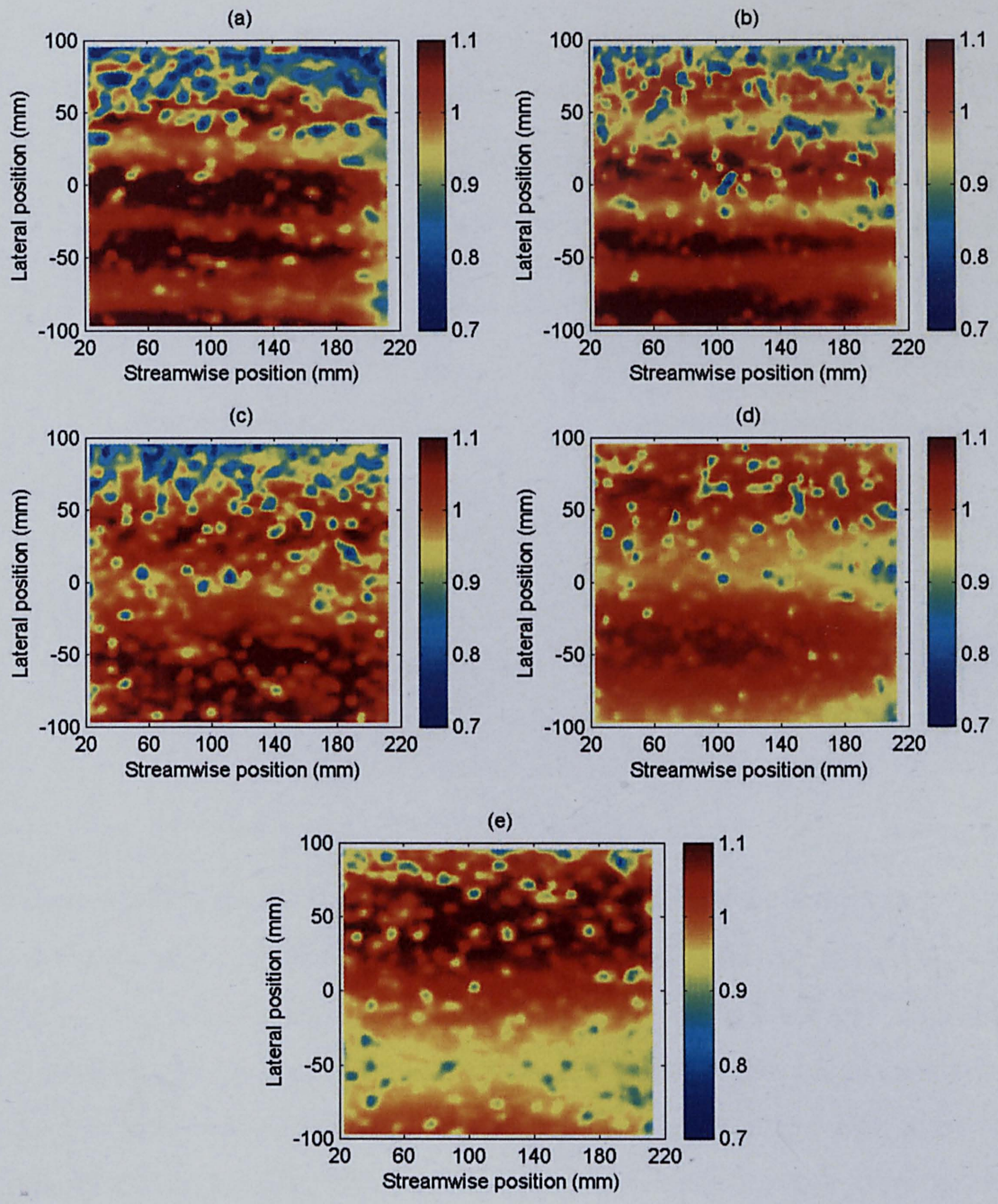

Figure 4.23. The spatial distribution of $\overline{u}/\langle\overline{u}\rangle$ over the unimodal bed at $z/d = 0.22$ for the experimental runs performed at a single bed slope with (a) $d/D_{84} = 4.1$; (b) $d/D_{84} = 5.6$; (c) $d/D_{84} = 6.9$; (d) $d/D_{84} = 9.0$; and (e) $d/D_{84} = 12.9$, where $\overline{u}$ is the time-averaged streamwise velocity, $\langle\overline{u}\rangle$ is the double-averaged streamwise velocity, z is the height above the maximum bed elevation, d is flow depth and D_{84} is the grain size at which 84 per cent of the bed material is finer. A lateral position of 0 mm denotes the centreline of the flume and the streamwise position relates to the position in the DEM of the bed (Figure 4.19).

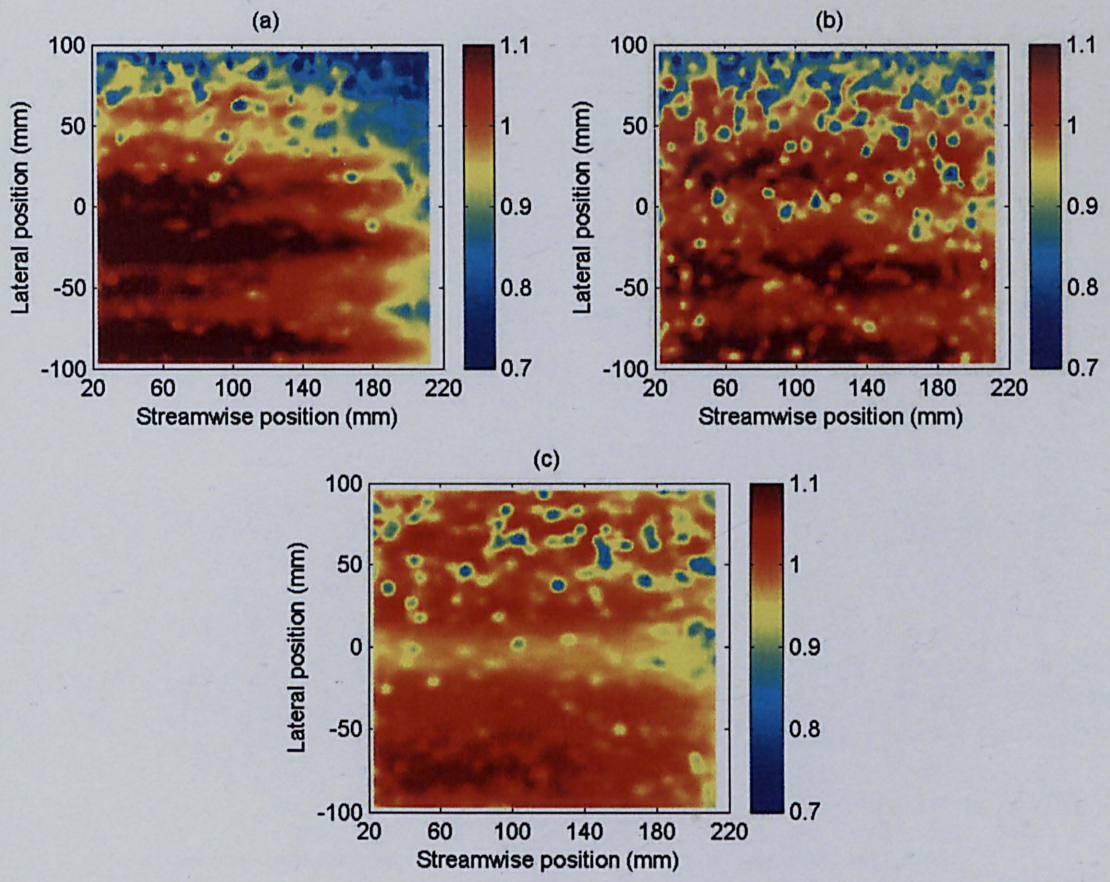

Figure 4.24. The spatial distribution of $\overline{u}/\langle\overline{u}\rangle$ over the unimodal bed at $z/d = 0.27$ for the experimental runs performed at a single bed slope with (a) $d/D_{84} = 2.6$; (b) $d/D_{84} = 5.6$; (c) and $d/D_{84} = 6.9$, where $\overline{u}$ is the time-averaged streamwise velocity, $\langle\overline{u}\rangle$ is the double-averaged streamwise velocity, z is the height above the maximum bed elevation, d is flow depth and D_{84} is the grain size at which 84 per cent of the bed material is finer. A lateral position of 0 mm denotes the centreline of the flume and the streamwise position relates to the position in the DEM of the bed (Figure 4.19).

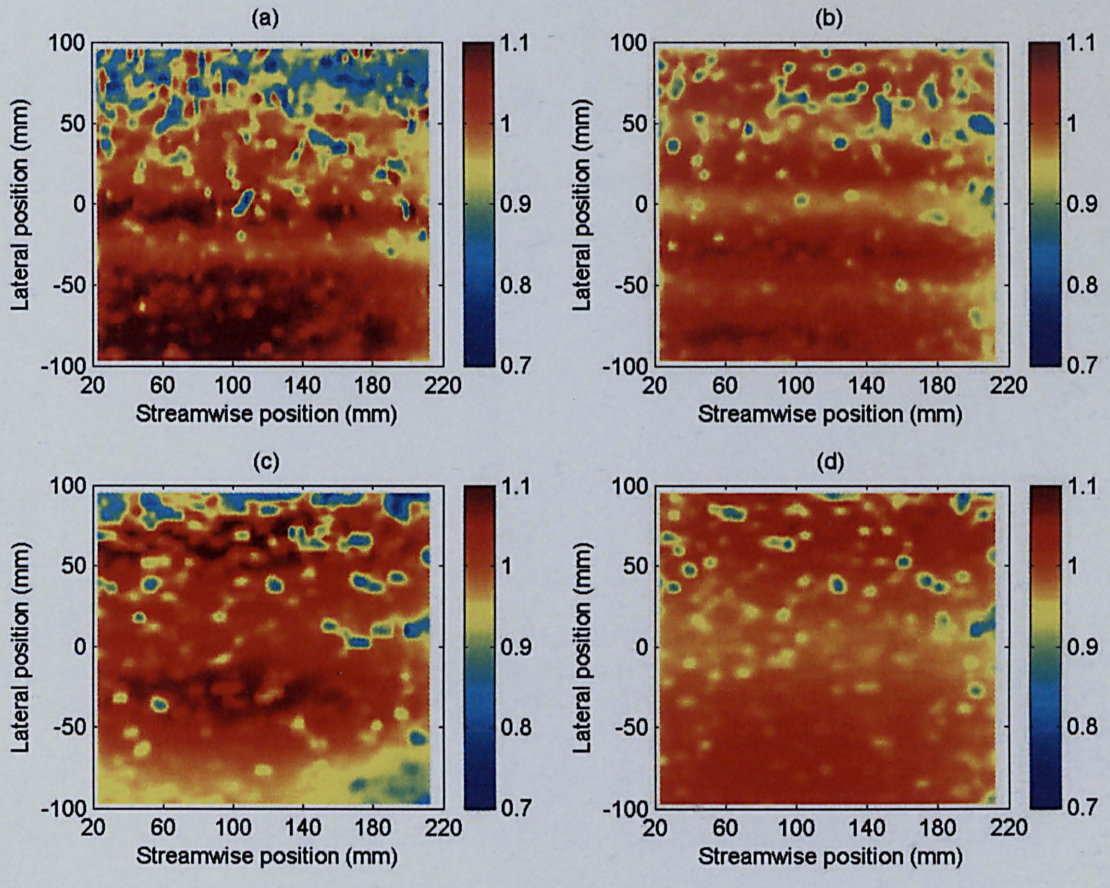

Figure 4.25. The spatial distribution of $\overline{u}/\langle\overline{u}\rangle$ over the unimodal bed at $z/d = 0.33$ for the experimental runs performed at a single bed slope with (a) $d/D_{84} = 2.6$; (b) $d/D_{84} = 4.1$; (c) $d/D_{84} = 6.9$; and (d) $d/D_{84} = 12.9$, $\overline{u}$ is the time-averaged streamwise velocity, $\langle\overline{u}\rangle$ is the double-averaged streamwise velocity, z is the height above the maximum bed elevation, d is flow depth and D_{84} is the grain size at which 84 per cent of the bed material is finer. A lateral position of 0 mm denotes the centreline of the flume and the streamwise position relates to the position in the DEM of the bed (Figure 4.19).

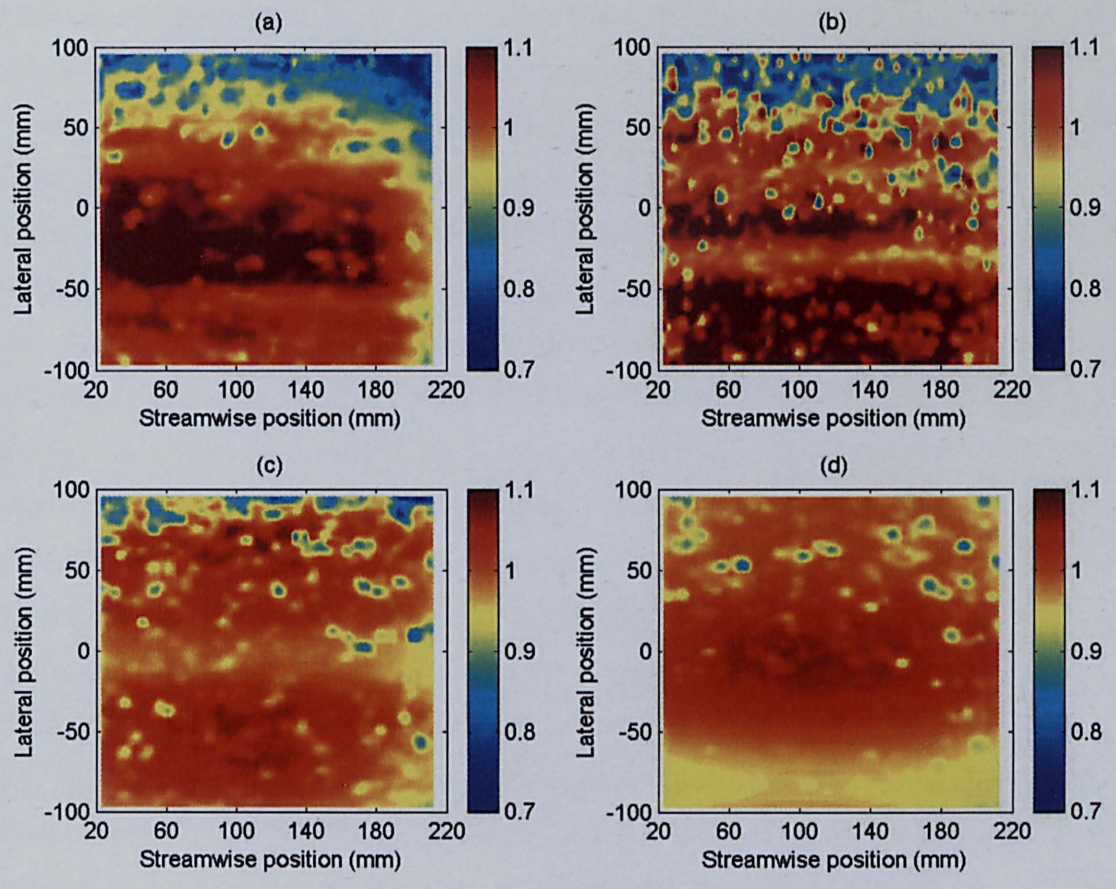

Figure 4.26. The spatial distribution of $\overline{u}/\langle\overline{u}\rangle$ over the unimodal bed at $z/d = 0.45$ for the experimental runs performed at a single bed slope with (a) $d/D_{84} = 2.6$, (b) $d/D_{84} = 4.1$, (c) $d/D_{84} = 6.9$, and (d) $d/D_{84} = 12.9$, $\overline{u}$ is the time-averaged streamwise velocity, $\langle\overline{u}\rangle$ is the double-averaged streamwise velocity, z is the height above the maximum bed elevation, d is flow depth and D_{84} is the grain size at which 84 per cent of the bed material is finer. A lateral position of 0 mm denotes the centreline of the flume and the streamwise position relates to the position in the DEM of the bed (Figure 4.19).

4.9.2 Bimodal Bed

A DEM of the bed surface topography of the bimodal bed is provided in Figure 4.27. The change in the spatial distribution of the spatial deviations with relative submergence over the bimodal bed is shown in Figure 4.28 at $z/d = 0.08$. At a relative submergence of 5.7 it is striking that a similar pattern of streamwise streaks of higher velocity and thinner streaks of lower velocity are also noticeable over this bed (Figure

4.28a) as with found over the unimodal bed. These streaks occupy the whole streamwise length of the bed. Again, overlain on these streaks are discrete areas of the bed experiencing slower than average flow. The pattern is more speckled than that over the unimodal bed, suggesting that some of these flow features are smaller and more localised. An increase in relative submergence to 6.9 results in the disappearance of one of the high velocity streaks in the lower half of the bed through the amalgamation of two streaks (Figure 4.28b). But the location of the remaining high-speed streaks is remarkably similar to those at a relative submergence of 5.7. Indeed, this also applies to the spots of slower fluid, with all the spots seen earlier also appearing here. At a relative submergence of 9.0, still only two high-speed streaks remain, but the lower streaks have become less defined (Figure 4.28c). The area of lower velocity between the streaks has grown, causing the width of the streaks to decrease. There are still small, discrete areas of the bed experiencing slower fluid, but their spatial location no longer correlates with those at the two lower submergences. They have also grown in spatial extent, and are less distinct. A further increase in relative submergence to 12.8 results in the total disappearance of the streaks of both high- and low-speed fluid, and a reduction in the number of low-speed spots over the bed (Figure 4.28d). This pattern of change in the spatial distribution with relative submergence is very similar to that observed over the unimodal bed.

At $z/d = 0.13$ this same pattern is observed (Figure 4.29). At a relative submergence of 4.1, the same alternating pattern of high- and low-speed streaks appear over the bed (Figure 4.29a), located in almost exactly the same position as seen for the lowest submergence at $z/d = 0.08$ (Figure 4.28a). All the same spots of slower fluid are also present and again appear in the same spatial locations. An increase in relative submergence causes a reduction in the number of streaks over the bed, through an amalgamation of the streaks. The spatial locations of the low-speed spots again become less and less associated with those from other plots, but this occurs at a lower relative submergence than seen at $z/d = 0.08$. Overall, the degree of spatial organisation continues to decrease with increases in relative submergence.

A further increase in z/d to 0.16 has yet to cause the alternating pattern of slower and faster streaks to disappear (Figure 4.30). However, the locations of the spots of slower fluid no longer correlate with those seen at the lower relative heights, and they have also

become larger. An increase in relative submergence again appears to produce similar effects on the spatial pattern, with the progressive reduction in the number of high-speed streaks and the reduction in the number of slow-speed spots, but also an increase in their spatial extent. This change continues at $z/d = 0.22$ (Figure 4.31), but not as consistently as is seen at the lower relative heights. At the highest relative submergence of 12.8, it is the first occurrence of the streaky pattern not being present (Figure 4.31f). This process of change in the spatial organisation with relative submergence continues up to $z/d = 0.34$ (Figure 4.32), beyond which the high-speed streaks have totally disappeared, and the number of low-speed spots have decreased (Figure 4.33). At these heights above $z/d = 0.34$, increases in relative submergence now only cause an overall increase in the spatial homogeneity and a reduction in the spots of slower fluid, rather than any change associated with the high-speed streaks. This was observed to continue further up into the flow.

4.10 Vertical Change in the Pattern of Spatial Deviations over the Bed

The contour plots of $\overline{u}/\langle\overline{u}\rangle$ over both of the beds have shown that its spatial pattern can change quite markedly for similar values of z/d but different relative submergences. Therefore, flow depth may be a key control on the spatial pattern at a given z/d, but it does not appear to scale its vertical variability. For example, over the unimodal bed at $z/d = 0.45$ and a relative submergence of 4.1 the streamwise streaks of higher velocity are still present (Figure 4.26b), but are not present at $z/d = 0.33$ for the two highest relative submergences (Figure 4.25c and d). A further example can be drawn from the contour plots from the bimodal bed. At $z/d = 0.34$ the streaks are present at a relative submergence of 5.7 (Figure 4.32a) but have disappeared at $z/d = 0.22$ for a relative submergence of 12.8 (Figure 4.31d). It would appear that the absolute height of the measurements of $\overline{u}$ might have a greater influence on the vertical variability in the spatial pattern of $\overline{u}/\langle\overline{u}\rangle$. For example, it has been seen that the spatial locations of the low-speed spots remain fairly constant at the same z/D_{84} close to the bed, and that increases in z/D_{84} can cause this persistence to reduce and for the spots to become larger and less numerous. Furthermore, it has been observed that the high-speed streaks become less distinct, decrease in number and ultimately disappear with increases in z/D_{84}. To examine this relationship between the spatial pattern of $\overline{u}/\langle\overline{u}\rangle$ and z/D_{84},

contour plots of $\overline{u}/\langle\overline{u}\rangle$ at the same z/D_{84} have been produced for those experimental runs analysed above.

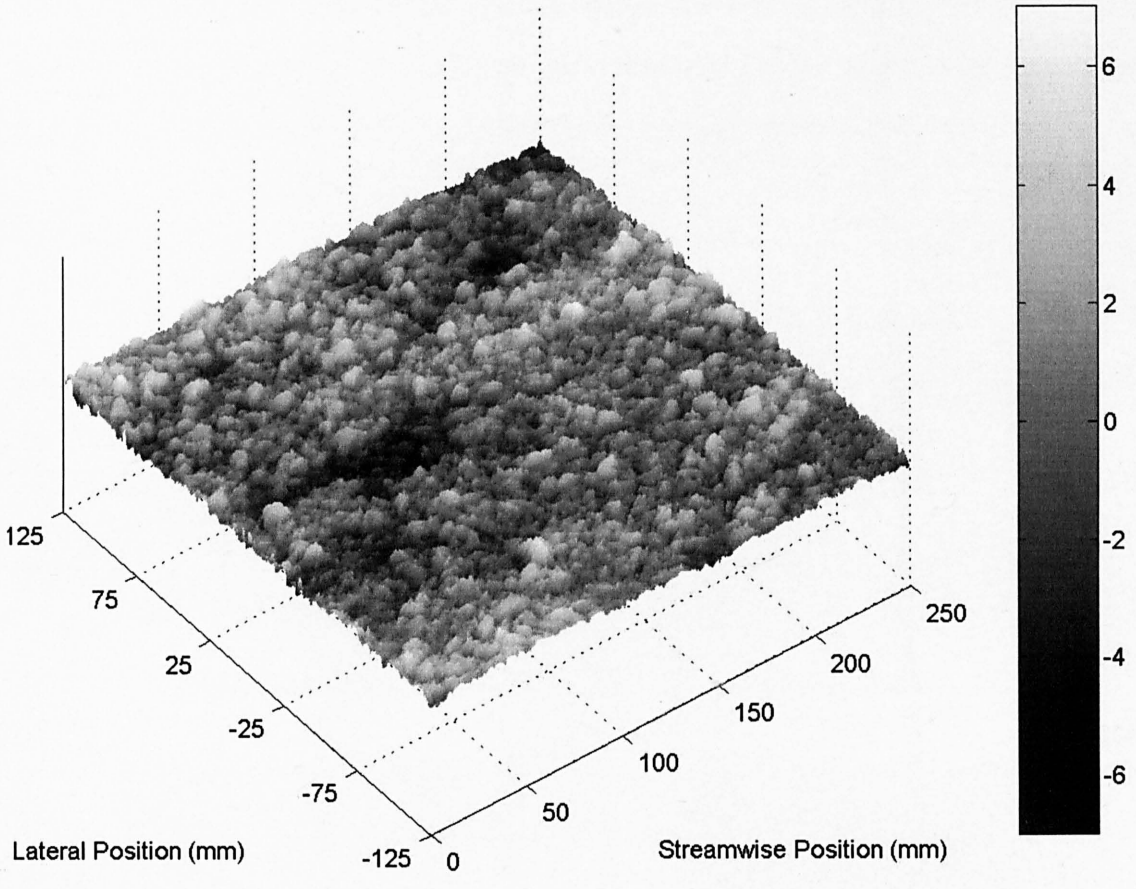

Figure 4.27. A Digital Elevation Model of the bed surface topography of the bimodal bed produced by a laser bed scanner. The grayscale relates to the departure in elevation from the zero mean surface elevation (mm). A lateral position of 0 mm denotes the centreline of the flume and the increasing values in the streamwise position are in the direction of the flow. This scan was taken over the same area as in Figure 4.19 and has the same grayscale.

4.10.1 Unimodal Bed

The distribution of the spatial deviations at $z/D_{84} = 0.43$ over the unimodal bed is shown in Figure 4.34. It shows that the spatial pattern is more consistent at the same $z/D_{84} = 0.43$ than it was at the same z/d. The high-speed streaks and the low-speed

spots display a greater persistence across all the experimental runs. There is also a greater deal of correspondence in the spatial locations of the low-speed spots between the plots. However, the influence of relative submergence is still present. An increase in relative submergence again causes a decrease in the number of high-speed streaks and low-speed spots, and an enlarging of these spots. Since these plots are produced from measurements at the same z/D_{84}, it demonstrates that the effect of the roughness of the bed cannot fully account for the variability in the spatial pattern between the plots.

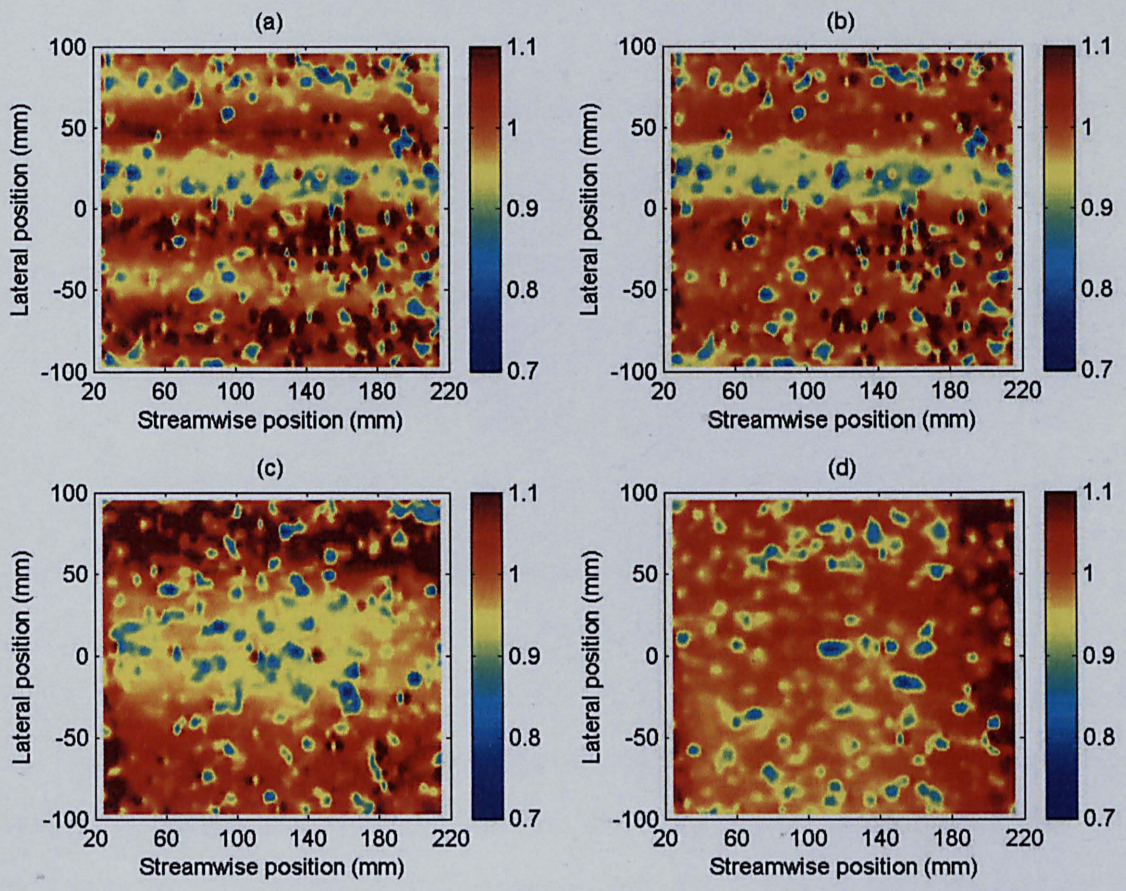

Figure 4.28. The spatial distribution of $\overline{u}/\langle\overline{u}\rangle$ over the bimodal bed at $z/d = 0.08$ for the experimental runs performed at a single bed slope with (a) $d/D_{84} = 5.7$, (b) $d/D_{84} = 6.9$; (c) $d/D_{84} = 9.0$; and (d) $d/D_{84} = 12.8$, $\overline{u}$ is the time-averaged streamwise velocity, $\langle\overline{u}\rangle$ is the double-averaged streamwise velocity, z is the height above the maximum bed elevation, d is flow depth and D_{84} is the grain size at which 84 per cent of the bed material is finer. A lateral position of 0 mm denotes the centreline of the flume and the streamwise position relates to the position in the DEM of the bed (Figure 4.27).

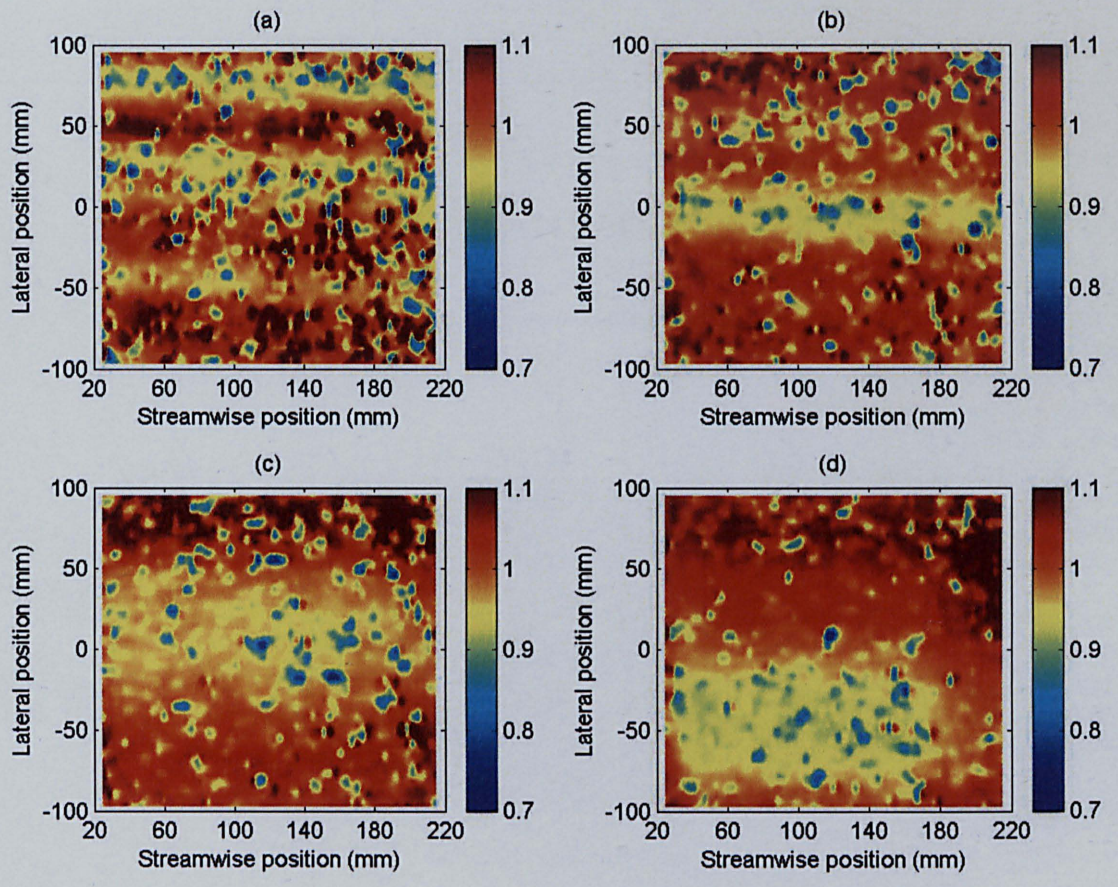

Figure 4.29. The spatial distribution of $\overline{u}/\langle\overline{u}\rangle$ over the bimodal bed at $z/d = 0.13$ for the experimental runs performed at a single bed slope with (a) $d/D_{84} = 4.1$; (b) $d/D_{84} = 6.9$; (c) $d/D_{84} = 9.0$; and (d) $d/D_{84} = 12.8$, $\overline{u}$ is the time-averaged streamwise velocity, $\langle\overline{u}\rangle$ is the double-averaged streamwise velocity, z is the height above the maximum bed elevation, d is flow depth and D_{84} is the grain size at which 84 per cent of the bed material is finer. A lateral position of 0 mm denotes the centreline of the flume and the streamwise position relates to the position in the DEM of the bed (Figure 4.27).

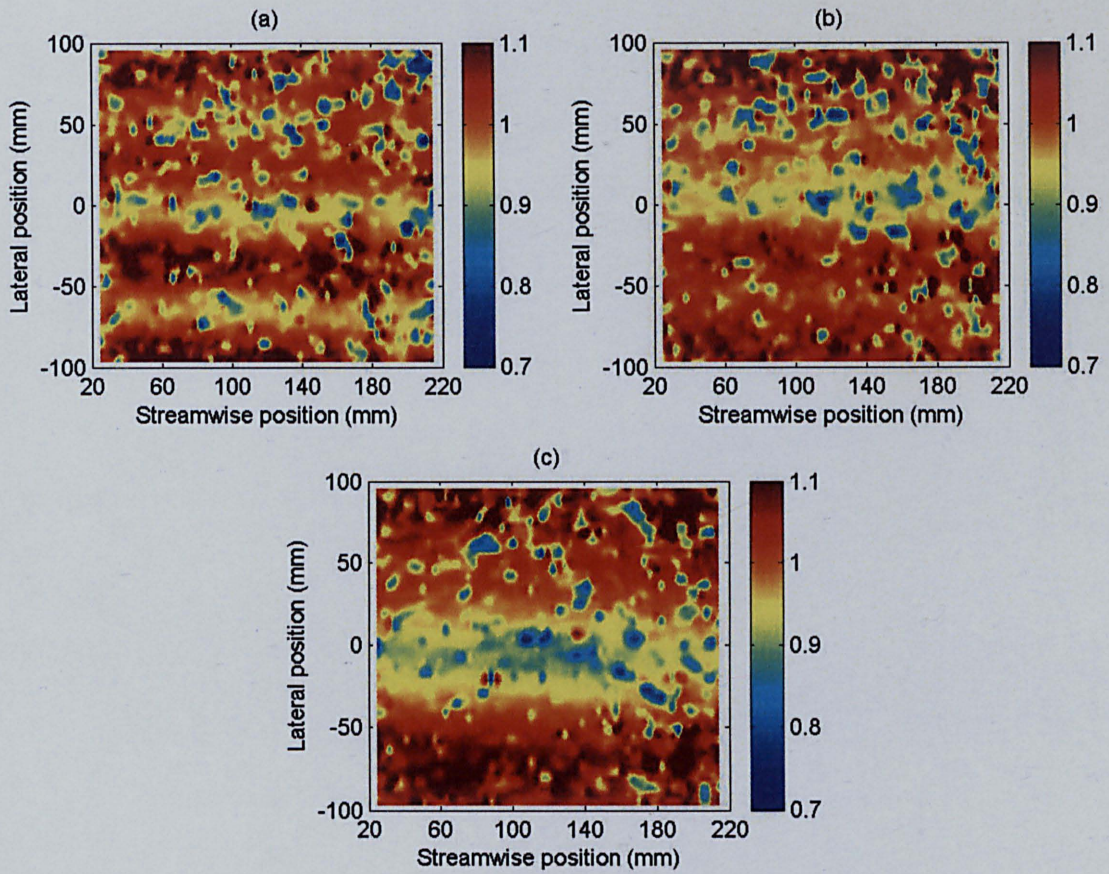

Figure 4.30. The spatial distribution of $\overline{u}/\langle\overline{u}\rangle$ over the bimodal bed at $z/d = 0.16$ for the experimental runs performed at a single bed slope with (a) $d/D_{84} = 5.7$; (b) $d/D_{84} = 6.9$; and (c) $d/D_{84} = 9.0$, where $\overline{u}$ is the time-averaged streamwise velocity, $\langle\overline{u}\rangle$ is the double-averaged streamwise velocity, z is the height above the maximum bed elevation, d is flow depth and D_{84} is the grain size at which 84 per cent of the bed material is finer. A lateral position of 0 mm denotes the centreline of the flume and the streamwise position relates to the position in the DEM of the bed (Figure 4.27).

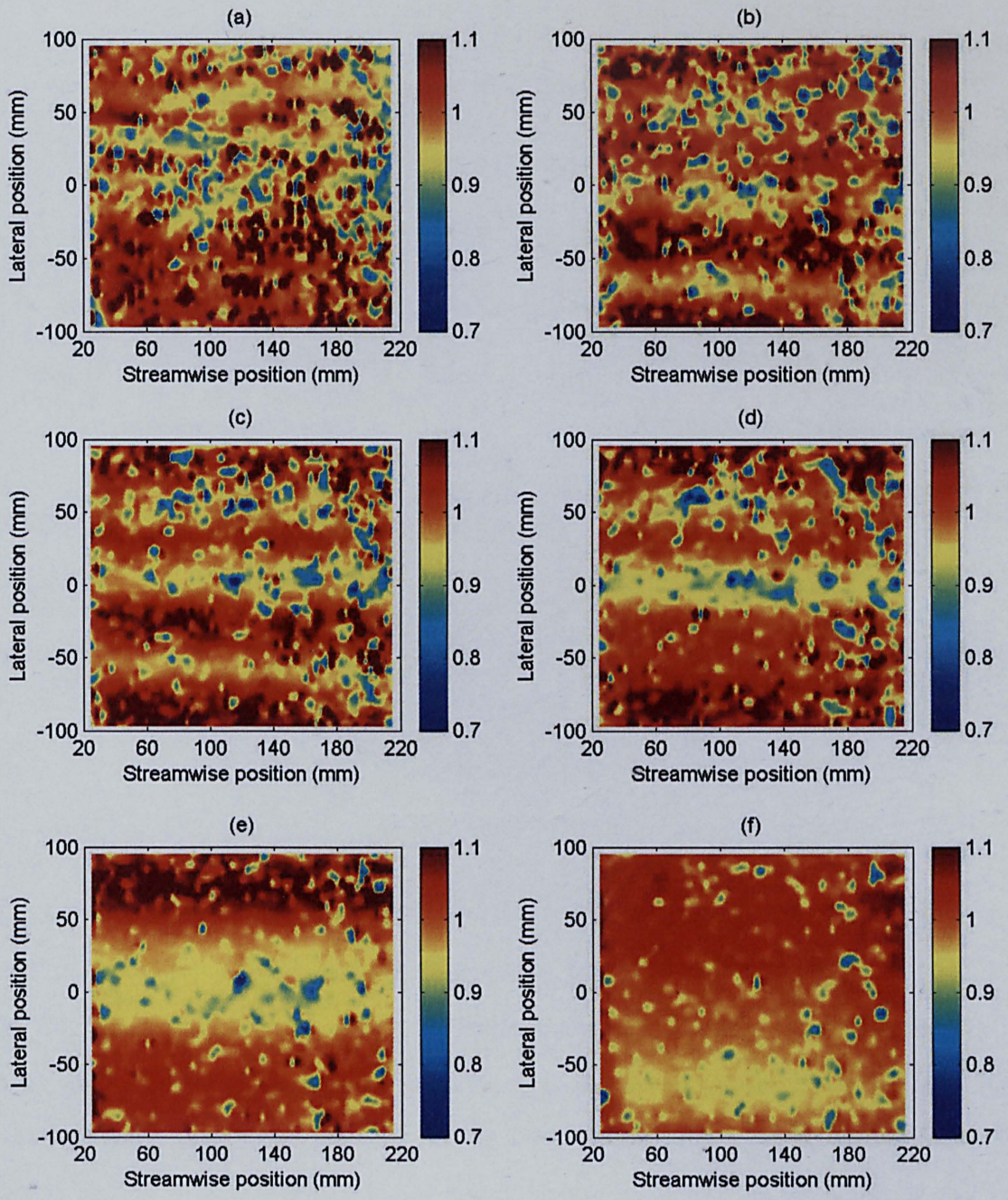

Figure 4.31. The spatial distribution of $\overline{u}/\langle\overline{u}\rangle$ over the bimodal bed at $z/d = 0.22$ for the experimental runs performed at a single bed slope with (a) $d/D_{84} = 2.6$; (b) $d/D_{84} = 4.1$; (c) $d/D_{84} = 5.7$; (d) $d/D_{84} = 6.9$; (e) $d/D_{84} = 9.0$; and (f) $d/D_{84} = 12.8$, where $\overline{u}$ is the time-averaged streamwise velocity, $\langle\overline{u}\rangle$ is the double-averaged streamwise velocity, z is the height above the maximum bed elevation, d is flow depth and D_{84} is the grain size at which 84 per cent of the bed material is finer. A lateral position of 0 mm denotes the centreline of the flume and the streamwise position relates to the position in the DEM of the bed (Figure 4.27).

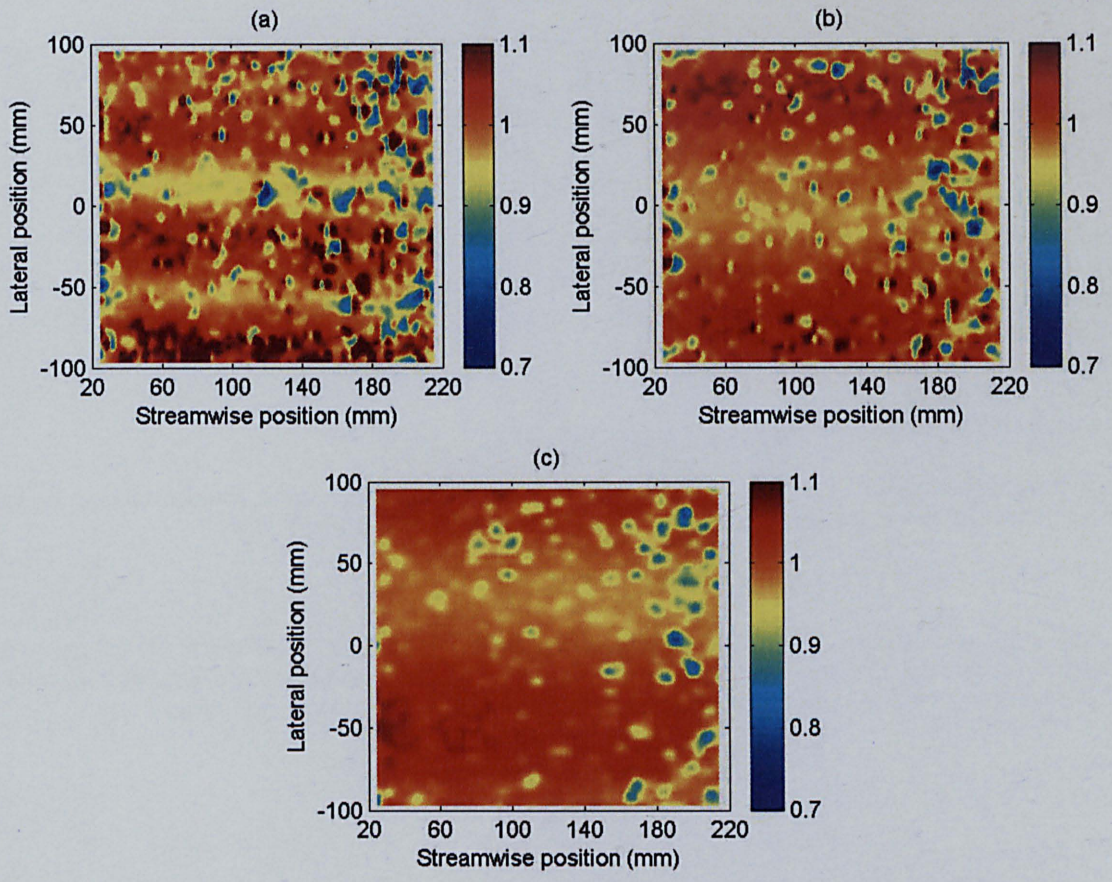

Figure 4.32. The spatial distribution of $\overline{u}/\langle\overline{u}\rangle$ over the bimodal bed at $z/d = 0.34$ for the experimental runs performed at a single bed slope with (a) $d/D_{84} = 5.7$; (b) $d/D_{84} = 9.0$; and (c) $d/D_{84} = 12.8$, $\overline{u}$ is the time-averaged streamwise velocity, $\langle\overline{u}\rangle$ is the double-averaged streamwise velocity, z is the height above the maximum bed elevation, d is flow depth and D_{84} is the grain size at which 84 per cent of the bed material is finer. A lateral position of 0 mm denotes the centreline of the flume and the streamwise position relates to the position in the DEM of the bed (Figure 4.27).

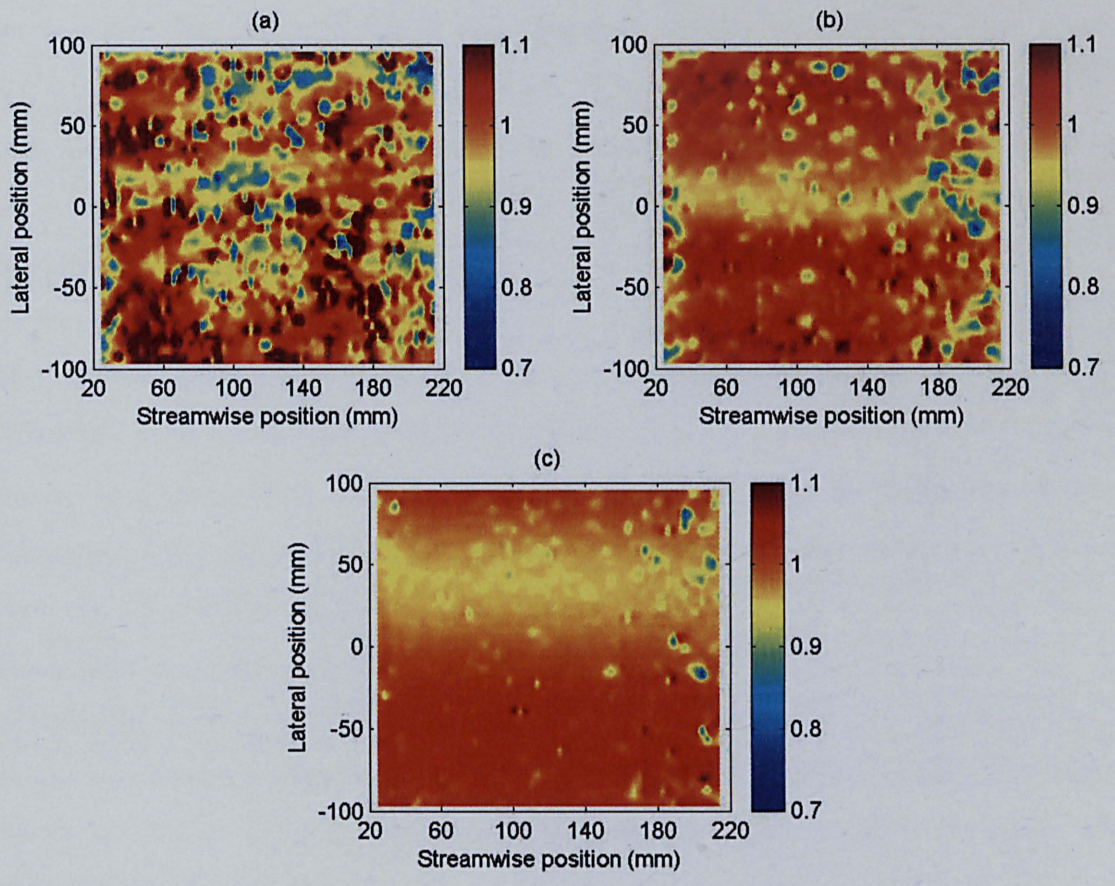

Figure 4.33. The spatial distribution of $\overline{u}/\langle\overline{u}\rangle$ over the bimodal bed at $z/d = 0.45$ for the experimental runs performed at a single bed slope with (a) $d/D_{84} = 2.6$; (b) $d/D_{84} = 6.9$; and (c) $d/D_{84} = 12.8$, $\overline{u}$ is the time-averaged streamwise velocity, $\langle\overline{u}\rangle$ is the double-averaged streamwise velocity, z is the height above the maximum bed elevation, d is flow depth and D_{84} is the grain size at which 84 per cent of the bed material is finer. A lateral position of 0 mm denotes the centreline of the flume and the streamwise position relates to the position in the DEM of the bed (Figure 4.27).

At $z/D_{84} = 0.71$, the movement away from the bed surface has caused the distinction of the high-speed streaks to reduce, but the low-speed spots that appeared at $z/D_{84} = 0.43$ are present in the same locations, although several new spots have now appeared (Figure 4.35). There is still some degree of spatial persistence in some of the spots across the plots. This also applies at $z/D_{84} = 1.00$ and $z/D_{84} = 1.29$ (Figures 4.36 and 4.37), but there is less of a spatial correspondence with the lower measurement heights.

At these higher z/D_{84} the effect of relative submergence is now unclear, as the high-speed streaks begin to amalgamate and disappear, as seen earlier for the plots above $z/d = 0.34$. This continues at $z/D_{84} = 1.57$, with nearly all the plots showing that the high-speed streaks have disappeared. There is also a large reduction in the number of low-speed spots (Figure 4.38). The spatial patterns at $z/D_{84} = 2.57$ further confirm this (Figure 4.39).

The vertical change in the pattern can be seen by examining the contour plots of an individual experimental run at different values of z/D_{84}. Two examples of this are shown in Figures 4.40 and 4.41 for the experimental runs carried at relative submergences of 5.7 and 12.9, respectively. These are indicative of the two types of vertical change that occurs in the spatial pattern of $\overline{u}/\langle\overline{u}\rangle$ for the six experimental runs. The former demonstrates how the spatial pattern of several high-speed streaks over the bed transforms from the bed surface towards the water surface, and the latter how a pattern that consists of just one large area of higher velocity changes vertically. It also shows how the spatial correspondence in the low-speed spots changes vertically, and with relative submergence.

At a relative submergence of 5.6, it can be seen that there is a consistent and progressive disappearance of the four high-speed streaks with height above the bed, such that close to the water surface, there is a fairly homogeneous pattern over the bed (Figure 4.40). This largely occurs through a progressively greater amalgamation of the four high-speed streaks which appear at the lowest z/D_{84}. It also shows that only a small number of low-speed spots occur at the same locations in all of the plots, and this number decreases with height above the bed. However, there are a number of low-speed spots that only occur in one of the plots. This progressive amalgamation of the high-speed streaks and decrease in spatial persistence in the low-speed spots with height above the bed also occurred at relative submergences of 2.6, 4.1 and 6.9. At a relative submergence of 9.0, the high-speed streaks were not so clearly present close to the bed so the vertical change in the spatial pattern was not associated with a progressive amalgamation of the high-speed streaks, but instead with a progressive increase in the spatial uniformity of the flow. These consistent vertical changes in the spatial pattern of $\overline{u}/\langle\overline{u}\rangle$ for an individual experimental run at the five lowest submergences correspond with the fairly uniform decrease in $\sigma_{\overline{u}}$ with z/d seen in Figure 4.6.

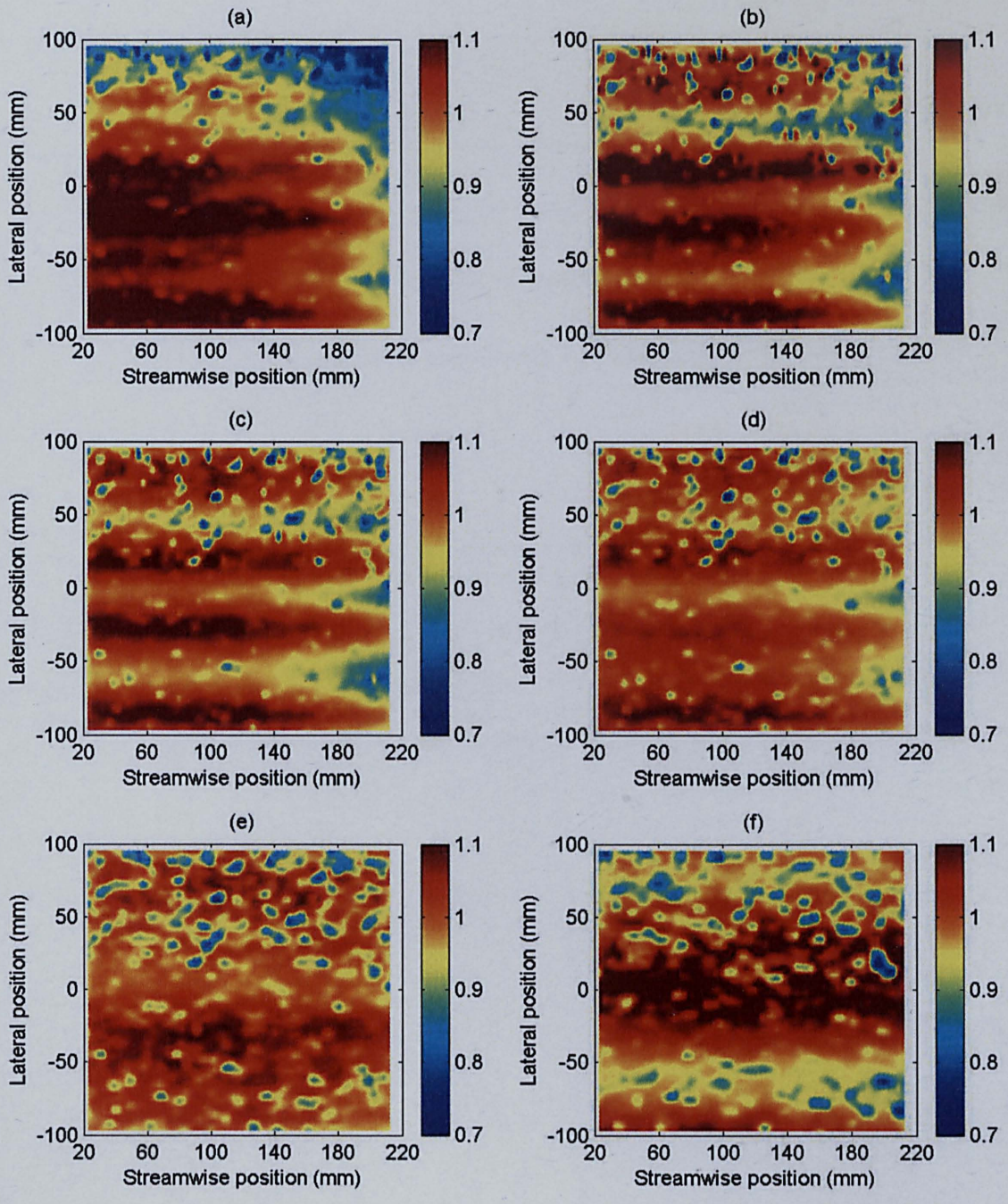

Figure 4.34. The spatial distribution of $\overline{u}/\langle\overline{u}\rangle$ over the unimodal bed at $z/D_{84} = 0.43$ for the experimental runs performed at a single bed slope with (a) $d/D_{84} = 2.6$; (b) $d/D_{84} = 4.1$ (c) $d/D_{84} = 5.6$; (d) $d/D_{84} = 6.9$; (e) $d/D_{84} = 9.0$; and (f) $d/D_{84} = 12.9$, where $\overline{u}$ is the time-averaged streamwise velocity, $\langle\overline{u}\rangle$ is the double-averaged streamwise velocity, z is the height above the maximum bed elevation, d is flow depth and D_{84} is the grain size at which 84 per cent of the bed material is finer. A lateral position of 0 mm denotes the centreline of the flume and the streamwise position relates to the position in the DEM of the bed (Figure 4.19).

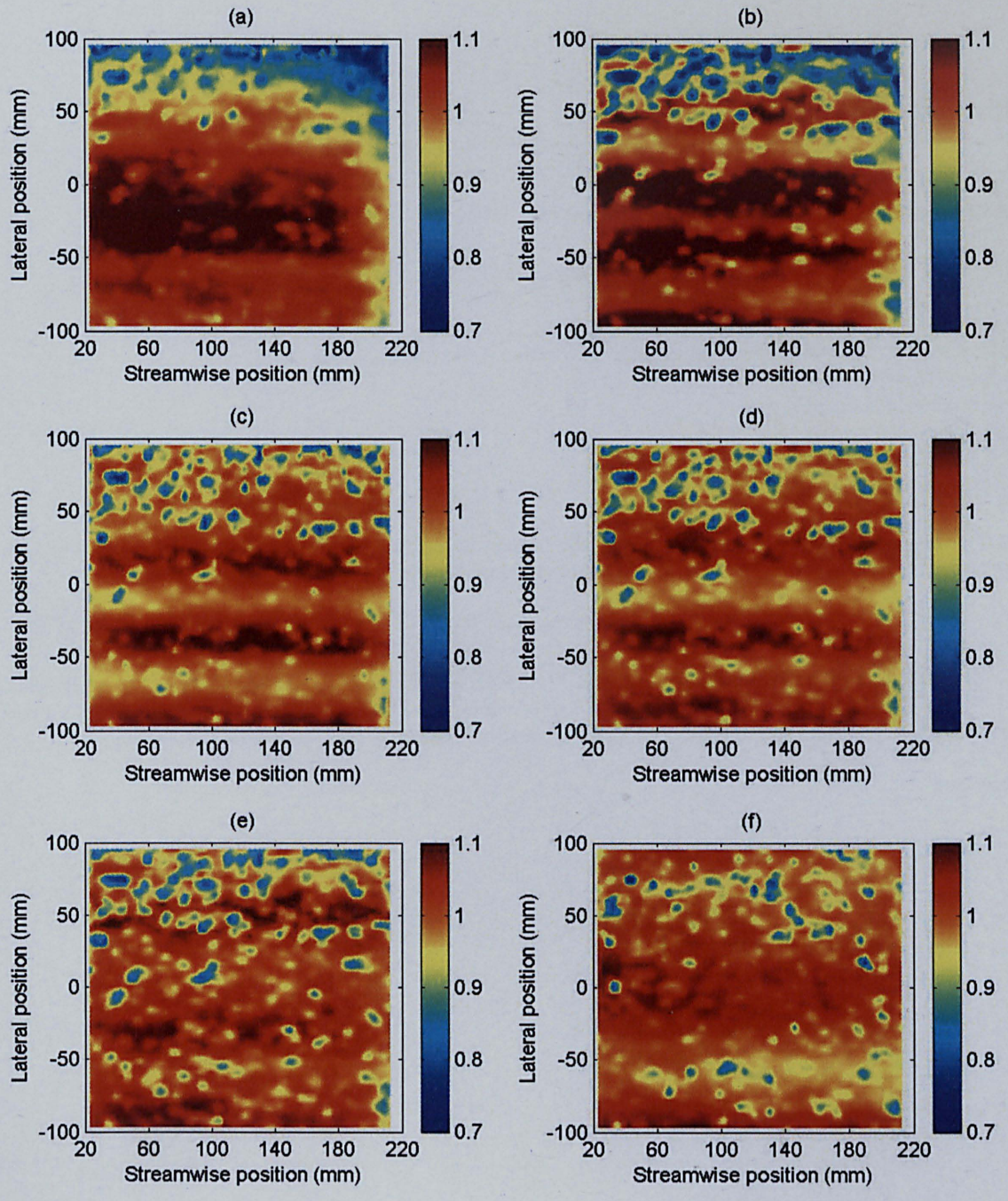

Figure 4.35. The spatial distribution of $\overline{u}/\langle\overline{u}\rangle$ over the unimodal bed at $z/D_{84} = 0.71$ for the experimental runs performed at a single bed slope with (a) $d/D_{84} = 2.6$; (b) $d/D_{84} = 4.1$ (c) $d/D_{84} = 5.6$; (d) $d/D_{84} = 6.9$; (e) $d/D_{84} = 9.0$; and (f) $d/D_{84} = 12.9$, where $\overline{u}$ is the time-averaged streamwise velocity, $\langle\overline{u}\rangle$ is the double-averaged streamwise velocity, z is the height above the maximum bed elevation, d is flow depth and D_{84} is the grain size at which 84 per cent of the bed material is finer. A lateral position of 0 mm denotes the centreline of the flume and the streamwise position relates to the position in the DEM of the bed (Figure 4.19).

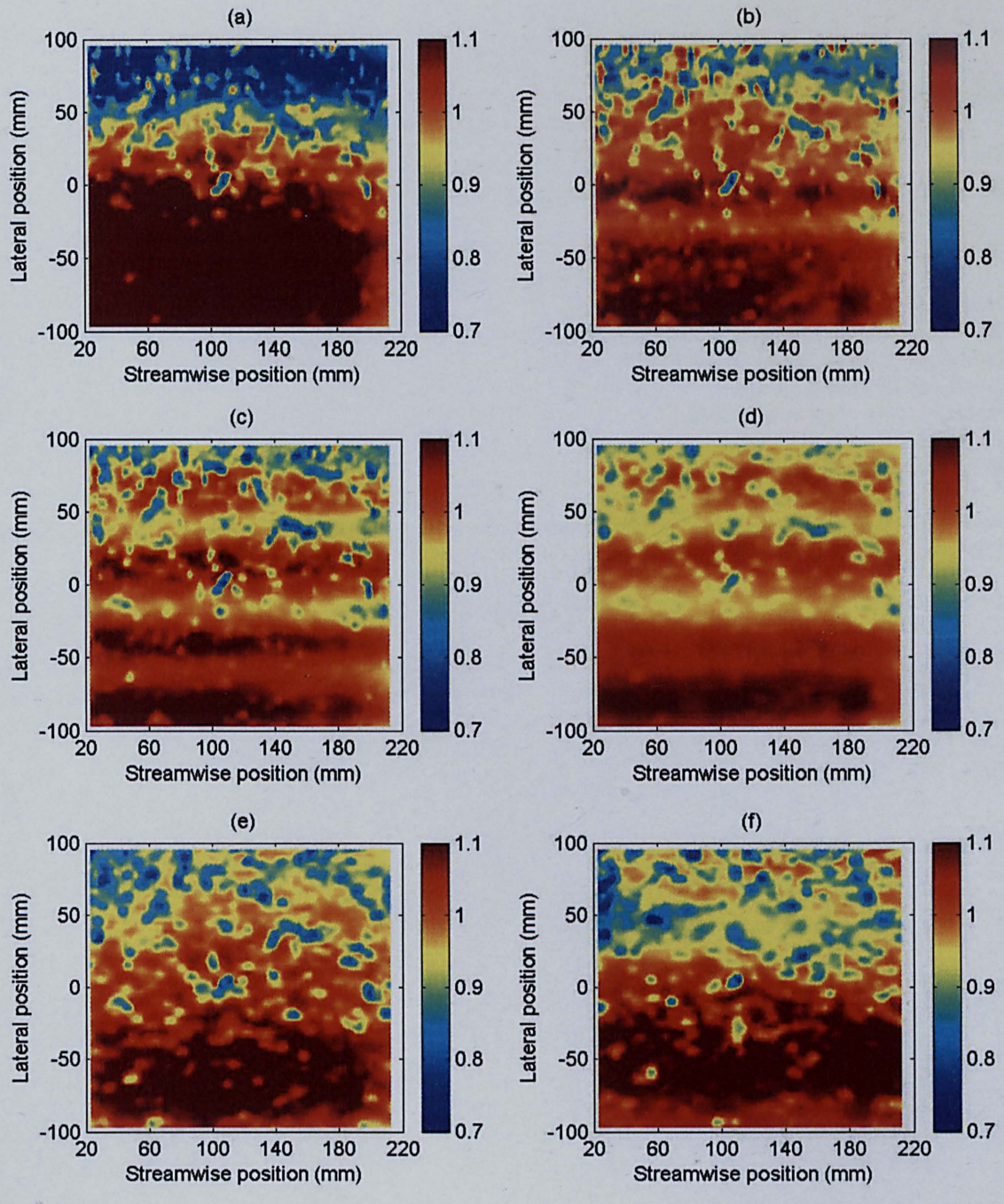

Figure 4.36. The spatial distribution of $\overline{u}/\langle\overline{u}\rangle$ over the unimodal bed at $z/D_{84} = 1.00$ for the experimental runs performed at a single bed slope with (a) $d/D_{84} = 2.6$; (b) $d/D_{84} = 4.1$ (c) $d/D_{84} = 5.6$; (d) $d/D_{84} = 6.9$; (e) $d/D_{84} = 9.0$; and (f) $d/D_{84} = 12.9$, where $\overline{u}$ is the time-averaged streamwise velocity, $\langle\overline{u}\rangle$ is the double-averaged streamwise velocity, z is the height above the maximum bed elevation, d is flow depth and D_{84} is the grain size at which 84 per cent of the bed material is finer. A lateral position of 0 mm denotes the centreline of the flume and the streamwise position relates to the position in the DEM of the bed (Figure 4.19).

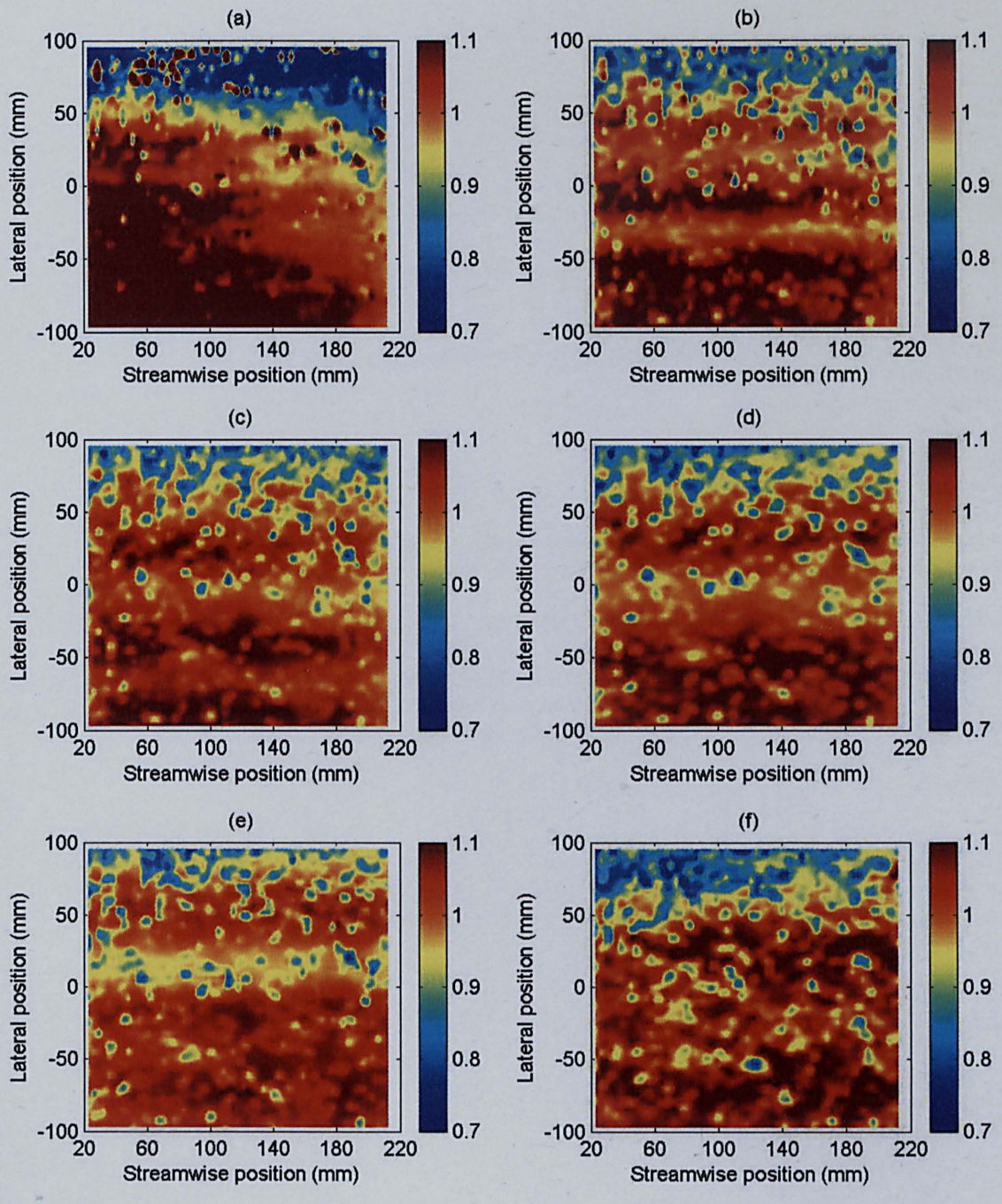

Figure 4.37. The spatial distribution of $\overline{u}/\langle\overline{u}\rangle$ over the unimodal bed at $z/D_{84}=1.29$ for the experimental runs performed at a single bed slope with (a) $d/D_{84}=2.6$; (b) $d/D_{84}=4.1$ (c) $d/D_{84}=5.6$; (d) $d/D_{84}=6.9$; (e) $d/D_{84}=9.0$; and (f) $d/D_{84}=12.9$, where $\overline{u}$ is the time-averaged streamwise velocity, $\langle\overline{u}\rangle$ is the double-averaged streamwise velocity, z is the height above the maximum bed elevation, d is flow depth and D_{84} is the grain size at which 84 per cent of the bed material is finer. A lateral position of 0 mm denotes the centreline of the flume and the streamwise position relates to the position in the DEM of the bed (Figure 4.19).

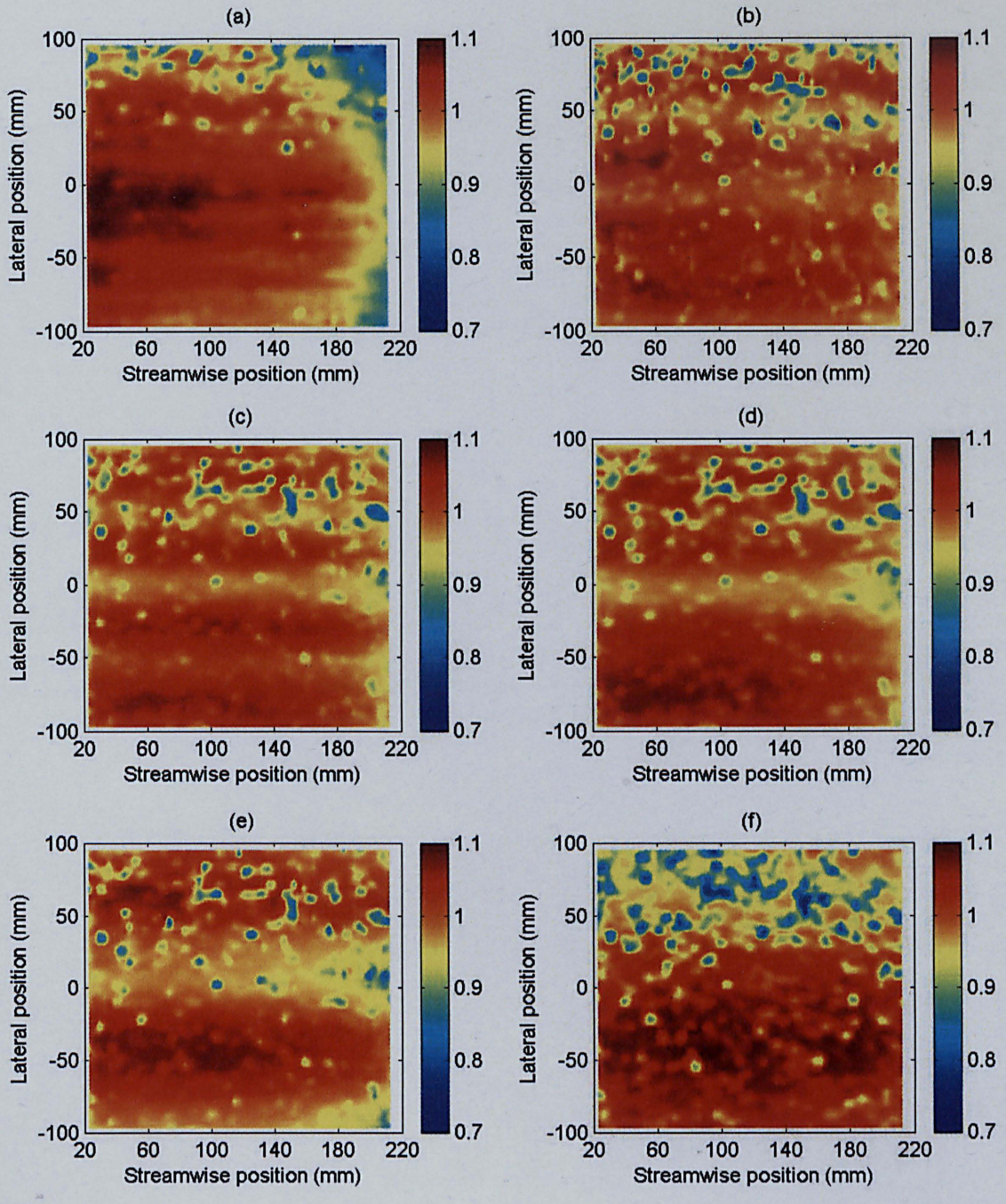

Figure 4.38. The spatial distribution of $\overline{u}/\langle\overline{u}\rangle$ over the unimodal bed at $z/D_{84}=1.57$ for the experimental runs performed at a single bed slope with (a) $d/D_{84}=2.6$; (b) $d/D_{84}=4.1$ (c) $d/D_{84}=5.6$; (d) $d/D_{84}=6.9$; (e) $d/D_{84}=9.0$; and (f) $d/D_{84}=12.9$, where $\overline{u}$ is the time-averaged streamwise velocity, $\langle\overline{u}\rangle$ is the double-averaged streamwise velocity, z is the height above the maximum bed elevation, d is flow depth and D_{84} is the grain size at which 84 per cent of the bed material is finer. A lateral position of 0 mm denotes the centreline of the flume and the streamwise position relates to the position in the DEM of the bed (Figure 4.19).

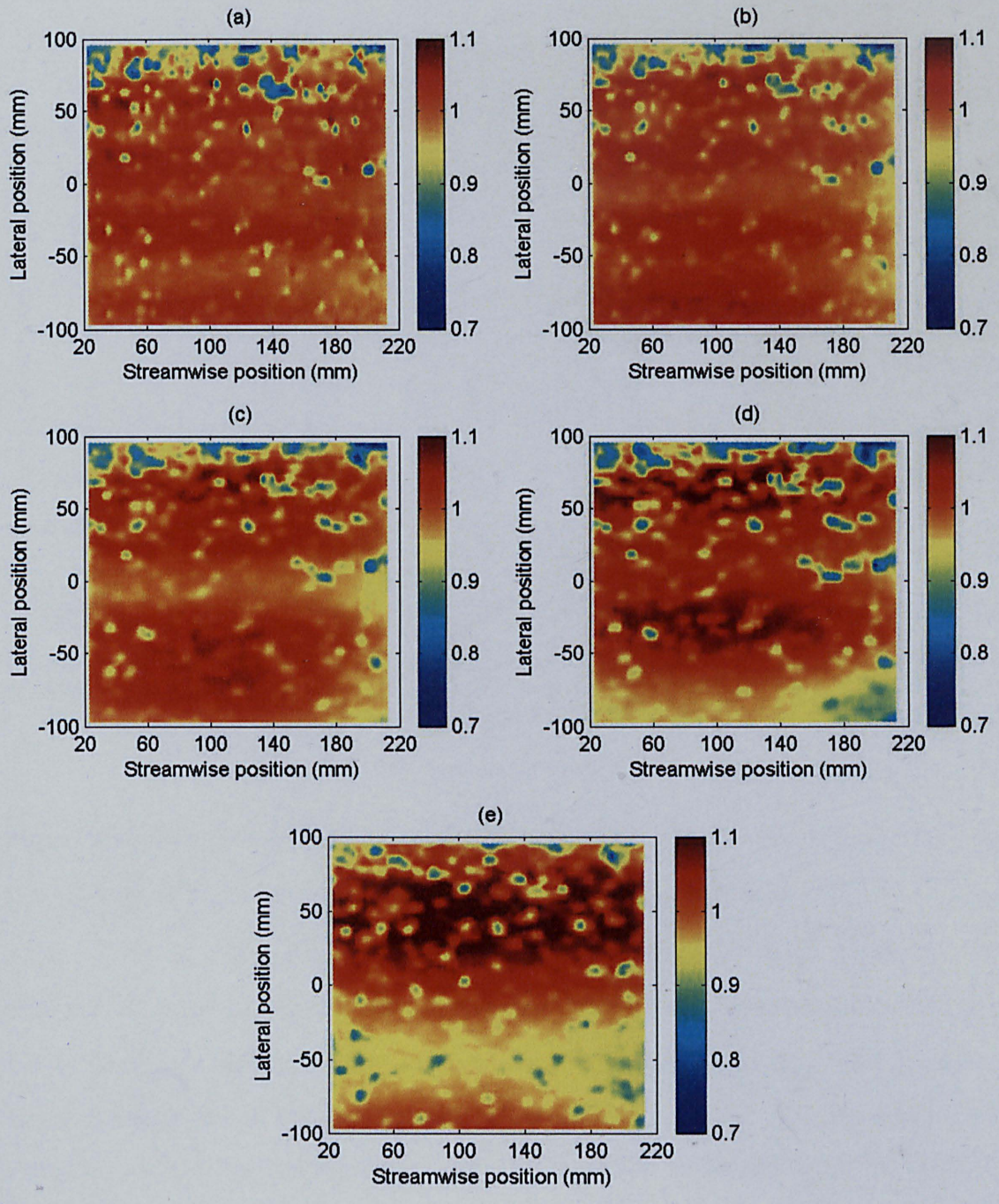

Figure 4.39. The spatial distribution of $\overline{u}/\langle\overline{u}\rangle$ over the unimodal bed at $z/D_{84} = 2.57$ for the experimental runs performed at a single bed slope with (a) $d/D_{84} = 4.1$; (b) $d/D_{84} = 5.6$; (c) $d/D_{84} = 6.9$; (d) $d/D_{84} = 9.0$; and (e) $d/D_{84} = 12.9$, where $\overline{u}$ is the time-averaged streamwise velocity, $\langle\overline{u}\rangle$ is the double-averaged streamwise velocity, z is the height above the maximum bed elevation, d is flow depth and D_{84} is the grain size at which 84 per cent of the bed material is finer. A lateral position of 0 mm denotes the centreline of the flume and the streamwise position relates to the position in the DEM of the bed (Figure 4.19).

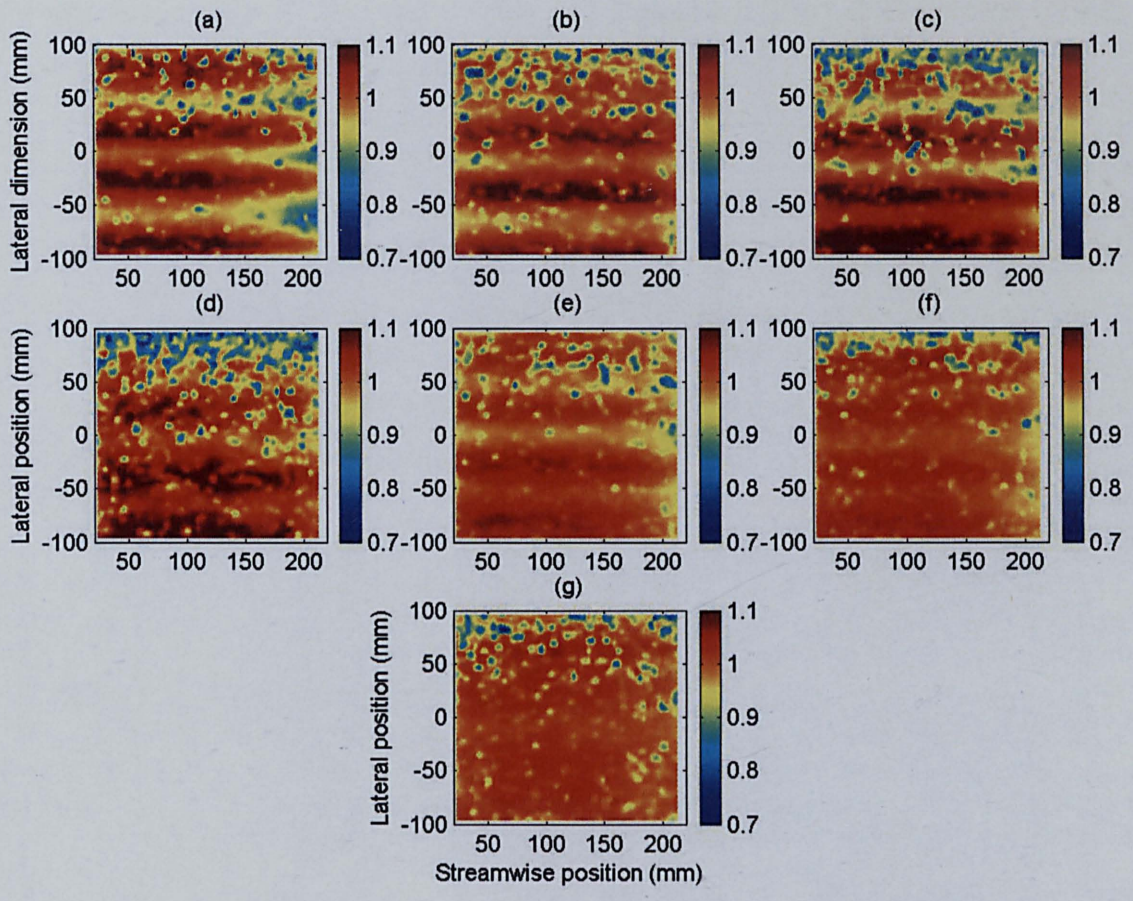

Figure 4.40. The spatial distribution of $\overline{u}/\langle\overline{u}\rangle$ over the unimodal bed for experimental run 3U with $d/D_{84} = 6.9$ at (a) $z/D_{84} = 0.43$; (b) $z/D_{84} = 0.71$; (c) $z/D_{84} = 1.00$; (d) $z/D_{84} = 1.29$; (e) $z/D_{84} = 1.57$; (f) $z/D_{84} = 2.57$; and (g) $z/D_{84} = 4.15$, where $\overline{u}$ is the time-averaged streamwise velocity, $\langle\overline{u}\rangle$ is the double-averaged streamwise velocity, d is flow depth, z is the height above the maximum bed elevation and D_{84} is the grain size at which 84 per cent of the bed material is finer. A lateral position of 0 mm denotes the centreline of the flume and the streamwise position relates to the position in the DEM of the bed (Figure 4.19).

The contour plots at a higher relative submergence of 12.9, however, show a very different vertical change in the spatial pattern of $\overline{u}/\langle\overline{u}\rangle$ (Figure 4.41). Although on the whole the flow becomes more uniform with increases in height above the bed, there is no progressive and consistent vertical change in the spatial pattern. It often alternates from becoming more uniform to more variable with height above the bed, such as between plots (a), (b) and (c). This could explain why this experimental run had such a different vertical profile in $\sigma_{\overline{u}}$ in comparison to the other runs. The contour plots

further confirm that the low-speed spots and high-speed areas display lower spatial persistence at the higher relative submergences.

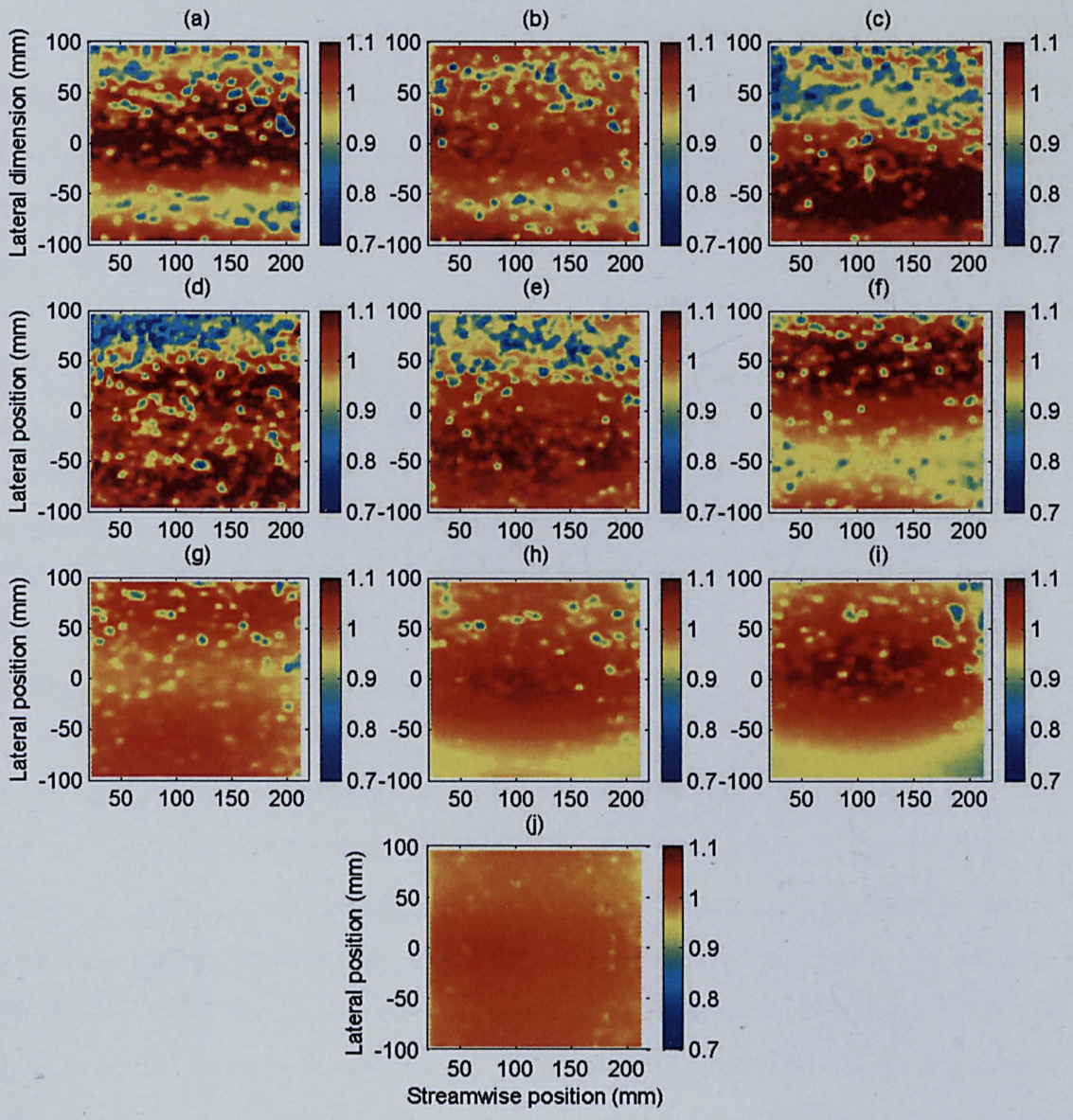

Figure 4.41. The spatial distribution of $\overline{u}/\langle\overline{u}\rangle$ over the unimodal bed for experimental run 6U with $d/D_{84}=12.9$ at (a) $z/D_{84}=0.43$; (b) $z/D_{84}=0.71$; (c) $z/D_{84}=1.00$; (d) $z/D_{84}=1.29$; (e) $z/D_{84}=1.57$; (f) $z/D_{84}=2.57$; (g) $z/D_{84}=4.15$; (h) $z/D_{84}=5.43$; (i) $z/D_{84}=7.58$; and (j) $z/D_{84}=11.44$, where $\overline{u}$ is the time-averaged streamwise velocity, $\langle\overline{u}\rangle$ is the double-averaged streamwise velocity, d is flow depth, z is the height above the maximum bed elevation and D_{84} is the grain size at which 84 per cent of the bed material is finer. A lateral position of 0 mm denotes the centreline of the flume and the streamwise position relates to the position in the DEM of the bed (Figure 4.19).

4.10.2 Bimodal Bed

The spatial distribution of the deviations at $z/D_{84} = 0.42$ over the bimodal bed is shown in Figure 4.42. It can be seen that the patterns are again not as variable as seen at the same z/d, with the same changes occurring with relative submergence as seen over the unimodal bed. Indeed, the changes in the spatial patterns with z/D_{84} also closely match those seen over the unimodal bed, and are therefore not shown here. The high-speed streaks disappear at a slightly higher height of $z/D_{84} = 2.58$ than that seen over the unimodal bed.

The vertical change in the spatial pattern for the five lowest submergences was very similar to that seen over the unimodal bed for the same submergences. At the highest submergence, there was again no consistent vertical change in the spatial pattern, with an alternation between an increase in uniformity and variability, with height above the bed. The result is that the changes in the vertical structure of the spatial patterns between the highest and the five lowest submergences again reflect the differences in the vertical profiles of $\sigma_{\bar{u}}$ in Figure 4.6.

It would appear that over both the beds the spatial pattern has a greater similarity between the experimental runs at the same z/D_{84} than at the same z/d, particularly for the low to mid relative submergences. If high-speed streaks are present they tend to occur across all the experimental runs, apart from at the highest relative submergence and the low-speed spots tend to show greater spatial persistence than seen at the same z/d. It would appear that bed roughness controls the appearance of the high-speed streaks over the bed, with the disappearance occurring at nearly the same z/D_{84} for each of the experimental runs. However, because at the same z/D_{84} the spatial patterns are comparable at similar relative submergences, it suggests that the effect of bed roughness could be some function of relative submergence. It is therefore likely that the spatial pattern of $\bar{u}/\langle\bar{u}\rangle$ is influenced by a combination of bed roughness and flow depth. Bed roughness appears to be the main influence on the spatial pattern of $\bar{u}/\langle\bar{u}\rangle$ at the low and mid relative submergences, but there is some smoothing out of the effects of the bed at the higher submergences.

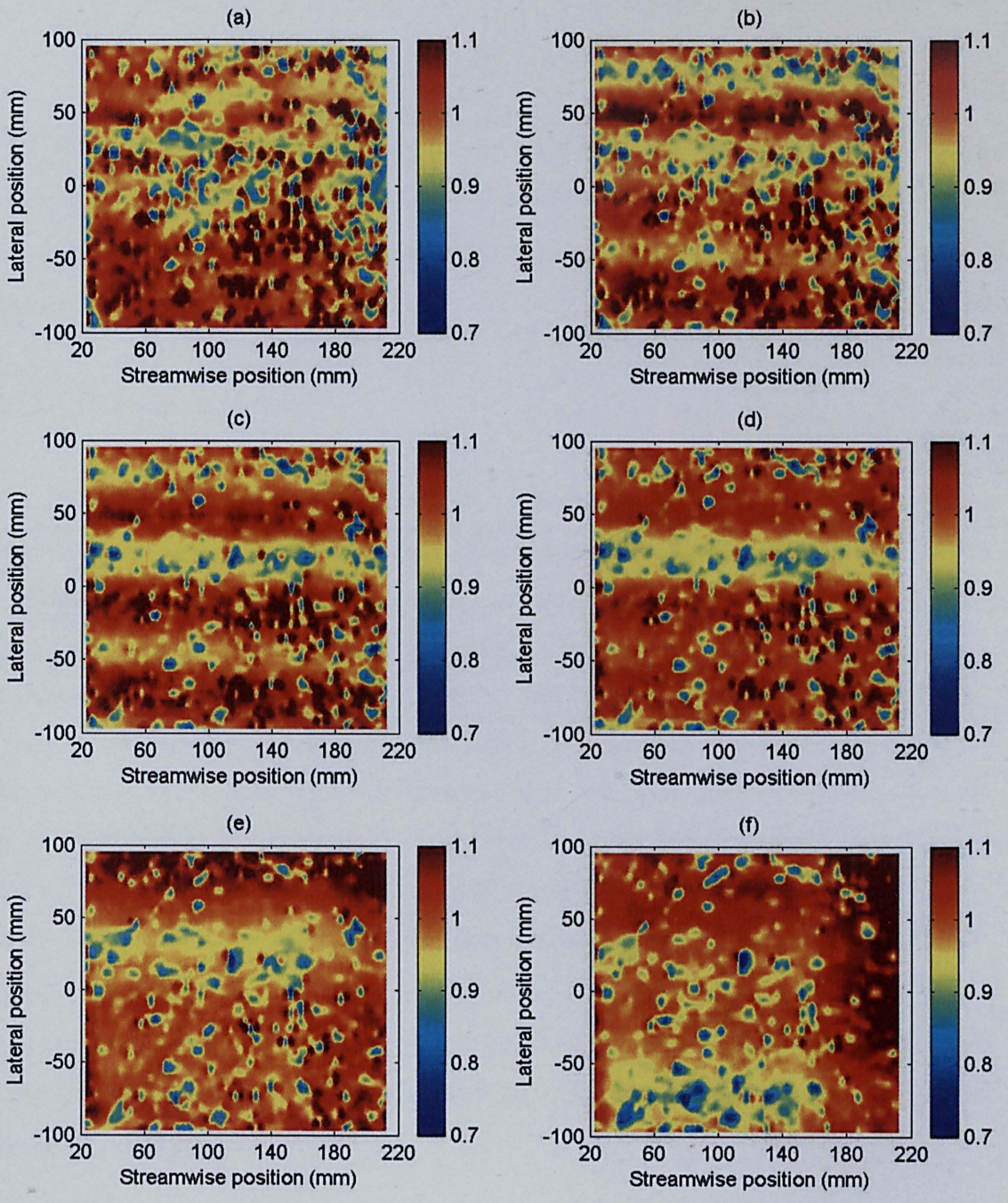

Figure 4.42. The spatial distribution of $\overline{u}/\langle\overline{u}\rangle$ over the bimodal bed at $z/D_{84} = 0.42$ for the experimental runs performed at a single bed slope with (a) $d/D_{84} = 4.1$; (b) $d/D_{84} = 5.7$; (c) $d/D_{84} = 6.9$; (d) $d/D_{84} = 9.0$; and (e) $d/D_{84} = 12.8$, where $\overline{u}$ is the time-averaged streamwise velocity, $\langle\overline{u}\rangle$ is the double-averaged streamwise velocity, z is the height above the maximum bed elevation, d is flow depth and D_{84} is the grain size at which 84 per cent of the bed material is finer. A lateral position of 0 mm denotes the centreline of the flume and the streamwise position relates to the position in the DEM of the bed (Figure 4.27).

4.11 The Relationship between the Pattern of Spatial Deviations and Bed Surface Topography

The DEMs of the two beds were used so that a simple visual comparison can be firstly made between the contour plots of $\overline{u}/\langle\overline{u}\rangle$ and the bed surface topography. This will be followed by a more rigorous treatment of the relationship between $\overline{u}/\langle\overline{u}\rangle$ and bed surface elevation.

4.11.1 Visual Examination

The DEM for the unimodal bed shows the following, moving from the highest lateral position to the lowest. There is a zone of higher elevations towards the top right of the plot, followed by a larger zone of lower elevations which is diagonally orientated, and then a small area of lower elevations located in the bottom right of the plot where a depressed diagonal zone is evident from the bottom left to the mid-right of the DEM (Figure 4.19). If there was a simple correlation between bed surface elevation and $\overline{u}$, this topography would suggest that there would be matching areas of higher and lower velocity, caused by the bed surface, on average, inducing acceleration and deceleration in the flow as it flows over the varying elevations. It can be seen that in no contour plots of $\overline{u}/\langle\overline{u}\rangle$ does this occur. Many of the plots instead display a greater number of high-speed streaks (and in some cases low-speed streaks) than such a correlation would indicate, and none of the streaks are orientated towards the top right of the plot. It would appear that the large-scale organisation of $\overline{u}/\langle\overline{u}\rangle$ over the bed does not resemble that of the bed surface elevations.

This is also seen over the bimodal bed. The DEM of the bimodal bed shows that, unlike the unimodal bed, there is no clear structuring of the bed, but just local depressions and local areas of higher elevation (Figure 4.27). It is unlikely therefore that such a topography could induce the streaks of high and low-speed fluid over the bed. The fact that high-speed streaks were found to occur over both beds, which have different surface topographies, further indicates that bed surface topography is unlikely to have induced such features.

There were small, discrete areas of the bed experiencing slower than average flow over both beds. These varied in size from approximately D_{50} to the order of two to four D_{50}. There are localised areas of higher and lower elevations over both beds that could induce flow features like these. It could be that the small-scale organisation of $\overline{u}/\langle\overline{u}\rangle$ may be better associated with the surface topography of the bed. However, a visual comparison between the DEM of the two beds and the spatial pattern of $\overline{u}/\langle\overline{u}\rangle$ suggests that this is unlikely. This is further suggested by the fact that new spots appear and the spatial locations of existing spots change from close to the bed to further up into the flow.

4.11.2 Cross-correlation

To discover whether there is any association between the spatial pattern of $\overline{u}/\langle\overline{u}\rangle$ and the bed surface topography a more formal examination is required. This is achieved through a simple cross-correlation between $\overline{u}/\langle\overline{u}\rangle$ and bed surface elevation. This is only carried out for the measurements of $\overline{u}/\langle\overline{u}\rangle$ and bed surface elevation that have the same lateral positions over the bed. This clearly does not take into account any lateral correlation in bed surface elevation that could influence $\overline{u}/\langle\overline{u}\rangle$. In other words it does not account for the effect of any spatially coherent bed structure that could influence $\overline{u}/\langle\overline{u}\rangle$. A cross-correlogram was used to quantify the spatial covariance between pairs of $\overline{u}/\langle\overline{u}\rangle$ and bed surface elevation measurements. A series of streamwise lags l_x between $\overline{u}/\langle\overline{u}\rangle$ and bed surface elevation z_b were applied to take into account the streamwise propagation of the flow relative to the bed. Using a cross-correlogram in this way means that the cross-covariance C between $\overline{u}/\langle\overline{u}\rangle$ and z_b is given by

$$C(l_x) = \frac{1}{N_C} \sum_{x=3.150}^{N_C} \frac{\overline{u}}{\langle\overline{u}\rangle}(x) \cdot z_b(x - l_x) - m_{\overline{u}/\langle\overline{u}\rangle} \cdot m_{z_b} \qquad (4.7)$$

where

$$m_{\overline{u}/\langle\overline{u}\rangle} = \frac{1}{N_C} \sum_{x=3.150}^{N_C} \frac{\overline{u}}{\langle\overline{u}\rangle}(x) \qquad (4.8)$$

$$m_{z_b} = \frac{1}{N_C} \sum_{x=3.150}^{N_C} z_b(x - l_x) \tag{4.9}$$

and N_C is the number of cross-correlated measurements and x is the streamwise position within the measurement section. The $C(l_x)$ values depend on the magnitudes of $\overline{u}/\langle\overline{u}\rangle$ and z_b so a cross-correlogram was used to calculate the correlation coefficient η to provide a more bounded measure of spatial cross-correlation (Legleiter *et al.*, in press):

$$\eta(l_x) = \frac{C(l_x)}{\sqrt{\sigma^2_{\overline{u}/\langle\overline{u}\rangle} \cdot \sigma^2_{z_b \Delta x}}} \in [-1, +1] \tag{4.10}$$

where

$$\sigma^2_{\overline{u}/\langle\overline{u}\rangle} = \frac{1}{N_C(l_x)} \sum_{x=3.150}^{N_C} \left[\frac{\overline{u}}{\langle\overline{u}\rangle}(x) - m_{\overline{u}/\langle\overline{u}\rangle} \right]^2 \tag{4.11}$$

and

$$\sigma^2_{z_{bl_x}} = \frac{1}{N_C} \sum_{x=2.265}^{N_C} \left[z_b(x - l_x) - m_{z_b} \right]^2 \tag{4.12}$$

A maximum lag of 100 mm was chosen to account fully for the propagation possible for the range of $\langle\overline{u}\rangle$ values. This resulted in less than the whole matrix of $\overline{u}/\langle\overline{u}\rangle$ values being available for the correlation, given the streamwise length of the DEMs. But it still resulted in 2170 paired measurements of $\overline{u}/\langle\overline{u}\rangle$ and z_b being cross-correlated for each l_x. The cross-correlation was firstly performed for all these $\overline{u}/\langle\overline{u}\rangle$ values, and then for the paired measurements where $\overline{u}/\langle\overline{u}\rangle > 1$ and finally for those paired measurements where $\overline{u}/\langle\overline{u}\rangle < 0.9$, to examine whether there is a lesser or greater correlation between the high-speed and low-speed flow features with the bed surface topography. Therefore the latter two correlations should provide information on whether the large-scale and/or the small-scale organisation of the flow is related to the bed surface topography.

The η values are shown in Figure 4.43 for the unimodal bed at $z/D_{84} = 0.43$. A η value of 1 indicates that there is a perfect linear positive correlation between $\overline{u}/\langle\overline{u}\rangle$ and z_b, -1 that there is a perfect linear negative correlation, and 0 that there is almost no linear correlation. The results show that for the correlation involving all the $\overline{u}/\langle\overline{u}\rangle$ values, there is a poor association between $\overline{u}/\langle\overline{u}\rangle$ and z_b (Figure 4.43a). The η values for $\overline{u}/\langle\overline{u}\rangle > 1$ are not noticeably different. This also applies for $\overline{u}/\langle\overline{u}\rangle < 0.9$, expect for the experimental run performed at the lowest relative submergence of 2.6. Over the bimodal bed at $z/D_{84} = 0.42$, the relationship between $\overline{u}/\langle\overline{u}\rangle$ and z_b is even poorer (Figure 4.44). These results for both of the beds were also found for higher values of z/D_{84}. Clearly neither the large-scale or small-scale spatial organisation of $\overline{u}/\langle\overline{u}\rangle$ is related in any simple manner to the bed surface elevation. However, given that a η value of zero does not necessarily mean that there is no correlation at all, the results do not rule out any subtle or more complicated association between $\overline{u}/\langle\overline{u}\rangle$ and z_b, such as a high non-linear correlation, or a relationship between $\overline{u}/\langle\overline{u}\rangle$ and any spatially coherent bed features.

Legleiter *et al.* (in press) examined the association between $\overline{u}/u_*$ and bed roughness d/k_s, where k_s is the equivalent sand roughness height. This was based on ADV measurements carried out within North Folk Cache La Pudre River, Colorado, a cobble-bedded river. This was performed over a riffle at three different discharges. They also discovered that the correlation was weak for all three flows, but that it did become a little stronger with an increase in relative submergence.

However, because of the low spatial resolution of velocity measurements within the reach and the low number of bed roughness measurements on which to relate these measurements of velocity to, their conclusions may not well supported. Only five streamwise lags were possible, with each having a metre separation between them. Therefore, the effects of bed roughness on the flow could only be very coarsely determined. Furthermore, the correlation was based on averaging $\overline{u}$ measurements taken within a vertical profile at one location to give a single value of $\overline{u}$ for that location over the bed. Often this was based on only one or two measurements in the profile, and it is unclear, at each location, how many $\overline{u}$ values were averaged and the measurement height of these averaged values. The measurement height would heavily

influence the averaged value. This may become clearer in the final published version of their study. Furthermore, measurements were not possible very close to the bed because of errors arising in the ADV measurements and problems with accurately positioning the probe. It is difficult to assess the effect of relative submergence on the strength of the association between $\overline{u}/u_*$ and d/k_s from only three discharges, and they acknowledge that at the mid discharge the flow patterns could not be well-defined because several of the measurements were discarded due to poor quality.

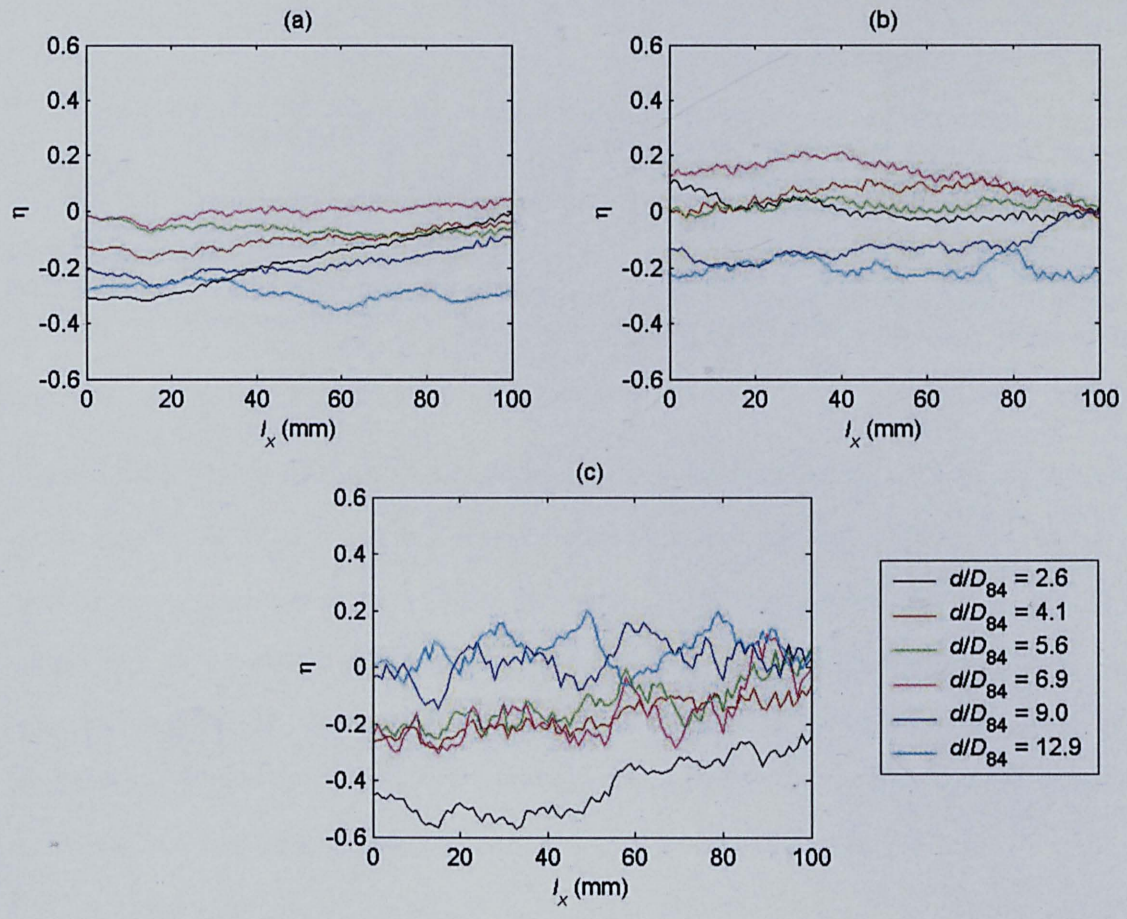

Figure 4.43. The coefficient of cross-correlation η between (a) $\overline{u}/\langle\overline{u}\rangle$ and bed surface elevation; (b) $\overline{u}/\langle\overline{u}\rangle > 1$ and bed surface elevation; and (c) and $\overline{u}/\langle\overline{u}\rangle < 0.9$ and bed surface elevation, at $z/D_{84} = 0.43$ for the experimental runs carried out at a single bed slope over the unimodal bed, where $\overline{u}$ is the time-averaged streamwise velocity, $\langle\overline{u}\rangle$ is the double-averaged streamwise velocity, z is the height above the maximum bed elevation, d is flow depth, D_{84} is the grain size at which 84 per cent of the bed material is finer and l_x is the streamwise lag between $\overline{u}/\langle\overline{u}\rangle$ and bed surface elevation.

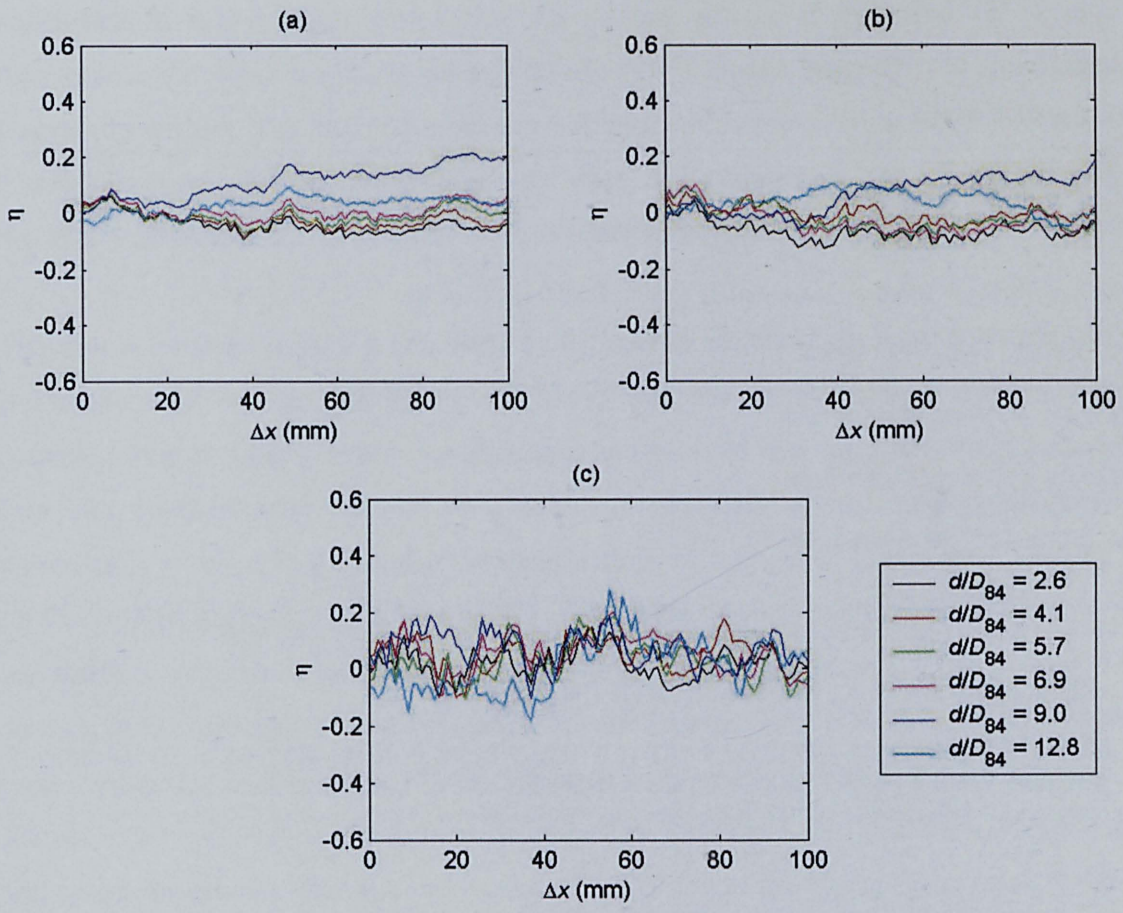

Figure 4.44. The coefficient of cross-correlation η between (a) $\overline{u}/\langle\overline{u}\rangle$ and bed surface elevation; (b) $\overline{u}/\langle\overline{u}\rangle > 1$ and bed surface elevation; and (c) and $\overline{u}/\langle\overline{u}\rangle < 0.9$ and bed surface elevation, at $z/D_{84} = 0.43$ for the experimental runs carried out at a single bed slope over the bimodal bed, where $\overline{u}$ is the time-averaged streamwise velocity, $\langle\overline{u}\rangle$ is the double-averaged streamwise velocity, z is the height above the maximum bed elevation, d is flow depth, D_{84} is the grain size at which 84 per cent of the bed material is finer and l_x is the streamwise lag between $\overline{u}/\langle\overline{u}\rangle$ and bed surface elevation.

The results in Figures 4.43 and 4.44 are not surprising given that the DEMs and the structure function plots (Figures 3.15 and 3.16) indicated that the beds were organised in a different manner, yet there is a remarkable similarity in the spatial pattern of $\overline{u}/\langle\overline{u}\rangle$. This spatial pattern was also found for preliminary tests over a different unimodal bed that had a narrower grain-size distribution, but was produced in the same way as described for the unimodal and bimodal beds. It may be that this kind of organisation of the time-averaged flow field is an inherent feature or instability of turbulent flows over

water-worked gravel beds. Given that the spatial pattern is modified by relative submergence, which is known to modify the flow, this further suggests it is an inherent feature of the flow. The fact that it occurred at high width/depth ratios (all were greater than 4) suggests that secondary currents were not responsible for its appearance, especially given that the pattern was more evident at the highest ratios.

The spatial pattern displays a similarity to the spatial structure observed for turbulent, instantaneous flow fields. Kline *et al.* (1967) was one of the first to discover this pattern. Using hydrogen bubble visualisation he observed that the flow was organised into long, spatially separated streaks which were essentially aligned in the streamwise direction. It resulted in a lateral alternating pattern of regions of relatively high-speed and low-speed regions. The instantaneous streamwise velocities within this later region are retarded relative to the time-averaged velocity and have been termed low-speed streaks. In the regions between the steaks, the streamwise velocities are in excess of the time-averaged velocity and are therefore termed high-speed regions or streaks. They are known to be a persistent and dominant feature of the near-wall flow for both smooth and rough boundaries (Smith and Metzler, 1983; Smith *et al.*, 1991; Grass *et al.*, 1991; Nezu and Nakagawa, 1993; Defina, 1996; Grass and Mansour-Tehrani, 1996). It has been seen, for example, over regularly packed spheres and gravel clasts. This streaky pattern has also been shown to occur for atmospheric boundary layers (e.g. Klewicki *et al.*, 1995; Schoppa and Hussain, 2002; Drobinski and Foster, 2003; Kanda *et al.*, 2004). Further information on low-speed streaks and the mechanism of their formation can be found in a review by Smith (1996).

A further similarity between patterns observed in $\overline{u}/\langle\overline{u}\rangle$ and this instantaneous streaky pattern is the way in which the pattern changes with height above the boundary. Measurements of the instantaneous velocity flow field and further streamwise observations of this pattern (e.g. Smith and Schwartz, 1983) have shown that it persists at a good distance from the boundary. This too was also seen for $\overline{u}/\langle\overline{u}\rangle$. Furthermore, the instantaneous streaky pattern has been shown to become progressively more broadly spaced, and less organised, until it essentially disappears (Smith, 1996). Again this was observed for $\overline{u}/\langle\overline{u}\rangle$.

The fact that the instantaneous streaky pattern has been found over boundaries of various roughness and bed configurations has led many to believe that these streaks are

a universal feature of boundary layer turbulence irrespective of wall roughness condition (Grass and Mansour-Tehrani, 1996, Smith, 1996). Grass *et al.* (1991) said that the remarkable feature of rough wall flow is the apparent ability to order itself very rapidly over a small vertical distance above the roughness elements and for it to be decoupled from the local influence of individual elements. The bed surface topographies of the unimodal and bimodal bed were different and yet produced a similar pattern of $\overline{u}/\langle\overline{u}\rangle$ over the bed, and showed no strong linear correlation with bed surface elevation, which is in line with these thoughts.

The fact that this can occur and yet the spatial pattern of $\overline{u}/\langle\overline{u}\rangle$ also showed some scaling with bed roughness, with it being more consistent at the same z/D_{84} rather than the same z/d, appear to be contrasting conclusions. However, the same has been found for the streaky pattern of the instantaneous flow field. It is an inherent feature of turbulent flows, regardless of the topography beneath, but bed roughness does affect its spatial structure, largely through its effect on the mean streamwise spacing and streamwise coherence of the low-speed streaks (Grass *et al.*, 1991; Defina, 1996; Grass and Mansour-Tehrani, 1996). There is again another similarity between the spatial patterns of $\overline{u}/\langle\overline{u}\rangle$ and the instantaneous flow field.

This does not necessarily suggest that what has been observed in the spatial pattern of $\overline{u}/\langle\overline{u}\rangle$ is a result of these turbulent features. For the instantaneous streaky pattern to be observed within the time-averaged flow field it would mean that it must be both temporally and spatially persistent. In other words it must occur in the same location and to be large enough in magnitude and to occur frequently enough to still appear after time averaging. For example, if the turbulent structures have a similar departure from $\overline{u}$, they must occur in the same location for more than 50 % of the time to cause the high-speed streaks in the spatial pattern of $\overline{u}/\langle\overline{u}\rangle$. Previous studies do not provide any extensive information on whether this would be possible, but it does appear to be unlikely. For example, Grass and Mansour-Tehraini (1996) found over a gravel boundary that low-speed streaks randomly shift their lateral position with time, and are therefore unlikely to have the spatial persistence required. Instead, it is likely that what has been observed is a different class of flow features: spatially coherent time-averaged flow structures. This class of structure has been observed over smooth boundaries. Large, outer region structures which appear to span the majority of the turbulent

boundary layer and dominate the flow when viewed on a time-averaged basis have been reported (e.g. Kovasznay *et al.*, 1970; Falco, 1977; Smith *et al.*, 1991). However, while significant energy is contained within these motions, Smith (1996) believes that they are inactive, dissipative and extract little energy from the time-averaged flow. Time-averaged vortical structures between regularly spaced 2-D transverse ribs (Campbell, pers. comm.), and over fixed 2-D dune shaped bedforms (Clunie, pers. comm) have also been discovered. Numerical simulations of airflow over arrays of cubes to simulate urban-like roughness using Large Eddy Simulation (Kanda *et al.*, 2004) using Reynolds-averaged Navier-Stokes (RANS) equations (Lien and Yee, 2004) and double-averaged Navier-Stokes equations (Coceal *et al.*, submitted) have also discovered the same structures.

The small, discrete areas of the bed experiencing slower than average flow over both of the beds are unlikely to be just transient eddies because of the length of the time-averaging window. It implies that the fixed-location spots may be caused by repeated bursting from certain locations on the bed, at positions somewhere a little upstream.

4.12 Summary

It has been investigated whether time-averaged streamwise velocities are spatially variable over two water-worked gravel beds. It was discovered that particular areas of the bed can experience values as low as 60 %, but also as high as 140 % of the double-averaged streamwise velocity. It means that some areas of the bed can have velocities that are over two times higher than those over other parts of the bed. Remarkably, this also applied to neighbouring locations over the bed. It resulted in the range of time-averaged streamwise velocities over the beds being similar in magnitude to the double-averaged streamwise velocity.

The velocities showed a considerable degree of organisation close to the beds. They were organised into streamwise streaks of high-speed fluid which were overlain by spots of low-speed fluid. This was consistent over the two beds, and has been observed over another water-worked gravel bed. A different class of flow features has therefore been recognised: spatially coherent time-averaged flow structures. This spatial organisation was found to be heavily dependent on relative submergence, but to show little association with bed surface topography. It suggests that the time-averaged flow

structures observed here might be an inherent feature of turbulent flows over water-worked gravel beds.

Increases in relative submergence caused a progressive decrease in the number of high-speed streaks over the bed, and their eventual disappearance. Furthermore, it resulted in a reduction in the distinction, number and spatial persistence of the low-speed spots. Overall, it caused an increase in the homogeneity of the distribution of time-averaged streamwise velocities over the bed. Nevertheless, flow depth did not fully scale the vertical variability in the spatial pattern. Instead, bed roughness appeared to control more heavily the spatial pattern observed across the different experimental runs, and to determine the height at which the organised spatial pattern disappeared and became homogenised. However, the effect of bed roughness could be some function of relative submergence. It is therefore likely that the spatial pattern is influenced by a combination of bed roughness and flow depth. Bed roughness appears to be the main influence on the spatial pattern at the low and mid relative submergences, but there is some smoothing out of the effects of the bed for the deeper flows.

The degree of spatial variability in the time-averaged streamwise velocities was more formally explored by examining the standard deviation in these values over the bed. It was found that the degree of spatial variability was large over both beds, but to be of a similar size over both beds, despite the differences in the bed surface topography of the two beds. It remained a reasonable size well into the upper reaches of the flow, indicating that spatial variability does not disappear within the logarithmic and outer layer as previously thought. This suggested that spatial variability is not entirely induced by bed surface topography. The vertical variation in relative spatial variability for an individual experimental run could be well approximated by an exponential function, of the form used to describe the vertical variation in turbulence intensity. However, a universal equation that could successfully approximate the degree of spatial variability could not be developed. The spatial variations are less significant than the temporal variations in instantaneous streamwise velocities. This indicates that spatial variations in the time-averaged flow are likely to transfer lower degrees of momentum within the fluid than turbulence.

The degree of spatial variability in time-averaged streamwise velocities was scaled by the double-averaged streamwise velocity, rather than bed shear velocity, and its vertical

variability was scaled by flow features that scale with flow depth rather than bed roughness. Furthermore, the degree of spatial variability through the whole of the flow depth was shown to increase clearly with relative submergence, such that it could be three times higher at the higher relative submergences than at the lower submergences. It shows that increases in relative submergence could result in a change in how much momentum is transferred by turbulent and spatial fluctuations in the flow, even when the mean bed shear stress is the same. It demonstrates that relative submergence could potentially have as important an influence on momentum transfer over water-worked gravel beds as bed surface topography.